An investigation into the dissolution of pyroxene: A precursor to mineral carbonation of PGM tailings in South Africa

Nicole Anne Meyer

a thesis submitted for the degree of
MSc in Engineering in Chemical Engineering
at the University of Cape Town,
South Africa.

2014

I know the meaning of plagiarism and declare that all the work in the document, save for that which is properly acknowledged, is my own.

Nicole Anne Meyer

9 June 2014

Synopsis

Carbon sequestration through mineral carbonation is becoming an increasingly attractive alternative for mitigating excess CO_2 in the atmosphere. Mineral carbonation is a natural process whereby CO_2 is fixed to CaFeMg-silicates to form Ca-, Fe-, and Mg-carbonates. This process is thermodynamically favourable and the products are benign and stable over millions of years. Pyroxene-rich tailings generated from the processing of PGM ores in South Africa have the potential to sequester significant amounts of CO_2 ($\sim$14 Mt per annum). In the indirect pH swing method, silicate minerals are initially leached at low pH and then carbonated at high pH. A previous study on these tailings highlighted the slow extraction of cations from orthopyroxene, the major Mg-host. The low reactivity of the orthopyroxene resulted in an overall low conversion of tailings to carbonates with only 30 % for Ca, 3 % for Mg and 9 % for Fe. Under similar experimental leach conditions, $\sim$100 % dissolution of olivine and serpentine can be achieved.

The stability caused by the polymerisation of the Si-O tetrahedra in the pyroxene structure decreases the rate of acidic dissolution to between 12 and 14.5 mol.cm^{-2}.s^{-1}, which is much slower than the rate for olivine (between 10.8 and 12 mol.cm^{-2}.s^{-1}). Polymerisation requires a bridging oxygen to link the Si-O tetrahedra together. The bridging oxygen to silicon bond is strong, and needs to be broken for the silicate mineral to dissolve. Therefore an understanding of silicate reactivity and reaction kinetics is needed if the reactivity of the orthopyroxene in these PGM tailings is to be increased. This study investigated the dissolution of pyroxene in two phases: 1) the reactivity of the pyroxene-rich PGM tailings in a mixture of mineral (HCl) and organic (oxalic acid and EDTA) acids; and 2) the effect of pyroxene composition (enstatite, diopside, augite, and wollastonite), particle size, and temperature on mineral dissolution.

The first phase of experiments investigated the contribution of organic chelators to silicate mineral dissolution. Although the extraction of Ca, Fe, Mg, and Si were relatively low under all conditions investigated, particularly for the case of Mg (between 3.3 % and 5.0 % extraction); the presence of oxalate generally increased the extraction of Si. Organic ligands increased dissolution by increasing the apparent solubility of silica in the solution, which allows for further metal cation extraction. A comparison of the extents of leaching with the mineralogical composition of the tailings indicated that the extracted Mg originated primarily from clinopyroxene, while orthopyroxene remained relatively inert under all experimental conditions. Plagioclase was the most reactive, especially in the presence of organic acids, and attained $\sim$30 % Ca dissolution.

The second phase of experiments showed that an increase in temperature and a decrease in particle size increased the reactivity of enstatite, augite, and diopside; however, the increase in temperature had a greater relative effect on the larger particle size fraction. The reactivity of the pyroxene group was wollastonite $>$ augite = diopside $>$ enstatite. The reactivities within the pyroxene group can be linked to their chemistry, with Ca-rich pyroxenes being more reactive than Mg-rich pyroxenes. The increase in cation size from Mg to Ca changes the coordination of the M2 site from 6- to 8-fold, thus decreasing the M2-O bond strength. Elemental distribution on the surface of reacting grains showed that the removal of Ca, Fe, and Mg was congruent with the removal of Si from the surface of the grains, and chemical analysis of the leachate revealed nonstoichiometric dissolution for augite, diopside, and wollastonite, but stoichiometric for enstatite. Again, chemical and mineralogical analyses confirmed the low reactivity of the pyroxenes investigated, except for wollastonite, which had almost complete dissolution of Ca. SEM images showed distinctive ‘stepped’ features on the surface of reacting pyroxene, which suggests a cleavage-dominated reaction mechanism.

From these results, a pyroxene reaction mechanism for dissolution in acidic solution was proposed. In this mechanism, the effect of the cleavage planes controls the metal cation release through the exposure of metal cation sites when the minerals cleaves. Because pyroxene mineral dissolution is reaction-controlled, the increase in temperature increased the reactivity; and the reduction in the particle size increased the surface area through the creation of jagged edges on the particles. The increase in high energy sites on the smaller size fraction resulted in a reaction that showed more attributes of diffusion-limited kinetics instead of reaction-limited kinetics.

The low reactivity of orthopyroxene significantly decreases the potential storage of the Bushveld PGM tailings for CO_2. The results from the second phase showed that the extent of orthopyroxene leaching can be increased appreciably by increasing the surface area on the cleavage planes (by selective mineral breakage). Furthermore, the addition of organic chelators increases the reactivity of silicate dissolution by complexing available Si in solution. Therefore, for Bushveld PGM tailings to be considered a viable CO_2 storage resource, the reactivity of the orthopyroxene mineral needs to be increased through the increase in high-energy sites by an increase in cleavage area. However, the favourable extraction of Ca in organic acids from plagioclase, the major Ca host in these tailings, is encouraging for future studies on the use of Bushveld PGM tailings for CO_2 storage.

Publications and Presentations

Meyer, N., Vögeli, J., Becker, M., Broadhurst, J., Reid, D. L., and Franzidis, J.-P. (2014). Mineral carbonation of PGM mine tailings for CO_2 storage in South Africa: A case study. *Minerals Engineering*, **59** 45-51.

Meyer, N. A., Becker, B., Broadhurst, J. L. and Franzidis, J-P. (2013). An investigation into the dissolution of pyroxene: A precursor to mineral carbonation of PGM tailings in South Africa. *Proceedings of the 6th Minerals to Metals Initiative Student Research Day*. 7 November 2013. Cape Town: 23.

Meyer, N. A., Becker, B., Broadhurst, J. L. and Franzidis, J-P. (2013). A kinetic investigation into the dissolution of pyroxene: A precursor to mineral carbonation of PGM tailings in South Africa. *Proceedings of the Southern African Institute of Mining and Metallurgy Conference*. 7-8 August 2013. Cape Town.

Meyer, N. A., Vogeli, J., Becker, B., Broadhurst, J. L. and Reid, D. L. (2013). Mineral carbonation of PGM mine tailings for CO_2 storage in South Africa: A case study from Lonmin. *Proceedings of the 4th International Conference on Accelerated Carbonation for Environmental and Materials Engineering*. 9-12 April 2013. Leuven: 505.

Meyer, N. A. and Reid, D. L. (2012). Natural carbonation of Karoo dolerites at New Denmark Colliery: A case study for engineered carbonation. *Inkaba yeAfrica: 9th Annual Workshop*. 25-30 November. Potsdam.

Meyer, N. A., Vögeli, J., Becker, B., Broadhurst, J. L., Reid, D. L. and Franzidis, J-P. (2012). Mineral carbonation of PGM mine tailings for CO_2 storage in South Africa. *Proceedings of the 5th Minerals to Metals Initiative Student Research Day*. 12 November 2012. Cape Town: 13.

Meyer, N. A., Becker, B., Broadhurst, J. L. Petersen, J., Reid, D. L. and Franzidis, J-P. (2012). A kinetic investigation into the dissolution of pyroxene: A precursor to mineral carbonation of PGM tailings in South Africa. *Proceedings of the Southern African Institute of Mining and Metallurgy Conference*. 2-3 August 2012. Cape Town: SP08.

Meyer, N. A., Becker, B., Broadhurst, J. L. Petersen, J., Reid, D. L. and Franzidis, J-P. (2012). A kinetic investigation into the dissolution of pyroxene: a precursor to mineral carbonation of PGM tailings in South Africa. *Proceedings of the Anglo American Hydrometallurgy Initiative: Post-graduate Student Symposium*. 1 August 2012.

Acknowledgements

I would like to thank my supervisor, Megan Becker, and co-supervisors Jenny Broadhurst and Dave Reid for providing the opportunity to develop my skills as a young researcher in the sciences. Thank you for imparting on me your knowledge and teaching me the necessary skills to make my own scientific deductions.

A special thank-you to the following people:

- J-P Franzidis and Mymoena van der Fort for your continued support of the project through the Minerals to Metals research Initiative and the Financial support from the NRF SARChI Chair in Mineral Beneficiation. *This work is based on the research supported by the South African Research Chairs Initiative of the Department of Science and Technology and National Research Foundation of South Africa.*
- Jacques Vögeli for the use of his data and consultation.
- Jochen Petersen for chemistry consultation.
- Shireen Govender for the administration in the Centre for Mineral Research laboratory
- Gaynor Yourath for the QEMSCAN analysis and Lorraine Nkemba for disk preparation
- Kirsten Corin in the Centre for Minerals Research for QXRD analysis
- Stephanie Snoek in the Analytical laboratory for ICP-OES analysis
- Alex Opitz for organising the Acid Rock Drainage meetings and encouraging discussion on the group's projects
- Christelle Tinguely in the Department of Geological Sciences for ICP-MS analysis
- Ernest Stout in the Department of Geological Sciences for the preparation of the XRF fusion disks
- Miranda Waldron at the Electron Microscope Unit for SEM analysis
- Riana Rossouw at the Central Analytical Facility, Stellenbosch University for ICP-MS analysis

- The Geological Sciences department for the office and the use of the crushing room

To my friends and family, thank you for your support over the period of my Masters degree. Your support and encouragement is greatly appreciated.

Contents

List of Tables

List of Figures

Glossary

Al	Aluminium, Al^{3+} as aluminium free ions, Al_2O_3 as aluminium oxide
Anthropogenic	Human impact on the environment
bar	1 bar = 100 000 Pa
BET	Brunauer, Emmett and Teller, (1938) – Surface area analytical technique
Bridging oxygen	Oxygen bonded to two silicon atoms in a silicate mineral
BSE	Backscattered electrons
Bushveld	Bushveld Igneous complex in South Africa, a layered mafic igneous intrusion which hosts the world's largest deposit of PGMs
Ca	Calcium, Ca^{2+} as calcium free ions, CaO as calcium oxide
Calcium carbonate	$CaCO_3$
Carbonation	The reaction of silicate mineral with CO_2 to form carbonate minerals
CCMC	Carbon capture and mineral carbonation
CCS	Carbon capture and storage
Cleavage	The preferential parting of a mineral along a specific plane
CO_2	Carbon dioxide
Congruent	Congruent reaction is the release of cations and Si in their stoichiometric ratio as calculated from the mineral formula
Coordination	A measure of an atom's nearest neighbours
Deportment	The proportion of an element in each of the mineral phases present
Direct carbonation	The carbonation reaction of minerals in a one-stage reaction

Dissolution	The reaction that breaks up a mineral into its chemical components
EDS	Energy Dispersive Spectroscopy – Element analysis technique
EDTA	Ethylenediaminetetraacetic acid
EMP	Electron microprobe – Element analysis technique
Ex-situ	Off-site reaction
Fe	Ferric iron, Fe^{2+} as iron free ions, FeO as iron oxide
Fe(III)	Ferrous iron, Fe^{3+} as iron free ions
Felsic	Igneous rocks with a SiO_2 content of > 69 wt.%
Geologic storage	Storage of compressed CO_2 in underground aquifers
Geological time periods	Hundred thousand to millions of years
GHG	Greenhouse gasses
Gt	Gigatonne, 10^9 t
h	Hour
HCl	Hydrochloric acid
HCO_3^-	Carbonic acid
Heat treatment	Heating of a mineral to remove chemically bound water, usually for serpentine
Hydrolysis	Hydrolysis is the cleavage of chemical bonds by the addition of water
ICP-MS	Inductively coupled plasma mass spectrometry
ICP-OES	Inductively coupled plasma atomic emission spectroscopy
Incongruent	Opposite to a congruent reaction, it is the release of cations and Si in any proportion other than stoichiometric
Indirect carbonation	The carbonation reaction of minerals by a multi-stage reaction
In-situ	On-site reaction
kt	Kilotonne, 10^3 t
Leach	Reaction of mineral to remove a selected species, e.g. Ca
Ligand-promoted	Dissolution reaction driven by a complex-forming ligand with the surface

Lonmin	Location of the pyroxene-rich tailings. Operations based in Marikana on the southwestern section of the Bushveld Igneous Complex
Mafic	Igneous rocks rich in Fe and Mg with a SiO_2 content of 45-52 wt.%
Magnesium carbonate	$MgCO_3$
Mechanical activation	The physical size reduction or surface disordering of a mineral during dissolution
Merensky	Merensky Reef, a platinum rich horizon of the Bushveld ingeous complex
Mg	Magnesium, Mg^{2+} as magnesium free ions, MgO as magnesium oxide
μm	Micron, 10^{-6} m
Milling	Particle size reduction of a mineral
min	Minutes
Mt	Megatonnes, 10^6 t
Olivine	Mg-silicate, $(Mg^{2+}, Fe^{2+})_2SiO_4$
Organic ligands	An ion or molecule that binds to a central metal atom to form a coordination complex
Oxalate	Organic chelator ($C_2O_4{}^{2-}$) anion, $H_2C_2O_4$ as oxalic acid
Peridotite	Olivine and pyroxene-rich mafic igneous rock
PGM/E	Platinum group mineral/element
Plagioclase	Al-Ca-rich silicate, $NaAlSi_3O_8$ $CaAl_2Si_2O_8$
ppb	Parts per billion
ppm	Parts per million
Pre-treatment	Any change in the mineral before the rection proceeds (e.g. size reduction)
Product layer	Precipitated Si-rich passivating layer on the surface of a reacting grain
Proton	H^+ ion
Proton-promoted	Dissolution reaction driven by the hydrolysis reaction
Pyroxene	Silicate mineral with the general formula $(M2)(M1)(Si,Al)_2O_6$

Pyroxenoid	Pyroxene group mineral with a distorted structure
QEMSCAN	Quantitative Evaluation of Mineralogy through Scanning Electron Microscopy – Mineralogical analysis
RCO_2	Mass ratio of mineral needed to carbonate one unit of CO_2
Reaction-controlled	A reaction rate that is controlled by the slow chemical reaction step, surface-controlled
SEM	Scanning electron microscope
Sequestration	The ability to bind free cations, used to store CO_2 as chemically bound carbonate
Serpentine	Mg-rich silicate, $Mg_3(OH)_4(Si_3O_5)$
Si	Silicon, Si^{4+} as silicon free ions, SiO_2 as silicate
Si-O tetrahedra	${SiO_4}^{4-}$ molecule
Stoichiometry	The ratio of elements to each other in a mineral
t	Tonne, 10^6 g
Tailings	The waste mineral material from the processing of ore
Transport-controlled	A reaction rate that is controlled by the slow movement of the solvent. diffusion-controlled
Weathering	Natural reaction to break down rocks and minerals over geologic time periods
Wt.%	Weight percentage
X_{Al}	Extraction percentage of Al from sample
X_{Ca}	Extraction percentage of Ca from sample
X_{Fe}	Extraction percentage of Fe from sample
X_{Mg}	Extraction percentage of Mg from sample
XRF	X-ray Fluorescence spectrometry – Element analysis technique
X_{Si}	Extraction percentage of Si from sample

Chapter 1

Introduction

1.1 Storage of anthropogenic CO_2

The rise in anthropogenic carbon dioxide (CO_2) is a growing concern as it causes significant changes in the climate (Lackner *et al.*, 1995), and South Africa contributes more than $\sim$430 Mt CO_2 per annum (recorded for 2008) through the burning of fossil fuels (Boden *et al.*, 2011). Consequently, the South African government has committed to significant reductions in greenhouse gas emissions over the next decade (Winkler *et al.*, 2002; Hietkamp *et al.*, 2004). A widely advocated method for CO_2 reduction involves the trapping of CO_2 via injection into deep underground geological formations. An investigation into the CO_2 storage possibilities in South Africa shows that an estimated 150 Gt of CO_2 can be stored in geological formations. However, less than 2 % of this storage is on land, with the remainder being located in off-shore basins (Cloete, 2010). With the lack of suitable on-shore reservoirs for CO_2 storage in South Africa, the possibility of CO_2 sequestration through mineral carbonation is becoming more attractive (Lackner *et al.*, 1995; Huijgen and Comans, 2003; Park *et al.*, 2003; Teir *et al.*, 2007).

Mineral carbonation is the chemical fixation of CO_2 to metal cations which produces carbonates. It is a favourable alternative to geologic storage as the process is thermodynamically favourable and the products are stable and benign over geological time periods (millions of years, Lackner *et al.*, 1995). Not only can the products (typically Ca-, Mg-carbonates) be reused in industrial processes, the system can accommodate a wide variety of input materials (Figure 1.1). Ideal sources for CO_2 fixation include solid and aqueous wastes, however Mg-rich minerals are also targeted. For example, a number of potentially suitable solid mine wastes produced from the beneficiation of various ores exist in South Africa, including kimberlite diamond dumps (serpentine-rich), Nkomati nickel dumps (pyroxene- and

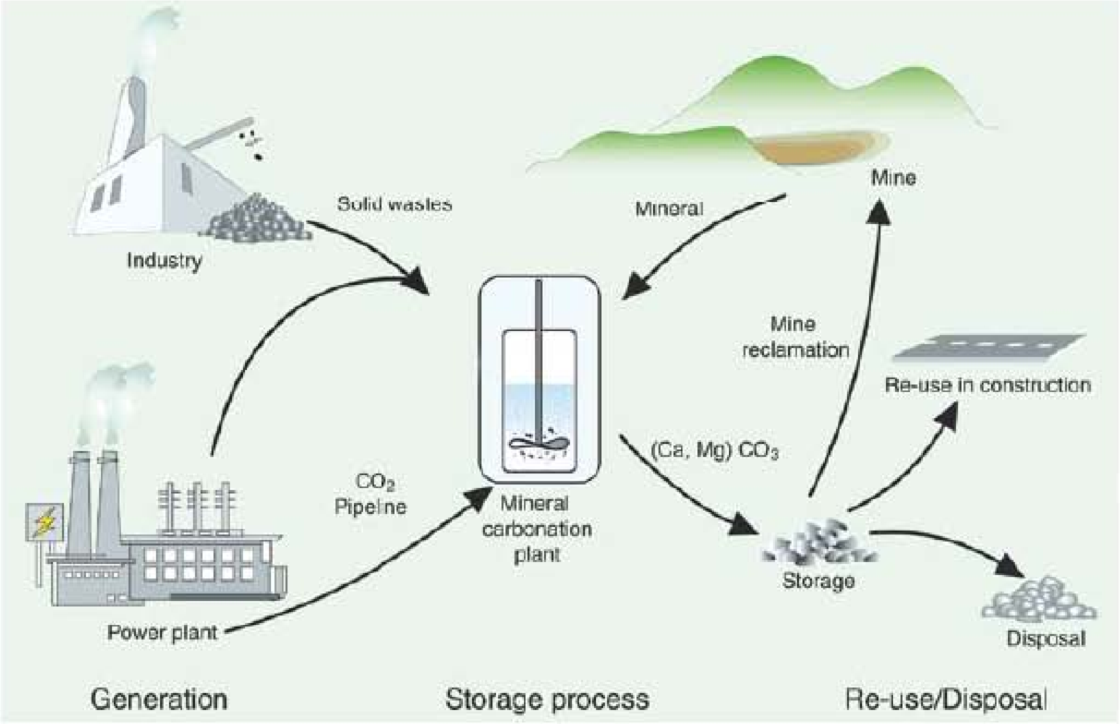

Figure 1.1: Illustration of *ex-situ* mineral sequestration process steps of silicate rock or industrial residues. From the Intergovernmental panel on climate change (Mazzotti *et al.*, 2005).

olivine-rich), Okiep copper dumps (pyroxene-rich), and Bushveld platinum dumps (pyroxene-rich). A scoping study on the use of Bushveld Merensky tailings for CO_2 storage by Vögeli *et al.* (2011), showed that these tailings could store the large amounts of CO_2 produced by the synthetic fuels industry in South Africa, however the low reactivity of the platinum tailings limits this possibility. The low reactivity of orthopyroxene, which hosts up to 80 % of the Mg, thus limits the total carbonation capacity of the tailings. This project aims to investigate the factors affecting the reactivity of pyroxene and pyroxene-rich feedstocks for its future as an engineered mineral carbonation resource.

1.2 Mineral carbonation

Carbon sequestration through mineral carbonation mimics the natural weathering process of minerals as shown by the generalised equation, Eq 1.1. During weathering, cations are removed from the silicate mineral (Eq 1.2) and transported into oceans via rivers. Dissolved CO_2 in sea water (Eq 1.3) forms carbonate and bicarbonate ions that react with dissolved cations to form calcium-, magnesium- or iron-carbonates (Eq 1.4).

$$(Ca, Mg, Fe)_xSi_yO_{x+2y} + xCO_2 \rightarrow x(Ca, Mg, Fe)CO_3 + ySiO_2 + heat \tag{1.1}$$

$$(Ca, Mg, Fe)_xSi_yO_{x+2y} \rightarrow (Ca, Mg, Fe)^{x+} + ySiO_2 \tag{1.2}$$

$$CO_2 + H_2O \leftrightarrow H_2CO_3 \leftrightarrow H^+ + HCO_3^- \leftrightarrow 2H^+ + CO_3^{2-} \tag{1.3}$$

$$(Ca, Mg, Fe)^{x+} + CO_3^{2-} \rightarrow x(Ca, Mg, Fe)CO_3 + heat \tag{1.4}$$

Natural carbonation is thermodynamically favourable, but suffers from slow kinetics on the order of hundreds to thousands of years (Doucet, 2011; Alexander *et al.*, 2007). An example of natural carbonation is observed in the mafic-rich formations of the Samail Ophiolite of Oman. Peridotites, an olivine-rich rock, have been storing CO_2 as carbonates for an average of 26 000 years – and a maximum of 43 000 years – on the thin weathering horizon of the peridotite. Additionally, when the data for the region is considered, an estimated 40 kt of atmospheric CO_2 per annum for the last 26 000 years has been consumed and subsequently stored (Kelemen and Matter, 2008). Similarly, mafic-rich mine dumps have also been known to store CO_2. Researchers at the Diavik diamond mine and the Mount Keith nickel mine in Australia identified secondary carbonates at centimetre-scale depths in the mine dumps (Dipple *et al.*, 2005). Despite the efficacy of natural carbonation on geological time scales, it cannot cope with the rate of anthropogenic CO_2 increase, therefore engineered solutions that enhance this process are of interest.

Current process routes for engineered carbon capture and mineral carbonation (CCMC) can be classified into two distinct types, namely *'ex-situ'* and *'in-situ'* process routes, with 'other' defining those that do not fit into either of the categories (Figure 1.2, Lackner *et al.*, 1995; Lackner, 2002; Huijgen and Comans, 2003). The *in-situ* method was developed as an optimisation of geologic storage. CO_2 is injected into Mg-rich rocks under optimal pressure and solution conditions, not only to store CO_2 in underground formations, but also to accelerate the natural carbonation of the minerals in the host rock. The CarbFix project in Iceland injects 2.2 kt of dissolved CO_2 per annum into a basaltic well at a depth of 400 m to 800 m (CarbFix, 2010). Improvements on *in-situ* CCMC include the improved sealing of geologic storage sites and the injection of CO_2 into more reactive and Mg-rich rocks such as peridotites. Despite the positive results and pilot-scale tests in the northern hemisphere (Olajire, 2013), the limitations of underground CO_2 storage in South Africa excludes *in-situ* mineral carbonation routes for consideration. On the other hand, *ex-situ* process routes involve the carbonation of extracted or pretreated natural minerals or industrial wastes (Olajire, 2013). *Ex-situ* mineral

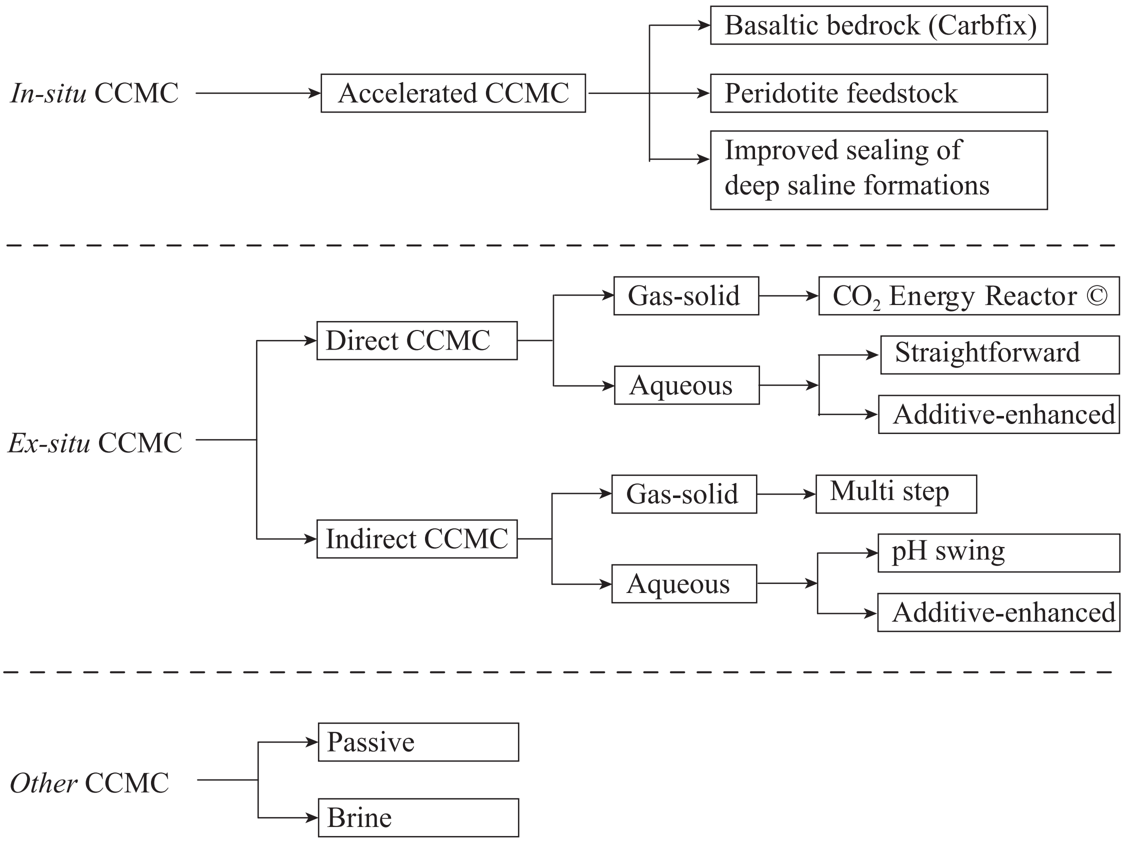

Figure 1.2: Current engineered mineral carbonation process routes and the research ideas corresponding to each process route. 'Other' CCMC process routes include all processes that do not fit into the above categories but are not discussed in the text because of slow progress in their field. Adapted from Huijgen and Comans (2003), Sipilä *et al.* (2008), and Torróntegui (2010).

carbonation process routes have the greatest potential in South Africa as a result of the large volumes of historical and current mine wastes (Hietkamp *et al.*, 2004; Vögeli *et al.*, 2011).

Ex-situ mineral carbonation can be divided into direct and indirect routes. Direct mineral carbonation combines the release of the metal cation (Eq 1.2) and the formation of a carbonate (Eq 1.4) in the same step. This can be done by gas-solid interaction which involves the direct reaction of gaseous CO_2 with solid mineral or alkaline waste. The direct gas-solid reaction suffers from very slow reaction rates and is thus less likely to develop into an industrial-scale route (Doucet, 2011; Olajire, 2013). Direct aqueous mineral carbonation involves the reaction of carbonated water, which liberates ions from the feedstock that immediately react with the bicarbonate in solution to form carbonate precipitates. Carbonic acid is very weak and to increase reactivity, a variety of pretreatment methods are used. The CO_2 Energy Reactor project uses unique geothermal heat to make the process viable (Energy reactor, http://www.innovationconcepts.eu). Another promising direct aqueous carbonation route is the Albany Research Centre route, which carbonates olivine and heat-treated serpentine in a solution of sodium carbonate and sodium chloride, but at high temperature (155 °C to 185 °C) and pressure (115 atm to 155 atm CO_2, Table 1.1, O'Connor *et al.*, 2001).

Table 1.1: Direct and indirect *ex-situ* mineral carbonation processes of interest. The process and research group is noted in the left column.

Direct Process	**Description**
Albany Research Centre Direct, additive enhanced O'Connor *et al.* (2001)	-37 μm, heat-treated serpentine at 600 °C in a solution of 0.5 M $NaHCO_3$ and 1 M NaCl with 150 atm CO_2 at 155 °C to produce 82 % conversion in 1 h; and -37 μm olivine in a solution of 0.5 M $NaHCO_3$ and 1 M NaCl with 115 atm CO_2 at 185 °C to produce 84 % conversion in 6 h.
Indirect Process	**Description**
ÅA process Indirect, gas-solid Zevenhoven (2011)	168 μm $Mg(OH)_2$ produced from serpentine at 535 °C for 30 min, followed by the carbonation of $Mg(OH)_2$ with 20 atm CO_2 at 490 °C to produce 54 % conversion in 9 min.
Indirect, pH-swing Park *et al.* (2003)	First step: -75 μm serpentine in a solution of 1 vol % orthophosphoric acid, 0.9 wt % of oxalic acid and 0.1 wt % EDTA with internal grinding media at 70 °C to produce 65 % Mg extraction after 1 h. Second step: Increased pH to 9.5 by addition of NH_4OH followed by the addition of 1 atm CO_2 at ambient temperature to produce 65 % Mg conversion in 30 min.
Indirect, additive-enhanced Teir *et al.* (2007)	First step: 100 μm serpentine in a solution of 4 M HCl at 70 °C to produce 93 % Mg extraction after 2 hours. Second step: Excess acid removed and H_2O added to leachate, and a pH of 9 maintained by the addition of NaOH after the addition of CO_2 at 1 $l.min^{-1}$ in 30 °C to produce 79 % Mg conversion in 30 min.

In contrast to the direct method, an indirect or multi-step reaction benefits from better optimisation by the separation of the cation liberation reaction (Eq 1.2) from the carbonation reaction (Eq 1.4). The ÅA indirect, gas-solid, multi-step process carbonates $Mg(OH)_2$ from serpentine to produce 54 % conversion after 9 min (Zevenhoven, 2011). The gas-solid routes are usually energy intensive, but an aqueous reaction can overcome the need for very high temperatures and pressures. For example, the two-stage, pH-swing method described by Park *et al.* (2003) starts with the primary dissolution reaction at low pH (pH $\sim$1) followed by the carbonation reaction at elevated pH (pH $\sim$8). The pH-swing method increases the maximum carbonation efficiency of the sample by removing the cations at low pH, where the sample dissolves under protonation reaction, and forming carbonates at high pH where they are stable. It is therefore possible to reach extraction efficiencies of ~100 % during silicate dissolution with only slightly increased temperatures (~70 °C), while simultaneously maintaining a low temperature (ambient to 30 °C), for carbonation (Park *et al.*, 2003; Park and Fan, 2004). The indirect aqueous, pH-swing route by Teir *et al.* (2007) produced an overall conversion of 79 % from serpentine. Other benefits for indirect carbonation include the selection of the acid and its recovery after dissolution. Further enhancements through the pre-treatment of the minerals by size reduction, chemical additives, heat treatment, and mechanical activation have also been found to increase the reaction rates (Mazzotti *et al.*, 2005). Size reduction and mechanical surface activation are an inherent process of milling and therefore present in mine tailings, making it an ideal source material for mineral carbonation (Vögeli *et al.*, 2011).

1.3 Suitable mineral feedstocks for engineered CCMC processes

The capacity of a mineral to store CO_2 is quantified by R_{CO_2}, which is defined as the mass ratio of ore necessary to carbonate one unit of CO_2 (Lackner *et al.*, 1995). Minerals with a higher metal cation to silica ratio have a lower R_{CO_2} value, and can store more CO_2 per tonne of feedstock. Therefore, the research and development of mineral carbonation processes have largely been focused on olivine, because of its high Mg molar concentration (R_{CO_2} = 1.8) and high reactivity; and serpentine ($R_{CO_2} \approx 2.3$), a more abundant Mg-silicate (Lackner *et al.*, 1995). Table 1.2 compares the reactivity and CO_2 storage potential of the major pyroxene group minerals to olivine and serpentine, and anorthite, a common Bushveld tailings mineral. At pH = 2, the rates of reaction of olivine and anorthite are greater than the rates of reaction of the pyroxene group minerals (Paktunc, 1999).

A scoping study on the use of Bushveld PGM (platinum group mineral) tailings for CO_2 storage by Vögeli *et al.* (2011) showed that these tailings alone have a capacity to store ~14 Mt of CO_2 per annum. The Bushveld area in South Africa produced in the order of 77 Mt of tailings from June 2009 to June 2010 from the mineral beneficiation of PGMs from Merensky, UG2 and Platreef operations (Vögeli *et al.*, 2011). The suitable characteristics of the Bushveld PGM tailings for mineral carbonation are attributed to the vast quantities of fine-grained (d50 of 25 µm to 126 µm) Ca-Mg-Fe-bearing silicate waste material. Preliminary mineralogical classification of the tailings from four Merensky tailings dams (Northam, BRPM, Implala and Lonmin) highlighted the abundance of potentially sequesterable minerals (88 wt.% to 95 wt.%). These include orthopyroxene, plagioclase and clinopyroxene; and minor amounts of the more reactive minerals olivine and serpentine. Although

Table 1.2: The reactivity of pyroxene, olivine and serpentine under direct carbonation. Adapted from Paktunc (1999); Klein and Dana (2007) and O'Connor *et al.* (2005)

Mineral		**Formula**	**Ideal Concentration in Feed (wt.%)**			**R_{CO_2}[1]**	**Rate[2]**
Group	**End Member**		**Ca**	**Fe**	**Mg**		**($mol.cm^{-2}.s^{-1}$)**
Feldspar	Anorthite	$CaAl_2Si_2O_8$	10.3	3.1	4.8	4.4	9.3 to 14.5
Pyroxene	Enstatite	$MgSiO_3$	0.4	4.0	20.8	2.4	13.9 to 14.5
	Diopside	$CaMgSi_2O_6$	18.5	0.5	11.3	2.4	12 to 14
	Augite	$Ca(MgFe)Si_2O_6$	15.6	9.6	6.9	2.7	13.5
Pyroxenoid	Wollastonite	$CaSiO_3$	31.6	0.5	0.3	2.8	12.4
Olivine	Forsterite	Mg_2SiO_4	0.1	6.1	27.9	1.8	12
	Fayalite	Fe_2SiO_4	0.6	44.3	0.3	2.8	10.8
Serpentine	Antigorite	$Mg_3Si_2O_5(OH)_4$	<0.1	2.4	24.6	2.1	–

[1] Mass ratio of ore necessary to carbonate unit mass of CO_2, unitless

[2] Rate calculated at pH 2, and low -log R values indicate higher reactivity (Paktunc, 1999)

poor in olivine and serpentine, the relatively low R_{CO_2} value of between 2.87 and 3.7 for the Bushveld PGM tailings makes it a viable source material for mineral carbonation (Vögeli, 2012).

The theoretical mineralogical results indicated a potentially favourable CO_2 storage material, but the preliminary leaching results indicated that the kinetics of the Lonmin PGM tailings sample may not favour mineral carbonation with the current methods used. The Mg, Fe, and Si cation dissolution is slow in 2 M HCl at 70 °C after 5 h. The low extraction of Mg is attributed to the seemingly unreactive nature of orthopyroxene, the major Mg host (Vögeli, 2012). The low cation extraction resulted in an overall low conversion of tailings to carbonates. The net conversion to carbonates for this sample was only 29.9 % for Ca, 2.9 % for Mg and 8.9 % for Fe (Meyer *et al.*, 2014).

1.4 Problem statement and objectives

The shortage of viable geosequestration sites in South Africa and the increased need for carbon-based fuels has put the spotlight on mineral carbonation for South Africa's carbon dioxide management. Opportunity exists to potentially sequester $\sim$14 Mt of CO_2 per annum in PGM tailings from the Bushveld area; and the extraction of residual platinum group elements from these tailings could make this process economically viable. However, preliminary studies have indicated that in practice the carbonation capacity is limited because of the relativity low reactivity of orthopyroxene during acid dissolution. Understanding the reactivity of orthopyroxene is key for the viable storage of CO_2 in Bushveld PGM tailings. Studies on the mineral carbonation of pyroxene appear to be limited; and thus the factors affecting pyroxene reactivity are not well understood.

1.5 Objective and Scope

The objective of this study is to investigate the acid leach behaviour of the pyroxene group minerals and pyroxene-rich PGM tailings, as a future potential resource for carbon dioxide sequestration by mineral carbonation. By comparing extraction percentages from dissolution reactions at varying solution chemistry, mineralogy, temperature, and particle size; an overall mechanism for pyroxene reactivity in pyroxene-rich feedstocks will be defined.

A graphical representation of the scope is shown in Figure 1.3. This study will investigate the dissolution of (1) pyroxene-rich Lonmin PGM tailings in mineral-organic acid solutions and

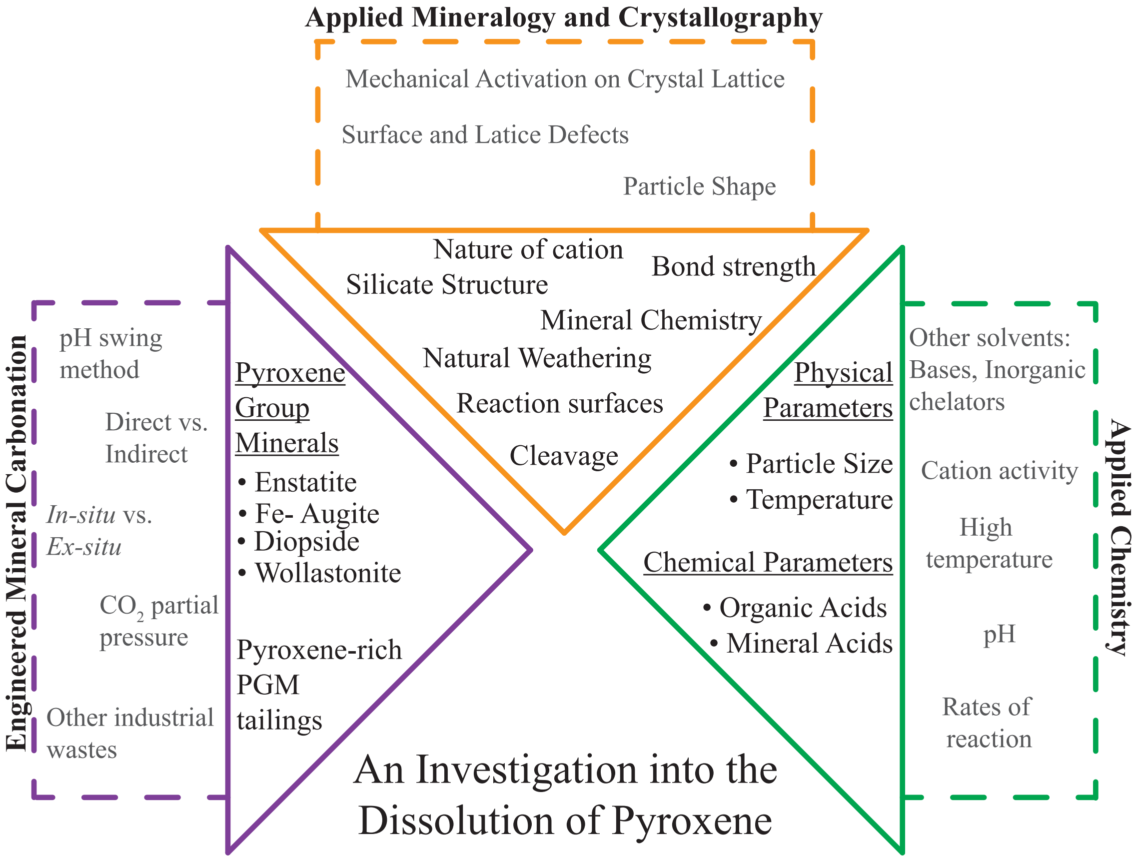

Figure 1.3: Diagram of the scope of the project. Research fields are listed in bold and outlined in colour. Subject fields included in the scope of this project are outlined with a solid line, and subject fields outside the scope are outlined by a dashed line

(2) pyroxene group minerals (namely enstatite, augite, diopside, and wollastonite) in a mineral acid for an overall understanding of the PGM tailings reactivity for future mineral carbonation studies. These experiments will be limited to the physical (particle size and temperature) and chemical effects (mineral chemistry and solvent chemistry) on mineral dissolution. The aspects to be investigated in this project are broadly grouped into: applied mineralogy and crystallography, applied chemistry, and engineered mineral carbonation. The individual parameters of each discipline to be investigated are grouped and highlighted in the triangular spaces of Figure 1.3. All ideas in the dashed boxes fall outside the scope of this study. This study does not attempt to calculate the rate of dissolution for these pyroxenes, nor does it aim to achieve an engineered solution for mineral carbonation of PGM tailings.

1.6 Organisation of the dissertation

This dissertation (Figure 1.4) begins with an introduction to the CO_2 problem, the storage options available, and the potential for PGM storage in South Africa. This is followed by a literature review covering: an introduction to the structure of silicate minerals and its effects on the reactivity of the various minerals, reaction kinetics of the dissolution reaction, the chemical and physical parameters affecting dissolution, an outline of Lonmin PGM tailings mineralogy, and an in-depth review of the pyroxene group minerals. The literature review concludes with the proposal of the hypotheses and key questions. Chapter 3, experimental methods and materials, details the individual experiments and mineralogical characterisation of the samples. The results are split into Chapter 4: the effect of organic acids on pyroxene-rich PGM tailings dissolution; and Chapter 5: the effect of mineral chemistry, temperature and particle size on pyroxene dissolution. Chapter 6 discusses the outcomes from the two result sections and answers the key questions outlined at the end of Chapter 2. Finally, Chapter 7 summarises the key findings of this project, remarks on the effect of pyroxene reactivity on the use of PGM tailings for mineral carbonation, and provides recommendations for future projects. All results and calculations are listed in the appendix in the order: (A) calculations, (B) feed characterisation, (C) leachate solutions, and (D) residue characterisation.

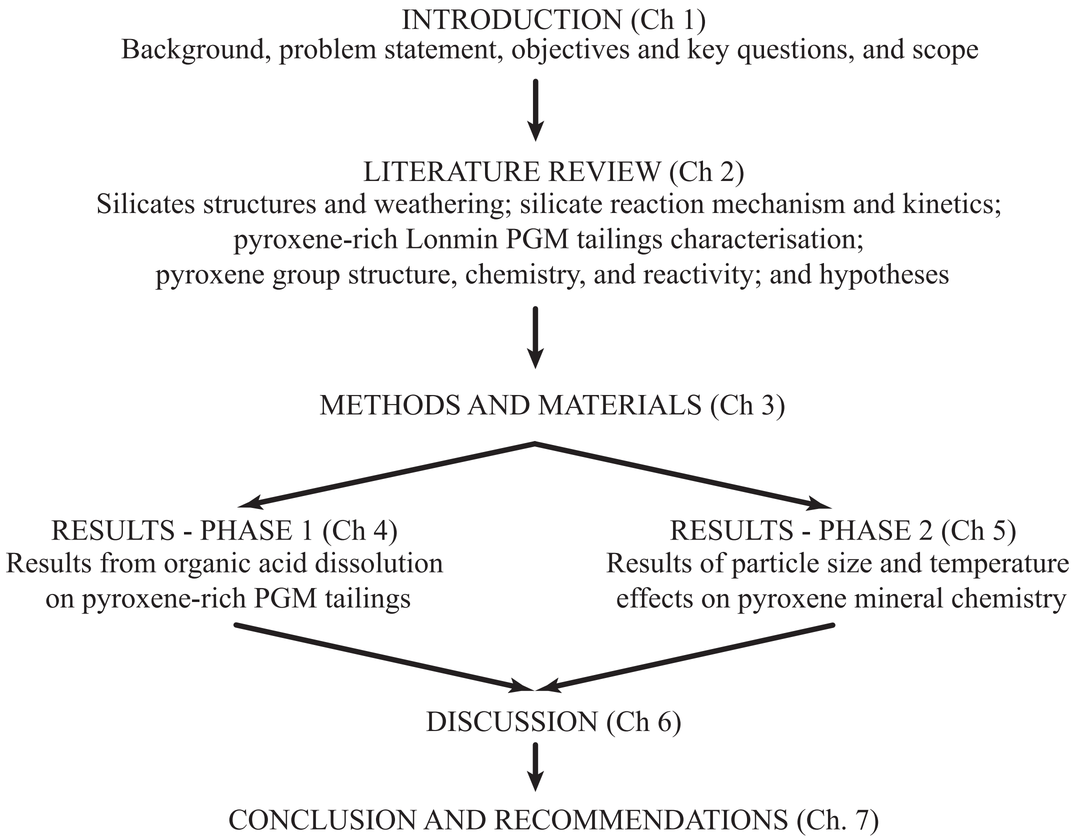

Figure 1.4: Diagram detailing the structure of the thesis

Chapter 2

Literature Review

The low reactivity of pyroxene group minerals must be addressed for Bushveld PGM tailings to be a viable CO_2 storage resource. Therefore an in-depth understanding of pyroxene is needed. This includes the pyroxene group structure and mineralogy, and the effect these have on the mineral's reactivity. This literature review begins with an introduction to silicate mineral structure and its impact on the natural weathering reactions. This is followed by a molecular-scale and particle-scale overview of the dissolution reaction of silicate minerals, then a summary of parameters optimised to increase the leaching of silicate minerals. Lastly, an overview of the Bushveld PGM tailings is given and an in-depth review of pyroxene mineralogy is covered. This chapter concludes with a summary of the major aspects covered in the review. From the literature reviewed, hypotheses and key questions are proposed.

2.1 An introduction to silicates

Silicate minerals are the largest group of minerals on Earth, making up over 90 % of the crust (Klein and Dana, 2007). The basic structural unit of all silicate minerals is the Si-O tetrahedron: a single Si atom surrounded by four oxygen anions to produce a pyramid-shaped SiO_4^{4-} molecule (Figure 2.1). The dual nonmetal-metal nature of Si results in a very stable Si-O tetrahedron that is responsible for the chemical and physical stability of the crust. The strong Si-O bonds (bond energy of 368 $kJ.mol^{-1}$, Silberberg, 2011) combine almost equal amounts of both covalent and ionic bond types, owing to the 1.7 electronegativity difference between Si and O (Pauling, 1980). The Si-O bond has roughly 55 % double-bond character because, unlike C, Si is large and cannot form double bonds with O, which results in a close 1.61 Å bond length for Si-O (Silberberg, 2011). The Si-O tetrahedron is polymerised in nature through the linking of oxygens – to form a bridging oxygen – to create a very strong and interconnected structure, thereby increasing its stability. The formation of a bridging oxygen causes the Si-O bond to increase in length from between 1.59 and 1.60 Å for a non-bridging oxygen to between 1.65 and 1.66 Å for a bridging oxygen. Thus the bridging oxygen has a more covalent, double bond character than the non-bridging oxygen which has ionic, single-bond character (Ramberg, 1952). Cations (e.g. Ca, Fe, Mg) are arranged in 12-, 8-, 6- or 4-fold coordination (coordination refers to the number of anions surrounding the cation, e.g. oxygen atoms, OH^- ions) linking the Si-O tetrahedra in various arrangements to produce the major rock forming minerals. The various arrangements play a major role in a mineral's reactivity and will be discussed in more detail in Section 2.1.2.

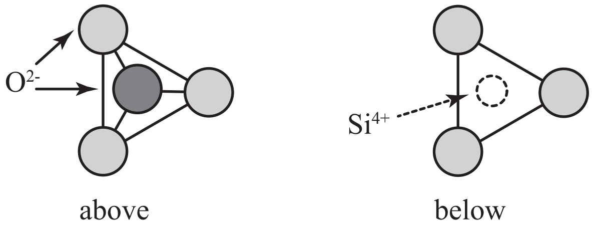

Figure 2.1: Diagram of simple Si-O tetrahedra – a single Si atom surrounded by four oxygen anions to produce a pyramid shape – when viewed from above (left) and below (right).

2.1.1 Silicate structures

There are seven different silicate structures observed in nature as described in Table 2.1 by Deer *et al.* (1992) and Klein and Dana (2007). The simplest silicate structure is an orthosilicate which links independent Si-O tetrahedra together through ionic bonds of interstitial cations (Mg, Ca, Fe, etc.) for neutrality. There is no sharing of oxygen ions (i.e. non-bridging oxygens) and the bond strengths are equal in all directions. The most common mineral with this structure is olivine and it has a Si:O ratio of 1:4. Si-O tetrahedra when joined through one bridging oxygen produce the isolated, double Si-O tetrahedra groups of the sorosilicates. This structure is represented by the epidote group and has a Si:O ratio of 2:7. The joining of two apical oxygens can produce either a closed-ring or a single chain structure. Closed-ring structures (or cyclosilicates) bond three, four or six Si-O tetrahedra together at the apical oxygens. The more common six-ringed cyclosilicates are characterised by cordierite, which have a Si:O ratio of 1:3.

On the other hand, single-chain structures (inosilicates) share only two corner oxygens to produce an infinite parallel chain of Si-O tetrahedra, which are aligned along the shared oxygens and the apices

Table 2.1: Classification of the major silicate structures. Only the oxygen atoms are imaged in each structure, with the dark grey positioned at the top and the light grey positioned at the bottom of the tetrahedra. Adapted from Klein and Dana (2007).

Class	**Arrangement of SiO_4 tetrahedra (central Si^{4+} not shown)**		**Common example**
Nesosilicate (orthosilicate)	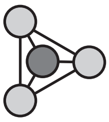	SiO_4^{4-}	Olivine $(Mg,Fe)_2SiO_4$
Sorosilicate	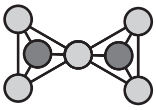	$Si_2O_7^{6-}$	Epidote Group $Ca_2(Fe^{3+},Al)Al_2O(SiO_4)$ $(Si_2O_7)(OH)$
Cyclosilicate (ring silicate)	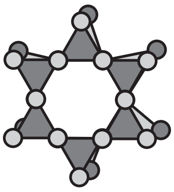	$Si_6O_{18}^{12-}$	Cordierite $(Mg,Fe)_2Al_4Si_5O_{18}.nH_2O$
Inosilicate (Single chain silicate)	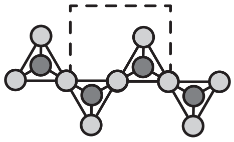	$Si_2O_6^{4-}$	Pyroxene Group e.g. Enstatite $MgSiO_3$ e.g. Diopside $CaMgSi_2O_6$
Inosilicate (Double chain silicate)	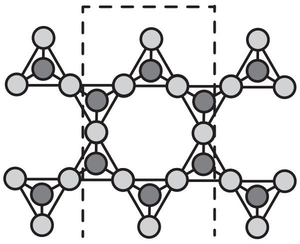	$Si_4O_{11}^{6-}$	Amphibole Group e.g. Hornblende $(Ca,Na)_{2\text{-}3}(Mg,Fe,Al)_5$ $(Al,Si)_8O_{22}(OH,F)_2$
Phylosilicate (sheet silicate)	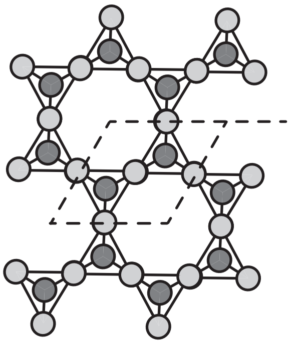	$Si_2O_5^{2-}$	Serpentine Group e.g. Lizardite $Mg_3Si_2O_5(OH)_4$ Mica Group e.g. Phlogopite, $KMg_3(AlSi_3O_{10})(OH)_2$
Tectosilicate (framework silicate)	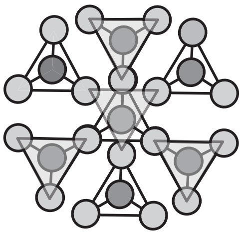	$(Si_2O)^0$	Quartz SiO_2 Feldspar e.g. $CaAl_2Si_2O_8$

of the basal oxygens jut out on alternating sides of the chain. Single chain silicates are characterised by the pyroxene group. The bonds within the pyroxene chains are strong, however the bonds between the chains are weak and therefore the mineral breaks easily along these planes (Klein and Dana, 2007).

When two parallel single chains are joined at the apex-oxygen, they produce the double-chained inosilicate with Si:O = 4:11. The Si-O tetrahedra alternately share two and three oxygens and are characterised by the amphibole group (Misra, 2012, p31). The joining of infinite chains where all three of the basal oxygens are shared between adjacent Si-O tetrahedra produce sheet-like layers or phyllosilicates. These individual layers are held either loosely together by van der Waals bonds in the mineral lizardite, or by ionic bonds in the mica group to produce Si:O = 2:5.

Lastly, when all four oxygens are shared in a continuous 3D network, they produce the framework silicates (called tectosilicates). This network produces a stable and strongly bonded structure with Si:O = 1:2. The two mineral groups with this structure are feldspars and quartz. In feldspars, Al replaces Si to form Al-O tetrahedra, where up to half the structure is replaced by Al-O tetrahedra (Deer *et al.*, 1992). The feldspar mineral structure is rendered neutral by the inclusion of cations and because of the large spaces in the framework structure, it can include large cations (e.g. K, Na). The SiO_2 group does not contain any other cations and is electronegatively neutral. It has nine polymorphs, which are stable at very high temperatures (> 1800 °C) and pressures (> 100 kbar, Klein and Dana, 2007).

2.1.2 Silicate weathering, a natural reaction

Weathering is the natural adjustment of minerals and rocks to the Earth's surface conditions, and results in the redistribution of elements and continental mass. Weathering processes are slow and occur on geological timescales (thousands to millions of years, Carroll, 1970, p5). Weathering processes are separated into two pathways: physical and chemical weathering. Physical weathering involves the physical disintegration of a larger rock or mineral with the use of mechanical methods (e.g. expansion, collision, abrasion). This process is important for the size reduction of the more stable (i.e. non-reactive) minerals. For example, quartz grains are reduced in size through collision with other grains in river channels. In this process, the chemistry of the reduced particle remains the same. In contrast, chemical weathering involves the leaching of cations in water at low temperature (below 30 °C), and results in either complete disintegration or mineralogical and chemical change from the parent mineral (Carroll, 1970).

Igneous minerals that initially formed deep in the crust at high temperature and pressure are in disequilibrium at the Earth's surface and are susceptible to chemical weathering reactions. These reactions can be classified into: solution, oxidation and reduction, carbonation, hydration, chelation, and hydrolysis (Table 2.2, Ollier, 1969, p30-36). These reactions arise from either ionic dissociation, addition of water and CO_2, hydrolysis, or oxidation (Krauskopf, 1967, p80). Oxidation reactions are slow but are important for the formation of the oxide minerals and also occur on the surfaces of the more reactive minerals (e.g. Fe in olivine to iron oxides). Hydrolysis weathering is slightly faster than oxidation as water can carry other dissolved constituents. These reactions can occur simultaneously to speed up the weathering reaction. Where only water is present, it ionises slightly and donates its protons to hydrolyse the silicate mineral to remove cations. Yet with dissolved CO_2, carbonic acid (H_2CO_3, pH = 5.7) is formed to aid in mineral dissolution (Krauskopf, 1967, p85). Another type of dissolution is biological, where organic acids produced by organic matter, usually in the soil, create strong ligands that complex the metal cations in the silicate mineral (Berg and Banwart, 2000). These organic acids can decrease the pH of the solvent to between 4.5 and 5.0 (Krauskopf, 1967).

Chemical weathering reactions can be classified into either congruent or incongruent reactions. Congruent reactions completely dissolve the mineral into its base ions, for example the dissolution of calcite into Ca^{2+} and CO_3^{2-} ions. On the other hand, incongruent reactions chemically alter the parent mineral to form secondary minerals. For example, the parent mineral is altered to a mixture of clays or oxides, silicic acid, and cations. In nature, the weathering of Fe-, Mg-rich silicates results in the formation of Fe-, and Mg-rich clays (phyllosilicates, the most common weathering products) and dissolved constituents; whereas feldspar (K-feldspar) weathers to Al-rich clay, silica and dissolved constituents of K^+ and Na^+ (Table 2.2).

The rate of weathering depends on: crystal size, crystal shape, crystal perfection, and the transport of chemical reagent and removal of the weathered product (Ollier, 1969, p53). As weathering is purely a surface reaction, an increase in surface area by a decrease in the particle size improves the weathering rate. But imperfections on the surface of the reacting grain also increase its reactivity. Lattice dislocations within the crystal structure produce uneven surfaces on grains such as kinks or admolecules. Terraces on the surface of the grain (created by preferentially weak planes, i.e. cleavage planes), point defects, and grain boundaries are also sites of high energy (Figure 2.2, Noack *et al.*, 1993). The more imperfect the grain, the faster it reacts (Wieland *et al.*, 1988). Minerals with preferential weak planes allow solutions to penetrate the underlying layers through transport along these planes. Breakage along these planes produces more sharp corners, which are also sites of high energy (Ollier, 1969, p53). An increase in surface dislocations increases the dissolution rate, which

Table 2.2: Weathering reactions of selected silicate minerals at the Earth's surface.

Type	**Description**
Solution reaction	This reaction occurs in the presence of water and may precipitate chemicals, which can lead to volume change, e.g. the dissolution of limestone. $CaCO_3 \rightarrow Ca^{2+} + {CO_3}^{2-}$ Calcite in the presence of solution congruently dissolves into its constituent cations
Oxidation and reduction	Oxidation reactions are simple REDOX reactions which cause cations to change their oxidation state, e.g. Fe^{2+} to Fe^{3+}. $8(Mg,Fe)_2SiO_4 + 16H^+ + O_2 \rightarrow 2Mg_3Si_4O_{10}(OH)_2 + 2FeO(OH) + 8Mg^{2+} + 5H_2O$ Olivine in acidic water hydrolyses incongruently to form iddingsite (a mixture of saponite and ironhydroxides)
Carbonation	The reaction of carbonate or bicarbonate ions with minerals. $Mg_2SiO_4 + 4CO_2 + 4H_2O \rightarrow 2Mg^{2+} + 4HCO^{3-} + H_4SiO_4$ Olivine in the presence of dissolved carbon dioxide, dissociates completely into magnesium ions and silicic acid
Hydration	The addition of water to a mineral's structure. This is important for the formation of clays, e.g. feldspar to kaolinite. $2KAlSi_3O_8 + 3H_2O \rightarrow Al_2Si_2O_5(OH)_4 + 4SiO_2 + 2K(OH)$ Potassium feldspar in acidic water hydrolyses incongruently to kaolinite + quartz + potassium hydroxide
Chelation	The holding of an ion (usually a metal ion) within a ring structure of organic origin. $Mg_2SiO_4 + 2X^{2-} + 4H^+ \rightarrow 2MgX + H_4SiO_4$ Olivine in the presence of any ligand (X) dissociates completely into magnesium ions, which are complexed by the ligand, and silicic acid
Hydrolysis	The chemical reaction between a mineral and water. H^+ and OH^- ions from water interact with the ions in the mineral's structure. $Mg_2Si_2O_6 + 2H^+ \rightarrow Mg_7Si_8O_{22}(OH)_2 + Mg^{2+} + 2H^+ \rightarrow Mg_6Si_8O_{20}(OH)_4 + Mg^{2+}$ Enstatite is hydrated to a Mg-serpentine and then further hydrated to talc (Mg-clay), liberating free magnesium at each step (incongruent reaction)

has been observed for calcite. Highly strained calcites have shown a 2 to 3 times increase in their dissolution rate when compared to unstrained calcite (Brantley, 2008).

The mean lifetime between silicate minerals differs by ~30 million years, with olivine as the most reactive mineral and quartz the least reactive mineral (Figure 2.3). The disparity between these reaction rates is based on the structure and chemistry of the minerals. The degree of Si-O tetrahedra polymerisation has a direct influence on the mineral's stability – the higher the Si:O ratio, the fewer cations are needed to balance the equation – and results in a more covalently bonded structure (Kehew, 2001). Therefore minerals with a high Si:O ratio are more resistant to chemical weathering.

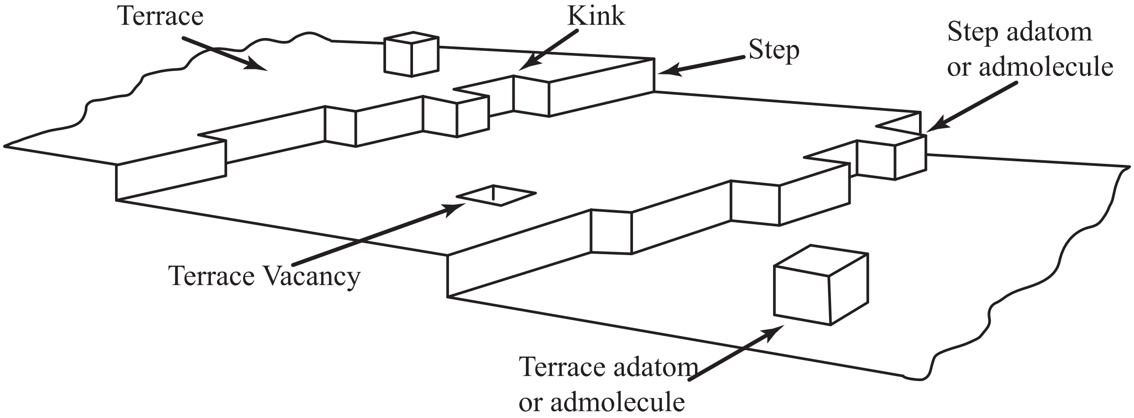

Figure 2.2: Surface features of an imperfect crystal. Lattice dislocations within the crystal structure produce uneven surfaces on grains such as kinks or admolecule. Terraces on the surface of the grain created by preferentially weak planes (i.e. cleavage planes). Adapted from Hochella (1995)

This identification led Goldich (1938) to list the order of reactivity of silicate minerals (Figure 2.3) in the same order as the formation of minerals during crystallisation (referred to as the Bowen's reactivity series). Ramberg (1952) ordered the reactivity of the silicates as: orthosilicate $>$ single chain $>$ double chain $>$ phyllosilicate $>$ tectosilicate. During magma crystallisation, simple silicates (nesosilicates) are first to form as they have the lower Si:O ratio and a higher metal to silica ratio. As crystallisation proceeds, the system's energy decreases which lowers the energy required for the more complex silicate structures to form and increases the silicate polymerisation (DeVore, 1955). Thus minerals that form first during crystallisation of a magma are more reactive than later-formation minerals. The crystallisation reactivity series in Figure 2.3 has two simultaneous pathways: mafic and felsic. Mafic minerals are enriched in the heavier metals Mg and Fe (SiO_2 = 49-52 wt.%), whereas felsic minerals are enriched in the lighter metals: Si, Al, Na, and K ($SiO_2 > 69$ wt.%). Minerals that crystallise first are the most reactive and weather easily; and minerals that form later are more polymerised and thus more stable on the Earth's surface. This is confirmed by the contrast in weathering rates for the silicate minerals (Table 1.2). Furthermore, the difference in weathering rates of minerals compared to the reactivity series is shown in Figure 2.3, with the mean lifetime of a 1 mm crystal at pH 5 and 25 °C (values in red).

Natural weathering reactions provide an important base-line for engineered weathering reactions. In order to store CO_2 as mineral carbonates, the reaction rates of the feedstock mineral need to be

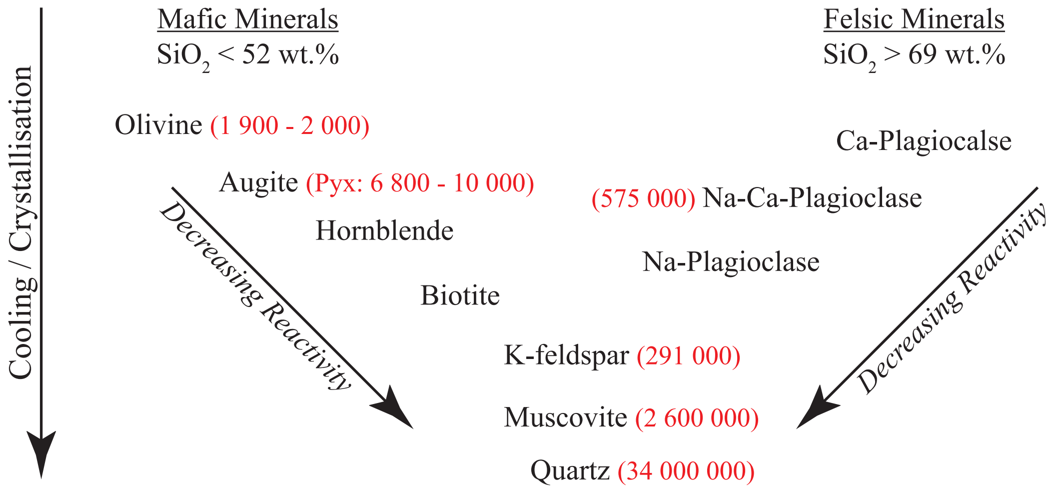

Figure 2.3: Stability of silicate minerals as shown by Bowen's reactivity series, adapted from Goldich (1938). The stability of the minerals is proportional to silicate polymerisation. The crystallisation series proceeds from top to bottom of the figure. The numbers in brackets next to each mineral represent the mean lifetime of a 1 mm crystal at 25 °C at pH = 5 from reaction rates by Lasaga (1995) and Brantley (2003).

sufficiently high to make the process viable. However, a basic understanding of the kinetics of silicate dissolution is needed in order to identify opportunities to maximise the kinetics of the dissolution reaction.

2.2 Reaction mechanism of silicate mineral acid dissolution

The previous section detailed the dissolution reactions of silicate minerals under weathering conditions at low temperature (below 30 °C) and atmospheric pressure. However, in an engineered environment the rate of silicate dissolution can be increased to make the reaction rates more favourable. But first an understanding of the reaction mechanism for silicate mineral dissolution is important before the reaction rate can be improved.

2.2.1 Molecular-scale dissolution mechanism

At the molecular level, the dissolution of a primary silicate mineral is described by the surface protonation model: a general hydrolysis reaction, where protons (H^+) in solution attach to bridging oxygens or hydroxyl groups on the surface of the grain (Furrer and Stumm, 1986). H^+ ions are supplied in the solution by: partially ionised water, carbonic acid, or any other acid. The protons are assumed to be mobile on the reaction surface and can be shifted from OH groups to neighbouring bridging oxygens (Wieland *et al.*, 1988). The attachment of the proton to the bridging oxygen dramatically lengthens the Si-O bond from 1.611 Å to 1.724 Å, which lowers the activation energy for dissolution (Lasaga, 1995). Protons attach to oxygens and bridging oxygens of the Si-O tetrahedra until all of the anchoring oxygens are bonded to two hydrogen atoms. Sufficient weakening of the metal-oxygen bond (M-O) occurs when the neighbouring oxides or hydroxide groups have been fully protonated. Protonation promotes dissolution because protons create highly polarised O-H bonds in close proximity to the M site cation, thus facilitating the detachment of the hydrated Si-O tetrahedron, $Si(OH)_4$ (Prigiobbe and Mazzotti, 2011). $Si(OH)_4$ desorbs from the surface of the mineral and enters the solution, where it will either form silicic acid or polymerise to precipitate Si (Furrer and Stumm, 1986; Wogelius and Walther, 1991). Similarly, the adsorption of the OH^- leads to the hydroxylation of the metal cation. The reaction of OH^- with the M site cation destabilises the M-O bond and facilitates the desorption of the cation as $M(OH)_{(aq)}$ (Prigiobbe and Mazzotti, 2011; Wieland *et al.*, 1988). Removal of the metal species exposes the underlying metal bonds to further interaction with the solvent (Furrer and Stumm, 1986). The general dissolution reaction for olivine is given as:

$$Mg_2SiO_{4(s)} + 4H^+_{(aq)} \leftrightarrow H_4SiO_{4(s)} + 2Mg^{2+}_{(aq)} \tag{2.1}$$

The dissolution reaction for olivine proceeds as shown in Figure 2.4. Initially (step 1), the protons attach to the oxygens of the Si-O tetrahedra on the surface of the mineral. The new H-O bond weakens the adjoining M-O bond. The electrostatic force, which holds the metal to the oxygen of the Si-O tetrahedra, becomes strained (dashed line, step 2). Hydration of the neighbouring Si-O tetrahedra adjacent to the M site further weakens the M-O bonds, and simultaneously, a negative ion (OH^- in this case) attaches to the M site (step 3). Once the Si-O tetrahedra are fully hydrated (with H^+ ions) and the M-O bonds weakened, the hydrated $Si(OH)_4$ leaves the mineral surface (step 4). The removal of the surface silicate tetrahedra exposes the underlying metal cations for liberation (Wieland *et al.*, 1988; Furrer and Stumm, 1986; Wogelius and Walther, 1991; Lasaga, 1995).

When only H^+ ions are involved in the dissolution reaction, the process is termed ‘proton-promoted’; however, when organic ligands (e.g. an oxalate ion) are involved in the dissolution reaction, the process is termed ‘ligand-promoted’ (Figure 2.5). A ligand is a molecule that binds to a central metal atom to form a coordination complex through donation of the ligand’s electron pairs. In the ligand-promoted mechanism, the ligands form inner-sphere complexes with the metal ion. This shifts the electron density towards the metal ion which weakens the M-O bond (Prigiobbe and Mazzotti, 2011). Ligands can act as both proton- and ligand-promoted species in that they can donate protons to bond with bridging oxygens or hydroxide groups; and they can bond with the metal species

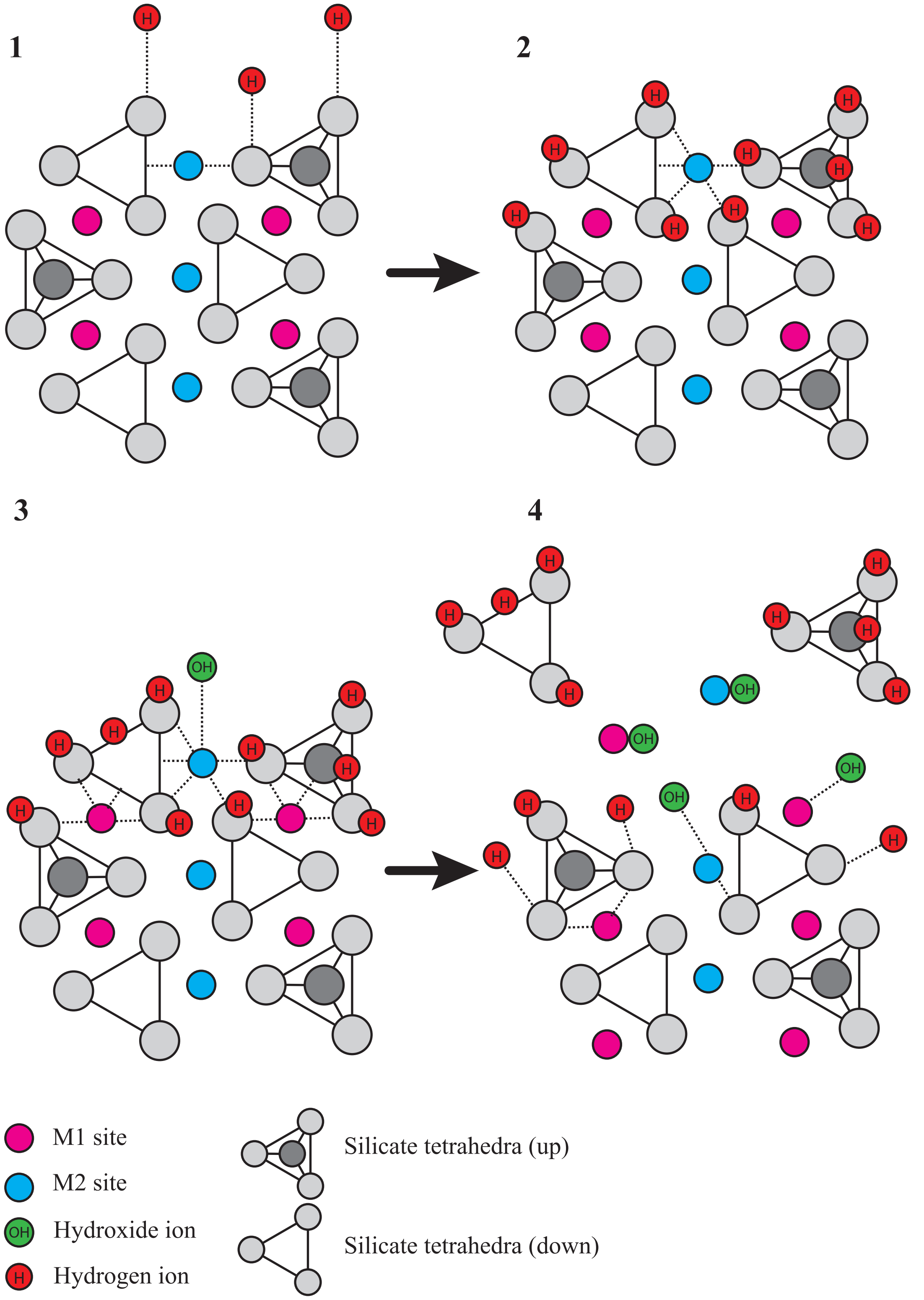

Figure 2.4: Surface protonation model for the dissolution of olivine. Discrete stages of dissolution are explained in text. Adapted from Wieland *et al.* (1988), Furrer and Stumm (1986); Wogelius and Walther (1991), and Lasaga (1995).

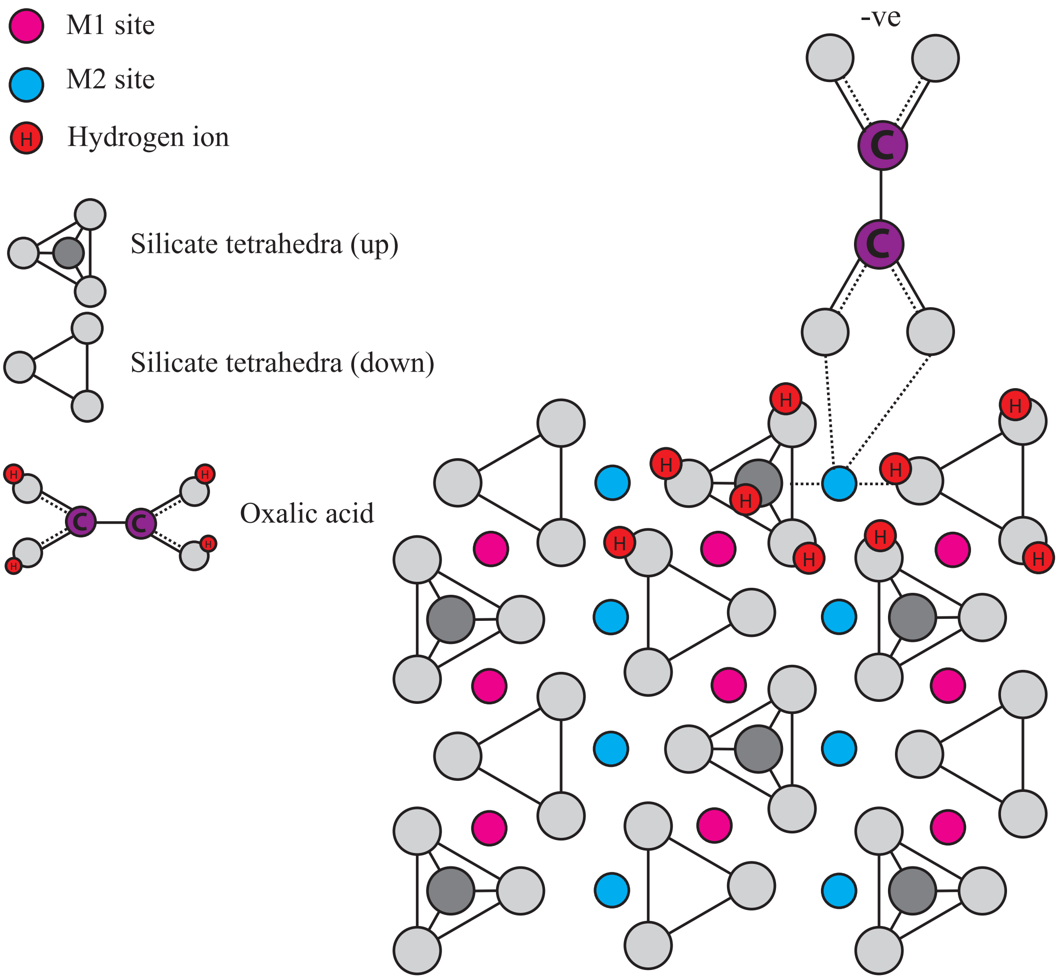

Figure 2.5: Ligand-promoted mechanism for the dissolution of olivine. In this model, the metal site is co-ordinated by an organic ligand (oxalate). The remainder of this reaction proceeds with the breaking of the metal-oxygen bond and the removal of the hydrated Si-O tetrahedra. Adapted from Furrer and Stumm (1986), Lasaga (1995), Bennett and Casey (1994), Liu *et al.* (2006), and Prigiobbe and Mazzotti (2011).

via donation of their electron pairs (Figure 2.5, Furrer and Stumm, 1986). The coupled ligand-promoted (Eq 2.2) and proton-promoted (Eq 2.1) reaction has been observed to be faster than the proton-promoted-only reaction under the same conditions (Bennett and Casey, 1994; Prigiobbe and Mazzotti, 2011).

$$Mg_2SiO_{4(s)} + 2L^{2-}_{(aq)} + 4H^{+}_{(aq)} \leftrightarrow 2MgL_{(aq)} + H_4SiO_{4(aq)} \tag{2.2}$$

2.2.2 Particle-scale dissolution mechanism

The mechanism for proton- and ligand-promoted dissolution has been described previously on an atomic scale, however, on the larger particle-scale, the silicate dissolution reaction is more complex. At the particle-scale, solute transport is as important as the reaction on the mineral surface. The silicate dissolution reaction on the surface of a particle can be described by five discrete steps as shown in Table 2.3.

Table 2.3: Stages of silicate mineral dissolution at the particle surface. Adapted from Berner (1978), Bales and Morgan (1985), Wieland *et al.* (1988), Velbel (1993) Fouda *et al.* (1996), Levenspiel (1999, p570), and Paktunc (1999).

Step	Description
Step 1:	Mass transport of reagent through the gas film surrounding the particle to the mineral surface
Step 2:	Penetration of reagent through the solid product layer (if present) to the mineral surface and adsorption of reagent onto mineral surface
Step 3:	Chemical reaction of reagent with solid mineral at the reaction front
Step 4:	Detachment of products from mineral surface and diffusion of the products back through the solid product layer (if present)
Step 5:	Mass transport of products through the gas film into the bulk solution

The dissolution of silicate minerals is limited by either the chemical reaction at the surface (reaction-limited) or the transport of the reagent to the reaction front (transport-limited, Luce *et al.*, 1972; Bales and Morgan, 1985; Brantley, 2008). Reaction-limited kinetics are caused when the reaction at the surface, and not the movement of solvent to the reaction front, is the rate determining step. In silicate minerals, reaction-limited kinetics arises from the slow desorption of the solute from the silicate mineral structure. The strong Si-O bonds in the mineral require a high activation energy in order to break the M-O bond. The strong M-O bond, caused by the silicate polymerisation, inhibits metal cation desorption (Bennett and Casey, 1994). The main contribution to the forces stabilising a cation in the silicate structure is the Madelung site energy: the electrostatic potential energy required to move an ion an infinite distance from its equilibrium position in the crystal structure (i.e. the energy required to break the anion-cation bond) and for one mole of an ionic solid under standard conditions it is referred to as the lattice energy (Ohashi and Burnham, 1972). The Madelung site energy increases as the degree of polymerisation of the Si-tetrahedra increases. The cation with the lower absolute Madelung energy is bonded more weakly and is more mobile (Chen and Brantley, 1998). Thus cations in more complex silicate structures require more energy to be removed than those in more simple structures (e.g. Mg in pyroxene and olivine, respectively). As the reaction progresses, the dissolved, outer layer will be completely removed (Brantley, 2008). The reaction kinetics for reaction-limited dissolution (Figure 2.6) shows a particle that decreases in size as the reaction proceeds (i.e. conversion), where the degree of dissolution is constant throughout the particle. On the other hand, transport-limited kinetics are controlled by the movement of the chemical solvent to the reaction surface. This can occur by diffusion of the solvent or solute through the fluid film or through a solid product layer (Luce *et al.*, 1972). Figure 2.6 shows that the transport of H^+ (L & H^+, for ligand-promoted dissolution) to the particle's reaction front (grey particle) and the transport of Mg^{2+}, $Si(OH)_4$ (Mg-L-H, for ligand-promoted dissolution) from the reaction front into the bulk solution is slow through the product layer (white). This type of mechanism results in a large particle with a shrinking, unreacted core after high conversion and a thick, outer layer (Luce *et al.*, 1972; Berner, 1978; Schott and Berner, 1985).

A product layer can be present in both reaction- and transport-limited reactions. In a reaction-limited reaction, a product layer forms from the precipitation of insoluble or slightly insoluble minerals (e.g. Si). When the metal leaves the mineral surface, the $Si(OH)_4$ is also removed from the structure. The $Si(OH)_4$ is either taken into the bulk solution or precipitated on the surface of the mineral to form a protective 'product' layer (Hellmann *et al.*, 2003; Putnis and Ruiz-Agudo, 2013). A product layer can also form from the preferential leaching of metal cations from a silicate mineral. This occurs when there is a variety of cation compositions and the energy differs for multiple M sites within one mineral. This product layer may inhibit the transport of reactant and reacting species to the reacting surface and solution, respectively. However some authors (e.g., Luce *et al.*, 1972; Knauss *et al.*, 1993; Weissbart and Rimstidt, 2000; Bonfils *et al.*, 2012) believe that the transport of the solvent or solute is not hindered by a protective product layer, and even if a solid product layer were to form, it will be porous enough to not limit transport. An example of this is the surface of the olivine in

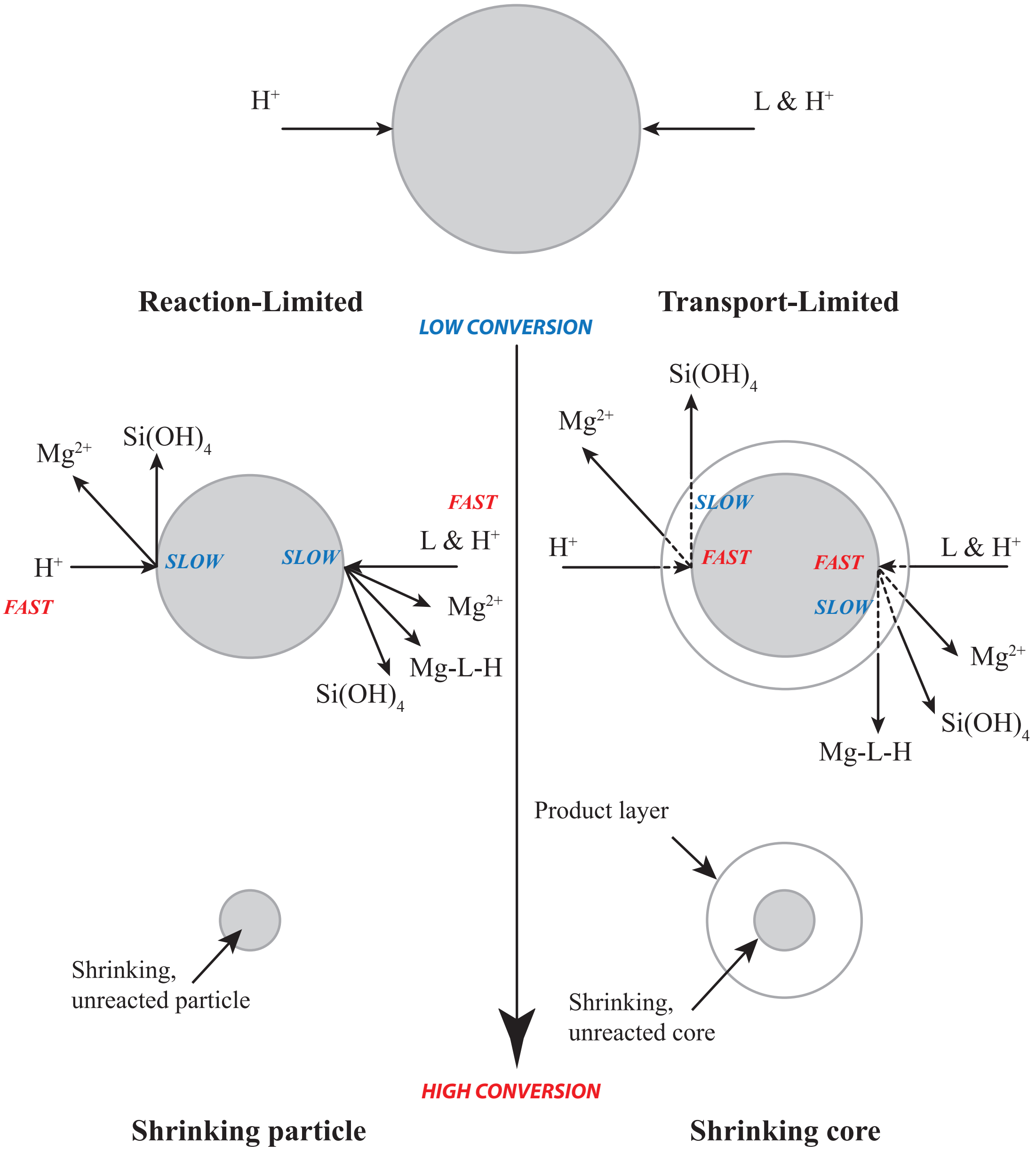

Figure 2.6: Reaction-limited vs. transport-limited reactions for dissolution via proton and ligand dissolution. The reaction-limited mechanism is characterised by the slow detachment of the metal cation and the hydrated silicate; whereas the transport-limited reaction is characterised by the slow diffusion of constituents through the product layer but the fast detachment of the metal cation and the hydrated silicate. At high conversion of a spherical particle, the reaction-limited mechanism produces smaller particles with the same chemistry as the starting material; however the transport-limited mechanism produces a slightly smaller particle with a product (leached) layer surrounding the whole particle. This product layer inhibits the movement of solvent to the reaction surface. Adapted from Levenspiel (1999, p567) and Teir *et al.* (2007).

Figure 2.7, where a porous, leached layer covers the reaction surface. As shown previously, there is much controversy over the formation of a product layer, with some studies showing no product layer formation and in studies where a product layer has formed, it has been attributed to either leaching or precipitation.

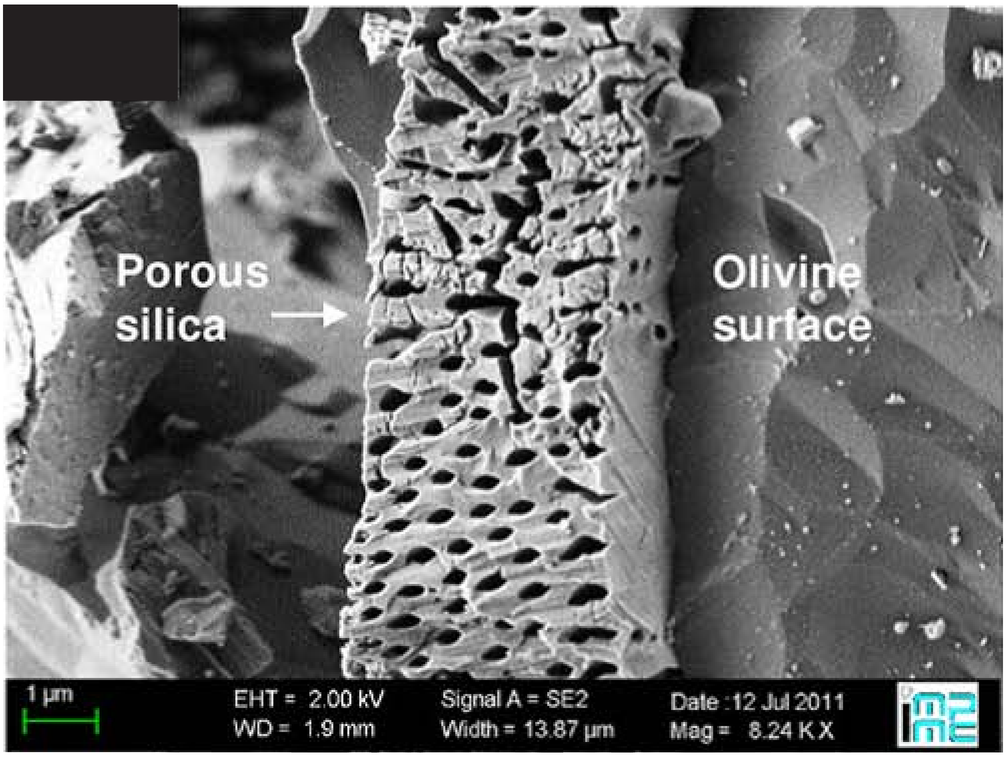
[redacted]

Figure 2.7: FEG-SEM images of solid olivine after 1 h reaction in 0.1 M oxalate, 120 °C, and 20 bar CO_2. From Bonfils *et al.* (2012).

Reaction-limited kinetics has been argued for olivine, as transport calculations of a 100 µm grain at 25 °C show that diffusion through a silica layer is 10^4 times higher than the rate of detachment of the reacting species (Jonckbloedt, 1998). This agrees with the silicate structure of olivine, as a leached surface layer is unlikely to form due to the ease with which protonated silica tetrahedra can detach from the mineral surface. However, Bonfils *et al.* (2012) showed the formation of a highly porous silica product layer on olivine after dissolution in 0.1 M oxalate salt at 120 °C and 20 bar CO_2. In inosilicate minerals the breaking of the Si-O-Si linkages is slow, but is required for complete dissolution. Therefore partially detached Si-O tetrahedra are left on the surface of reacting grains. This which has been observed for both enstatite and wollastonite (Weissbart and Rimstidt, 2000; Oelkers, 2001; Oelkers and Schott, 2001).

Another factor to consider for reaction-controlled kinetics is the appearance of etch pits on the surface of leached grains. Dissolution of silicates is not a general attack of the surface, but rather distinctive, crystallographically-controlled etch pits (Berner *et al.*, 1980) as shown in Figure 2.8. Etch pits are defined by the sum of horizontal movement of atomic-scale steps which define incomplete surface layers and the removal of atoms in the mineral (Brantley, 2008). Dissolution experiments on olivine by Grandstaff (1978) showed that the specific surface area of the grains increased by a factor of 7 after the first 100 hours. The surfaces of the grains were significantly altered with the removal of more than 1 μm of material and the formation of edges and etch pits. Edges were created by the rounding of intersecting cleavage or lattice dislocations (Grandstaff, 1978). Pitted surfaces indicate a reaction-controlled mechanism, whereas smooth, rounded surfaces indicate a transport-controlled mechanism (Chen and Brantley, 1998). Brantley (2008) argued that highly soluble minerals have a greater likelihood that they will become transport-limited; whereas low solubility minerals are likely to be reaction-limited.

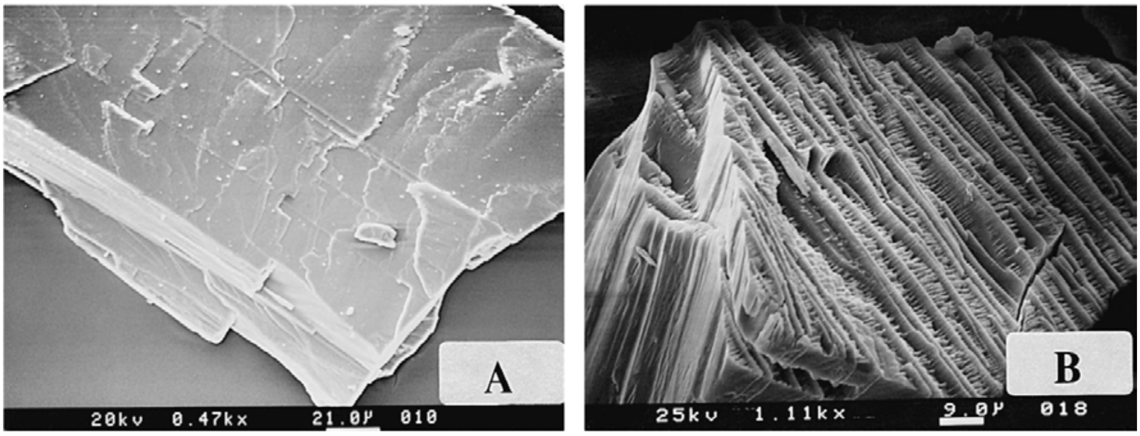

Figure 2.8: SEM images which shows (A) an unleached diopside grain, and (B) a diopside grain leached at 90 °C and pH 2.17 after 1830 hours. From Chen and Brantley (1998).

A recent study by Park *et al.* (2003) proposed a mixed rate-limiting step for the dissolution of serpentine, with the initial dissolution rate controlled by surface reactions, and the latter part of the reaction controlled by diffusion as indicated by the plateauing of the dissolution rate. Furthermore, silicate minerals with mixed cations can show preferential loss of each cation during dissolution. This preferential dissolution is driven by differences in site energies, and has been reported for inosilicate minerals (pyroxene and amphiboles Berner *et al.*, 1980; Chen and Brantley, 1998). The metal sites in the silicate preferentially release their cations during dissolution, especially at lower pH values (Brantley, 2008). Preferential leaching of cations over Si will lead to the formation of a leached layer, which has experimentally been shown to be up to a couple of microns thick (Figure 2.7). Nonstoichiometric dissolution, which leads to incongruent dissolution, is usually due to the leaching of impurities, precipitation of a secondary phase or the preferential leaching of cations (e.g. dissolution of the pyroxene jaedite, Brantley, 2008). New evidence from Hellmann *et al.* (2003) at the nano-scale (from high-resolution transmission electron microscopy) suggests that a coupled extraction and precipitation mechanism of Si limits the rate of dissolution. Therefore the dissolution of the mineral is in fact stoichiometric but the subsequent precipitation of a new solid phase results in this non-stoichiometric observation (Daval *et al.*, 2011; Putnis and Ruiz-Agudo, 2013). However, Brantley (2008) suggests that preferential leaching of cations does occur when Ca is involved. In feldspars, the substitution of Al in the silicate structure can lead to the preferential leaching of the Al from the Si-Al-tetrahedra, especially at low pH, where proton attack of Al-O-Si is favoured over the Si-O-Si bond and a resulting leach layer does occur (Lasaga, 1995).

2.3 Parameters of aqueous silicate dissolution

Natural mineral carbonation proceeds at very slow rates, depending on the degree of silicate polymerisation. Research to increase the reaction rates of aqueous silicate dissolution has focused mainly on the effect of solvent composition, temperature, pressure, and particle size. The rate of dissolution for any silicate mineral is described by the change in solution concentration or mineral surface with time (Lasaga, 1995). The factors affecting the rate of an equation include, but are not limited to: temperature, surface area, and pH. These factors will be discussed further.

The general form of the rate law for heterogeneous mineral surfaces as described by Lasaga (1995) in Eq 2.3 is:

$$Rate = k_0\, A_{min}\, e^{\frac{-E_a}{RT}}\, a_{H+}^{n_{H+}}\, g(I) \prod_i a_i^{n_i}\, f(\Delta G_r) \tag{2.3}$$

Where, k_o is an intensive rate constant with units of mol.cm^{-2}.s^{-1}, which incorporates the pre-exponential factors involving mineral surface dynamics; A_{min} is the reactive surface area of the mineral in cm^2; E_a is the apparent activation energy for the overall reaction in kJ.mol^{-1}; R is the molar gas constant; T is the temperature in Kelvin; a_{H+} and a_i are the activity of the H$^+$ ion and any other species (i) in solution; $g(I)$ is the effect of ionic strength; and $f(\Delta$Gr) accounts for the variation of rate with deviation from equilibrium (where at equilibrium, $f(\Delta$Gr) = 0, Lasaga, 1995).

Activation energies for dissolution far from equilibrium on the order of 10-20 kJ.mol^{-1} indicate a transport-controlled mechanism (by solute diffusion), and 50-80 kJ.mol^{-1} indicate a reaction-controlled mechanism (by detachment of the metal cation of Si^{4+}, Lasaga, 1984; Casey and Sposito, 1992). The activation energy of a silicate mineral should remain constant when the experimental parameters are changed (e.g. temperature, particle size, solution chemistry). The activation energy for selected minerals of the pyroxene group minerals are listed in Table 2.4 and their values indicate a reaction-controlled dissolution mechanism (Brantley, 2003). Work by Casey and Sposito (1992) has shown that dissolution activation energies are much lower than what was previously predicted from detailed models of surface reactions. From their observations, experimental activation energies from proton-promoted dissolution include energy contributions from: activation enthalpy, enthalpy of proton adsorption (and desorption), and enthalpy contribution from long-range electrostatic interactions. They further explain that the activation energies of dissolution are highly dependent on solution pH. Several other authors have attributed this discrepancy to the variability in Brønstead acid-base chemistry at mineral surfaces under differing temperatures and pH values. Furthermore, activation energies can change with a change in solution chemistry, especially with the addition of organic acids which decreases activation energy (Brantley, 2003). Experiments on kaolinite (an Al-rich clay) decreases its activation energy of 77 kJ.mol^{-1} at pH 1 to 15 kJ.mol^{-1} pH 8 (Casey and Sposito, 1992).

Table 2.4: Activation energy (Ea) of selected pyroxene group minerals. Activation energy (Ea) in kJ.mol^{-1}, k is the rate constant and n is the unitless order of the reaction (Brantley, 2003). Lower Ea values indicate a more reactive mineral.

Mineral	**Acid mechanism**			**Neutral mechanism**	
	log k	Ea	n	log k	Ea
Enstatite	-9.02	80.0	0.600	-12.72	80.0
Augite	-6.82	78.0	0.700	-11.97	78.0
Diopside	-6.36	42* to 96.1**	0.710	-11.11	40.6
Wollastonite	-5.37	54.7	0.400	-8.88	54.7

* Knauss *et al.* (1993)

** Chen and Brantley (1998)

2.3.1 Solvent composition and chemical additives

The surface protonation model described in Section 2.2 relies on the supply of H^{+} ions to protonate the oxygens, which weakens the critical metal-oxygen bond. In the presence of water-only (anaerobic), water dipoles are responsible for the breaking of the M-O and Si-O bonds, which results in reactions that proceed at geological time periods (Wieland *et al.*, 1988; Brady and Walther, 1989).

However in nature (aerobic), CO_2 forms carbonic acid in the presence of water, and although a weak acid, it can aid in silicate mineral dissolution. The addition of carbonic acid only is not always sufficient to leach cations from silicate minerals in a short time period (Park *et al.*, 2003). Other additives that aid in natural dissolution include organic acids produced in soil. A number of solvents: acidic, basic, and organic, have been investigated for mineral carbonation, or their effect on silicate mineral dissolution (Table 2.5). The important mineral acids include hydrochloric acid, sulphuric acid, and nitric acid. Important organic acids include: acetic acid, ascorbic acid, citric acid, oxalic acid, and succinic acid. Furthermore, the majority of these experiments have been conducted on olivine and serpentine minerals, with little or no experimentation on pyroxene minerals.

In mineral carbonation studies, solution conditions can be optimised to increase the dissolution rate. The dissolution rate based on pH is defined in Eq 2.4, where k_H is the rate constant and n is the reaction order that varies with mineral composition (Drever and Stillings, 1997).

$$R_H = k_H[H^+]^n \tag{2.4}$$

Acidic dissolution increases the reaction rate with a decrease in pH (below pH = 7) as shown in Figure 2.9 for diopside. A decrease in pH increases the concentration of H^+ ions to protonate the Si-O tetrahedra (Wieland *et al.*, 1988; Knauss *et al.*, 1993). The rate of dissolution increases exponentially

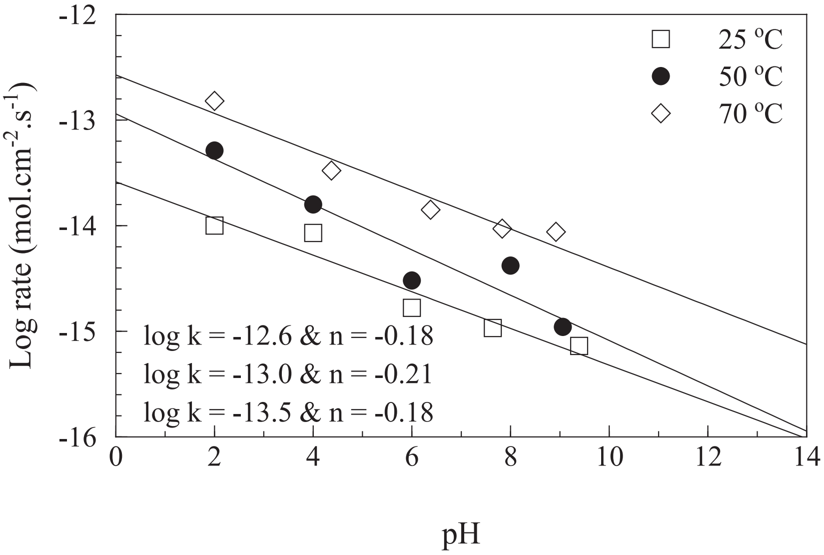

Figure 2.9: Steady-state log r_{diop} based on Si release for runs at 25 °C, 50 °C, and 70 °C and between pH 2 and 10. The regression results from each temperature and the apparent activation energy for diopside. From Knauss *et al.* (1993).

Table 2.5: Chemical additives investigated for dissolution of a specific mineral for mineral carbonation studies, and their references.

Additive	**Chemical Formula**	**Mineral**	**Reference**
Acetic acid	CH_3COOH	Serpentine	Welch and Ullman (1993)*
		Serpentine	Teir *et al.* (2007)
		Serpentine	Fagerlund *et al.* (2010)
		Wollastonite	Badyga *et al.* (2010)
Ascorbic acid	$C_6H_8O_6$	Serpentine	Park *et al.* (2003)
Citric acid	$C_5H_6O_7$	Plagioclase	Welch and Ullman (1993)
		Olivine, serpentine, and wollastonite	Prigiobbe *et al.* (2009)
		Serpentine	Krevor and Lackner (2009)
		Olivine	Prigiobbe and Mazzotti (2011)
EDTA	$C_{10}H_{16}N_2O_8$	Serpentine	Park *et al.* (2003)
		Serpentine	Krevor and Lackner (2009)
Hydrochloric acid	HCl	Olivine	Chen and Brantley (2000)*
		Serpentine	Park *et al.* (2003)
		Serpentine	Teir *et al.* (2007)
		Olivine, serpentine, and wollastonite	Prigiobbe *et al.* (2009)
Nitric acid	HNO_3	Serpentine	Teir *et al.* (2007)
Orthophosphoric acid	H_3PO_4	Serpentine	Park *et al.* (2003)
Oxalic acid	$H_2C_2O_4$	Plagioclase and amphibole	Mast and Drever (1987)*
		Plagioclase	Welch and Ullman (1993)
		Serpentine	Park *et al.* (2003)
		Serpentine	Krevor and Lackner (2009)
		Olivine	Prigiobbe and Mazzotti (2011)
Succinic acid	$C_4H_6O_7$	Plagioclase	Welch and Ullman (1993)*
		Wollastonite	Badyga *et al.* (2010)

*Studies not related to mineral carbonation with increasing H^+ concentration at 25 °C, 50 °C, and 70 °C (Figure 2.9, Knauss *et al.*, 1993; Drever and Stillings, 1997; Chen and Brantley, 2000). At higher pH, usually around 4 to 5, the activation energy for the dissolution of silicate minerals is independent of pH as the reaction changes (Drever and Stillings, 1997; Chen and Brantley, 1998; Wogelius and Walther, 1991). An increase in temperature increases pH-dependence of the dissolution reaction. Experimental reaction order, n, with respect to H^+ for diopside increased from 0.19 ± 0.06 at 25 °C to 0.76 ± 0.08 at 90 °C. Anthophyllite (a Mg-Fe amphibole) increased from 0.24 ± 0.03 at 25 °C to 0.63 ± 0.04 at 90 °C (Chen and Brantley, 1998). The larger difference for n at a higher temperature signifies that the pH-dependence increases faster with an increase in temperature.

Researchers have found that the dissolution of silicates is also dependent on solution chemistry. Research carried out by Teir *et al.* (2007) showed that mineral acids (in decreasing strength), namely: sulphuric acid (H_2SO_4), hydrochloric acid (HCl) and nitric acid (HNO_3); and basic solvents, namely: sodium hydroxide (NaOH), potassium hydroxide (KOH), ammonia (NH_3), ammonium chloride (NH_4Cl), ammonium sulphate ($(NH_4)_2SO_4$), and ammonium nitrate (NH_4NO_3), were able to leach Mg and Fe from serpentine at 20 °C over a period of 1 h (Figure 2.10). Dissolution in basic solvents leached significantly less Mg from serpentine over 1 h when compared to the mineral and organic solvents. The high pH of the basic solvents favours the formation of carbonates, which are not stable at pH < 8 (Krauskopf, 1967). In summary, H_2SO_4 was the most effective at removing Mg from serpentine, but in the presence of Ca-bearing silicates (e.g. diopside and plagioclase in PGM tailings), H_2SO_4 will form gypsum precipitates, lowering the potential sequestering ability of the sample.

Other organic solvents (as listed in Table 2.5) have also been considered to aid in mineral dissolution. Due to its presence in soil, the effectiveness of organic acids for silicate mineral dissolution have been studied by Grandstaff (1978), Furrer and Stumm (1986), Mast and Drever (1987), Wogelius and Walther (1991), Welch and Ullman (1993), Barker *et al.* (1997), Park *et al.* (2003), Golubev and Pokrovsky (2006); and Teir *et al.* (2007). Although generally weak, organic solvents can affect the rate of mineral dissolution by complexing with metals in solution and through the addition of the ligand-promoted dissolution mechanism, as discussed in Section 2.2.1 (Bennett and Casey, 1994; Welch and Ullman, 1993). Complexing of the available metals in solution increases its apparent solubility, which forces the reaction to proceed (Prigiobbe and Mazzotti, 2011; Bennett and Casey, 1994; Furrer and Stumm, 1986). Catechol forms the water-soluble, activated complex $Si(Cat)_3^{2-}$ during the dissolution of olivine, Mg-clay minerals, and pyroxenes (Poocharoen, 1972). A number of Si-oxalate complexes have been proposed, for example unidentate and bidentate silicic acid-oxalate esters, but these have yet to be identified in Si-rich solutions (Bennett and Casey, 1994; Poulson *et al.*, 1997).

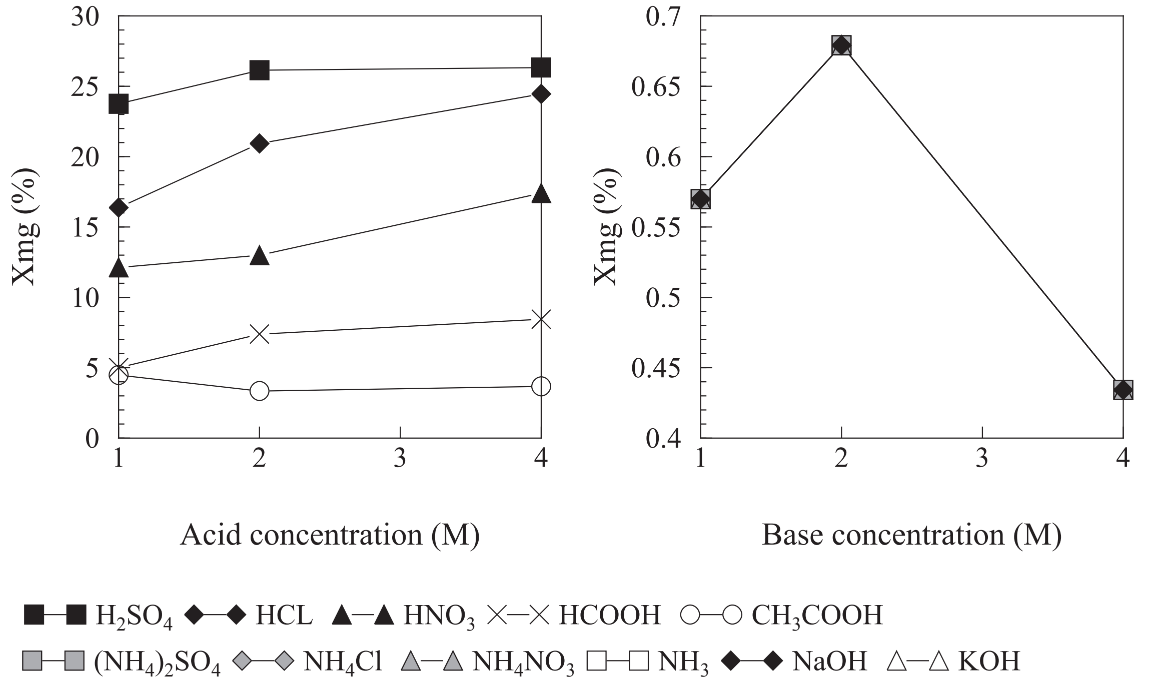

Figure 2.10: Fraction of Mg extracted from serpentinite (74 125 μ) at 20 °C for 1 h from acidic (left) and basic (right) solutions. From Teir *et al.* (2007).

Oxalate does form strong complexes with Al and Ca, which replaces almost half of the Si in the Si-O tetrahedra of plagioclase (Welch and Ullman, 1993). In the study the reactivity of the plagioclase was greatest for the Ca end-member than the Na end-member under the same experimental conditions.

Dissolution of silicates with organic acids is most effective at neutral pH, where the effect of proton-promoted dissolution is smallest (Welch and Ullman, 1993); but dissolution of silicates with mineral acids is most effective at low pH values, where the concentration of H^+ ions is high. However, organic acids are not as effective at low pH values as chelates open and the ligand can no longer be effective in the removal of cations. Oxalate is a strong chelator, especially for Al, and is most effective between pH of 4 and 5 and is independent of pH between 2 and 5 (Welch and Ullman, 1993). Organic acids can have multiple coordination sites in one molecule as shown for the organic acids in Figure 2.11. In acetate and oxalate, the negative charge is localised over two and four oxygens, respectively. Other organic ligands include citrate and succinate. Ethylenediamineteraacetic acid (EDTA) has also been used in mineral dissolution and has multiple (6) coordination sites, however the size of the molecule may hinder its effectiveness.

With the use of organic additives, Grandstaff (1978) showed that buffered solutions of sodium acetate and acetic acid can leach Mg and Fe from olivine. This was confirmed on SEM images

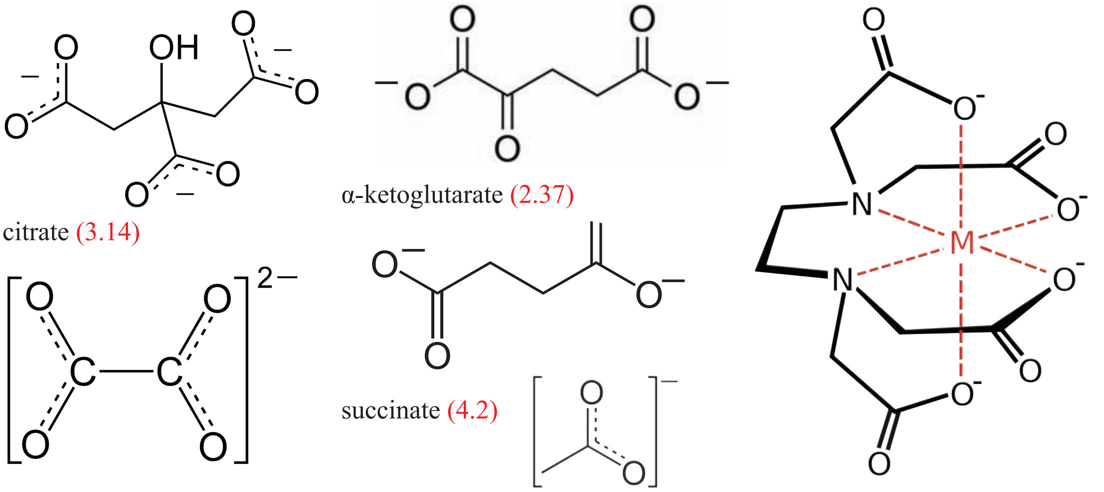

citrate (3.14)

α-ketoglutarate (2.37)

succinate (4.2)

oxalate (1.25)

acetate (4.76)

ethylenediaminetetraacetate (1.782)

Figure 2.11: A selection of chelate-forming organic ligands common to mineral dissolution and carbonation studies with the first ionisation constant of the acid in parentheses.

by the formation of etch pits on the surface of the olivine. Studies by Furrer and Stumm (1986) and Wogelius and Walther (1991) used organic ligands at concentration levels found in soils, and at higher concentrations, respectively, to enhance dissolution. They concluded that the most effective organic ligands are surface chelate-forming ligands such as bi- or multidentate (e.g. oxalate and citrate respectively) and that monodentate ligands have a negligible effect. Higher membered rings are progressively less efficient (e.g. the effect of malonate is greater than succinate). The order of effectiveness of the dissolution enhancement of organic molecules on silicate minerals roughly matches the order of the metal-ligand stability constants (Krevor and Lackner, 2009). Bonfils *et al.* (2011) found that EDTA and citrate enhance dissolution more strongly than acetate An important discovery from Park *et al.* (2003) showed that a solution of 1 vol.% orthophosphoric acid, 0.9 wt.% oxalic acid and 0.1 wt.% EDTA was more effective than 0.1 M HCl at ambient temperatures in the leach reaction of serpentine. Furthermore, Bennett and Casey (1994) showed that oxalate and citrate increased the solubility of quartz at high concentrations only. UV-visible spectroscopy suggest that oxalate and citrate interact with SiO_2 via an electron-donor electron-acceptor interaction at near-neutral pH. Golubev and Pokrovsky (2006) found that the addition of EDTA, citrate, oxalate, acetate, gluconate and 2,4-DHBA increased the dissolution of diopside at neutral pH as shown in Figure 2.12. From these experiments, very high concentrations (0.01 - 0.1 M) of organic ligands are necessary to appreciably affect the mineral dissolution rate of most minerals. A study by Welch and Ullman (1993) on the dissolution of plagioclase showed that the dissolution rates of plagioclase were two to five times greater in solutions of oxalate, citrate, succinate, α-ketoglutarate, and pyruvate than in inorganic solutions at pH 3 to 4. Furthermore, the plagioclase dissolution rates in oxalate at pH 3 (1 mM) were more than three-times the dissolution rate in HCl at the same pH (1 mM). The rate of plagioclase dissolution was a further order of magnitude greater in oxalate and citrate solutions near-neutral pH (pH = 6) than for inorganic solutions at near-neutral pH. This suggests that organic solvents have an advantage over inorganic solvents at near-neutral pH, where the effect of protonation is low and dissolution by the ligand-promoted mechanism is dominant. Brantley (2008) showed that the effect of millimolar concentrations of organic ligands on dissolution is less than a factor of $\sim$10 for neso- and inosilicates; and when organic ligands are present at concentrations observed for soils, its effect is less than a factor of 5 on dissolution rates. Teir *et al.* (2007) showed that an increase in concentrations of the acids investigated resulted in slightly higher dissolution of serpentine with respect to Mg (Figure 2.10). For reactions at lower concentrations, the reaction needs to be run for a longer extent in order to attain the same extraction at higher acid values (Alexander *et al.*, 2007). For example, to achieve the same extraction, the difference between 3 M and 4 M or 5 M sulphuric acid concentrations requires 3 to 5 times the amount of reaction time respectively.

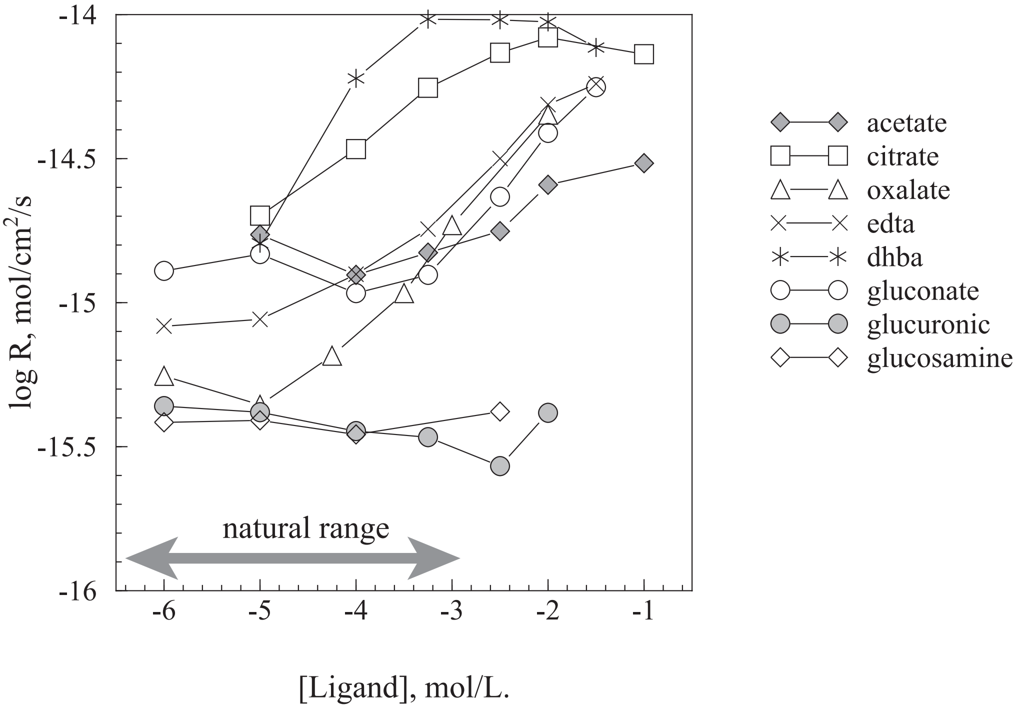

Figure 2.12: Diposide dissolution in organic-bearing solutions at 25 °C and 5.3 < pH < 7.0 (Golubev and Pokrovsky, 2006). DHBA is 2,4-dihydroxybenzoic acid.

2.3.2 Physical parameters of dissolution: temperature and particle size

For many elementary reactions, the temperature-dependence is expressed by the Arrhenius equation (Eq 2.5), where k' is the temperature-independent, pre-exponential factor in mol.cm^{-2}.s^{-1}; Ea is the activation energy in kJ, R is the gas constant, and T is the absolute temperature in Kelvin (Kump *et al.*, 2000).

$$k = k' e^{-\frac{Ea}{RT}} \tag{2.5}$$

A study by Levenspiel (1999, Table 2.6) showed that at an activation energy of 40 kJ.mol^{-1} at 0 °C the rate would double for an 11 °C temperature increase; and for the same activation energy at 2 000 °C, the rate would double for a 744 °C temperature increase. But for an activation energy of 400 kJ.mol^{-1} at 0 °C the rate would double for only a 1.1 °C temperature increase. Therefore from Table 2.6, it can be seen that the higher the activation energy, the lower the temperature increase needed to double the dissolution reaction rate (Levenspiel, 1999). In the dissolution of a silicate mineral, an apparent activation energy of 62.8 kJ.mol^{-1} will produce an increase in the reaction rate by one order of magnitude between 0 °C and 25 °C; and another order of magnitude between 25 °C and 55 °C (Lasaga, 1995).

Table 2.6: Temperature increase needed (in °C) to double the rate of reaction for a specific activation energy and a specified average initial temperature. Read in text for further explanation. From Levenspiel (1999, p28)

Initial	**Activation energy (Ea)**			
Temperature	40 kJ.mol^{-1}	160 kJ.mol^{-1}	280 kJ.mol^{-1}	400 kJ.mol^{-1}
0 °C	11	2.7	1.5	1.1
400 °C	65	16	9.3	6.5
1 000 °C	233	58	33	23
2 000 °C	744	185	106	74

Experimental temperature dependence reaction is demonstrated in Figure 2.13 from a study by Park *et al.* (2003), where an increase in temperature shows a direct, linear correlation with an increase in cation extraction (Figure 2.13, left). Furthermore, Teir *et al.* (2007) demonstrated the difference in the amount of Mg and Fe leached from serpentine at 50 and 70 °C, with 100 % of Mg leached after 2 hours at 70 °C, and only 85 % Mg leached after 2 h at 50 °C (Figure 2.13, right).

Particle size reduction has a two effects on the increase in dissolution rates. First, structural defects are imparted onto the grain in the grinding process through the destruction or disordering of the mineral lattice; and second, there is an increase in the exposed surface area by the decrease in particle

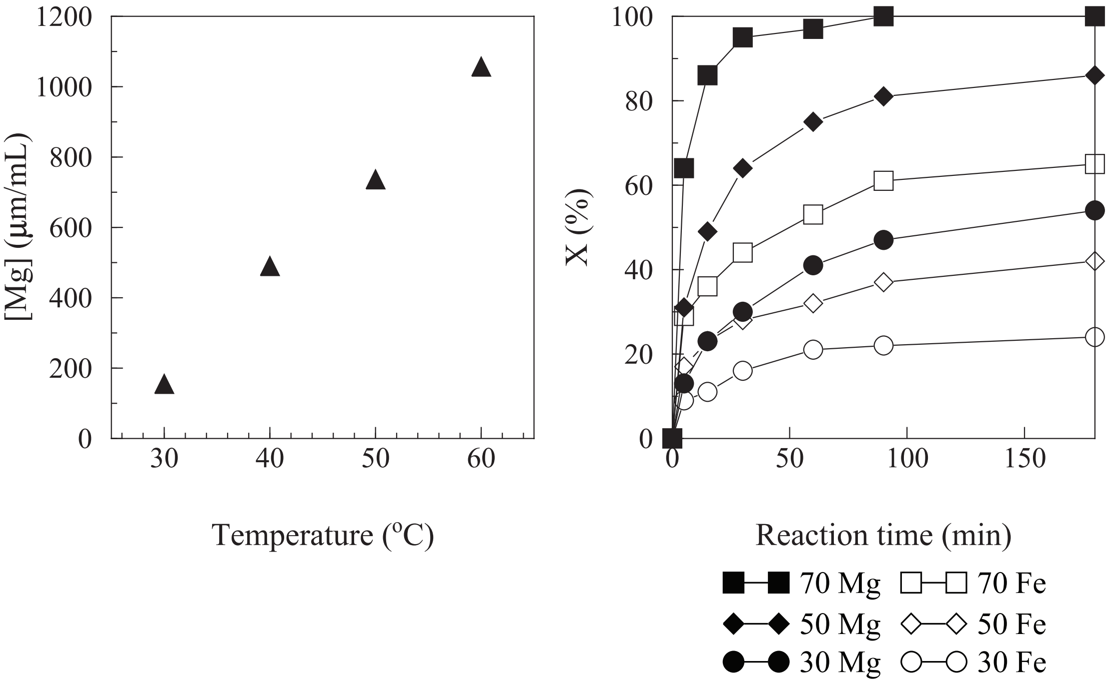

Figure 2.13: Effect of temperature on the extraction of Mg and Fe from the dissolution of serpentine (left); and the effect of temperature on the solution concentration of Mg and Fe from serpentine at 50 °C and 70 °C (right). From Park *et al.* (2003) and Teir *et al.* (2007), respectively.

size (Alexander *et al.*, 2007; Juhász, 1998). During elastic deformation of silicate minerals the lattice is distorted in a reversible way, but during plastic deformation, the structure of the crystal is destructed to such an extent that the crystallinity of the material is lost. Juhász (1998) showed that this process comes about after intensive grinding when the plastic deformation of particles (mechanochemical amorphisation) becomes the main processes rather than particle size reduction. The author further states that below a specific size, the energy from grinding is no longer used to reduce the size of the particle, but instead deforms the minerals structure through plastic deformation. Experiments on serpentine disks in 7 M HCl at 95 °C showed an extraction depth of between 300 µm to 400 µm resulted in a dissolution rate independent of particle size on particles with a diameter of less than 600 µm. Therefore regardless of the particle size characterisation, in order for complete dissolution, one dimension must be less than 300 µm in radius. However, Alexander *et al.* (2007) and Penner *et al.* (2003) showed that for serpentine samples (normalised to Mg) with a particle size only below 125 µm, the particle size has no effect on Mg extraction. A study by Teir *et al.* (2007) also showed that a decrease in particle size from 500 µm to 74 µm increased the extent of Mg extraction from 80 to 100 % from serpentine over the 170 min reaction period, but that the rate of extraction of Mg (Figure 2.14 left) for the different particle size fractions was the same up to 60 % extraction. The Fe

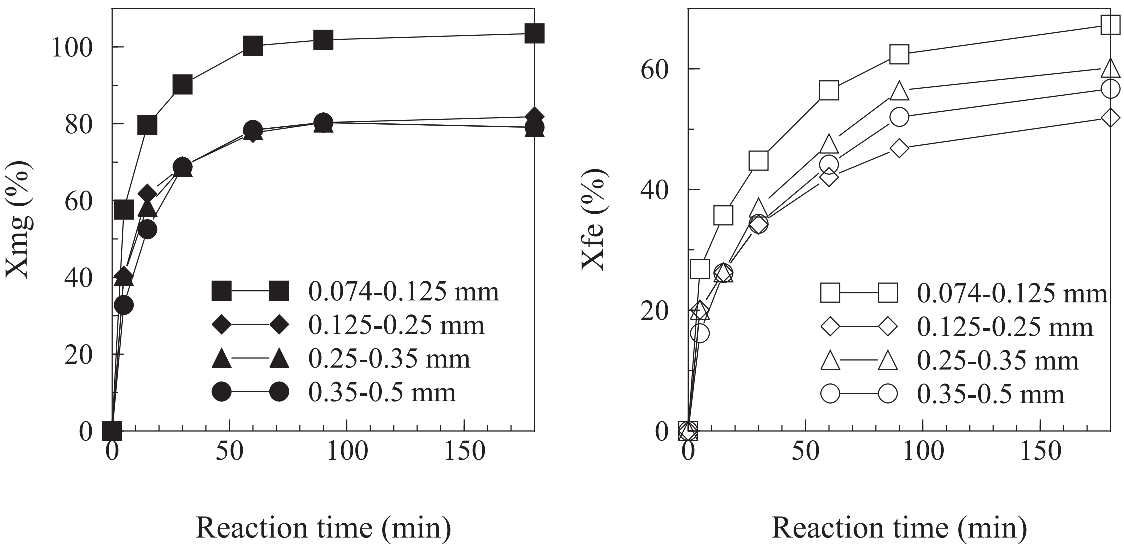

Figure 2.14: The effect of particle size on the dissolution of Mg (left), and Fe (right) from serpentine at 70 °C in 2 M HCl (Teir *et al.*, 2007).

extraction from serpentine increased from 60 to 70 % over the same time period. The +125/-250 μm, +250/-350 μm, and the +350/-500 μm size fractions had similar Mg and Fe extraction over the same extent of reaction, however the decrease in size to the +75/-125 μm size fraction had a much larger effect (Figure 2.14). Therefore Teir *et al.* (2007) shows that for serpentine, the minimum size is below 125 μm, which agrees with the work by Penner *et al.* (2003) and Alexander *et al.* (2007).

Work by Park and Fan (2004) showed that the removal of the diffusion-limiting silica layer would promote further dissolution. Penner *et al.* (2003) showed that pre-treatment increased surface area; however, Jonckbloedt (1998) found that it was necessary to physically agitate (by stirring) reacting samples to prevent silica polymerisation on the grain surface. Several methods for physical activation have been used previously which include: internal grinding, ultrasound, acoustic, and microwave. Park and Fan (2004) proposed an internal (*in-situ*) attrition grinding system to investigate its effect on serpentine dissolution with and without the addition of any chemical additives. 20 vol.% of both glass beads (2 mm diameter) and zirconia balls (5 mm diameter) were used as the grinding media; however, the physical activation by grinding alone did not did not significantly enhance the dissolution of serpentine (Figure 2.15). The final mean particle size was reduced from 29 μm to 17 μm. Figure 2.15 shows that the combination of chemical and physical activation results in a significant, overall improvement in serpentine dissolution. Results from the Albany Research Centre showed that with their mechanical pre-treatment, they were able to reduce the mean particle size to 2 μm. How-

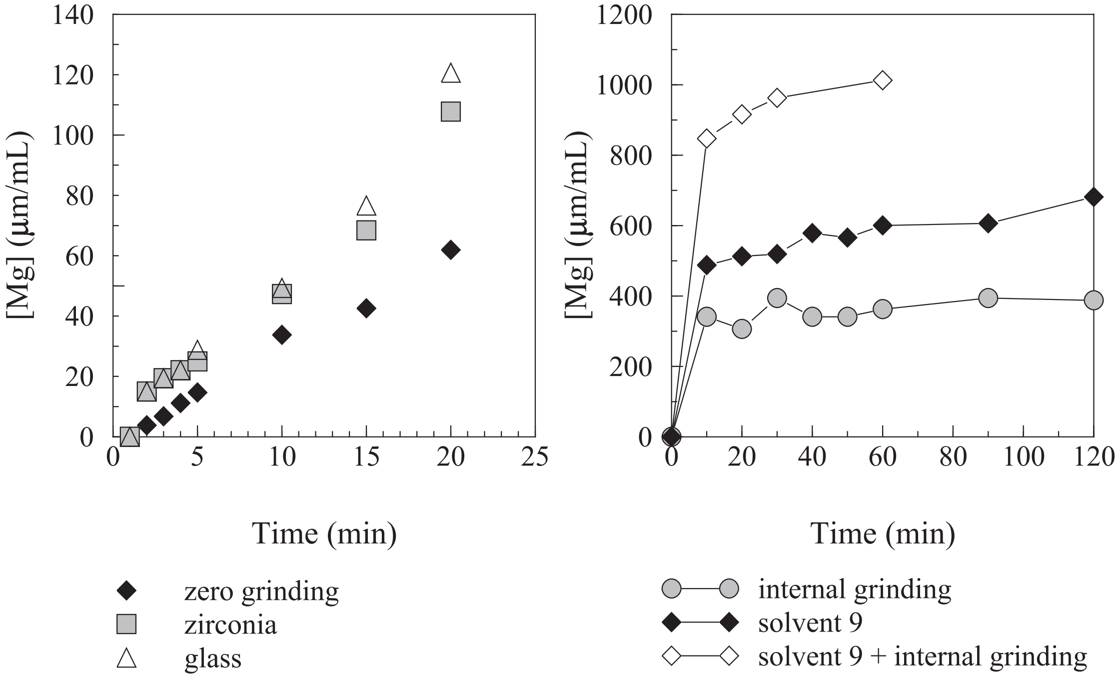

Figure 2.15: The effect of internal grinding media on Mg solution concentration from serpentine dissolution: without any chemical additives under neutral pH conditions and (left) with chemical additives under acidic conditions (right). From Park and Fan (2004).

ever, this process is more energy intensive than the process by Park and Fan (2004) and in accordance with Alexander *et al.* (2007), such a small particle size does not influence the reaction rates.

Other methods used in the activation of minerals include the heat activation of serpentine. Serpentine is a hydrous mineral and has about 14 wt.% bound water but the same mineral chemistry as olivine. Heating serpentine to above 630 °C removes the chemically bound water from the structure and makes the mineral more susceptible to reaction (Teir *et al.*, 2007; Penner *et al.*, 2003). This increases the reactivity of the mineral during dissolution. Heat treatment methods only work on minerals with chemically bound water (hydrous minerals) and therefore would not work for pyroxene or feldspars minerals. Although heat treatment increases the reaction rates of hydrous minerals, it carries an energy penalty of 300 kW.h.t^{-1} of sample material (Alexander *et al.*, 2007).

2.4 Reactivity of Bushveld PGM tailings: A case study from Lonmin

The study by Vögeli *et al.* (2011) investigated the potential storage for CO_2 in four Merensky PGM mine tailings: Northam, BRPM, Implala and Lonmin. Results from the study indicate that samples with high proportions of orthopyroxene were the least reactive. The pyroxene-rich PGM tailings from Lonmin are fine grained (D0.9 = 293 µm), have large available tonnages (868 kt per annum) and importantly, 95 % of the minerals are able to theoretically sequester CO_2. In the initial ranking scheme of the tailings, the Lonmin PGM tailings sample was placed third due to its high proportion of sequesterable, Mg-rich orthopyroxene (65.5 wt.%), followed by plagioclase (18.2 wt.%) clinopyroxene (5.3 wt.%) and amphibole (2.8 wt.%), and the more reactive sequesterable minerals, olivine and serpentine, in only minor amounts (0.3 wt.% and < 0.1 wt.%, respectively, Vögeli, 2012). After the reactivity of the sample was taken into account, its ranking was reduced to fourth place due to the low extents of dissolution of the orthopyroxene. At 70 °C for 8 h in 2 M HCl, the Mg, Fe and Si cation liberation is seemingly slow, with an extraction (of the total available cation) of 31.2 % Ca, 9.1 % Fe, 5.0 % Mg and 0.7 % Si (Figure 2.17, Vögeli, 2012). The extraction rate curves indicate a relatively rapid increase in cation dissolution until the first hour (Figure 2.16). Thereafter, the extraction begins to plateau for Mg and Fe, whilst continuing to increase gradually until termination of the leach in the

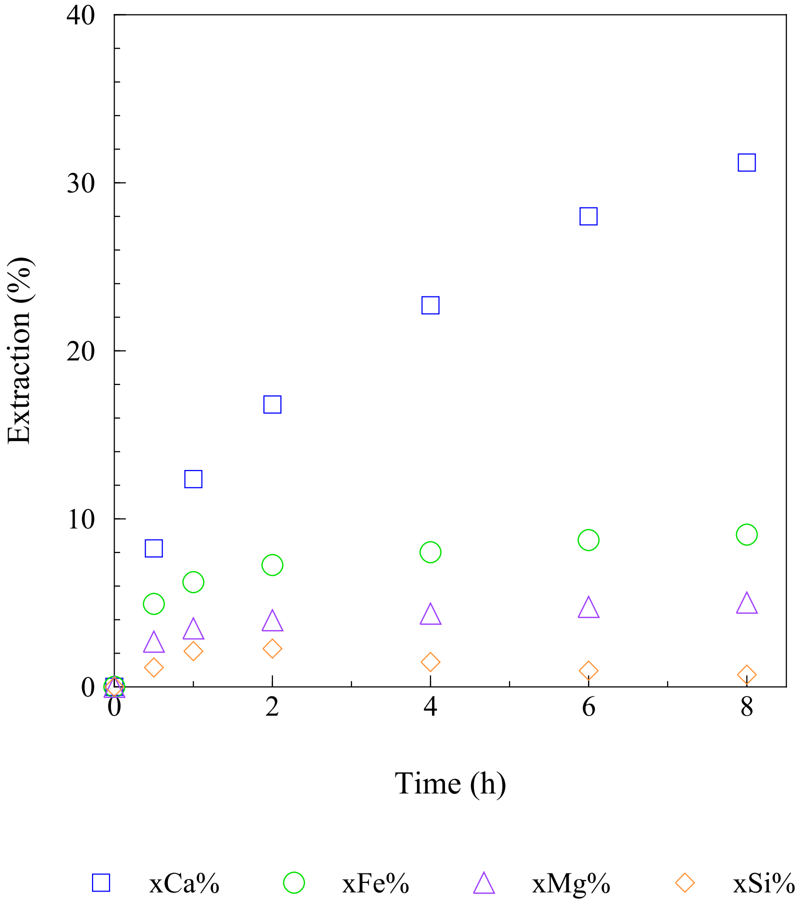

Figure 2.16: Extraction of Ca, Fe, Mg, and Si from Lonmin PGM tailings at 70 °C in 2 M HCl for 8 hours. (Vögeli, 2012).

case of Ca. Similar dissolution trends have been reported for serpentine by Park *et al.* (2003) and Teir *et al.* (2007). These researchers attributed the gradual decrease in the leaching rate of serpentine to a build-up of amorphous silica on the surface of the minerals, which becomes diffusion limiting with time. Mineralogical analysis of the extended leach experiment in this study also indicated that formation of secondary amorphous silicates occurs during acid leaching of the PGM tailings (Vögeli, 2012).

The low extraction of cations in the dissolution stage resulted in an overall low conversion to carbonate minerals due to the low initial concentration of the solution. The net conversion to carbonates for this sample was only 29.9 %, 8.9 %, and 2.9 % for Ca, Fe, and Mg, respectively (Meyer *et al.*, 2014). The mineralogical makeup of the tailings indicates a potentially high CO_2 storage capacity based on theoretical calculations; however, the large proportion of orthopyroxene has been likened to be the cause for the slow rate reaction. Orthopyroxene constitutes 65.5 wt.% of the tailings and is the major host of Mg (88 wt.%), Fe (74 wt.%) and Si (71 wt.%, Figure 2.17). The major host of Ca is plagioclase (18.2 wt.% in tailings) with 63 % CaO, followed by clinopyroxene with 26.4 % CaO.

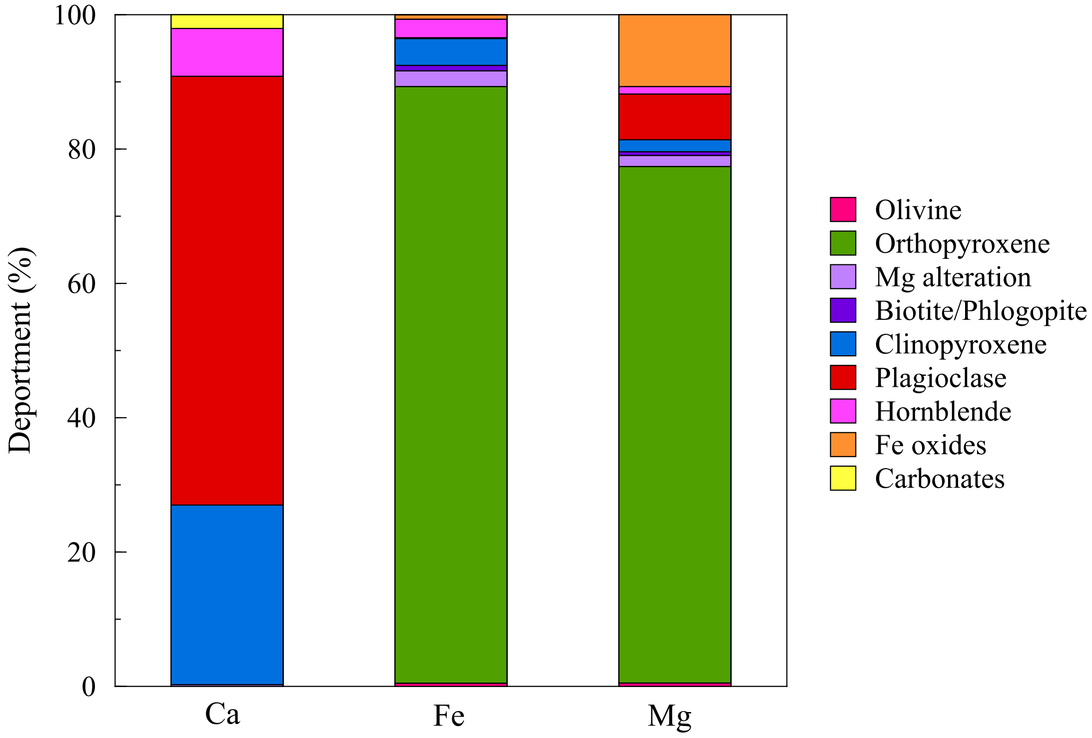

Figure 2.17: Elemental deportment of Ca, Fe, and Mg in Lonmin bulk tailings (Vögeli, 2012).

2.5 The pyroxene group: structure, chemistry, and reactivity

The low reactivity of the orthopyroxene in the Lonmin PGM tailings decreases the available CO_2 storage. In order to overcome the low conversion of pyroxene-rich tailings to carbonates, an in-depth understanding of pyroxene reactivity is needed. There are many factors that influence the reactivity of silicate minerals, such as: silicate structure, crystal shape and the nature of the cation (including chemistry, size, and arrangement). The silicate structure and external leach parameters have been discussed in Sections 2.1 and 2.3, respectively. Section 2.5 focusses on the internal structure of the pyroxene group minerals and the differences between the minerals in the group, a reaction mechanism for pyroxene dissolution, and concludes with a comparison of the reactivity of Mg-pyroxenes to other Mg-silicates.

2.5.1 Structure of the pyroxene group

The pyroxene group of minerals are an important, abundant group of ferromagnesian silicates. In the pyroxene structure, Si-O tetrahedra are linked through two bridging oxygens to form an infinite length chain, where the bases of the tetrahedra lie parallel to the z-axis. The chains are held together laterally by a sheet of cations (Figure 2.18). These cations can be placed in either the M1 site: located between the apices of the SiO_3 chains, or the M2 site: located between the bases of chains. The M1 and M2 cations are bonded to 6 or 8 neighbouring oxygens, to produce 6- or 8-fold coordination, which forms octahedra and polyhedral layers, respectively, between the tetrahedral layers of the silicates. Because the M1 site is between apices of chains, the coordinating oxygens are all non-bridging; whereas the M2 site is coordinated by bridging oxygens (Deer *et al.*, 1978).

The pyroxene structure has infinite silicate chains, when viewed down the z-axis, the chains are represented by two triangles, with their apices indicating the top apices of the chain (Figure 2.18A). The M1 and M2 sites are shown by pink and blue circles, respectively, with their sizes representing the relative size of the cations. The area of two tetrahedrally-coordinated facing chains and the octahedrally-coordinated M1 sites between them are called I-beams (named after the shape of the t-o-t area, shaded area in grey). The cleavage of the mineral is through the M2 sites at a $\sim 90^\circ$, as shown in red dashed lines (Figure 2.18B). The two shaded faces in green represent the orientation of the cleavage planes on an actual pyroxene crystal, as indicated in Figure 2.18C.

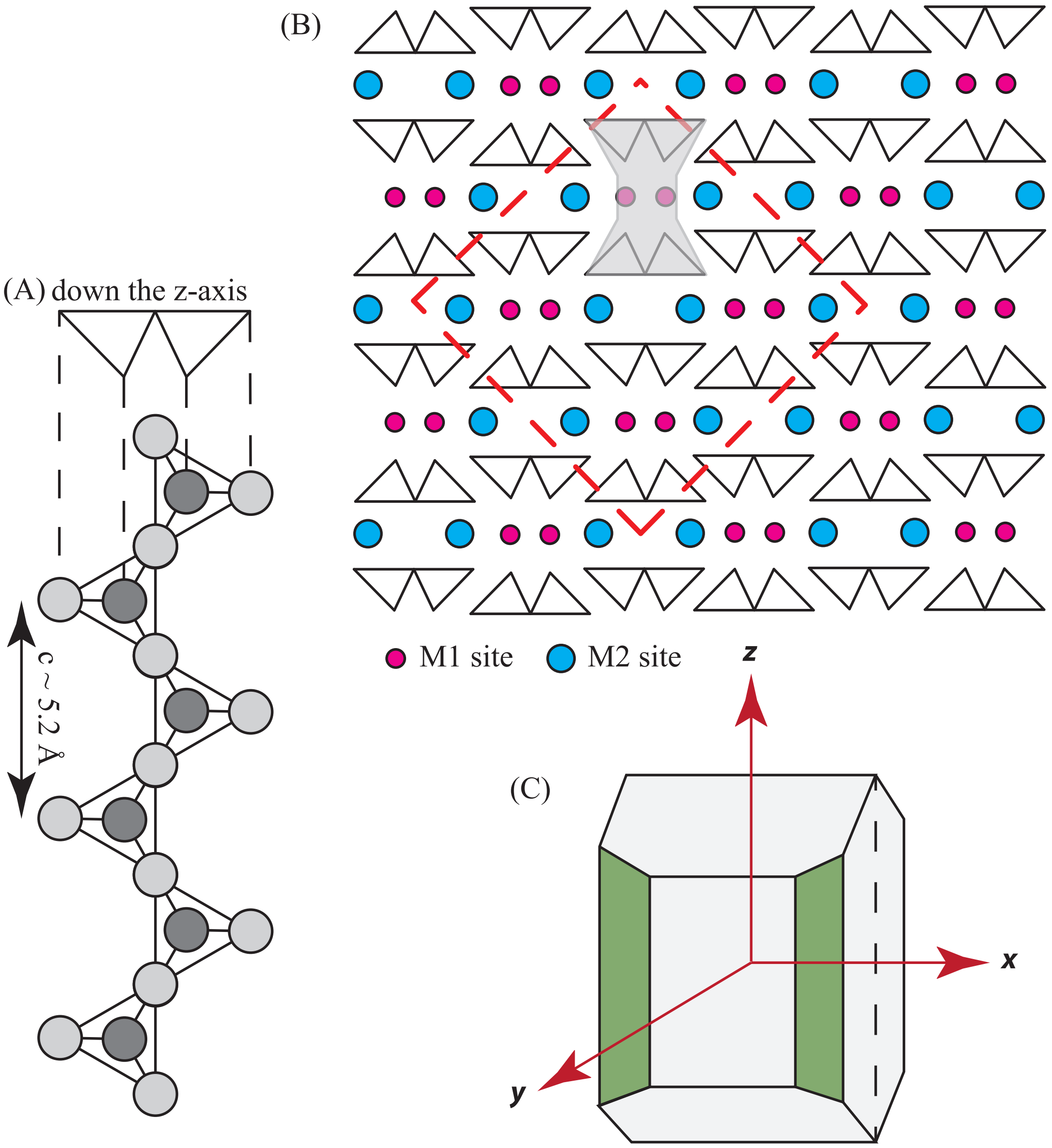

Figure 2.18: Ideal pyroxene structure (A) when viewed down the z-axis (top) and parallel to the z-axis (bottom); (B) when viewed down the z-axis with the M1 cations between the apices of chains and M2 cations between the bases of chains. The shaded area indicates an I-beam, and the red dashed line indicates the orientation of the cleavage planes parallel to the z-axis. (C) Idealised pyroxene crystal with the cleavage planes indicated by the shaded faces with vertical and horizontal lines. Adapted from Deer *et al.* (1978) and Klein and Dana (2007).

Pyroxenes can be split into three structural groups: orthopyroxenes, clinopyroxenes, and pyroxenoids. Orthopyroxenes have the simplest structure as the M1 and M2 cation sites are occupied by small cations (Mg and Fe) and therefore the M1 and M2 cations both have 6-fold coordination with the neighbouring oxygens. When the M2 site accommodates a larger cation (i.e. Ca) in the clinopyroxene structure, the octahedral shape distorts to accommodate an 8-fold (polyhedral) coordination of the M2 cation with the neighbouring oxygens (Deer *et al.*, 1992). Therefore the clinopyroxenes have a distorted octahedral layer between the silicate tetrahedral layers. When both the M1 and M2 sites accommodate a large cation (i.e. wollastonite) the silicate chain kinks, which results in an increased unit cell c length from 5.2 Å to 7.7 Å for the pyroxenoids (Deer *et al.*, 1992). The silicate tetrahedra in pyroxenoids are arranged slightly different, with three silicate tetrahedra instead of two per unit cell (Figure 2.19).

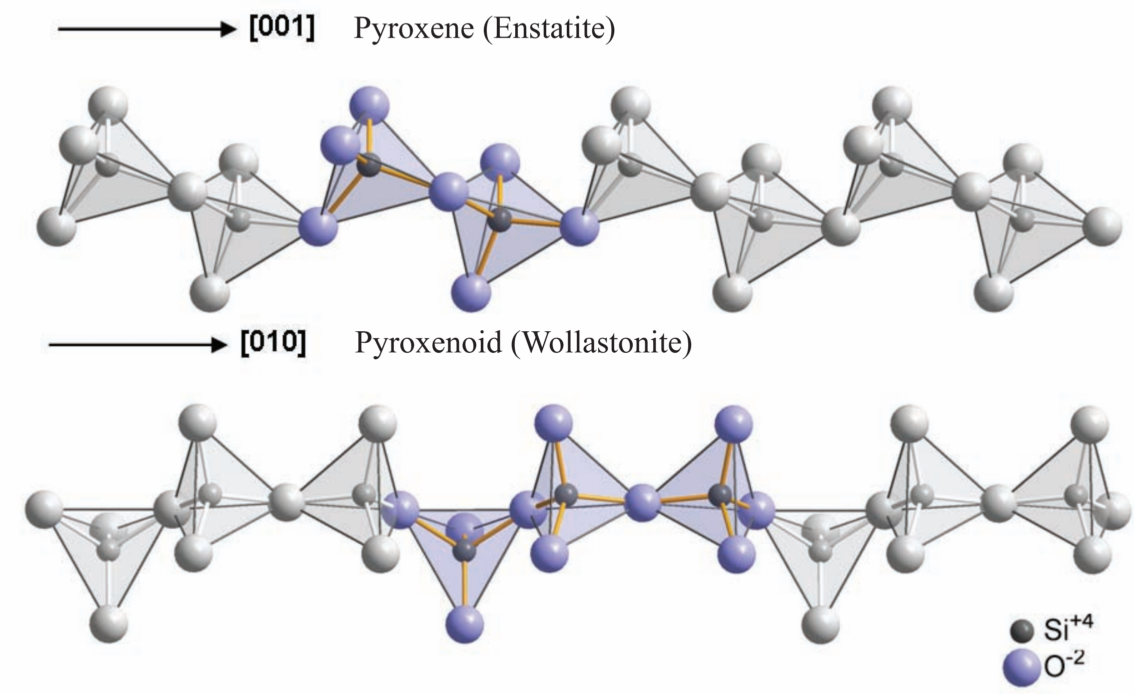

Figure 2.19: Pyroxene chain structure with the unit cell length shaded in blue: (top) with two silicate tetrahedra per unit cell for an ideal pyroxene, and (bottom) pyroxenoid structure with three silicate tetrahedra per unit cell in a distorted arrangement. Image created using *Diamond* software and sourced from Wikimedia commons.

2.5.2 Pyroxene chemistry

The general formula of pyroxene is described by Eq (2.6), where M2 and M1 are two divalent cations or one monovalent and one trivalent cation (Deer *et al.*, 1992; Cameron and Papike, 1980).

$$(M2)(M1)(Si, Al)_2O_6 \tag{2.6}$$

All pyroxene group minerals can be grouped by their $CaSiO_3$-$MgSiO_3$-$FeSiO_3$ composition and plotted on a ternary diagram, with the stable pyroxene compositions shaded (stable at ambient temperature and pressure, Figure 2.20). Pyroxene compositions that plot on the corners of the ternary diagram, take the name of that end-member composition. Pyroxenes with intermediate compositions are given ratios of two end-member compositions, e.g. a pyroxene directly between the diopside and hedenbergite composition are denoted as $Di_{50}He_{50}$. Orthopyroxenes include all mineral compositions between enstatite-ferrosilite, and clinopyroxenes include the compositions of pigeonite, augite, and all minerals between diopside-hedenbergite composition. The pyroxene end-members and solid solution series are named in Table 2.7 for the clinopyroxenes, orthopyroxenes, and pyroxenoids.

Table 2.7: Chemical formulae of the major pyroxene group minerals. Adapted from Deer *et al.* (1992).

Group	Name	Chemical Formula
Orthopyroxene	Enstatite	$Mg_2Si_2O_6$
	Ferrosilite	$Fe_2Si_2O_6$
Clinopyroxene	Diopside	$CaMgSi_2O_6$
	Hedenbergite	$CaFeSi_2O_6$
	Clinoenstatite	$Mg_2Si_2O_6$
	Clinoferrosilite	$Fe_2Si_2O_6$
	Pigeonite	$(Mg, Fe^{2+}, Ca)(Mg, Fe^{2+})Si_2O_6$
	Augite	$(Ca, Mg, Fe^{2+}, Al)_2(Si, Al)_2O_6$
	Omphacite	$(Ca, Na)(Mg, Fe^{2+}, Fe^{3+}, Al)Si_2O_6$
	Aegerine-augite	$(Ca, Na)(Mg, Fe^{2+}, Fe^{3+})Si_2O_6$
	Jadeite	$NaAlSi_2O_6$
	Aegerine	$NaFe^{3+}Si_2O_6$
	Spodumene	$LiAlSi_2O_6$
Pyroxenoid	Wollastonite	$Ca_2Si_2O_6$
	Rhodonite	$(Mn,Ca,Fe)_2Si_2O_6$

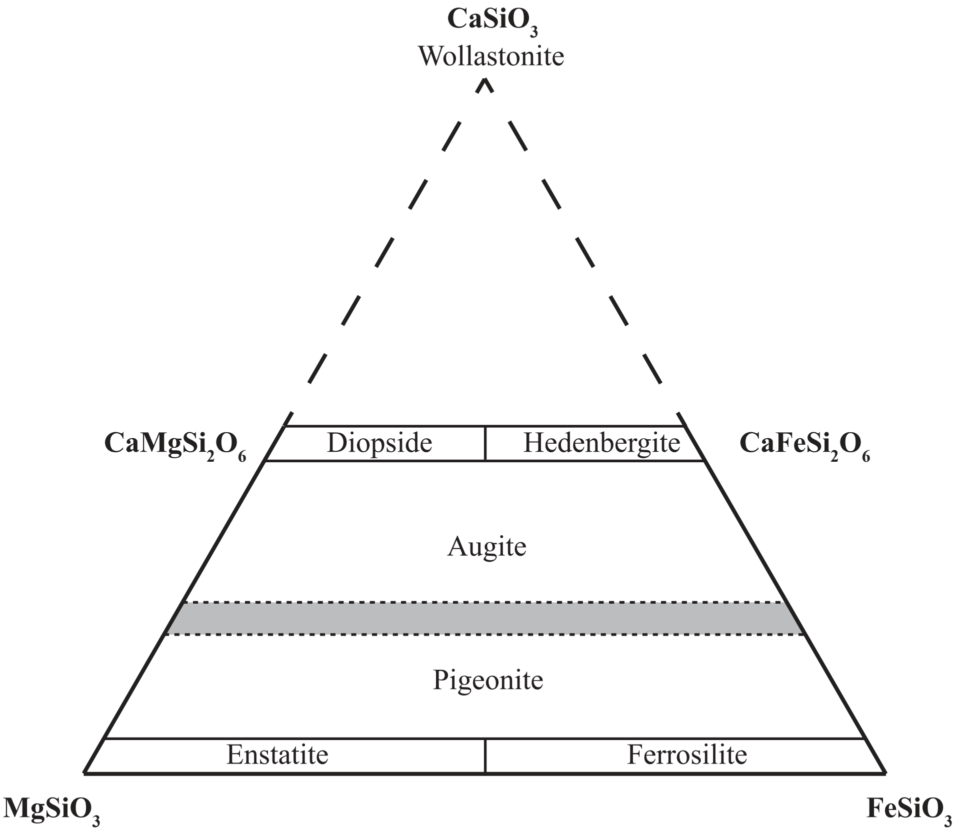

Figure 2.20: Pyroxene stability diagram for the system $CaSiO_3$-$MgSiO_3$-$FeSiO_3$. Adapted from Deer *et al.* (1992).

2.5.3 Pyroxene reactivity and reaction mechanism

The dissolution of pyroxene has been described by Schott and Berner (1985) for a range of pyroxene minerals. The dissolution mechanism of pyroxenes is reaction-controlled, where H^+ ions protonate the surface of the grain by attachment to the oxygens. As discussed in the reaction mechanism of silicate acid dissolution in Section 2.2, the attachment of the H^+ to the oxygen polarises and weakens the critical metal-oxygen bond, much like the reaction for olivine. The reaction of pyroxene (enstatite) proceeds via:

$$Mg_2Si_2O_6 + 2H^+ \rightarrow Mg^{2+} + H_2Mg(M1)Si_2O_{6(surf)} \tag{2.7}$$

Followed by removal of the cation at the M1 site (Zakaznova-Herzog et al., 2008):

$$H_2MgSi_2O_{6(surf)} + 2H^+ \rightarrow Mg^{2+} + H_4Si_2O_{6(surf)} \tag{2.8}$$

An illustration of the pyroxene reaction mechanism is given in Figure 2.21 by Zakaznova-Herzog *et al.* (2008). The diagram illustrates three important steps in the dissolution of pyroxene. These are: (a) hydroxylation of the surface of the grain and the subsequent removal of the top layer M2 site, (b) further reaction by nucleophilic attack of H_2O (+ve) on the Si at the centre of the tetrahedra and further removal of M1 and M2 site cations, and (c) the removal of $Si(OH)_4$ and the formation of a new surface (Zakaznova-Herzog *et al.*, 2008). Casey and Ludwig (1995) argue for a reaction-controlled dissolution mechanism for pyroxene. They highlight the fast adsorption of a proton to the mineral surface and conclude that the slow step in the reaction is the breaking of the M-O bond (detachment of the reacting species), which is confirmed by Mast and Drever (1987) who illustrated that the detachment of the Si rather than the Ca, Mg or Fe is the rate-limiting step.

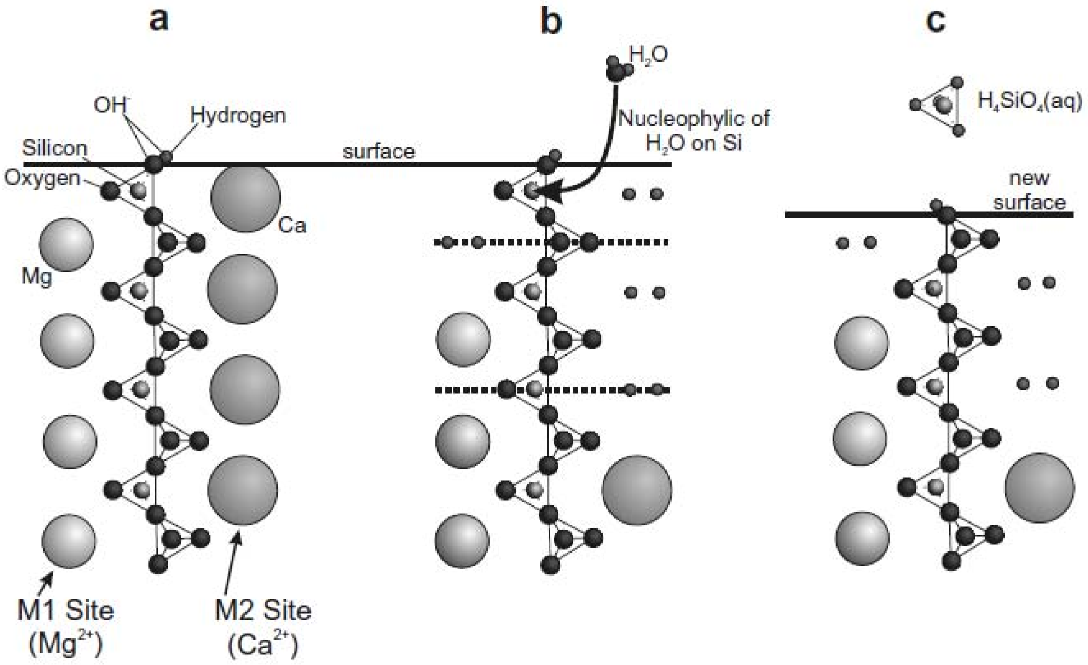

Hydroxylated surface but no electrophylic or nucleophylic reactions

Both electrophylic reactions proceed (dashed lines indicate rxn. fronts) but no nucleophylic reaction has occurred

Two electrophylic and a nucleophylic reactions have occurred

Figure 2.21: Schematic illustrating the important aspects of the leaching mechanism proposed for the pyroxenes – diagram for diopside but the same mechanism applies for the other pyroxenes. These are: (a) Hydroxylation of the surface oxygen, (b) two electrophylic reactions on the M1 and M2 site, where the M2 site reaction is more rapid, and (c) nucleophylic reaction with the release of $Si(OH)_4$ (Zakaznova-Herzog *et al.*, 2008).

The reaction of pyroxenes is initially fast for a short period, followed by a linear release of Si (for more than 600 hours, Schott and Berner, 1985). At pH 6 the reaction is congruent for Mg and Si dissolution from enstatite, but incongruent for Ca and Si from diopside. At lower pH (pH =1) the dissolution of Mg is faster than Si from enstatite and much faster for Ca than Si from diopside. The researchers concluded that the cations are more weakly bonded in the M2 than the M1 site of the pyroxenes, preferentially releasing the cations from the M2 site (Schott and Berner, 1985; Knauss *et al.*, 1993; Brantley, 2008). These findings are consistent with the Madelung site energies of the M1 and M2 sites in pyroxenes (Table 2.8). Natural and laboratory studies have demonstrated that the dissolution of pyroxene is cleavage-controlled, and the reaction proceeds along the cleavage planes and along grain boundaries (Barker *et al.*, 1997). Furthermore, etch pits occur at the outcrops of dislocations during pyroxene dissolution. These etch pits are lens-shaped and parallel to the z-axis. The end-to-end alignment of these etches pits results in deep striations (Figure 2.8) and often occurs along the boundaries of basal lamellae (Berner *et al.*, 1980). Etch pits on diopside are preferentially developed along the exsolution lamellar boundaries between bulk diopside and Mg, Fe-rich lamellae (Brantley, 2008).

Table 2.8: Site occupancy and Madelung site energies for some pyroxenes. Adapted from Schott and Berner (1985)

Mineral	**Site**	**Occupancy**	**Energy (kJ.mol^{-1})**
Diopside	M1	Mg	-4 346
	M2	Ca	-3 157
Enstatite	M1	Mg	-4 318
	M2	Mg	-3 940
Ferrosilite	M1	Fe	-4 133
	M2	Fe	-3 806
Hedenbergite*	M1	Fe	-4 187
	M2	Ca	-$\sim$3 266

*Ohashi and Burnham (1972)

The nature of the octahedral and polyhedral sites strongly influences the release of silica in other chemically similar minerals (Mg-silicates) with the order of reactivity being olivine $>$ serpentine $>$ enstatite (Luce *et al.*, 1972; Bales and Morgan, 1985; Jonckbloedt, 1998). The differences in reactivities for the different silicates can be linked to their different silicate structures, particularly with respect to the silicate connectedness (i.e. the number of bridging oxygens). Olivine, a nesosilicate, has individual silicate tetrahedra in alternating face-up and face-down arrangement that are linked by Mg and Fe cations in the M1 and M2 sites, respectively (Figure 2.22). Each M1 and M2 site is coordinated by six neighbouring, non-bridging oxygens (Klein and Dana, 2007, p445-6). The serpentine group (phyllosilicate) has 6-membered silicate rings with interstitial OH$^-$ ions which form infinite sheets that are linked by cations, octahedrally coordinated to apex non-bridging oxygens and the OH- ions.

The tetrahedrally coordinated silicate sheets and the octahedrally coordinated cations form a unit that is stacked vertically to form the mineral lizardite (the most common of the three serpentine polymorphs: lizardite, chrysotile, and antigorite). The t-o units are held together by weak van der Waals bonds, perpendicular to the z-axis, parallel to the cleavage plane. However, the imperfect fit of the octahedral and tetrahedral layers results in the bending of the sheets (Deer *et al.*, 1992; Klein and Dana, 2007, p462-7). Although the serpentine has a higher Si:O ratio, than pyroxene, it is more reactive as the cleavage of serpentine preferentially exposes the metal cations and hence more reactive (Terry, 1983). The silica tetrahedra in olivine are unpolymerised and therefore the least tightly held in place; which results in the least resistance to diffusion (Luce *et al.*, 1972). Bales and Morgan (1985) suggested that the easier dissolution of olivine is due to the fact that it does not need to break the strong bridging oxygen bonds that are present in pyroxene.

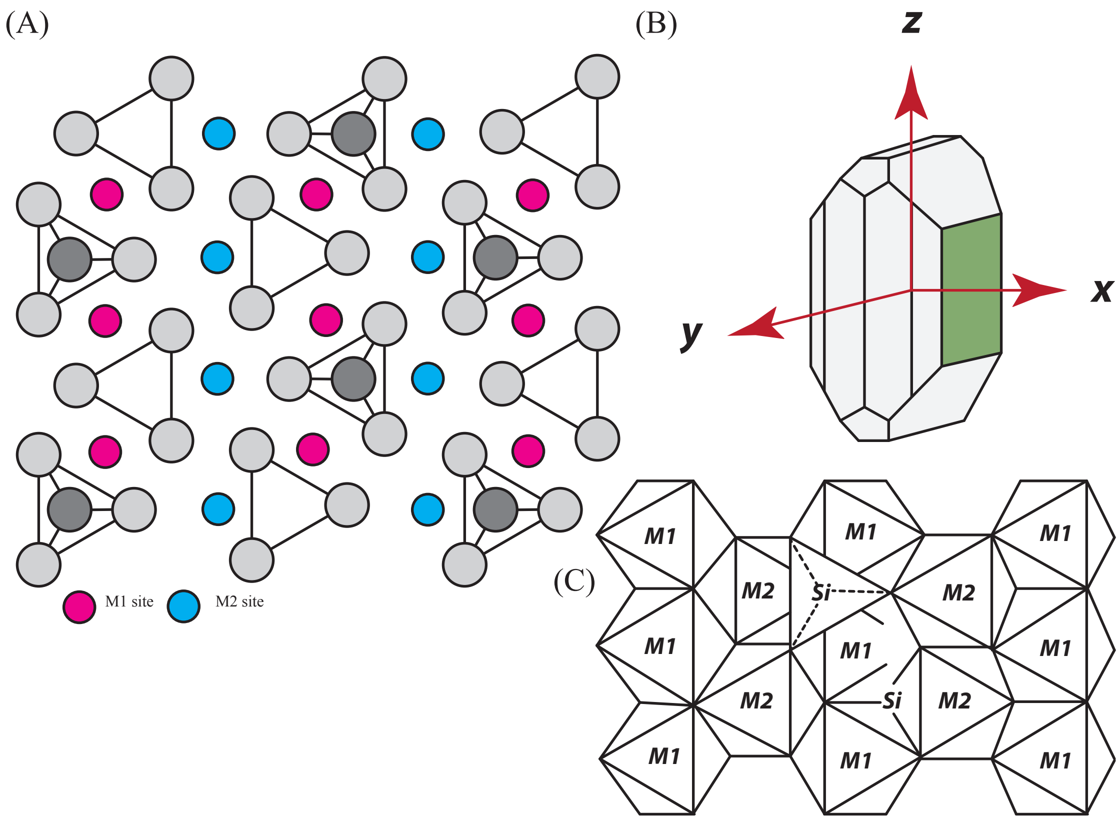

Figure 2.22: Idealised structure of olivine (A) down the z-axis showing the location and relative size of the M1 and M2 site cations, (B) the crystal shape of olivine with the (100) parting plane, and (C) the octahedral coordination of the M1 and M2 cations.

2.6 Summary

The literature has shown that the polymerisation of the Si-O tetrahedra is responsible for the reactivity of the silicate minerals. The strong Si-O bonds formed by bridging oxygens are responsible for the low reactivity of pyroxene (inosilicate) when compared to olivine (orthosilicate). This reactivity is reflected by natural processes where, during the weathering reaction, complex silicate minerals react incongruently, thereby forming secondary minerals such as clays and oxides. For example, a 1 mm crystal of olivine takes $\sim$2 000 years to completely dissolve, but pyroxenes take between 6 800 to 10 000 years to dissolve.

In the dissolution reaction, silicates dissolve in accordance to the surface protonation model. Protons hydrate the Si-O tetrahedra, which weakens the M-O bond and facilitates the removal of the cation by OH^-. The same reaction mechanism is responsible for both the proton-promoted and the ligand-promoted process. When both mechanisms are present, the overall reaction rate can be increased. However, on the particle scale, surface effects of the particle can hinder dissolution. Reaction-limited kinetics occur when the chemical reaction on the surface of the grain limits the overall reaction, and for silicate mineral dissolution, this is usually caused by the desorption reaction. On the other hand, transport-limited kinetics occur when the movement of reagent or product from the surface is slow and limits the overall reaction. These two kinetic limitations result in a shrinking particle and shrinking core scenario, respectively. The formation of a product layer on the surface of the grain has been debated extensively, and even if it were to form, most authors agree that it would be porous enough to allow uninterrupted transport of reagent and product.

A number of parameters can be manipulated to increase the dissolution rates of silicate minerals. Solvent chemistry is an important factor for mineral dissolution. Organic solvents have been used to increase the dissolution of most silicate minerals. Not only do they increase dissolution by the addition of the ligand-promoted mechanism, they also complex ions in solution to increase the apparent solubility. This is useful for Si, which has a relatively low solubility. A study by Park *et al.* (2003) showed that the addition of oxalate, EDTA, and orthophosphoric acid to HCl had a higher overall extraction of Mg from serpentine than a HCl-only solution. Physical parameters to increase the dissolution rate include temperature changes and particle size reductions. An increase in the temperature of the reaction increases the reaction rate exponentially by decreasing the activation energy needed for the mineral to dissolve. Decreasing particle size increases the surface area of the solid, which is directly proportional to the dissolution rate. However grinding mills used to decrease the particle size can also impart surface and lattice defects onto the surface of the grain, which increases the number of high energy sites.

The pyroxene-rich tailings from the Bushveld are fine-grained and have a high proportion of orthopyroxene (enstatite). Extraction calculations from leach experiments on these tailings at 70 °C in 2 M HCl for 8 h, show that the overall extraction of Ca, Fe, Mg, and Si was low. The low extraction leads to an overall low carbonation efficiency of the tailings. The net conversion to carbonates for this sample was only 29.9 %, 8.9 %, and 2.9 % for Ca, Fe, and Mg, respectively. The low extraction was due to the low reactivity of the pyroxene group minerals.

The pyroxene group minerals has a complex chemistry, which alters the structure of the individual minerals. Where the cations are small (e.g. Fe and Mg in the M1 and M2 site), the cations are octahedrally bonded to the surrounding oxygens; but where there is one larger cation (e.g. Ca in the M2 site), the M2 cation has polyhedral coordination to the surrounding oxygens and the M1 remains octahedrally coordinated. Where two large cations are incorporated (e.g. Ca in M1 and M2 site) the chains kink to accommodate the change. This results in highly strained M-O bonds, which increases the reactivity of the mineral. The location of the M1 and M2 site in the pyroxene creates a plane of preferential weakness (i.e. cleavage planes). The addition of the stronger Si-O bridging bonds reduces the reactivity of the pyroxene when compared same-chemistry silicates (e.g. Mg in olivine, pyroxene, and serpentine). Thus the order of reactivity of Mg-silicates is olivine $>$ serpentine $>$ enstatite. Therefore there are a number of factors that control the reactivity of the pyroxene group minerals, and selected parameters would need to be investigated to increase its dissolution rate.
Within this context, the following has been hypothesised:

1. For any given silicate mineral, the kinetics of dissolution can be enhanced through manipulation of key influencing parameters. Specifically: by increasing temperature which reduces the apparent activation energy, by decreasing particle size which increases the surface area, and by the addition of chelating organic acids which increases the apparent solubility of cations in solution.

2. In the pyroxene group, clinopyroxenes are more reactive than orthopyroxenes because the addition of a larger cation in the M2 site decreases the activation energy by increasing the metal-oxygen bond length.

To investigate these hypotheses, the following key questions have been proposed:

i Are low concentration organic solvents comparable to high concentration mineral acids on pyroxene-rich PGM tailings under the same leaching conditions?

ii Does increasing the temperature and decreasing the particle size lead to an overall increase in cation extraction?

iii Which of the pyroxene group minerals are more reactive and why?

iv Is the dissolution of pyroxene controlled by physical features on the surface of the grains?

v How do pyroxenes react in acidic conditions?

Chapter 3

Experimental methods and materials

The aim of this research is to investigate the dissolution of the pyroxene group minerals in an acidic solution. Leaching experiments are devised to show the change in extraction of cations at different mineral compositions and under different temperature and particle size conditions. The experiments in this study were split into two phases: firstly, experiments on pyroxene-rich PGM tailings with organic acid mixtures of varying concentrations (results in Chapter 4); and secondly, experiments on three pyroxene group minerals and one pyroxenoid mineral at varying temperature and particle size (results in Chapter 5). Sample mineralogical and chemical characterisation, experimental set-up and leach conditions for each experiment, and calculations related to this study are outlined in this chapter.

3.1 Sample procurement and preparation

Bulk Bushveld PGM tailings were collected as a grab sample from the tailings dam before mixing of the UG2 and Merensky streams. The samples were obtained unwashed prior to being split into 1 kg representative samples. Pure pyroxene/pyroxenoid mineral samples were collected at various localities in South Africa (Table 3.1). Mineral samples were crushed and milled in a Siebtechnik carbide-steel disc mill for varying lengths of time, and wet screened to produce the desired size fractions: -38 µm and +75/-106 µm. Screened samples were further split with a micro-riffler into $\approx$10 g sample sizes for leaching.

Table 3.1: Sample name, ideal composition, locality, and further preparation of the samples investigated.

Sample	Composition	Locality	Further Preparation
PGM tailings	Various Ca-Mg minerals	Lonmin, Marikana	–
Enstatite	$Mg_2Si_2O_6$	Clapham trough, Bushveld critical zone	–
Augite	$(Ca,Mg,Fe^{2+},Al)_2(Si,Al)_2O_6$	IRUP Lonmin UG2 pit	Removal of magnetic minerals
Diopside	$(Ca,Mg,Cr)Si_2O_6$	FOSKOR mine dumps, Phalaborwa	Removal of visible biotite
Wollastonite	$Ca_2Si_2O_6$	Namaqua wollastonite, Garies, Northern Cape	–

3.2 Sample characterisation

Powdered fractions of the five samples were characterised chemically, mineralogically and physically before and after leaching. All analyses were conducted at the University of Cape Town (UCT), unless otherwise stated. Chemical analysis were conducted at the Geological Sciences Department at UCT.

3.2.1 Chemical analysis

The elemental analyses for the five samples are listed in the Appendices in Table B.1. Bulk elemental analysis was performed using x-ray fluorescence spectroscopy (XRF) to provide a precise and accurate (1 % to 2 %) oxide composition, which can be applied over a wide range of concentrations (0.2 % to 100 % for major elements). $\sim$1 g of powdered sample, of each composition investigated, was dried at 110 °C and then ashed at 950 °C. A 0.7 g ashed sample was mixed with 6.0 g flux (47 % Li Metaborate and 53 % Li tetraborate) before fusion with a Claisse gas burner to create fusion disks (Willis, 1999). A Panalytical Axios Wavelength dispersive XRF spectrometer with a 4 kW Rh tube was used for analysis. Calibration standards include natural standards of SARM and USGS ranges. Matrix corrections make use of the Fundamental Parameter method as described in Willis and Duncan (2008) and references therein.

Elemental analysis of several single pyroxene/pyroxenoid grains were determined on polished mounts of the +75/-106 μm size fraction by the JEOL JXA-8100 Electron Microprobe (EMP) fitted with four wavelength dispersive spectrometers and a range of crystals. A ≈10 µm electron beam was positioned over a grain and the proportion of SiO_2, MgO, TiO_2, Al_2O_3, Na_2O, Cr_2O_3, CaO, MnO, and FeO, in the pyroxene/pyroxenoid determined. ≈30 readings were taken on each block and measurements with a total weight percent (wt. %) between 99 % and 101 %. The Ca, Fe, and Mg composition of the four samples were averaged and plotted on a $CaSiO_3$-$MgSiO_3$-$FeSiO_3$ composition diagram as shown in Figure 3.1. The enstatite, diopside, and wollastonite samples fall within their respective compositions and their respective chemical formulae are listed in Figure 3.1. The augite sample has a chemical formula of $Ca_{0.7}Mg_{0.6}Fe_{0.4}Al_{0.2}Si_2O_6$.

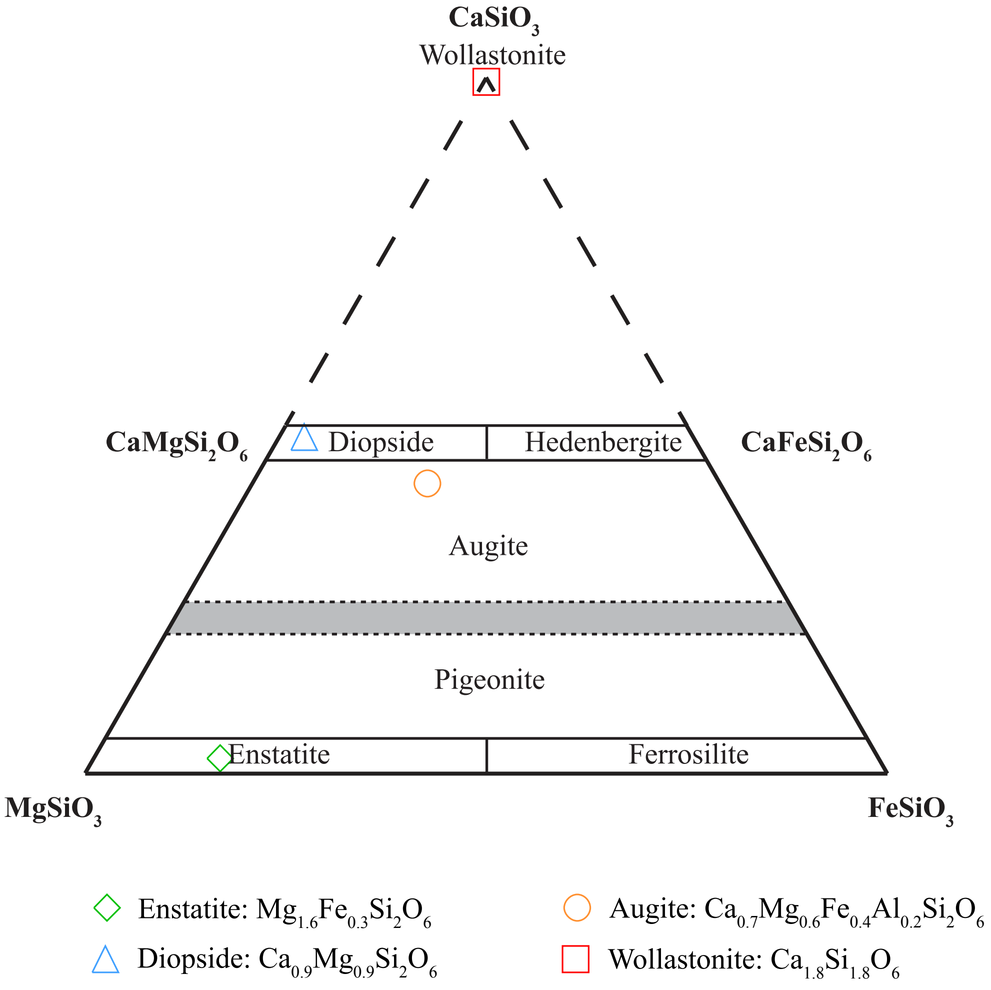

Figure 3.1: Composition of the pyroxene and pyroxenoid minerals plotted on a pyroxene stability triangle, where the shaded areas represent the miscibility gap. Chemical formula calculated from mineral analysis (Appendix A1 Deer *et al.*, 1992, p678).

3.2.2 Mineralogical analysis

Initially powdered bulk pyroxene/pyroxenoid samples were qualitatively analysed for mineralogy on a Philips PW 1390 XRD, which uses a Copper K-α X-Ray tube with x-ray wavelength of 1.542 Å, accelerating voltage of 40 kv and current of 25 mA. The resulting diffraction patterns were matched to their respective compositions using *X'Pert Graphics & Identify* software. The diffraction patterns for enstatite, augite, diopside, and wollastonite are shown in Figures B.1, B.2, B.3, and B.4, respectively. Quantitative XRD was performed on the -38 µm size fraction on a Bruker D8 diffractometer with a Vantec detector. Pre-weighed amounts of powdered corundum was added to the powdered pyroxene/pyroxenoid samples and *Topas Rietveld* refinement software was used for phase quantification (Table B.3).

An in-depth mineralogical characterisation of the five samples is listed in Table 3.2. The analyses were performed by quantitative evaluation of minerals by scanning electron microscopy (QEMSCAN) to determine both the mineralogy and the quantity of the minerals. The BMA (bulk modal analysis) measurement was used to determine the mineralogy of each sample. Sized samples of each composition were set into epoxy ore mounts for analysis. Samples were analysed with pixel spacing between 4 µm and 1 µm depending on the size fraction. Each pixel – the analysis point – was measured by win EDS spectrometers that sent x-ray energy and intensity data to the QEMSCAN software *iExplorer*, which allocated the results to a mineral species. The software allocates the pixel measured to a mineral on the basis of chemical composition and measured backscattered electron level. Where the unit does not fall into a specified mineral grouping, it is allocated to a 'trap' phase. This can occur at

Table 3.2: Mineralogical composition of bulk PGM tailings, pyroxene and pyroxenoid samples as determined by QEMSCAN in weight percent (wt.%).

Mineral	**PGM Tailings**	**Enstatite**	**Augite**	**Diopside**	**Wollastonite**
Orthopyroxene	67.5	95.6	3.1	0.3	1.1
Clinopyroxene	6.7	1.5	77.0	95.1	1.6
Wollastonite	–	0.01	0.01	0.06	85.4
Other Fe-Mg silicate*	3.6	0.4	12.6	3.0	6.3
Al-silicate**	18.3	1.3	1.6	1.1	0.7
Quartz	0.8	0.08	0.5	0.2	0.4
Fe-oxides	3.0	1.0	5.1	0.1	0.1
Carbonates	–	–	–	–	4.5
Total	100.0	100.0	100.0	100.0	100.0

*Other Fe-Mg silicate: olivine, serpentine, chlorite, talc, and amphibole

**Al-silicate: plagioclase, K-feldspar, and garnet the boundary of the grain or where thin grains are present. A working knowledge of the minerals is needed to assign the measured pixels to a mineral in the database and resolve any 'trap' phases. To simplify the mineralogy, the analyses were classified by their mineral group and minerals with trace concentrations were classified as either 'other Fe-Mg silicates': olivine, serpentine, chlorite, talc, and amphibole; or as an 'Al-silicate': plagioclase, K-feldspar, and garnet.

Elemental weight percent from the XRF analyses and calculated from the mineralogical analyses (based on the allocated mineral chemistry) were compared in Figure 3.2. Where the data points for the cations lie on the dashed line, the XRF and QEMSCAN agree. The composition of the cations for the samples by XRF and QEMSCAN agree for the PGM tailings, enstatite, and augite. However, the Ca for both diopside and wollastonite are overestimated. The discrepancy in the diopside is due to the presence of other Ca-rich minerals and the discrepancy in wollastonite is due to the abundance of calcite and Ca-garnet. The Ca-garnet and calcite grains are very small and were likely group under the wollastonite composition as the pixels were close to the grain boundary.

3.2.3 Physical characterisation

Surface area analysis was determined by BET on a Tristar instrument. Surface area was measured for a representative subsample of each of the five samples before reaction and for selected samples after leaching. Particle size distribution of the pyroxene-rich PGM tailings sample and pyroxene/pyroxenoid sized samples were determined using a Malvern Mastersizer 2000 (Figure 3.3). The refractive index for the analyses was 1.620. This was calculated through the factoring of the modal mineralogy, and the average density of each mineral phase. The distribution of enstatite, augite, diopside, and wollastonite were similar for the -38 µm size fraction. For the +75/-106 µm size fraction, the distribution of enstatite, augite, and diopside were similar but showed a much larger variation for wollastonite because of its needle-like grain shape. The bulk Lonmin tailings has a bimodal distribution with a large peak at $\sim$200 µm and a smaller peak at $\sim$40 µm as shown in Figure 3.3.

A Nova Nano SEM 230 was used to image the surface of reacted grains and determine the chemistry of the reacted surface. Dried residue of the desired sample was sprinkled onto the surface of a stub coated in carbon glue. Grains were selected based on their surface features and an image taken. Energy dispersive x-ray spectroscopy (EDS) was used on the surface of the grains to acquire a weight percent of an element (Ca, Fe, Mg, Si) on a selected area. The EDS is uncalibrated and the data obtained is treated as a semiquantitative analysis. EDS was used to get an indication of the morphology and mineralogy on the reacted surface, which would be destroyed by other analytical methods.

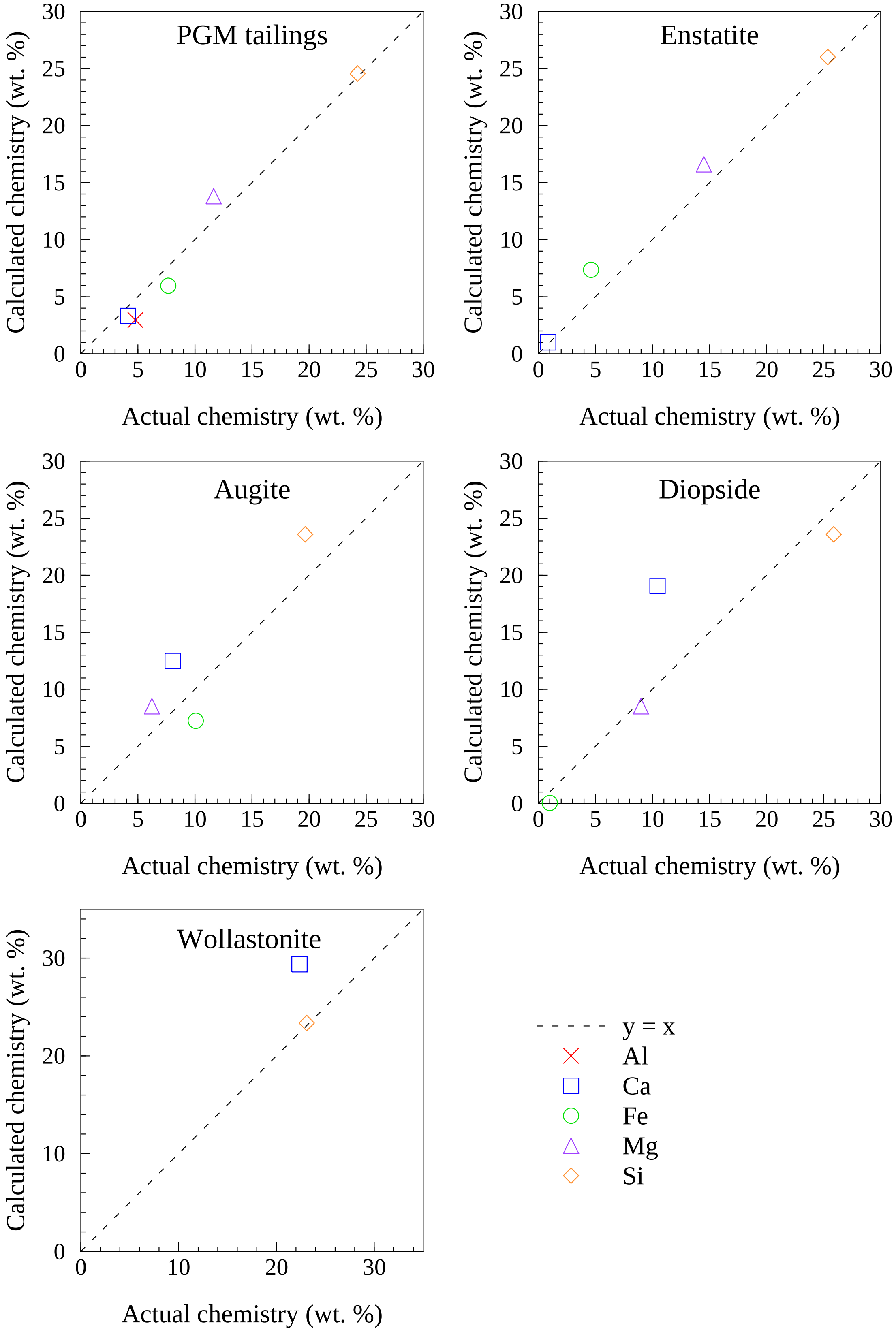

Figure 3.2: Mineral chemistry data validation of calculated chemistry (QEMSCAN data) and actual chemistry (XRF data) for the five samples. The XRF and microprobe data was used to adjust the mineral chemistry data applied to the results from the QEMSCAN data (e.g. increase the content of Ca in diopside and wollastonite, and Fe in augite) so that a more accurate representation was given.

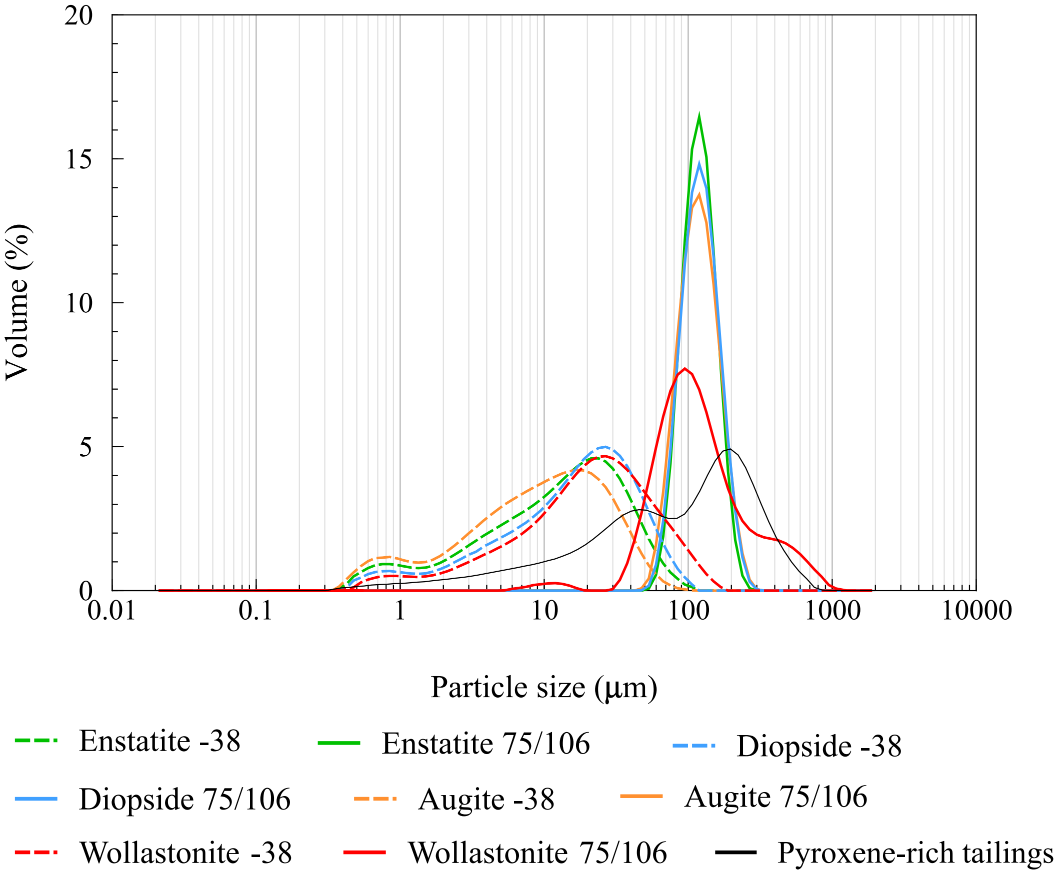

Figure 3.3: Particle size distribution of the -38 µm and +75/-106 µm sizes for each of the four pyroxene/pyroxenoid compositions

3.3 Leach

The experimental procedure and apparatus to leach cations from powdered samples was adapted from Teir *et al.* (2007). Pre-weighed powdered sample was added to a heated acidic solution in a 1 L round bottom flask with a liquid to solid ratio of 50:1 for varying periods of time. The slurry was agitated vigorously (∼750 rpm) using a Teflon-coated stirrer bar and the temperature was controlled by means of a temperature probe in the solution connected to the hot plate/stirrer (Figure 3.4). Liquid samples were collected with a pipette at discrete time intervals through a port on the side of the vessel and filtered with a 0.2 µm syringe filter and stored in a plastic 15 ml capillary tube and refrigerated. Solutions with a pH above 2 were acidified with 5 % nitric acid until a pH below 2 was attained. The concentrations of Ca, Fe, Mg, and Si, and Al (for the PGM tailings samples) in the leachate solutions were determined by inductively-coupled plasma optical emission spectroscopy (ICP-OES)

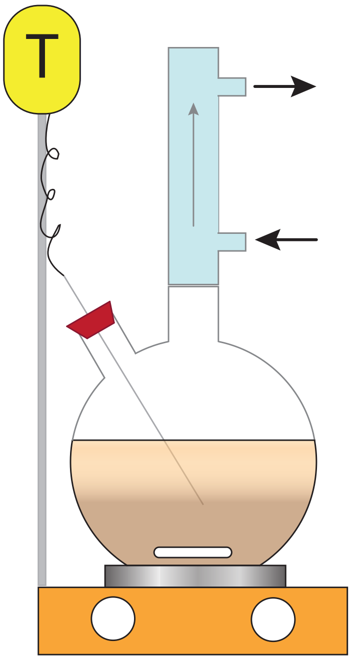

Figure 3.4: Experimental set-up of leaching apparatus after (Teir *et al.*, 2007). A 1 L round flask sits on a hot plate and magnetic stirrer, in which the temperature is maintained through a temperature probe in the solution. A condenser is connected to the flask at the top.

for the PGM tailings samples and inductively-coupled plasma mass spectrometry (ICP-MS) for the pyroxene samples. The residues of the leach were filtered with milli-Q water and left to dry for up to three days at room temperature. Selected sample residues were analysed for surface area and mineralogy.

The first phase of experimental leach reactions are outlined in Table 3.3 and were performed on PGM tailings with varying concentrations of mineral and organic solvents. *Design Expert* 8 software (Stat-Ease Inc, 2010) was used to determine the optimal number and position of design points for a three-component mixture. The solution was set to a maximum of 500 ml and the individual solutions, a mixture of 0.1 M HCl, 0.1 M oxalic and 0.05 M EDTA, were determined by the software. Cation extraction data was entered into the response field before the numerical optimisation function was used to find the most desirable factor settings for multiple responses simultaneously. In this setting, the most desirable acid combination was derived from the interaction between the three acids when the cation extraction for Ca, Mg and Fe was set to a maximum. Cation extractions were calculated using the equation described by Teir *et al.* (2007, Eq 3.1). Extraction calculations allowed for all experiments to be compared as it compensates for the loss of volume and changes in sample mass.

Table 3.3: Phase 1 experiments of organic mixtures on pyroxene-rich PGM tailings. Mixture experiments were run at 70 °C for 5 h and sampled every 30 min. The extended 100-day leach was run at ambient temperature and sampled once on days: 1, 2, 3, 4, 5, 6, 7, 8, 9, 10, 11, 13, 14,15, 18, 22, 25, 31, 37, 44, 51, 65, 80, 94, 100.

Acid	0.1M HCl (ml)	0.1M Oxalic (ml)	0.05M EDTA (ml)
Mixture 1	326	100	74
Mixture 2*	300	135	65
Mixture 3	329	149	22
Mixture 4	440	50	10
Mixture 5	357	50	93
Mixture 6	387	50	63
Mixture 7*	349	101	50
Mixture 8	300	190	10
Mixture 9	370	120	10
Mixture 10	349	101	50
Mixture 11	401	81	18
Extended 100-day	400	50	50

*Repeated experiment

Output from *Design Expert* was derived by means of a contour diagram and a prediction of the acid composition for the highest extraction of cations in the known solutions.

The second phase of leach experiments are outlined in Table 3.4. These experiments were performed on the pure pyroxene/pyroxenoid samples in 0.1 M HCl solution and varying temperatures and particle sizes.

3.4 Calculations

Chemical formula calculations were performed on the average of the EMP data for the four pyroxene/pyroxenoid samples. Calculations were made as described by Deer *et al.* (1992, p678) based on six oxygens for a pyroxene unit cell.

Cation extraction efficiencies were calculated using Eq 3.1 as described by Teir et al (2007). Extraction efficiencies allowed for all experiments to be compared as it compensates for the loss of volume and changes in sample mass. Where c$_{ij}$ is the concentration of dissolved ion in the solution in ppm, V'$_{j}$ is the volume of the solution in L and m'$_{i,j}$ is the total mass in mg of element i in the reactor prior to the jth sample.

$$X_{ij} = \frac{c_{ij}V_j^{'}}{m_{ij}^{'}} = \frac{c_{ij}[V_{initial} - V_{sample}(j-1)]}{m_{batch}\frac{m_i}{m} - V_{sample}\sum_2^{j-1} c_{ij}} \tag{3.1}$$

Congruency of dissolution for the pyroxene/pyroxenoid samples with respect to Si was estimated by comparing (1) the ratio of the mole fraction of the Si dissolved to the mole fraction of the metal cation dissolved, with (2) the mole ratio of the Si in the mineral to the mole ratio of the metal cation in the mineral (Huang and Keller, 1970). The ratio of metal cation (Ca, Mg, or Fe) to Si was calculated and plotted from both the leachate extraction and from the solid residue. The stoichiometric ratios of Ca:Si, Mg;Si, and Fe:Si for each mineral was calculated from the chemical formula in Figure 3.1.

Lastly, *Visual MINTEQ* 3.0 software is a thermodynamic equilibrium modelling programme (Gustafsson, 2011). Inputs of cation concentration (in ppm) and solution concentration for HCl, oxalic acid, and EDTA were input into the programme. Quartz, precipitated Si and Ca-, Fe-, and Mg-oxalate minerals were allowed to precipitate from solution. Outcomes from *Visual MINTEQ* are thermodynamic predictions for the chemistry and concentration of precipitated solid.

Table 3.4: Phase 2 experiments varying temperature and particle size for different compositions of pyroxene group minerals

Experiment	**Mineral**	**Particle Size** (μm)	**Temperature** (°C)	**Elements**
1	Orthopyroxene	-38	40	Mg, Fe, Si
2	Wollastonite	-38	40	Ca, Si
3	Diopside	-38	40	Ca, Mg, Si
4	Augite	-38	40	Ca, Mg, Fe, Si
5	Wollastonite	-38	22	Ca, Si
6	Orthopyroxene	+75/-106	40	Mg, Fe, Si
7	Diopside	+75/-106	40	Ca, Mg, Si
8	Augite	+75/-106	40	Ca, Mg, Fe, Si
9	Wollastonite	-38	70	Ca, Si
10	Orthopyroxene	-38	70	Mg, Fe, Si
11	Diopside	-38	22	Ca, Mg, Si
12	Orthopyroxene	-38	70	Mg, Fe, Si
13	Orthopyroxene	+75/-106	70	Mg, Fe, Si
14	Augite	+75/-106	70	Ca, Mg, Fe, Si
15	Wollastonite	+75/-106	70	Ca, Si
16	Wollastonite	+75/-106	70	Ca, Si
17	Wollastonite	-38	22	Ca, Si
18	Augite	-38	22	Ca, Mg, Fe, Si
19	Orthopyroxene	-38	22	Mg, Fe, Si
20	Augite	-38	70	Ca, Mg, Fe, Si
21	Augite	-38	70	Ca, Mg, Fe, Si
22	Diopside	-38	22	Ca, Mg, Si
23	Wollastonite	+75/-106	40	Ca, Si
24	Diopside	+75/-106	70	Ca, Mg, Si
25	Orthopyroxene	+75/-106	22	Mg, Fe, Si
26	Augite	+75/-106	22	Ca, Mg, Fe, Si
27	Diopside	+75/-106	22	Ca, Mg, Si
28	Diopside	-38	40	Ca, Mg, Fe, Si
29	Wollastonite	-38	40	Ca, Si
30	Orthopyroxene	-38	40	Mg, Fe, Si
31	Augite	-38	40	Ca, Mg, Fe, Si

Chapter 4

The effect of acid mixtures on pyroxene-rich PGM Tailings

This chapter presents the results from the first phase of leaching experiments on pyroxene-rich PGM tailings at varying organic-mineral acid mixtures. The aim of these experiments was to show how the addition of organic additives at low concentration affects the dissolution of silicate PGM tailings; and to investigate if low-concentration organic mixtures are comparable to a high-concentration mineral acid (HCl) for silicate mineral dissolution. Initially, 11 leach experiments (additional 2 repeats) with varying concentrations of HCl (0.06-0.088 M), oxalic acid (0.01-0.038 M), and EDTA (0.001-0.01 M) were conducted at 70 °C for 5 h. The results from these experiments are compared and the kinetics of the most favourable experiment are described. Then, based on the results from the mixture experiments, one experiment was carried out for an extended time period at ambient temperature. The results from the extended (100 days) leach describe the mineralogical and chemical changes of pyroxene-rich tailings after reaction in organic acids. Refer to Appendix C and Appendix D for the full leachate and residue results, respectively.

4.1 Trends in cation extraction from pyroxene-rich PGM tailings

Table 4.1 lists the total extraction of Al, Ca, Fe, Mg, and Si from both the 11 different mixture experiments after 5 h and the extended leach after 100 days. Cation extraction was calculated on the concentration of cation in solution with Eq 3.1. The maximum cation extraction from the 11 mixture experiments is highlighted in red. The highest extraction of the cations occurred in mixture 8. The actual highest extraction for Fe occurred in mixture 7, however the Fe extraction for mixture 7

Table 4.1: Cation extraction from pyroxene-rich tailings at the end of the reaction period. Mixtures 1 to 11 were performed at 70 °C in solutions of varying concentration of HCl, oxalic acid, and EDTA. The maximum extraction of each cation from the 11 mixture experiments is highlighted in red. The 100-day leach experiment was performed at ambient temperature in a solution of HCl, oxalic acid, and EDTA.

Solution	Effective concentration (M)			Cation extraction after 5 hours (%)				
Mixture	HCl	Oxalic	EDTA	Al	Ca	Fe	Mg	Si
1	0.065	0.020	0.007	22.1	15.6	6.6	3.8	2.2
2*	0.060	0.027	0.007	25.5 ± 1.7	19.7 ± 3.3	7.0 ± 0.3	4.0 ± 0.2	3.1 ± 0.9
3	0.066	0.030	0.002	31.4	21.7	6.9	3.8	3.8
4	0.088	0.010	0.001	28.2	17.4	7.2	4.1	2.9
5	0.071	0.010	0.009	26.9	18.4	6.9	4.0	2.0
6	0.077	0.010	0.006	28.8	17.5	7.5	4.1	2.1
7*	0.070	0.020	0.005	30.7 ± 2.7	18.4 ± 1.3	8.6 ± 0.5	4.2 ± 0.1	2.3 ± 0.2
8	0.060	0.038	0.001	39.5	29.9	7.8	4.3	6.4
9	0.074	0.024	0.001	32.3	19.9	7.3	4.1	2.8
10	0.070	0.020	0.005	28.2	17.5	6.9	4.0	2.5
11	0.080	0.016	0.002	21.3	12.9	5.8	3.3	1.7
100-day	0.080	0.010	0.005	46.2	34.4	8.2	4.4	3.7

*Averages and standard error computed for mixtures 2 and 7 from duplicate runs

and mixture 8 are within the 0.5 % standard error. Therefore mixture 8 is still the more favourable reaction. The extraction of Al and Ca was high in all the samples, with 21-40 % extraction of Al and 13-30 % extraction of Ca. However, the extraction of Fe, Mg, and Si was low (< 10 %) for all the acid mixtures investigated. The extraction of Ca and Mg are important for the formation of mineral carbonates, whereas the extraction of Si is important for understanding the dissolution mechanism. The extraction of Al and Fe will be used as additional indicators for the dissolution of silicate minerals in the pyroxene-rich tailings.

The time-related extraction curves of Al, Ca, Fe, Mg, and Si for mixture 8 are plotted in Figure 4.1. The trends of the extraction curves were similar for all the acid mixtures investigated; however only mixture 8 is shown as it had the most favourable extraction. The extraction curves for Fe, Mg, and Si start with an initial sharp increase for the first hour, followed by a plateau in the extraction. The extraction curves of Al and Ca also start with an initial steep increase, which continues for 3.5 h, after which they being to plateau around 4 h to 5 h, which indicates that the reaction would still proceed after 5 h. The parabolic shape of the reaction curve is due to an initial increase in extraction, followed by a more linear extraction before a plateau is reached. The initial steep curve is likely due to the reaction of the very fine particles from the grinding process (Anbeek, 1992).

The extraction curve for the 100-day leach in a mixture of HCl (0.08 M), oxalic acid (0.010 M), and EDTA (0.005 M) for a period of 100.3 days at ambient temperature is presented in Figure 4.2.

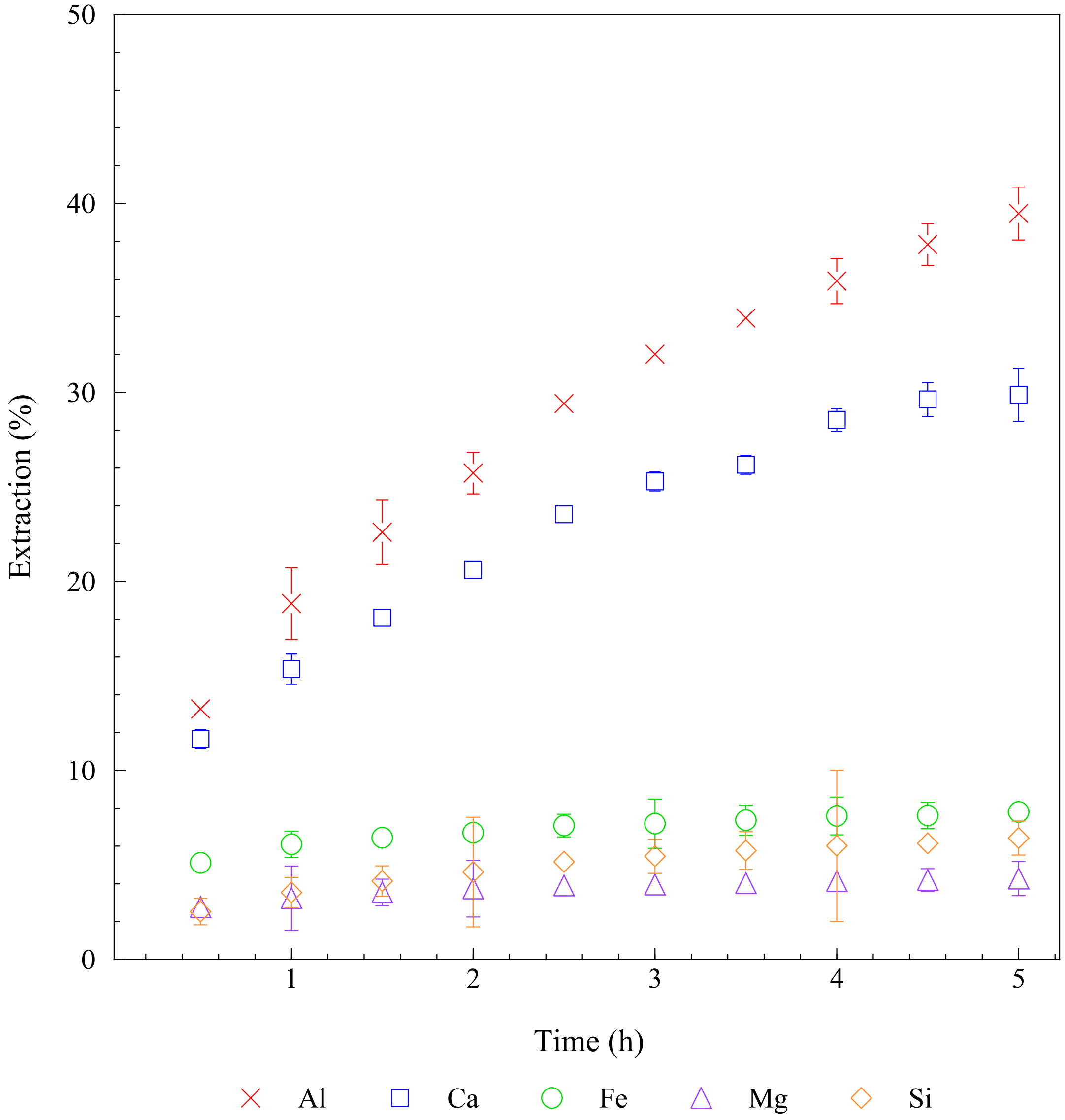

Figure 4.1: Reaction curve of pyroxene-rich PGM tailings from mixture 8 (0.060 M HCl, 0.038 M oxalic, and 0.001 M EDTA). Error bars represent the percent relative standard deviation (RSD %) of triplicate analyses from ICP-OES analysis.

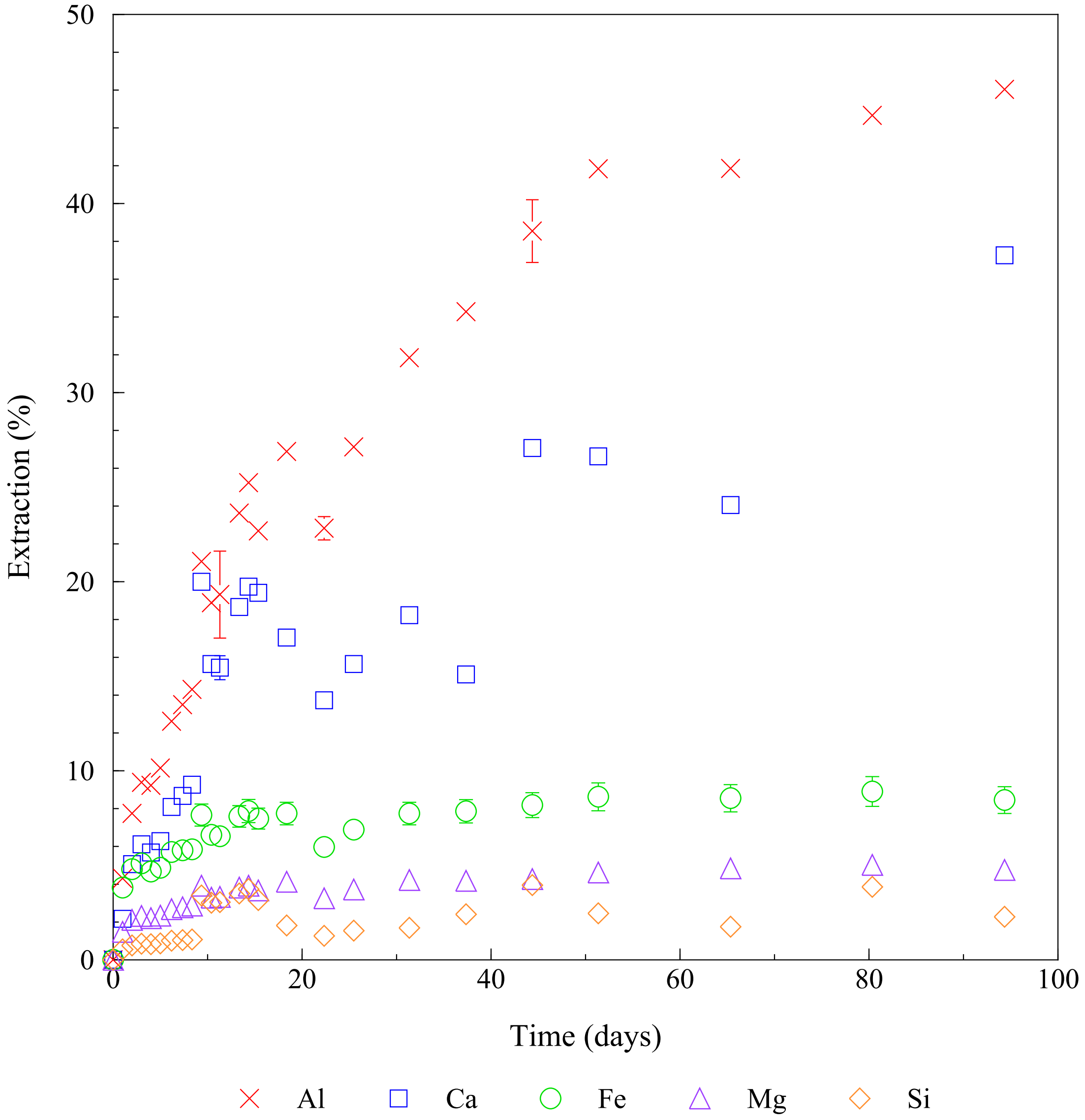

Figure 4.2: Graph of cation extraction on pyroxene-rich PGM tailings at ambient temperature for a period of 100 days. Error bars represent the percent relative standard deviation (RSD %) of triplicate analyses from ICP-OES analysis.

The parabolic extraction curves for the 100-day leach are similar to the extraction curves of mixture 8. The results show that Al and Ca cation dissolution continued to increase over the 100 day period, but Fe, Mg, and Si concentrations reached steady-state after 15 days where they remained for the duration of the reaction. Ca extraction was more variable and had multiple equilibrium points around day 15, 45, and 95. The maximum extraction for Al was 46.2 % at day 100, Ca was 37.1 % at day 94, Fe was 8.8 % at day 80, Mg was 5.0 % at day 80 and Si was 4.0 % at day 44. The variation in cation extraction after steady-state is reached indicates the precipitation of these cations. Al and Ca ions react for a much longer time period than the Fe, Mg, and Si ion, and the length of reactivity for Al and Ca is likely due to the selective dissolution of a reactive Al-Ca mineral.

4.2 Effect of organic acid mixtures on the dissolution of pyroxene-rich PGM tailings

Figure 4.3 compares the cation extraction after 5 h for the 11 different mixtures ordered by increasing oxalic acid and EDTA concentration, respectively. The final extraction result for each cation from the 11 mixture experiments was ordered by increasing concentration of oxalic acid (Figure 4.3, left) and EDTA (Figure 4.3, right). The figure shows that an increase in the concentration of oxalic acid had a positive effect on the extraction of Al, Ca, and Si. The maximum extraction, shown by each bar chart, for Al, Ca, and Si increases towards increasing concentration of oxalic acid (i.e. increased extraction towards the right). Mixture 8 (0.038 M oxalic acid) had $\sim$10 % greater Al extraction, $\sim$13 % greater Ca extraction, and more than double Si extraction over mixture 4 (0.01 M oxalic acid, i.e. lowest oxalic acid concentration). There is no discernible relationship between the maximum extraction values for Fe and Mg and a change in concentration of oxalic acid. An increase in EDTA concentration had no noticeable effect on the extraction of Al, Ca, Fe, Mg, and Si from the pyroxene-rich PGM tailings.

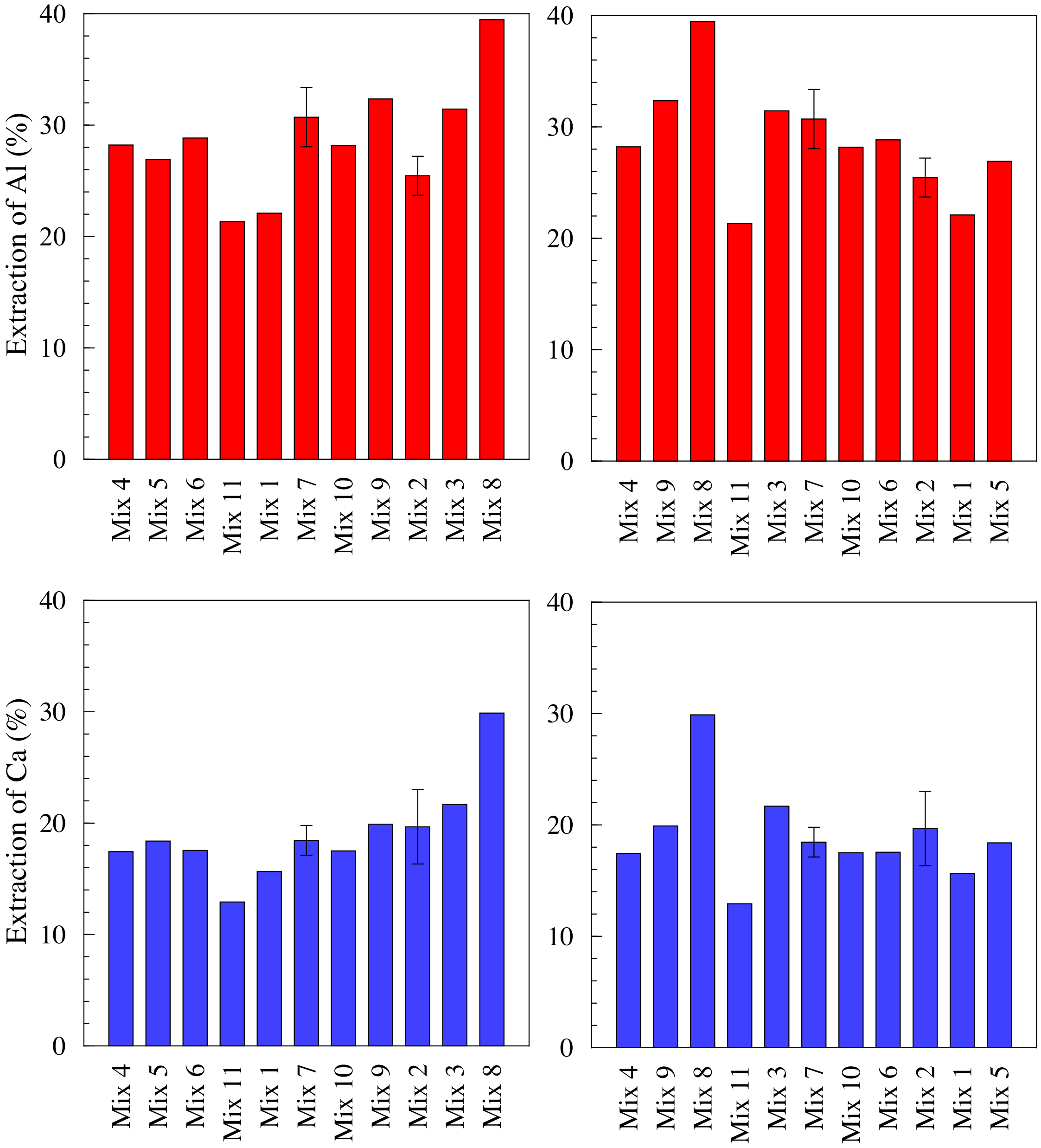

Figure 4.3: Extraction of Al, Ca, Fe, Mg, and Si from pyroxene-rich tailings after 5 hours at 70 °C for the 11 different mixture reactions. The maximum extraction for each cation from the 11 mixture experiments is grouped by mixture number based on increasing molarity of oxalic acid (0.01 to 0.038 M, left) and EDTA (0.01 to 0.001 M, right). The y-axis values are different for each cation graph as the maximum extraction varied dramatically between the cations investigated. Standard error calculated for mixtures 2 and 7 on duplicate experiments.

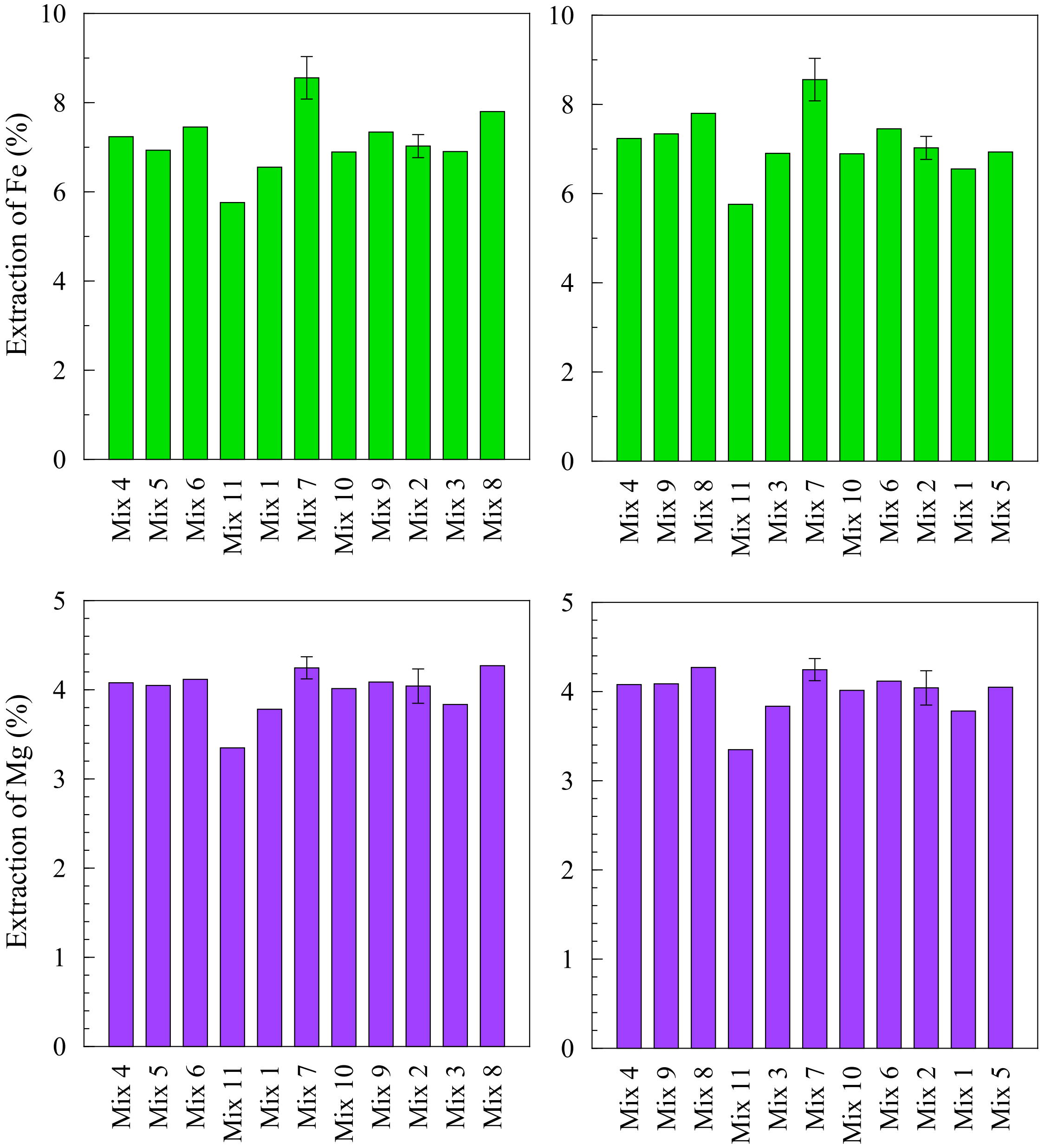

Figure 4.3: Continued

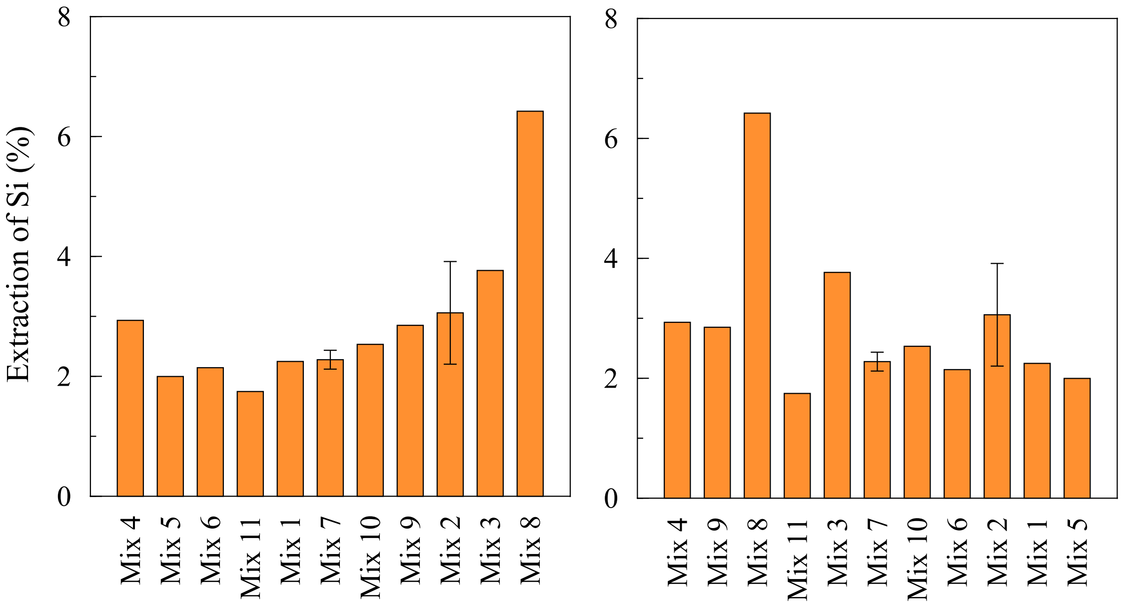

Figure 4.3: Continued

Design Expert 8 software modelled an optimal acid mixture for the dissolution of pyroxene-rich PGM tailings from the extraction data of the 11 mixture experiments (and two repeats) at 5 hours. The effect of A (HCl), B (oxalic acid), C (EDTA), and the interactions between: AB, AC, BC and ABC were modelled and the significance of each model was tested with ANOVA (analysis of variance). For the maximum extraction of each cation (Al, Ca, Mg and Fe), the model was not significant relative to noise (i.e. there was no significant difference between the maximum extraction value of each cation in the 11 mixture experiments after 5 h); however, the model was significant for Si. A contour graph modelled by *Design Expert* for each cation extraction shows that oxalic acid does have an effect on the extraction of Si from these PGM tailings (Figure 4.4). Areas in red indicate a high extraction of that cation. The areas of high extraction coincide with the maximum concentration of oxalic acid for the experiments. The *Design Expert* software modelled a maximum extraction of each cation from the mixture experiments based on the data entered into the programme and within the prescribed concentration limits. This model agrees closely with the experimental results from mixture 8, which shows that the highest extraction of Al, Ca, Mg and Si occurred at this condition.

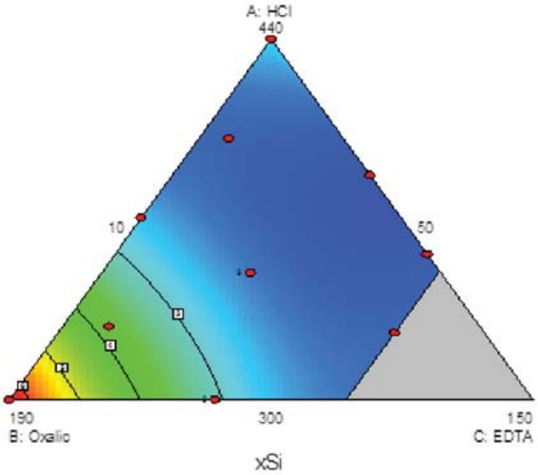

Cation	Prediction (%)	Actual (Mix 8, %)
Al	39.7 ± 3.7	39.5
Ca	29.4 ± 2.8	29.9
Fe	7.8 ± 0.9	7.8
Mg	4.2 ± 0.3	4.3
Si	6.4 ± 0.6	6.4

Figure 4.4: A contour diagram of Si cation extraction under the different mixture conditions as described by *Design Expert*. The maximum volume of solution was set to 500 ml, with the individual concentrations of 0.1 M HCl, 0.1 M oxalic acid, and 0.05 M EDTA ranging between 300 to 440 ml, 50 to 190 ml, and 10 to 100 ml, respectively. Blue areas indicate low concentrations and red areas indicate high concentrations. The red dots represent the design points of the 11 acid mixtures.

4.3 Mineralogical and physio-chemical changes in pyroxene-rich PGM tailings after 100-day leach at ambient temperature

The mineralogical and chemical changes in the extended 100-day leach residues are explained in Table 4.2 and Table 4.3, respectively. For the mineralogical balance, the mass of each mineral group was calculated from *iDiscover* for both the feed and residue samples. For the chemical balance the mass of each cation in the feed and residue was calculated from chemical assay (XRF). The extraction of each mineral and cation from the PGM tailings was calculated based on this data and grouped into categories as shown in Table 4.2 and Table 4.3, respectively.

Table 4.2: Mineralogical balance from QEMSCAN data on feed and residue sample. (Negative: $x < -5$, ∼zero: $-5 < x < 5$, low: $5 < x < 30$, medium: $30 < x < 60$, and high: $x > 60$). The full calculation for the mineral mass balance is listed in Table A.2.

Mineral	**Feed (g)**	**Residue (g)**	**Extraction**
Orthopyroxene	6.7	6.2	Low
Clinopyroxene	0.52	0.40	Medium
Plagioclase	1.7	1.0	Medium
Amphibole	0.29	0.36	Negative
Other Mg-minerals*	0.31	0.50	Negative
Fe-oxides/hydroxides	0.27	0.22	Low
Silica	0.09	0.29	Negative

*Other Mg-minerals: olivine, serpentine, chlorite, talc, and biotite/phlogopite

The mineralogy of the pyroxene-rich PGM tailings were described in detail in Section 2.4, and their chemistry detailed in Table B.1 and Table 3.2. Mineralogical analysis of the feed and residue sample from the extended leach showed that leaching occurred in plagioclase (~40 % extraction), clinopyroxene (~23 % extraction) and orthopyroxene (~7 % extraction, Table 4.2). The increase in amphibole is attributed to the formation of a hydrated layer on the surface of the dissolving silicate minerals (likely pyroxenes). Pyroxenes and amphiboles have similar mineral chemistry, but amphiboles have a hydrated (OH) layer. The 'other Mg-minerals' have a variable change due to the nature of minor (trace) concentrations of these minerals in both the feed and the residue. The low extraction of orthopyroxene is likely due to its complex silicate structure as discussed in Section 2.5. A negative change in SiO_2 in the solid suggests the formation of amorphous silica associated with leaching (QEMSCAN analyses the chemical composition of a substance but cannot discern crystallinity).

Table 4.3: Extent of cation extraction of selected cation of pyroxene-rich PGM tailings from the 100-day leach at ambient temperature. (Negative: $x < -5$, ~zero: $-5 < x < 5$, low: $5 < x < 30$, medium: $30 < x < 60$, and high: $x > 60$). The full calculation for the elemental mass balance is listed in Table **??**

Ion	Feed (g)	Leach Residue (g)	Extraction
Al	0.90	0.43	Medium
Ca	0.58	0.35	Medium
Fe	1.1	1.0	~Zero
Mg	1.9	2.0	~Zero
Si	5.2	4.9	Low

The cation extraction data for the leach residue of the 100-day leach experiment showed a decrease (i.e. extraction) of Al, Ca, and Si; and no change in Fe and Mg (Table 4.3). The change in cation concentration of Ca and Al corresponds to the decrease in the mineral plagioclase from the tailings. The low Mg extraction (close to zero change) is attributed to the Mg extraction from clinopyroxene and not orthopyroxene, the major Mg-host, as orthopyroxene was relatively unreactive. The chemical extraction ranges calculated from XRF data correlate to the extraction percentages calculated from the liquid leachate (Table 4.1). Al and Ca extraction calculated from both the leachate and residue were within the $30 < x < 60$ range, and Mg extraction calculated from both the leachate and residue was within the $-5 < x < 5$ range.

The surface area of the residue had a 6- to 31-fold increase on the starting material with a surface area of 1.211 ± 0.0054 $m^2.g^{-1}$. The 100-day leach had the highest surface area increase of 31 fold (Table 4.4). An increase in surface area correlates to an increase in surface roughness (Anbeek, 1992).

Table 4.4: BET of initial and final material from phase one experiments on pyroxene-rich PGM tailings.

Sample	**Surface area ($m^2.g^{-1}$)**	**Increase (x-fold)**
Mixture 1	8.157	6.7
Mixture 2	14.79	12
Mixture 3	15.67	13
Mixture 4	13.74	11
Mixture 5	12.09	10
Mixture 6	15.95	13
Mixture 7	16.65	14
Mixture 8	12.12	10
Mixture 9	15.58	13
Mixture 10	12.71	10
Mixture 11	9.624	8
100-days	37.45	31

4.4 Summary of leaching experiments on pyroxene-rich PGM tailings

Maximum cation extraction from PGM tailings was obtained in a solution of: 0.060 M HCl, 0.038 M oxalic acid, and 0.001 M EDTA; where the extraction of Al was 39.5 %, Ca was 29.9 %, Fe was 7.8 %, Mg was 4.3 %, and Si was 6.4 %. Under all conditions, the extraction of Ca and Al continued for the full 5 hours, whereas the extraction of Si plateaued after 3 hours and Fe and Mg extraction after 1.5 hours. The presence of oxalic acid had a positive effect on the extraction of Al, Ca and Si, whereas EDTA had a negligible effect. To this end, the *Design Expert* software model chose mixture 8 (0.060 M HCl, 0.038 M oxalic acid, and 0.001 M EDTA) as the most desirable conditions for cation extraction from pyroxene-rich PGM tailings. The model showed that the extraction of Si from the pyroxene-rich PGM tailings was significant in the presence of oxalic acid but not for EDTA. The predicted outcomes are close to the actual values for mixture 8.

Leaching of pyroxene-rich PGM tailings at ambient temperature for 100 days occurred mainly in the minerals plagioclase and clinopyroxene, with low extraction from orthopyroxene. The extractions of the more reactive Mg-minerals, serpentine and olivine, were variable because of the low concentration of these minerals in the feed. The formation of silica (amorphous) indicated the dissolution of silicate minerals and the subsequent precipitation of Si after saturation was reached. The chemical assay on leach residues from the extended 100-day leach closely correlates to the extraction calculated from the leachate. The low Mg extraction calculated from the leachate and XRF on the residue confirms that the orthopyroxene is relatively unreactive and that the Mg extracted from the feed is mainly from clinopyroxene and 'other Mg-minerals'.

Chapter 5

Dissolution of pyroxene group minerals

This chapter summarises the results from the second phase of experiments on pure pyroxene mineral samples of varying composition and at different temperatures and particle sizes. The aim of these experiments was to understand how changes in pyroxene chemistry affect mineral dissolution by analysing both the leachate concentrations and the reaction surface of the solid residue. These experiments further aim to assess the effect of temperature and particle size on the extraction of Ca, Fe, Mg, and Si from these minerals. A total of 23 experiments (additional 10 repeats) were conducted on pure pyroxene and pyroxenoid samples of enstatite, augite, diopside, and wollastonite, which were leached in a 0.1 M HCl solution at ambient temperature, 40 °C, and 70 °C and on a particle size fractions of -38 µm and -75/+106 µm for a period of between 48 and 264 h. The results from the pure pyroxene/pyroxenoid leach experiments are ordered by (1) the deportment of cations in each pyroxene sample, (2) the results from the 23 leach experiments at varying temperature and particle size, and (3) the changes in mineralogy, chemistry, and physical appearance of the residue samples.

5.1 Deportment of Ca, Mg, Fe, and Si in pyroxene samples

The chemical and mineralogical analysis of enstatite, augite, diopside, and wollastonite are presented in Table B.1 and Table 3.2, respectively. The percentage purity of each sample was greater than 90 % for enstatite and diopside, 85 % for wollastonite, and 77 % for augite; and thus sufficiently pure for the experiments. Enstatite is the Mg-rich pyroxene with 31 % MgO, and wollastonite the Ca-rich pyroxenoid with 48 % CaO. Diopside and augite have almost equal amounts of Ca and Mg, and Ca, Mg, and Fe, respectively. Diopside has 22 % Ca and 18 % Mg, and augite has 18 % Ca, 13 % Mg, and 16 % Fe.

Based on the mineral chemistry of each sample and the specified relative abundance of each cation in the mineral phase, the elemental deportment for each pyroxene/pyroxenoid sample could be calculated by with the *iExplorer* software. The pyroxene group minerals enstatite, and augite and diopside, are classified as orthopyroxene and clinopyroxene, respectively. The chemical mineralogy between the different clinopyroxene minerals (e.g. diopside and augite) is very similar and therefore the *iExplorer* software cannot accurately distinguish between the individual minerals, thus classifying them into pyroxene groups and not by mineral name. Figure 5.1 illustrates the cation deportment for Ca, Mg, Fe, and Si in each mineral phase for the four pyroxene/pyroxenoid samples. In the diopside and wollastonite samples, greater than 90 % of the Ca and Si is hosted in clinopyroxene and wollastonite, respectively. In the enstatite sample, greater than 90 % of the Fe, Mg, and Si is hosted in orthopyroxene. However, in the augite sample, $\sim$95 % of the Ca, but only 60 % of the Fe and 80 % of the Mg is hosted in clinopyroxene; with 20 % of the Fe and $\sim$15 % of the Mg hosted in other Fe-Mg minerals (mainly olivine and Fe-oxides). Therefore, extraction of Fe from augite will be influenced by the dissolution of Fe-oxides and olivine, a more reactive silicate mineral. The Si deportment in the enstatite, diopside, and wollastonite samples is greater than 90 %, but only $\sim$85 % in augite, with more than 15 % of the Si in the Fe-Mg-alteration minerals.

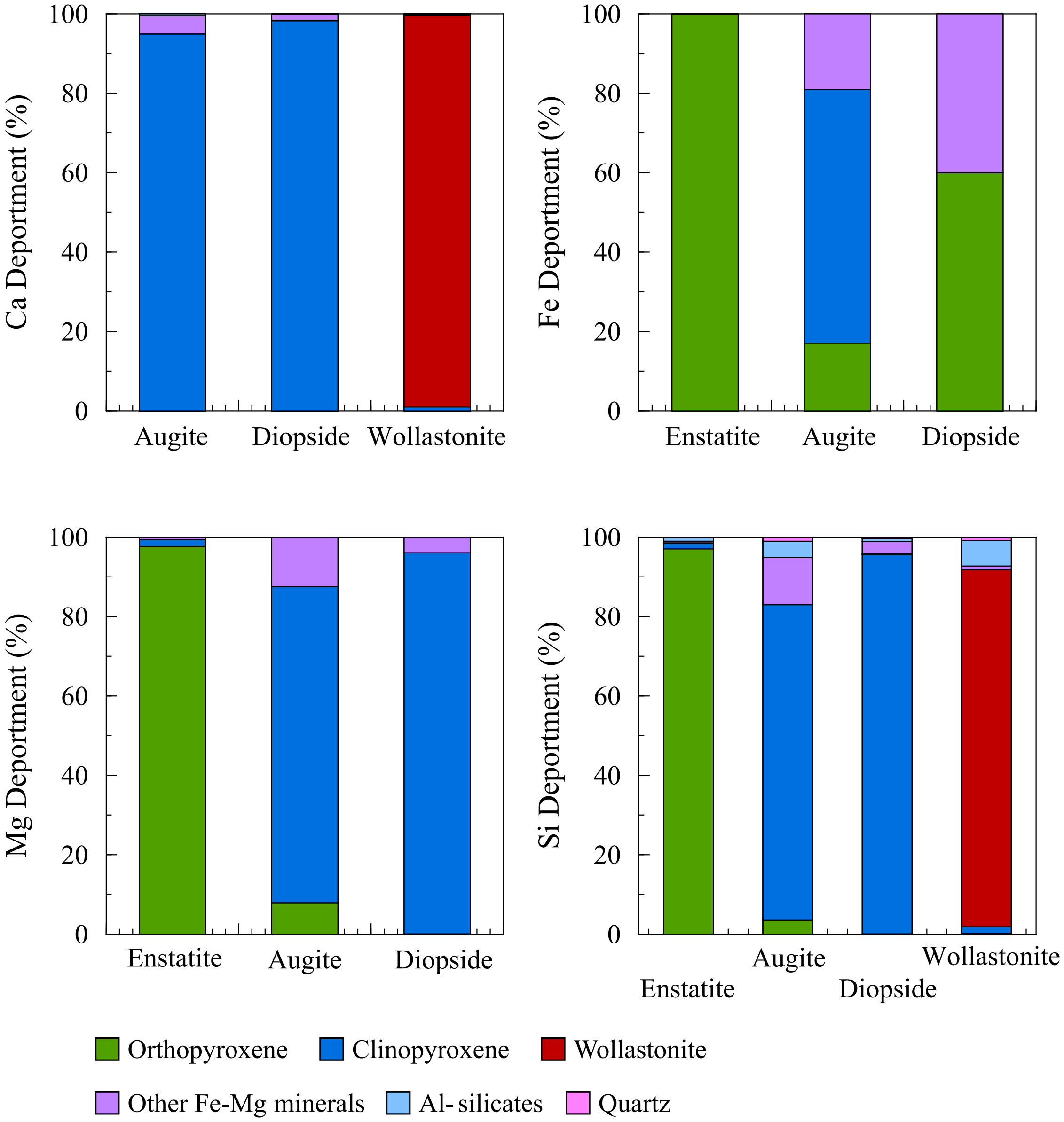

Figure 5.1: Elemental deportment of Ca, Fe, Mg, and Si of each mineral phase in the enstatite, augite, diopside, and wollastonite samples. Other Fe-Mg minerals: olivine, serpentine, Fe-oxides, chlorite, talc, and amphibole; Al-silicates: plagioclase, K-feldspar, and garnet. Read in text for orthopyroxene and clinopyroxene classification.

5.2 Soluble cation extraction

Table 5.1 compares the extraction of Ca, Fe, Mg, and Si from enstatite, augite, diopside, and wollastonite after leaching in a 0.1 M HCl solution for 48 h at varying temperature (ambient, 40 °C, and 70 °C) and particle size (-38 µm and -75/+106 µm). The values in parentheses have been removed because one extraction analysis was above 100 %. The results from this table were used to compare the effect of mineral chemistry, temperature change, and particle size change; as discussed in the following section.

Table 5.1: Cation extraction (in %) of the pure pyroxene/pyroxenoid samples at varying temperature (ambient, 40 °C, and 70 °C) and particle size (-38 µm and +75/-106 µm) after 48 h in 0.1 M HCl. Standard error calculated on duplicate runs. Values in parentheses have been removed because the analyses of one element was above 100 % and the whole analysis discarded.

Ion	**Temp**	**Enstatite**		**Augite**		**Diopside**		**Wollastonite**
	(°C)	-38	+75/-106	-38	+75/-106	-38	+75/-106	-38
Ca	25	–	–	3.1	1.1	68.7 ± 8.3	13.4	–
	40	–	–	3.4 ± 1.1	(20.2)	84.0	33.9	95.4
	70	–	–	(86.6 ± 34.3)	–	–	68.4	–
Fe	25	9.7	1.1	45.6	32.5	5.6 ± 0.9	1.01	–
	40	12.5 ± 1.5	5.8	54.2 ± 2.4	(468)	6.6	**	–
	70	23.6	–	(777 ± 35.8)	–	–	4.2	–
Mg	25	1.2	0.25	8.5	6.1	2.4 ± 0.7	0.44	–
	40	1.8 ± 0.26	0.9	12.8 ± 1.1	(97.1)	3.3	**	–
	70	4.9	–	(139 ± 24.8)	–	–	2.1	–
Si	25	0.9	0.13	3.1	2.9	1.4 ± 0.6	0.28	2.9
	40	1.8 ± 0.22	0.6	3.9 ± 1.2	**	2.0	**	30.8
	70	4.0	–	(43.5 ± 3.4)	–	–	2.0	–

– Experiment was not conducted

** Analysis removed because the sample leachate was contaminated

5.2.1 Effect of mineral chemistry

The time-related extraction curves of Ca, Fe, Mg, and Si for the 40 °C, -38 µm particle size sample experiments for enstatite, augite, diopside, and wollastonite are plotted in Figure 5.2. The extraction curves for all four pyroxene/pyroxenoid samples show an initial, sharp increase, followed by a more gentle increase until the maximum extraction was reached. After maximum extraction was reached, the reaction curves plateaued around the 7 h mark for enstatite, augite, and diopside. The Si and Ca extraction curves for wollastonite dipped at the 24 h mark, which indicated the precipitation of Ca and Si from the solution. The maximum extraction of cations was Ca $>$ Fe $>$ Mg $>$ Si, within each pyroxene mineral.

Within this set of experiments (40 °C and -38 µm), wollastonite had the greatest extraction of both Ca and Si over the other pyroxenes (Table 5.1); followed by diopside with the second highest Ca extraction, but a low extraction of Fe, Mg, and Si. Augite had a high extraction of Fe, and the highest extraction of Mg; and enstatite had the lowest extraction of Fe, Mg, and Si of all the samples. The overall extraction of Mg and Si was low in all the pyroxene samples ($<$ 3.1 %); but Si extraction was high in the pyroxenoid (wollastonite) sample.

Stoichiometric release of the leachate was calculated as described in Section 3.4 and is illustrated in Figure 5.3. For example, the ratio of Fe:Si and Mg:Si for enstatite is 0.15 and 0.8, respectively (calculated from the mineral formula in Figure 3.1). Thus for enstatite dissolution to be congruent, the ratio of Fe:Si and Mg:Si in the leachate needs to lie on the lines: $y = 0.15x$ and $y = 0.8x$, respectively. Figure 5.3 plots the ratio of cations against Si of each mineral for the 48 h dissolution reaction. The dashed lines indicate the mole ratio of Ca:Si, Fe:Si, and Mg:Si within the pure solid; and the markers indicate the mole ratio of Ca:Si, Fe:Si, and Mg:Si calculated from the leachate. The release of Ca, Fe, and Mg for augite is much greater than the release of Si at each time interval. The release of Ca from wollastonite is much greater than the release of Si from wollastonite for the entire reaction time. However, enstatite and diopside show almost congruent dissolution for Fe and Mg, and Ca, Fe, and Mg, respectively.

5.2.2 Effect of temperature and particle size

The extraction of cations from enstatite, augite, and diopside at ambient temperature, 40 °C, and 70 °C for each size fraction after 48 h is illustrated in Figure 5.4. The graphs show that an increase in temperature increased the extraction of enstatite, augite, and diopside; and a decrease in particle size increased cation extraction. Furthermore, the larger size fraction (+75/-106 µm, closed symbols) had a greater dependence on temperature change as the gradient of the connecting lines was steeper than for the smaller size fraction (-38 µm, open symbols) at the same temperature range. The effect of temperature on cation extraction generally appears to be linear between ambient temperature and 70 °C for both size fractions. From Eq 2.3, the curve is expected to be exponential but appears to be linear in Figure 5.4. This discrepancy in could arise from the low temperatures of the reactions (ambient temperature to 70 °C) and the limited data points.

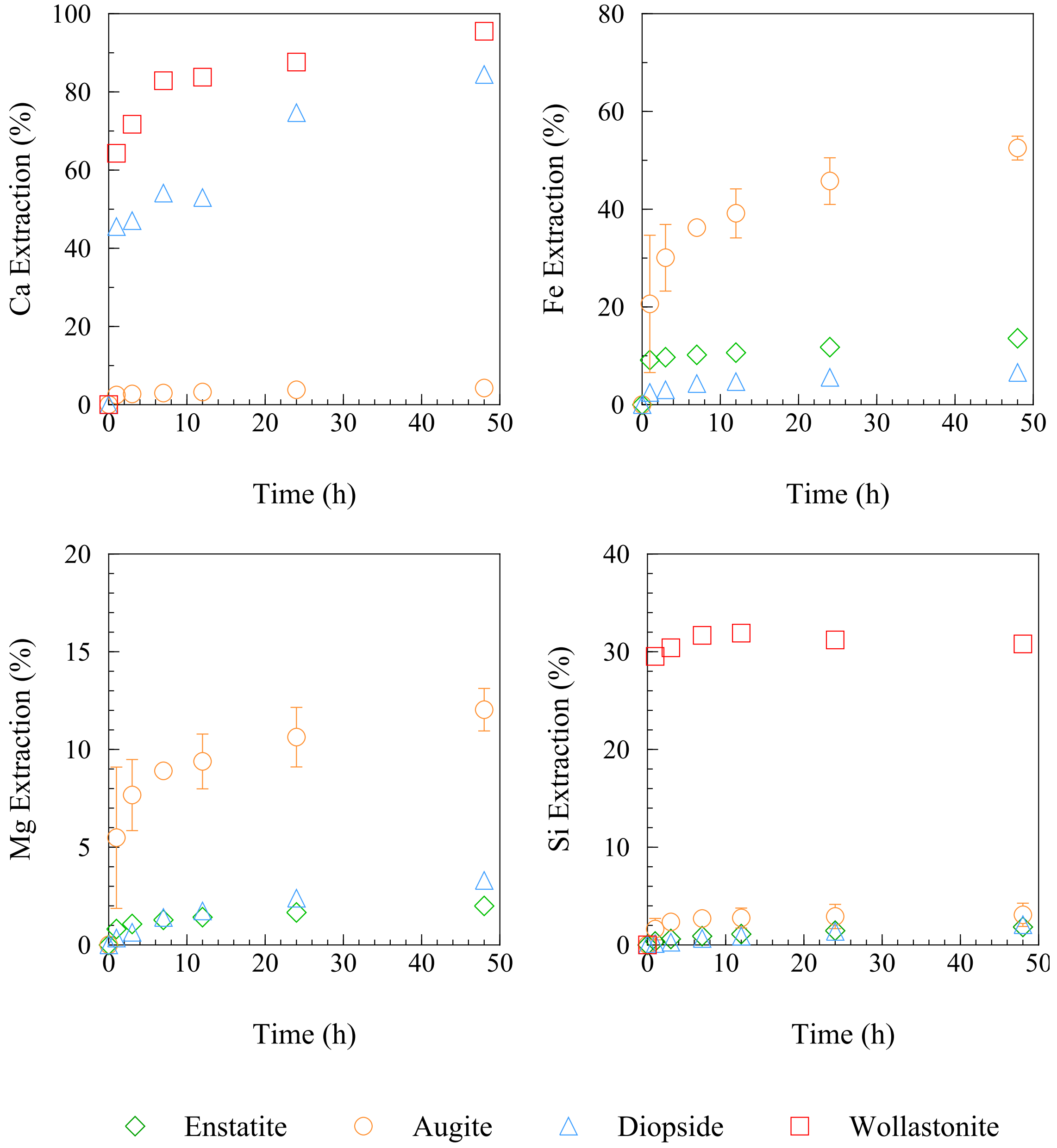

Figure 5.2: Extraction curves of Ca, Fe, Mg, and Si from enstatite, augite, diopside, and wollastonite of -38 µm particles at 40 °C after 48 h in 0.1 M HCl. Standard error calculated on duplicate runs.

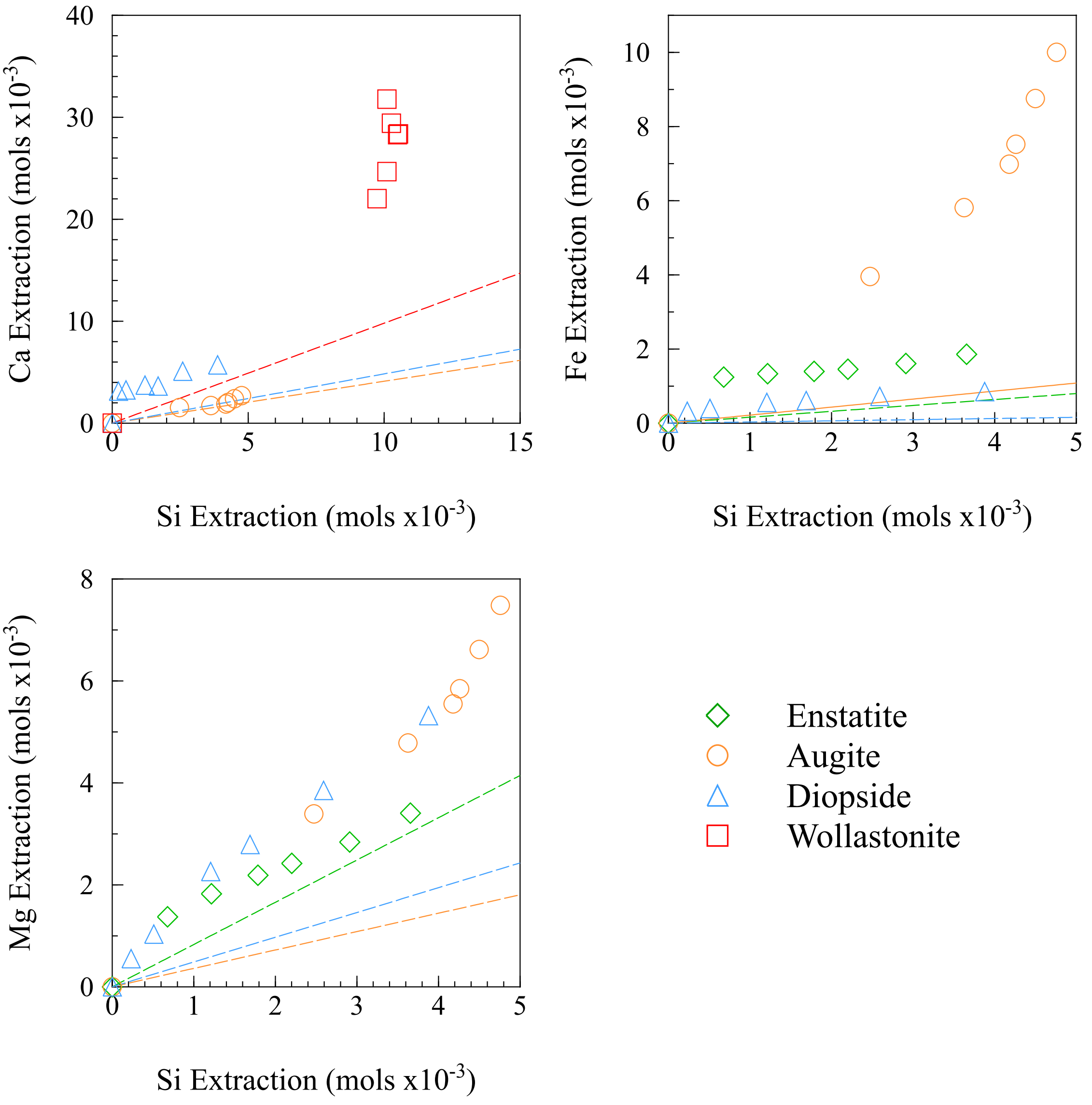

Figure 5.3: Stoichiometric ratio of Ca:Si, Fe:Si, and Mg:Si for enstatite, augite, diopside, and wollastonite of -38 µm particles at 40 °C after 48 h in 0.1 M HCl. Dashed lines indicate the stoichiometric ratio of Ca:Si, Fe:Si, and Mg:Si for each solid mineral and was calculated from mineral formula in Figure 3.1.

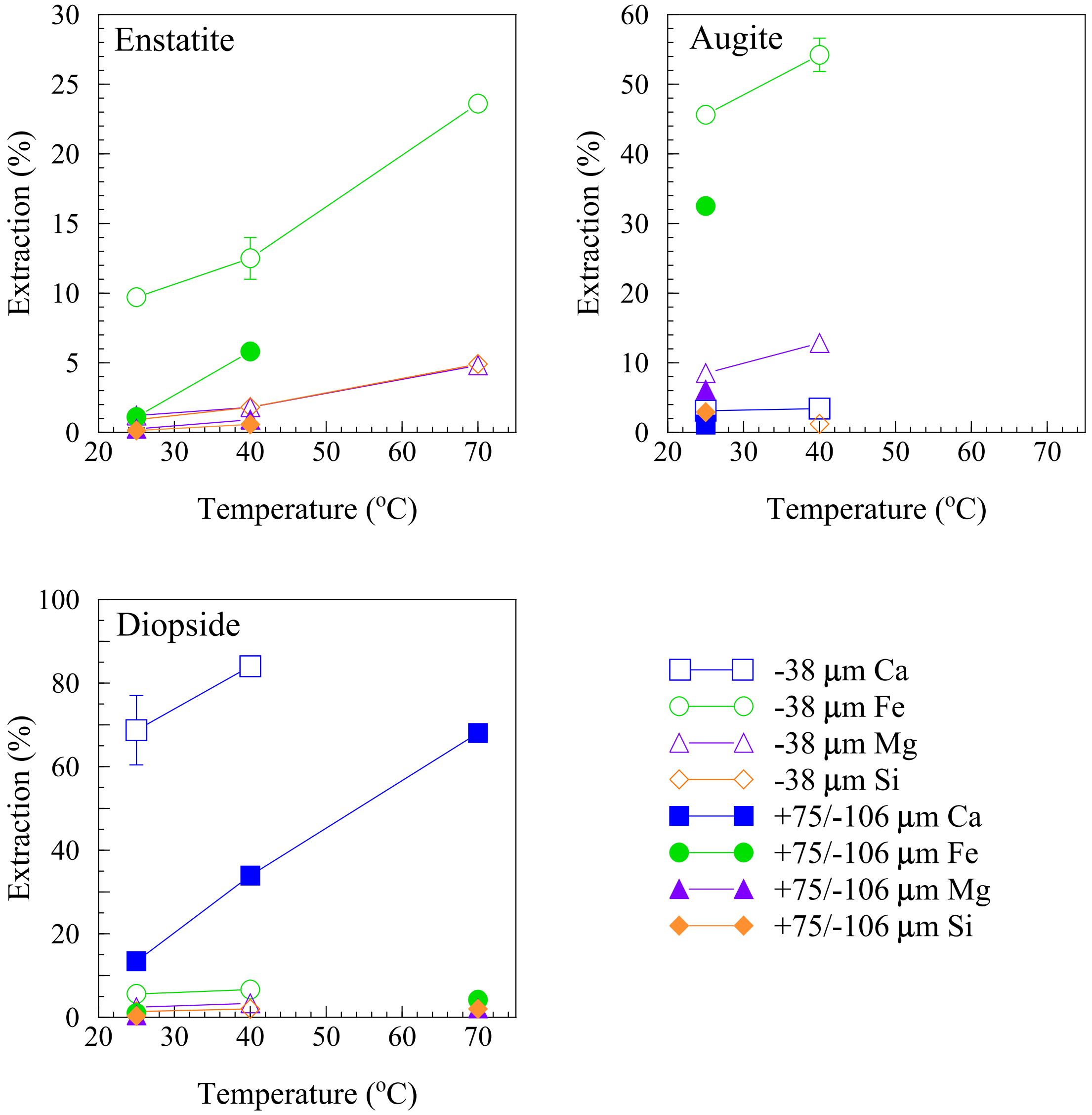

Figure 5.4: Extraction of Fe, Mg, and Si from enstatite at ambient, 40 °C and 70 °C for the -38 µm (open symbols) and +75/-106 µm (closed symbols). Lines between values are given to indicate the slope of the curve between the two temperature values. Standard error calculated on duplicate runs.

5.3 Mineralogical and physio-chemical changes in solid compositions after leaching

Table 5.2 lists the extent of each mineral phase extracted from the solid sample, represented in categories of: ∼zero: $-5 < x < 5$, low: $5 < x < 30$, medium: $30 < x < 60$, and high: $x > 60$. The QEMSCAN detects mineralogy but cannot discern crystallinity and because of thermodynamic constraints all precipitates calculated were amorphous. In the enstatite and diopside samples, the extraction of orthopyroxene and clinopyroxene, respectively, was low. In augite, the extraction of clinopyroxene was medium and orthopyroxene was high. The high extent of orthopyroxene is likely from its small concentration (< 1 %) in the feed and residue sample. In the wollastonite sample, the extraction of carbonates was high – carbonates are very reactive in acidic solution – but the extraction of wollastonite was low. The extraction percentages of Ca from wollastonite indicate a relatively reactive sample, however the system reached saturation early and precipitated Si-Ca. This likely resulted in the formation of an amorphous Ca-silicate close in composition to clinopyroxene on the surface of the grain; and would explain the formation of clinopyroxene in the wollastonite sample. Other amorphous Fe-Mg silicates (mainly talc but also includes serpentine, chlorite, and amphibole) and Fe-oxides formed in the enstatite, augite, and diopside. Amorphous silica formation occurred in enstatite, diopside, and wollastonite, indicating the dissolution of the primary silicate phase. The high percentage of quartz (amorphous Si) in the solid enstatite agrees with the low removal of SiO_2 as indicated by the leachate Si extraction (Table 5.1).

Table 5.2: Calculated extent of dissolution for each sample, using mineralogical data obtained from the QEMSCAN from feed and residue samples at 40 °C for 48 hours. (∼zero: $-5 < x < 5$, low: $5 < x < 30$, medium: $30 < x < 60$, and high: $x > 60$). The full calculation for the mineral mass balance is listed in Tables A.3, A.4, A.5, and A.6.

Phase	**Enstatite**	**Augite**	**Diopside**	**Wollastonite**
Orthopyroxene	Low	High	–	–
Clinopyroxene	–	Medium	Low	Negative
Wollastonite	–	–	–	Low
Other Fe-Mg silicate	Negative	Negative	Negative	Negative
Al-silicate	Negative	Negative	Negative	Negative
Silica	Negative	Low	Negative	Negative
Fe oxides	Negative	Negative	Negative	Negative
Carbonates	–	–	–	High

Other Fe-Mg mineral: olivine, serpentine, chlorite, talc, and amphibole

Al-silicate: plagioclase, K-feldspar, and garnet

The extent of cation extraction of Ca, Fe, and Mg from the solid phase is shown in Table 5.3, which was calculated from the changes in XRF data on the feed and residue samples. The extraction of each ion from the solid phase is shown in the same categories as used for the mineralogy. The extraction of Ca, Fe, and Mg from enstatite, augite, and diopside was low, except Ca extraction from diopside which was ∼zero. The ∼zero Ca extraction from diopside is likely due to precipitation of Ca once it entered the solution. However, the extraction of Ca from wollastonite was medium. Si extraction in all samples was ∼zero for augite, diopside, and wollastonite, and low for enstatite. The Si concentration for saturation in 0.1 M HCl at 40 °C is between 51 ppm and 404 ppm (from *Visual MINTEQ* and Pourbaix diagram, respectively). Augite, diopside, and wollastonite had a Si extraction of zero because the extracted Si was precipitated, however enstatite Si concentration did not exceed 103 ppm and therefore Si did not precipitate. Saturation calculations from *Visual MINTEQ* predicts that in experiments from enstatite, augite, diopside, and wollastonite of -38µm at 40 °C in 0.1 M HCl, only minor amounts of Si precipitated in the solution. The outcomes from these models predict a Si precipitation of 0.125 ppm, 0.164 ppm, 0.133 ppm, and 0.353 ppm for enstatite, augite, diopside, and wollastonite, respectively.

Table 5.3: Calculated extent of dissolution for each sample, using metal oxide data obtained from the XRF data from feed, and residue samples at 40 °C after 48 h. (∼zero: $-5 < x < 5$, low: $5 < x < 30$, medium: $30 < x < 60$, and high: $x > 60$). The full calculation for the cation mass balance is listed in Tables A.3, A.4, A.5, and A.6.

Ion	**Enstatite**	**Augite**	**Diopside**	**Wollastonite**
Ca	–	Low	∼Zero	Medium
Fe	Low	Low	Low	–
Mg	Low	Low	Low	–
Si	Low	Zero	∼Zero	Zero

The chemical extraction data supports the mineralogical extraction data for enstatite and diopside. The low extraction of orthopyroxene and clinopyroxene results in a low extraction of Fe, Mg, and Si, and Ca, Fe, Mg, and Si, respectively. However where the extraction from the mineral exceeded the saturation limit (e.g. for augite and wollastonite) the chemical and mineralogical extraction data contradict.

5.4 Particle topology changes on solid residue

Figure 5.5 shows micron-scale particle surfaces of enstatite, augite, diopside, and wollastonite after dissolution of -38 μm size fraction samples at 40 °C for 48 h in a 0.1 M HCl solution. Enstatite grains (Figure 5.5A) are block-shaped with smaller anhedral grains in the crevices of the larger grain. There are multiple stepped layers, which are ∼90° to each other (Figure 5.5B). These stepped layers at ∼90° are the cleavage planes of enstatite as illustrated in Figure 2.18C. The surface of the augite grain (Figure 5.5C) was similar in shape and topology to the enstatite grains. The augite sample shows small, finer particles on the surface of the grain, which shows the exposed cleavage intersections. The surface of the diopside (Figure 5.5D) is clean and smoother than the augite grains. However, the diopside shows an amalgamation of smaller grains which have been grouped on a larger diopside grain. The wollastonite grains (Figure 5.5E) show the highest degree of surface disruption. The elongate wollastonite grains are only slightly visible under the fluffy-textured precipitated silica. The precipitated silica (or Ca-silicate) on the surface of the wollastonite shows no discernible crystal shape and is likely amorphous Si gel (Figure 5.5F). Overall, none of the pyroxene grains showed any indication of pitting or etching on the surface. Furthermore, there was no visual indication of a passivating layer on the surface of the reacted grains.

The change in surface area (Table 5.4) of the pyroxene and pyroxenoid samples agrees with the SEM images of the residue surfaces. The wollastonite shows the greatest increase in surface area, which is more than 20-times greater than the surface area increase of enstatite, augite and diopside.

Table 5.4: Surface area change (in percentage) of cations from -38 μm-sized samples at 40 °C for enstatite, augite, and diopside after 48 hours in 0.1 M HCl solution.

Sample	**Surface area ($m^2.g^{-1}$)**		**Fold increase**	**Percent increase (%)**
	Feed	**Residue**		
Enstatite	2.316	3.928	1.7	70
Augite	3.760	4.566	1.2	21
Diopside	1.369	2.771	2.0	102
Wollastonite	0.9966	29.14	29.2	2825

Chemical analysis, by EDS from the SEM, analysed the proportion of Ca, Fe, Mg, and Si of selected spots on pyroxene residue grain surfaces. This data was plotted as a ratio of Ca:Si, Fe:Mg, and Mg:Si for each sample in Figure 5.6. In Figure 5.6, the open symbols represent the calculated ratio of the residue from EDS data, the solid symbols represent the analysed ratio in the feed from EMP data, and the dashed lines represent the ratio of Ca:Si, Fe;Si, and Mg;Si as calculated

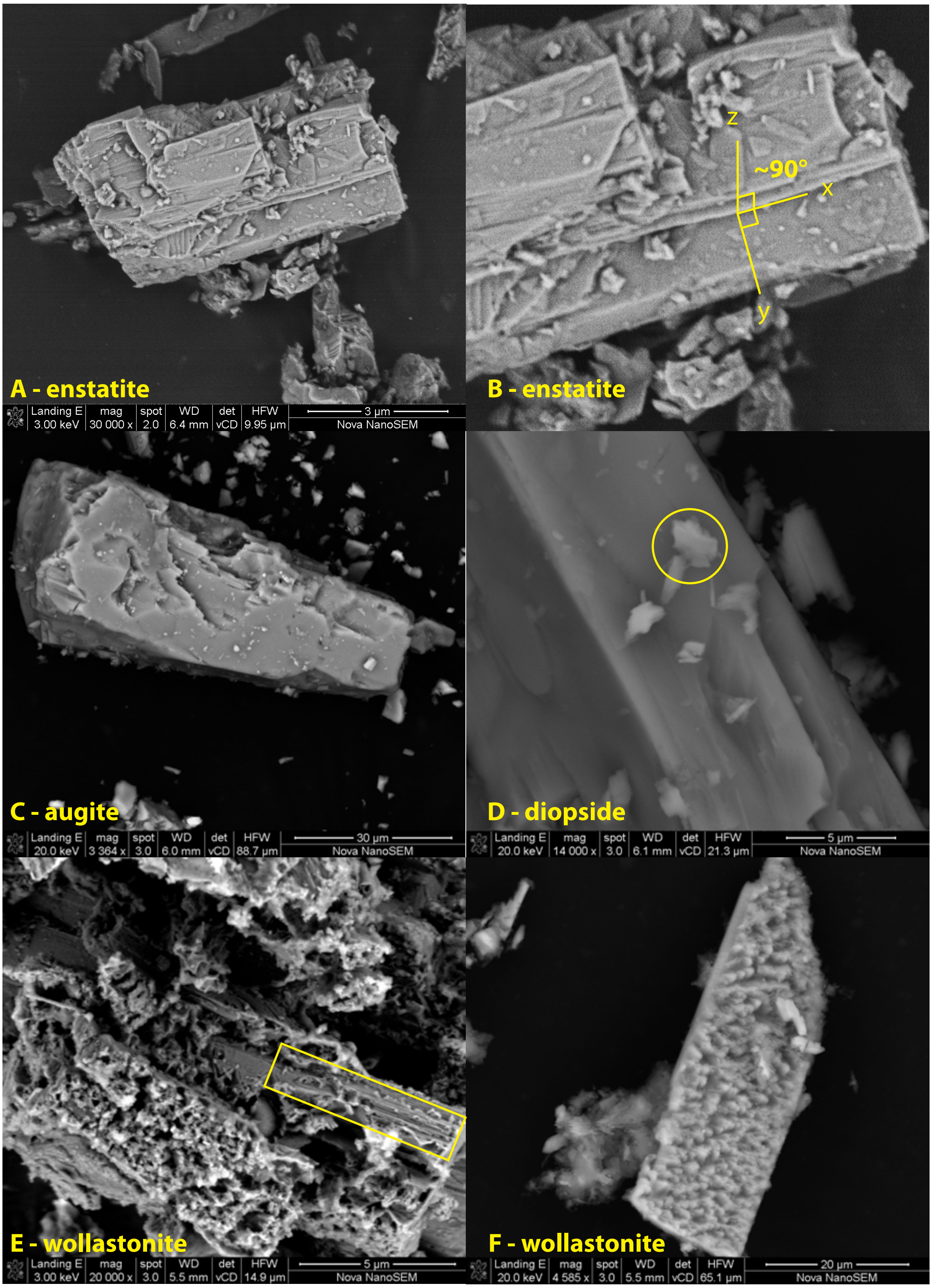

Figure 5.5: SEM images of pyroxene and pyroxenoid residue grains from reaction of 0.1 M HCl at 40 °C for 48 hours. (A): a block enstatite grain with (B) an enlargement showing the ~90° cleavage; (C): augite grains also show exposure of cleavage intersection; (D): diopside residue grain is relatively smooth; (E) wollastonite grain beneath the amorphous silica; and (F): a different morphology of precipitated silica on wollastonite. Read text for full description.

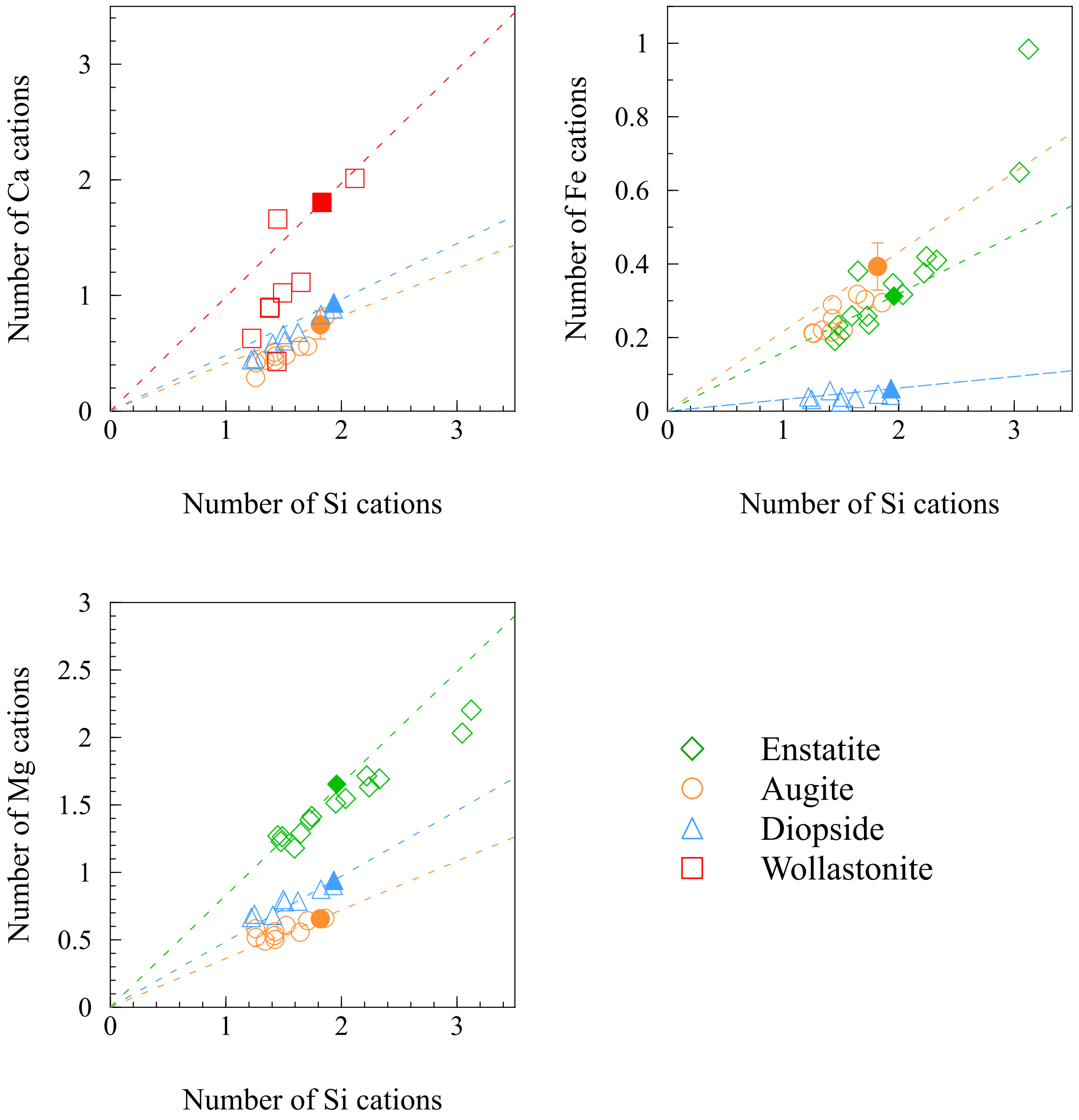

Figure 5.6: Number of cations (Ca, Fe, and Mg) plotted against the number of Si ions on the surface of the pyroxene and pyroxenoid grains. Closed symbols were calculated from the average of microprobe data. Open symbols were calculated from elemental distribution data from the surface of the grains from the semi-quantitative EDS analysis at selected sites on each mineral grain. Dashed lines indicate the stoichiometric ratio of Ca:Si, Fe:Si, and Mg:Si for each solid mineral and was calculated from mineral formula in Figure 3.1.

from the mineral formula in Figure 3.1. There was a general reduction in number of cations on the surface of these grains but in a stoichiometric ratio. Enstatite, augite, and diopside values all plotted along their mineral ratio functions (dashed lines), but the wollastonite residue sample grains were enriched in Si over Ca. Where the mineral residues remain on the dashed lines, congruent dissolution is present. Augite, diopside and wollastonite residue samples (open symbols) trend away from the measured probe data (closed symbols) towards the origin. However, enstatite shows a range of both reduction and enrichment in the number of cations on the surface of the grains for both Fe and Mg.

From the congruency diagram of the leachate and solid, the dissolution of pyroxene is generally stoichiometric; except for the dissolution of Ca from wollastonite, which is much greater than the dissolution of Si from wollastonite. This difference is greatest in the leachate solution because it measures the ratio of the cations as they are released from the mineral. The congruency of the solid takes into account the effect of precipitated sample on the surface of the grains and the analysing beam penetrates the upper surface layer of the mineral. Therefore if dissolution is nonstoichiometric and the leached layer (passivating layer) is negligible in thickness, the elemental concentrations will be contaminated by the concentration of the unreacted mineral.

5.5 Summary

The time-related extraction curves show parabolic extraction with wollastonite plateauing within the first 5 h and enstatite, augite, and diopside plateauing after 7 h. The extraction reactivity for the cations was: Ca $>$ Fe $>$ Mg $>$ Si within each mineral. The reactivity within the pyroxene group investigated was: wollastonite $>$ diopside = augite $>$ enstatite. Chemical analysis on the leachate during reaction showed that dissolution was nonstoichiometric for Ca and Fe from wollastonite and augite, respectively, but almost stoichiometric for Mg and Fe from enstatite and for Ca, Fe, and Mg from diopside.

An increase in temperature increased the extraction of Ca, Fe, Mg, and Si from enstatite, augite, and diopside. A decrease in particle size fraction from +75/-106 μm to -38 μm increased the extraction of Ca, Fe, Mg, and Si from enstatite, augite, and diopside. The relative cation extraction for the larger size fraction (+75/-106 μm) was more dependent in the change in temperature than for the cation extraction for the smaller size fraction (-38 μm) for the pyroxenes investigated.

Mineralogical results showed that there was low extent of extraction of orthopyroxene and clinopyroxene from the estatite and diopside samples, respectively. There was medium extraction of clinopyroxene from augite and negative extraction (i.e. formation) of clinopyroxene from wollastonite. The chemical results support the low dissolution of enstatite and diopside, but they indicate a medium extent of Ca removal from wollastonite. Thus the mineralogical and chemical extraction data in Table 5.2 and Table 5.3, respectively, gives an idea of the precipitating phases.

The surface of the reacting grains of enstatite and augite show right-angled steps which indicate cleavage planes. The surfaces of enstatite, augite, and diopside are relatively smooth, however the surface of the wollastonite grains are covered in precipitated Si. Chemical spot analysis on the surfaces of the residue grains indicate congruent dissolution, which follow a trend in their stoichiometric proportions. Wollastonite dissolution is incongruent and surface of the grains are enriched in Si over Ca.

Chapter 6

Discussion

The objective of this study was to investigate the mineralogical (composition and structure) and chemical (solution composition) effects of dissolution on pyroxene group minerals for an overall understanding of the pyroxene-rich PGM tailings reactivity for future mineral carbonation studies. This chapter discusses the results of pyroxene-rich tailings dissolution in organic acids (Chapter 4) and the effect of mineral chemistry, temperature changes, and particle size reduction on the dissolution of pyroxene group minerals (Chapter 5). The results are discussed in accordance to the hypotheses outlined at the end of Chapter 2, and further aims to answer the key questions for each hypothesis.

6.1 Factors affecting the kinetics of silicate mineral dissolution

The aim of this section is to answer the key question: "*Are low concentration organic solvents comparable to high concentration mineral acids on pyroxene-rich PGM tailings under the same conditions?*" This key question will be addressed on the basis of the results from the leach experiments on pyroxene-rich tailings using mixtures of organic (oxalic acid and EDTA) and mineral (HCl) acids at varying concentrations (results from Chapter 4). The second part of this section aims to answer the key question: "*Does increasing the temperature and decreasing the particle size lead to an overall increase in cation extraction?*" This key question will be addressed on the basis of the results from the leach experiments on pyroxene and pyroxenoid samples at varying temperature and particle size (results from Chapter 5).

6.1.1 The effect of organic additives on silicate dissolution

The dissolution reaction of pyroxene-rich tailings in a solution mixture of HCl (0.060 M to 0.088 M), oxalic acid (0.010 M to 0.038 M), and EDTA (0.001 M to 0.009 M) extracted a maximum of 40 % Al, 30 % Ca, 8.6 % Fe, 4.3 % Mg, and 6.4 % Si after 5 h at 70 °C (Table 4.1). The most favourable extraction of cations was in the solution with the highest concentration of oxalic acid (0.38 M in Mixture 8, Table 4.1). The maximum extraction of each cation, ordered in increasing concentration of oxalic acid (Figure 4.3), and the models from *Design Expert* show that the presence of oxalic acid increased the dissolution of pyroxene-rich tailings. The increase in oxalic acid concentration from 0.010 M to 0.038 M corresponded to an increase in Si and Ca extraction but not for Fe and Mg extraction. There was no noticeable trend for the effect of EDTA on an increase in cation extraction from pyroxene-rich PGM tailings. From the mineral balancing data of the pyroxene-rich tailings in Table 4.2, plagioclase had medium extraction. Thus the increase in extraction of Ca and Si is from plagioclase, which has more than double the weight percent of clinopyroxene, another source of Ca (Table 4.3).

It has been previously shown that organic acids dissolve silicate minerals by both the ligand- and proton-promoted dissolution mechanism (Furrer and Stumm, 1986). In the presence of mineral-acids only, the dissolution of silicate minerals proceeds by the proton-promoted mechanism as described in Figure 2.4. However, the addition of organic chelators enhances mineral dissolution by the addition of the ligand-promoted mechanism (Furrer and Stumm, 1986; Bennett and Casey, 1994; Prigiobbe and Mazzotti, 2011). In the ligand-promoted mechanism the protons associated with the organic acid hydrate the Si-O tetrahedra, and the organic ligands form complexes at the reaction front by covalent bonding between the oxygen of the organic compound and the surface metal. This shifts the electron density towards the metal ion, which weakens and breaks the M-O bond (Bennett and Casey, 1994). Proton-promoted dissolution is a slow process except at very acidic pH (Wiederhold *et al.*, 2006). Organic acids contribute significantly to mineral dissolution, especially at neutral pH, where the effect of proton promoted dissolution is smallest (Welch and Ullman, 1993).

A previous study on the same pyroxene-rich tailings, as used for experiments in Chapter 4, by Vögeli (2012), reacted these same pyroxene-rich tailings with a high-concentration mineral acid (2 M HCl) at 70 °C. The results from Vögeli (2012) and the results from mixture 8 (this study) are plotted together in Figure 6.1. Over the same time period investigated, the organic-mineral acid mixture experiment (0.060 M HCl, 0.038 M oxalic acid, and 0.001 M EDTA) had an overall higher extraction of Ca and Si from these tailings when compared to the 2 M HCl experiment. The extraction results

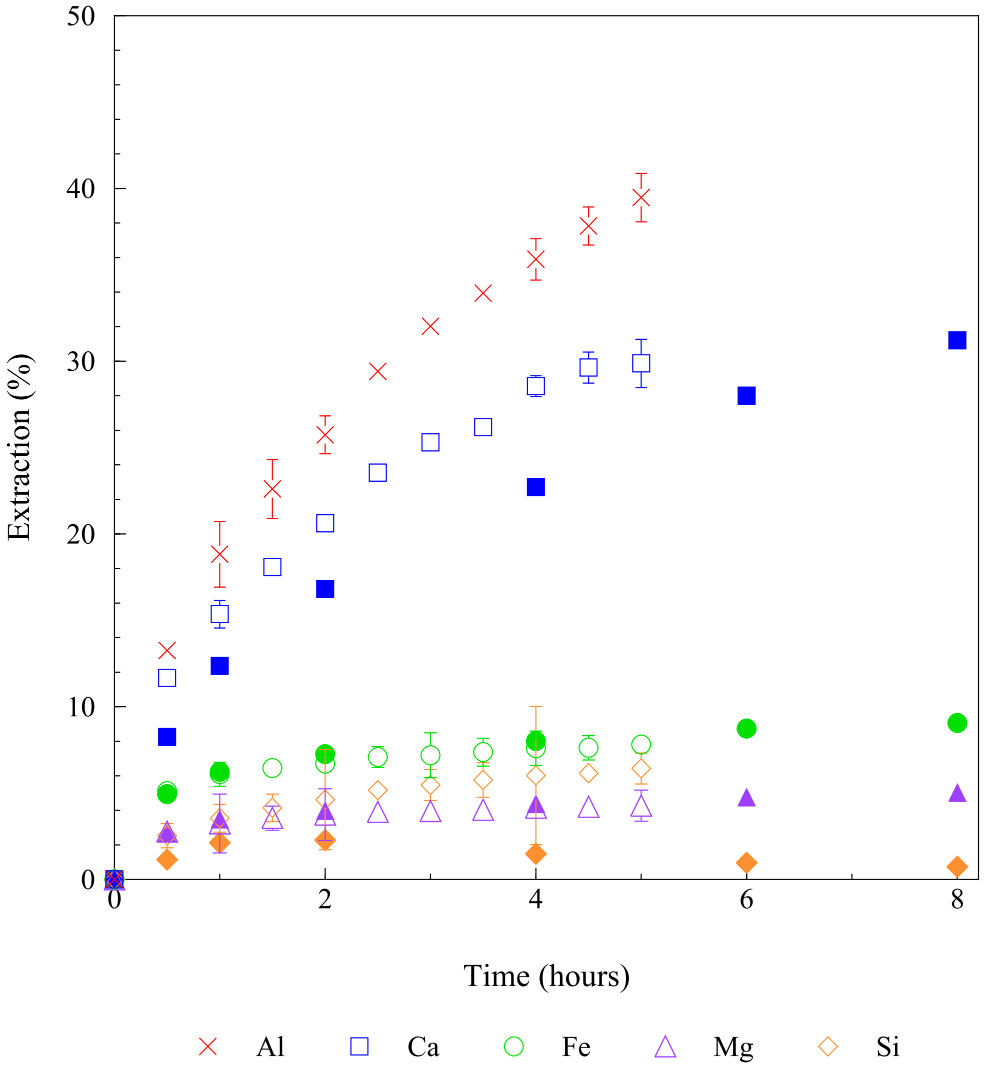

Figure 6.1: Extraction of Ca, Fe, Mg, and Si from the most successful mineral-organic mixture experiments (0.060 M HCl, 0.038 M oxalic acid, and 0.001 M EDTA) after 5 h (mixture 8, open symbols) and the extraction achieved in 2 M HCl solutions at 70 °C after 8 h from Vogeli (2012, closed symbols) on the same Lonmin bulk size fraction.

from the addition of oxalic acid at concentrations of 0.038 M to dilute mineral acid (0.060 M HCl) are comparable to, and in the case of Ca and Si, improved the extraction to that obtained with higher concentration mineral acids.

The increase in Ca and Si extraction with the addition of 0.038 M oxalic acid is caused by the dissolution of plagioclase, a Ca-Al-silicate. Plagioclase is the major host of Ca (Table 3.2) and had an overall larger dissolution (Table 4.3). Therefore the Ca extracted from the pyroxene-rich tailings was from the plagioclase and not clinopyroxene, the other Ca host. Oxalate has the ability to form complexes with Si (Bennett and Casey, 1994) and has an affinity for Al and Ca (Welch and Ullman, 1993). In the plagioclase structure, Al occupies up to 50 % of the Si sites in the Si-O tetrahedra (Deer *et al.*, 1992). The removal of the Al from the Al-O-Si tetrahedra would increase the extraction of the Ca and Si from the plagioclase.

Oxalic acid is very important for silicate mineral dissolution especially for silicates with a high Si:O. It complexes the slightly soluble Si in solution, which increases the extraction of Si and aids in increased cation extraction (Furrer and Stumm, 1986; Bennett and Casey, 1994; Prigiobbe and Mazzotti, 2011). A high concentration of Si in solution causes deposition of Si or Si-O polymers on the surface of reacting grains (Weissbart and Rimstidt, 2000). The deposition of Si forms product layers, as discussed in Section 2.2.2, which can be porous or hinder further dissolution on the mineral surface. The increase in Si solubility in solution allows for more Si to be extracted (i.e. more dissolution) before Si saturation is reached. Welch and Ullman (1993) suggested that the addition of organic ligands is most effective at near neutral pH. However, the results of the tests conducted in the mixture experiments at pH = 1, show that oxalic acid was still effective for Si extraction. Furthermore, precipitation prediction calculations using *Visual MinteQ* indicated that the leach solutions became saturated with respect to amorphous silica under both experimental conditions; but the extent of Si extraction reached a concentration of 312 ppm in the presence of oxalic acid versus only 32 ppm in the 2M HCl solution without oxalic acid. In the 2 M HCl dissolution experiment, the Si extraction reached a maximum of 111 ppm after 2 h but then steadily declined to a much lower concentration. EDTA had little or no effect on the dissolution of the pyroxene-rich PGM tailings sample even though it has 6 sites of coordination – two amines and four carboxylates, and oxalic acid has only two (Figure 2.11). However oxalic acid has a lower ionisation constant (pKa) of 1.25 and EDTA has a pKa of 1.782, which results in a stronger dissociation of oxalate than EDTA in solution.

The findings in this section are in accordance with the findings by other authors, where the addition of organic chelators to the solvent increases the dissolution of silicate minerals. Also, that the addition of oxalate increases the solubility of Si because it forms Si-oxalate complexes. The addition of organic acids increases the reaction rate through the addition of the ligand-promoted dissolution. The ligand-promoted mechanism is faster than the proton-promoted mechanism at neutral pH and at low temperature. The incorporation of the two mechanisms in the dissolution of the pyroxene-rich tailings has been shown to increase the reaction rate, but the overall increase in Ca, Fe, and Mg extraction is attributed to the high extraction of Si in the organic solution reactions. Calculations from the QEMSCAN software show that the majority of the Ca is extracted from plagioclase and the Mg from clinopyroxene, however it is difficult to determine where the organic acid has the most effect and if it has an affinity for a specific mineral (e.g. plagioclase dissolution over clinopyroxene). Pure mineral samples in organic acids and the reaction with multiple organic acids would be able to give more insight into the dissolution of mineral in organic solvents.

6.1.2 Temperature and particle size effects on pyroxene dissolution

The degree of extraction of Ca, Fe, Mg, and Si from enstatite, augite, and diopside in the 48 h reaction period increased with an increase in temperature from ambient to 70 °C and also with a decrease in particle size fraction from +75/-106 µm to -38 µm for the pyroxene samples investigated. The relative increase in cation extraction with an increase in temperature had the greatest effect on the +75/-106 µm size fraction. This is shown by the steeper gradient in the extraction of cations in Figure 5.4 (closed symbols).

In the dissolution rate equation by Lasaga (1995, Eq 2.3), the effect of particle size is represented by the active surface area (A_{min}), which is directly proportional to the rate of dissolution. An increase in surface area increases the number of sites that can be protonated. During the dissolution reaction, the mass of sample material decreases and the area generally increases as uneven surfaces are created by the formation of etch pits (Brantley, 2003). Based on measured surface area of each size fraction sample, the change in area was calculated. If a constant rate for the dissolution of enstatite were assumed, the rate of dissolution would theoretically increase 19 times (or 1 933 %) when the particle size is decreased from +75/-106 µm to -38 µm. Table 6.1 gives the increase in surface area between the two size fractions as determined by BET. Even though the enstatite sample had the greatest increase in surface area with a reduction in particle size, the particle size distribution was the same for all the samples. Therefore the increase in surface area is not the only factor that governs the reactivity of the mineral when particle size is reduced. Other factors to consider are the effects imparted onto the surface of minerals during grinding. An increase in grinding exposes cleavage intersections, and produces cracks which propagate through the mineral.

Table 6.1: Theoretical effect of particle size change on the calculated rate by using the dissolution rate equation of Lasaga (Eq 2.3, 1995)

Mineral	**Surface area ($m^2.g^{-1}$)**		**Percent increase (%)**
	-38 µm	+75/-106 µm	
Enstatite	2.32	0.120	1 933
Augite	3.76	0.274	1 372
Diopside	1.37	0.190	721
Wollastonite	1.00	0.133	752

The temperature dependence of the rate law is based on the activation energy, which is calculated from the Arrhenius equation (Eq 2.5). The activation energy of a reaction is indicative of the reaction mechanism and is calculated from surface interaction models (Casey and Sposito, 1992). The values ranges for a dissolution reaction are: 1 kJ.mol^{-1} $<$ diffusion limited $>$ 20 kJ.mol^{-1} $<$ intermediate $>$ 40 kJ.mol^{-1} $<$ reaction-limited. The activation energy of enstatite is 80 kJ.mol^{-1}, diopside is 96 kJ.mol^{-1}, and wollastonite is 54 kJ.mol^{-1} (Table 2.4, Brantley, 2003). The activation energy of a mineral should remain constant, however the apparent activation energy of a mineral can change when under different experimental conditions (Casey and Sposito, 1992).

From the temperature-extraction data for enstatite in (Table 5.1), a graph of the natural log of the rate (r, based on extraction of Mg) versus the reciprocal of the absolute temperate was plotted for the data between ambient temperature and 70 °C for each size fraction (Figure 6.2 and calculations in Table A.7). The negative gradient of the best-fit lines are equal to the activation energy divided the molar gas constant (where R = 8.314 m^2.kg.s^{-2}.K^{-1}.mol^{-1} and T is in Kelvin). From the slope of the best-fit line, the apparent activation energy for enstatite of each size faction was calculated (Table A.7). The calculated (apparent) activation energy for enstatite between ambient temperature and 70 °C was 27 kJ.mol^{-1} for the -38 µm size fraction and 66 kJ.mol^{-1} for the +75/-106 µm size fraction. This is much lower than the value of 80 kJ.mol^{-1} calculated for enstatite by Brantley (2003).

“Reactions with a high activation energy are more temperature-sensitive and reactions with lower activation energies are relatively temperature-insensitive” (Levenspiel, 1999, p28). The enstatite samples had the greatest increase in surface area from the -38 µm to the +75/-106 µm size fraction, but all four pyroxene minerals had the same or similar particle size distribution curve (Figure 3.3). Therefore the effect of particle size reduction was not the dominant physical mechanism. The activation energy for enstatite is given in the literature as 80 kJ, a reaction-limited dissolution; but the calculated activation energy for the enstatite reaction at the different particle sizes shows that for the smaller size fraction (-38 µm), the dissolution reaction is intermediate, but closer to transport-limited kinetics. However, the larger size fraction (+75/-106 µm) has an apparent activation energy of 66 kJ and is therefore reaction-limited. The change in reaction kinetics shows that increased particle size reduction increases the number of reactive sites which moves the reaction mechanism from reaction-limited to transport-limited as the desorption of the solute is no longer limiting. Therefore silicate minerals with high low activation energies (i.e. increased grinding) can be easily accommodated for low temperature dissolution.

A study by Casey and Sposito (1992) showed the changes in experimental versus calculated activation energy. The change arises from the enthalpy of proton adsorption, which is negative and on

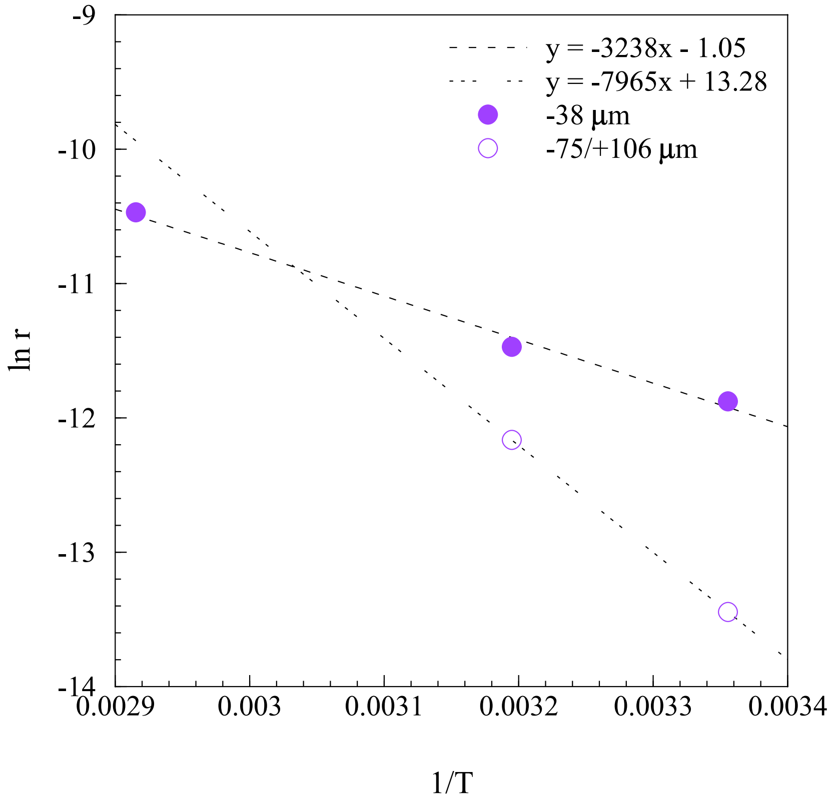

Figure 6.2: Rate (r) versus temperature (T) of enstatite extraction for the -38 µm and +75/-106 µm size fractions calculated from Mg extraction. The best-fit lines (equations indicated on graph) were used to calculated the apparent activation energy for enstatite. Refer to Appendix A.7 for calculation.

the order of 15-50 kJ.mol^{-1}. This energy is negative for proton-promoted dissolution and positive for hydroxyl-promoted dissolution. These results correspond to the change in calculated activation energy of 80 kJ.mol^{-1} to the experiment value of 66 kJ.mol^{-1} and 27 kJ.mol^{-1} for the +75/-106 µm and -38 µm size fractions, respectively. However, the change in apparent activation energy for the two size fractions may be due to small inclusions within the minerals as this sample was not a chemically pure enstatite (impurities highlighted in Figure 5.1). The pyroxenite layer is the hangingwall to the mineralised zone (Merensky Reef) of the upper critical zone of the Bushveld Igneous Complex, and its mineralogy changes from orthopyroxene to inverted pigeonite (Seabrook, 2005) as the sequence continues upward. Pigeonite is a high-temperature, low-calcium clinopyroxene that has the appearance of augite. Upon slow cooling, pigeonite re-equilibrates into an orthopyroxene host with exsolution lamellae of clinopyroxene. These clinopyroxenes increase the reactivity of the orthopyroxene sample and because the exsolution appear within the mineral grain, they can be preferentially exposed during grinding. Plagioclase is another mineral that is included in the orthopyroxenes of the critical zone pyroxenite (Cawthorn and Boerst, 2006). Grinding of these samples will liberate these 'more reactive' particles when the size fraction is reduced. A recent study by Hochella *et al.* (2008) showed that nanominerals and mineral nanoparticles commonly behave differently as a function of their size within the nanoscale size range. The increase in reactivity does not always directly correlate with the change in surface area. They suggest that the variations in reactivity with a change in particle size include structurally disordered, strained, and/or reconstructed surfaces, changes in the surface topography due to the different crystallographic surfaces exposed (Hochella *et al.*, 2008), and the breaking of valence bonds (Kalinkina *et al.*, 2001). The grinding of particles creates many very small particles. Dissolution experiments on quartz have shown that the many small particles produced from grinding increased the solubility of quartz from the value for quartz to the value for amorphous Si (in Holdren and Berner, 1979).

The temperature range was investigated at low temperatures as the cost of heating adds to the energy budget of the overall process; and the particle size range investigated was only on the order of the pyroxene-rich PGM tailings. Therefore the effect of a much smaller grain size (below -38 μm) was not investigated and thus the effects of grinding below this size fraction are unknown. The low temperature range and the small data set may not accurately show the apparent activation energy of these two pyroxene samples. To this end, the projection of the ln r vs 1/T straight line for the two size fractions may intersect at a higher or lower temperature or have a more shallow gradient. The effect of particle size is not well documented in the literature, but grinding creates sites of higher energy and increases the number of breaks along the cleavage planes. From the figures of the reacting grains (Figure 5.5), cleavage-controlled dissolution for pyroxene takes advantage of the exposed cleavage planes as these planes are more reactive. Therefore grain size reduction would increase the area of exposed cleavage planes, dependent on the type of grinding machinery used.

6.2 The reactivity of pyroxene group minerals

The reactivity of the pyroxene group minerals can depend on many factors such as: cation chemistry, cation location, bond length, coordination, and Si-O polymerisation. This section of the discussion aims to answer the key questions on pyroxene reactivity outlined at the end of Chapter 2. These key questions will be addressed on the basis of the results from the leach experiments on pure pyroxene samples and chemical and mineralogical balances from XRF and QEMSCAN, respectively. This section of the discussion will follow the order of the key questions:

i *Which of the pyroxene group minerals are more reactive and why?*

ii *Is the dissolution of pyroxene controlled by physical features on the surface of the grains?*

iii *How do pyroxenes react in acidic conditions?*

6.2.1 Order of pyroxene group reactivity

The order of experimental reactivity for pyroxene group minerals was: wollastonite $>$ diopside = augite $>$ enstatite at 40 °C for the -38 μm size fraction in 0.1 M HCl. In the same experiment, the extraction of Ca from wollastonite was 96 %, but only 84 % for diopside, and 3.4 % for augite. 12 % Mg was extracted from augite, 3.3 % Mg from diopside, but only 1.8 % Mg from enstatite. The Si extraction was 31 % from wollastonite and below 4 % for enstatite, augite, and diopside. The extraction of cations from wollastonite reached equilibrium after 5 h, whereas the extraction of cations from enstatite, augite, and diopside reached equilibrium after only 7 h. In addition, the extraction of Ca from wollastonite, Ca and Mg from diopside, Fe and Mg from augite, and Fe from enstatite was incongruent. Only the extraction of Ca from augite and Mg from enstatite were close to congruent. Furthermore the dissolution of Ca from diopside had a higher degree of incongruency than the dissolution of Mg. On the surface of the reacting grains, all minerals showed stoichiometric relationships, except for wollastonite which was depleted in Ca.

From the literature, it is well known that pyroxenoids are more reactive than pyroxenes and that clinopyroxenes are more reactive than orthopyroxenes (Cameron and Papike, 1981; Schott and Berner, 1985). The reactivity of these minerals has been observed in a number of experiments (detailed in Sections 2.3 and 2.5) and shown by the order of reactivity in Section 2.1. In addition to the experimental results, the order of reactivity of the pyroxene group mineral has been correlated with the Madelung site energy of the mineral's M1 and M2 cations (Brantley, 2008). Besides the absolute value of the Madelung site energy, there has been little that discusses why and how the reactivity changes between the pyroxene group minerals. From a combination of cation chemistry and mineral structure shown in Chapter 2, and validated with experimental results from Chapter 5, it is shown that the reactivity of a mineral is dependent on the metal cation and Si-O tetrahedra connectedness. As all pyroxene group minerals have the same Si-O tetrahedra arrangement, this section will discuss the effects of cation size and chemistry with regard to pyroxene reactivity.

The chemistry of the cation affects the reactivity of the pyroxenes through the changes in the electronegativity difference in the M-O bond. The higher the electronegativity difference, the more polar the bond and thus the more negative the oxygen site. In the surface protonation model described by Furrer and Stumm (1986), the attachment of protons to the oxygen lengthens the M-O bond and shifts the negative charge toward the oxygen and away from the metal site, thus facilitating the attachment of the OH^- to the cation and the subsequent removal of $M(OH)_{(aq)}$ (Prigiobbe and Mazzotti, 2011). The Si-O bond electronegativity difference is 1.7, thus a covalent bond, and the bond strength is 452 $kJ.mol^{-1}$ (Table 6.2). The bond strength is: Ca-O (402 $kJ.mol^{-1}$) $>$ Fe-O (390 $kJ.mol^{-1}$) $>$ Mg-O (363 $kJ.mol^{-1}$, Silberberg, 2011). The Mg-O bond is the weakest based on electronegativity, but from reactions far from equilibrium on diopside, Ca is released preferentially to Mg (Brantley, 2008). Therefore a pure cation-oxide bond strength is not the only force governing silicate mineral reactivity. Changes in ionic radius and charge (ionic strength) are also important controls for mineral reactivity (Terry, 1983). Transition metals in silicate mineral dissolve at rates which are proportional to the number of d-electrons (Casey *et al.*, 1993).

Table 6.2: Electronegativity difference, bond length and bond strength of selected oxide bonds found in the pyroxene structure.

Bond	**Electronegativity difference**	**Bond strength ($kJ.mol^{-1}$)**
H-O	1.4	463/459
Si-O	1.7	452
Ca-O	2.5	402.1 ± 16.7
Fe-O	1.7	390.4 ±17.2
Mg-O	2.3	363.2 ±12.6

Another factor to consider in pyroxene reactivity is the size of the cations in the M1 and M2 sites. An increase in size of the cation affects the octahedral coordination. The addition of a larger cation into the M2 site in clinopyroxenes distorts the coordination from octahedral to polyhedral and therefore changes the bond lengths (Deer *et al.*, 1992). Figure 6.3 shows the difference in the polyhedral shape and the M-O bond lengths associated with the M1 (yellow) and M2 (green) cation sites of enstatite (orthopyroxene, left) and diopside (clinopyroxene, right). The larger M2 site (i.e. Ca in augite and diopside) increases the M2-O bond length and the coordination from 6 to 8, but the M1-O bond length and coordination remains unchanged. The longer the bond length, the weaker the bond. Therefore where Ca is present (i.e. in the M2 site) the mineral has an overall higher reactivity than when not present. In wollastonite, the large Ca ion is present in both the M1 and M2 sites, further distorting the pyroxene structure. The difference in pyroxene and wollastonite cell length (along the z-axis) and tetrahedral angle in the chain, increases the reactivity of the wollastonite (Figure 2.19). This small change in the structure of the wollastonite chain drastically lengthens the individual Ca-O bonds holding the silicate chains together. Therefore during protonation of wollastonite, the weaker Ca-O bond decreases the energy required to dissolve the mineral.

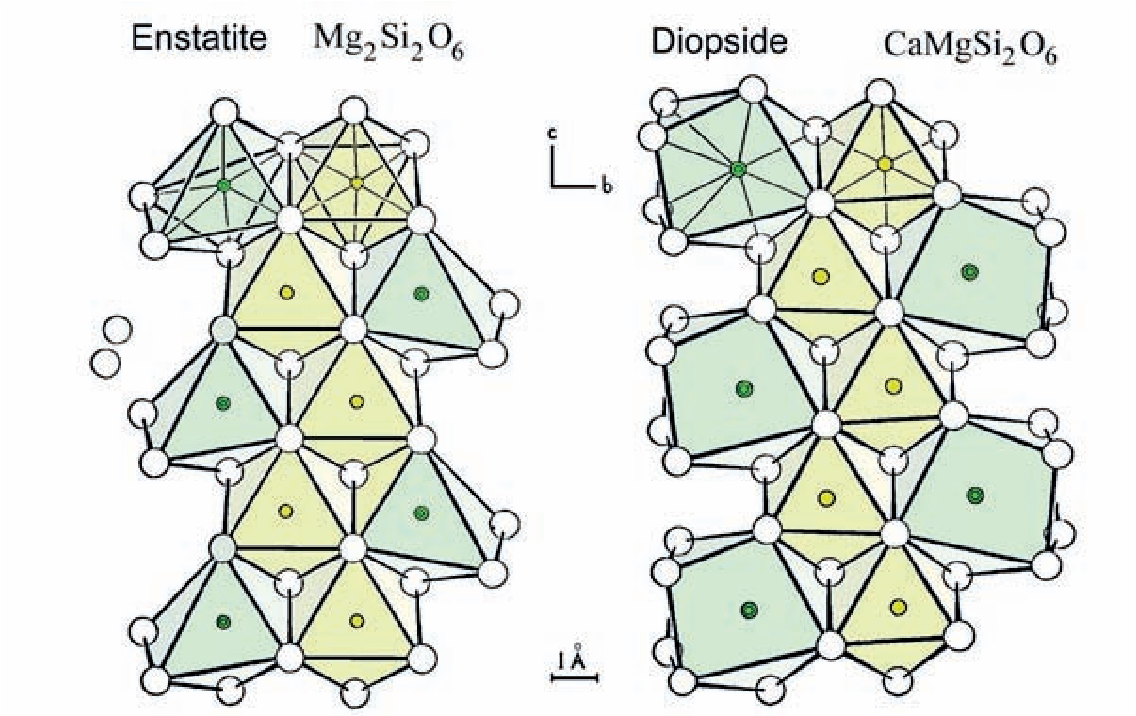

Figure 6.3: Comparison of orthopyroxene (enstatite) and clinopyroxene (diopside) polyhedral coordination shape. The M1 site is represented in yellow and the M2 site is represented in green. The corner oxygens of the Si-O tetrahedra are illustrated with white circles. The M1 and M2 sites of the orthopyroxene have 6-fold coordination; however in clinopyroxenes, the M1 site is unchanged and has 6-fold coordination whereas the M2 site has a larger 8-fold coordination and the size of the site is larger. Image sourced from: www.minerals.gps.caltech.edu.

The electronegativity difference and the size distortion of the cations effect can be grouped together as the Madelung site energy. The Madelung site energy for the M1 and M2 cations is listed in Section 2.5 (Table 2.8). The energy of the Ca is -3 157 kJ.mol^{-1} and Mg is -4 346 kJ.mol^{-1} in diopside. For enstatite, the difference in energy between the Mg in M1 and M2 sites is less with a M2 of -3 940 kJ.mol^{-1} and a M1 of -4 318 kJ.mol^{-1} (Schott and Berner, 1985). The Madelung site energy of the M1 and M2 sites has a direct impact on the overall apparent activation energy for the pyroxene group mineral, the stronger the metal cation is bonded, the higher the activation energy (Table 2.4). The activation energy (Ea) is the energy required to overcome dissolution, and it directly correlates to the stability of the pyroxene structure. Enstatite, the more stable of the pyroxenes, has a higher activation energy (Ea = 80 kJ.mol^{-1}) than wollastonite (Ea = 55 kJ.mol^{-1}), the most reactive of the pyroxenes investigated. Augite has a lower activation energy than enstatite due to the presence of the Ca in the M2 site. The activation energy of diopside should be lower than augite and enstatite, however it is not well constrained and ranges between 42 kJ.mol^{-1} and 96 kJ.mol^{-1} (Knauss *et al.*, 1993; Chen and Brantley, 1998; Brantley, 2003). This large range in activation energy for diopside makes it difficult to compare it to the other pyroxenes.

The reactivities between the pyroxene group minerals are in accordance with the findings by other authors as shown by the rates in Table 1.2. In addition, there is preferential dissolution of the M2 cation in all of the pyroxene group minerals investigated. This results in incongruent dissolution with regard to the leachate and agrees with the results of Huang and Keller (1970), Weissbart and Rimstidt (2000), and Brantley (2008). However, the cause of the congruent reaction shown by the solid residue will be discussed later. In this study, only the major cations that form stable carbonates (Ca, Fe, and Mg) were evaluated. The effect of trace elements or other major phase elements (e.g. Al, Na) were not taken into account. The inclusion of Al in clinopyroxenes for Si in the Si-O tetrahedra can also increase the clinopyroxene reactivity. The Al-O bond is weaker in the Al-O tetrahedra than the Si-O bond in the Si-O tetrahedra. The clinopyroxenes: omphacite, augite, and diopside, can have a large proportion of the Si replaced with Al; and jadeite can have a high weight percent of Al in the M1 site (Deer *et al.*, 1992, p152). Therefore any changes in mineral chemistry for a pyroxene will have a large effect on the mineral's reactivity.

6.2.2 Dissolution mechanism of orthopyroxene

The pyroxene reaction model of Zakaznova-Herzog *et al.* (2008), Figure 2.21, shows the general protonation reaction of dissolution and alludes to the favourable release of the M2 cation before the M1 cation because of the distance of the M1 and M2 site from the surface. However the reaction surface is perpendicular to the z-axis (perpendicular to the silicate chain), where there is no preferential cleavage or parting. Therefore a reaction mechanism as the one proposed in Figure 6.4 would be more suited to the the pyroxene group minerals. This is supported by SEM images (Figure 5.5B), which shows distinctive dissolution parallel to the cleavage planes by the presence of stepped terraces on the surface of the grain. Figure 6.4 shows the reaction mechanism of a simplified orthopyroxene (where the M2 site $>$ M1 site size) dissolution in an acidic solution (HCl solution). Pyroxene group minerals dissolve in accordance to the surface protonation model as outlined by Furrer and Stumm (1986) in Section 2.3. The reaction mechanism in Figure 6.4 is shown for the grain surface parallel to a cleavage plane, indicated by the solid red line.

An exposed mineral surface is protonated by H^+ ions in an acidic solution (step 1). Protons (red) attach first to anions (oxygens, light grey) with high energy. These anions are usually at sites

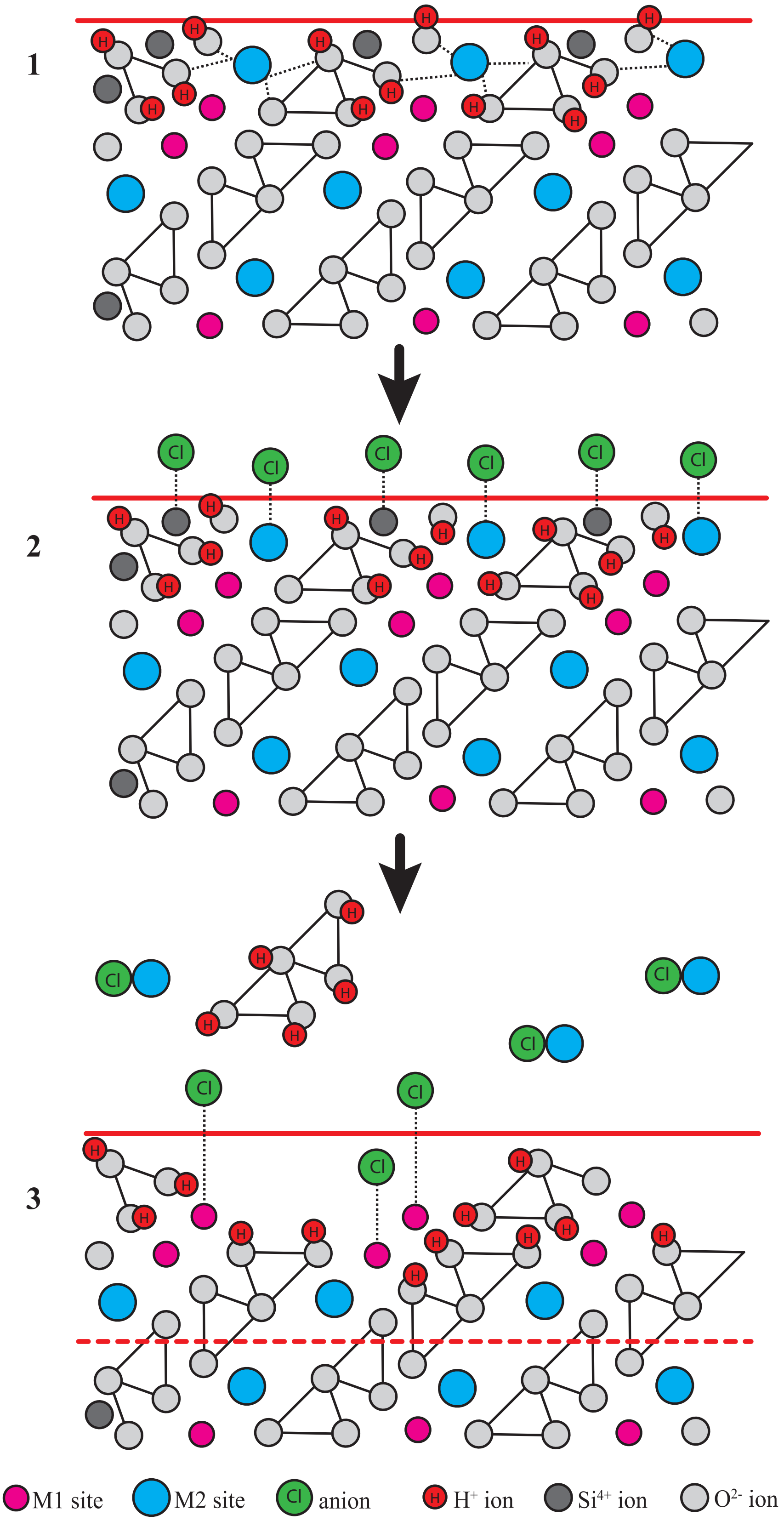

Figure 6.4: Attachment of H$^+$ ions (red) from solution onto the surface of the reacting grain (i.e. on the oxygen) strains the metal-oxygen bond by lengthening the bond. When all oxygen atoms of the silicate tetrahedra are protonated, the metal-oxygen bond breaks. The metal cation and hydrated silicate are free to leave to surface of the mineral, and thus exposing the underlying, unreacted silicate.

of breakage (from cleavage) and at the edges of grain boundaries. Second in proton attachment order are the non-bridging oxygens. These oxygens are more ionic than their bridging oxygen counterparts (Ramberg, 1952), and will attract protons before non-bridging oxygens because of their higher electron density. The protonation of oxygens increases the M-O and Si-O bond length. The metal cation is only released when all the neighbouring oxygens (6 for M1 and M2 but 8 for M2 in clinopyroxenes) have been protonated and the M-O bonds sufficiently weakened. The movement of the electron density away from the M site allows for the attachment of an anion (green) – usually Cl^- in a HCl solution – to the metal. This attachment allows for the metal to leave the silicate structure and enter the solution in the form of $M(OH)_{aq}$. When the surface metal cation has been removed, the underlying cations are susceptible to removal by the protonation and the removal of neighbouring silicate tetrahedra. Simultaneously the underlying and exposed metal cation is vulnerable to attachment of the anion and its subsequent removal from the surface of the reacting grain. As the removal of silicate tetrahedra and M1 and M2 cations continues, the reaction surface moves down (dashed red line). Therefore the mineral's surface remains flat and parallel to the cleavage plane throughout the dissolution reaction.

Unlike in the olivine reaction mechanism shown in Figure 2.4, the proposed pyroxene reaction (Figure 6.4) is complicated by the the joining of silicate chains and the presence of two cleavage planes within the crystal structure. The bridging-oxygen to silicon bond is shorter and therefore stronger than the pure oxygen-silicon bond (1.628 Å for bridging and 1.640 Å for non-bridging oxygens, Table 6.3). This increase in Si:O bond strength (i.e. decrease in bond length) requires more energy to break the silicate chain apart (along the z-axis), and results in the removal of hydrated SiO_2 chains rather than discrete $Si(OH)_4$. Figure 6.4 shows the reaction of pyroxene as viewed down the z-axis, the hydrated silicate is shown to be removed as an individual hydrated tetrahedra but it is likely removed as an intact, hydrated Si-O chain (Terry, 1983).

The cleavage planes in pyroxene expose the surface of the grain along the length of the chain and one M2 site, as it makes use of the larger distance between two M2 sites than two M1 sites (Figure 2.18B). The cleavage of the pyroxene preferentially exposes the M2 cation site and protects the M1 cation site from being released into solution as the M1 site is trapped below a silicate chain. The presence of cleavage has two effects on the mineral's dissolution. Firstly there is an increase in the concentration of M2 cations, confirmed by the Ca:Mg ratio in the solution of diopside, and secondly, the rate of reaction changes along each edge of the crystal. If it were assumed that the reaction favours the cleavage plane surfaces, then the dissolution of pyroxene would indeed increase the dissolution of M2 cations over the M1 cations. The reaction would proceed as described in Figure 6.4, by the removal of hydrated silicate chains and not discrete hydrated silicate tetrahedra.

Awad *et al.* (2000) showed that the changes in structure and chemistry down each of the crystallographic planes of olivine had a marked effect on the rate constant along each of the crystallographic axes. The rate constant for olivine (at pH 1 and 70 °C) varied from along the x-, y-, and z-axis at 2.7 x10^{-4}, 5.6 x10^{-3}, and 8.1 x10^{-4} mm.h^{-1}, respectively; and results in activation energy of 114.5 $\pm$ 23 kJ.mol^{-1}, 69.9 $\pm$ 8kJ.mol^{-1}, and 72.9 $\pm$ 15 kJ.mol^{-1}, respectively (Awad *et al.*, 2000). The increase in dissolution down the y-axis was attributed to the preferential protonation of the oxygens surrounding the M1 site (Figure 2.22). However, a good cleavage plane in olivine is situated along the (010) plane (shaded area), perpendicular to the y-axis (Figure 2.22, Deer *et al.*, 1992). Therefore it can be assumed that the presence of cleavage, even slight or imperfect, preferentially exposes a specific surface and causes preferential leaching. The Mg cations occupy both the M1 and M2 site in forsterite (Mg olivine) and the Si-O are bonds equal in all directions, the presence of cleavage would have a small effect on the overall dissolution of the mineral. Yet pyroxenes have a wider chemical composition and the bond lengths change along the different crystallographic axes, so the presence of cleavage has a larger impact on the dissolution of pyroxene.

With cleavage planes controlling the rate of the overall reaction, the rate of reaction could be increased by the increase in surface area parallel to cleavage by the preferential breaking along these planes. It also has an important explanation for why, during reaction, the metal cations from the M2 site are released before the M1 site. Further investigation into the dissolution along each crystallographic plane would be of interest for an overall understanding of the pyroxene reaction mechanism.

6.2.3 Effect of pyroxene reaction mechanism on its stoichiometry and kinetics

The dissolution of enstatite, augite, diopside, and wollastonite in the leachate was incongruent for Ca, Fe, and Mg; except for Mg from enstatite, which was almost congruent. However, the dissolution of enstatite, augite, and diopside analysed from the solid residue was congruent for Ca, Fe, and Mg, except for Ca from wollastonite, which was incongruent. On examination of the surfaces of the reacted grain, the surfaces were generally smooth but with multiple terrace intersections at 90°, the same orientation as the cleavage planes in pyroxene, for enstatite, augite, and diopside. The surface of wollastonite had a fluffy texture from the precipitation of amorphous Si on its surface.

From the discussion in Section 6.2.2 and Figure 6.4, the dissolution of pyroxenes was controlled by the cleavage planes on the mineral surface. The dissolution of pyroxene is a reaction-limited, and therefore the surface of the grain should be smooth. Because of the strong cleavage planes present in pyroxene, the reaction fronts proceeded along these planes. The lack of etch pits on the surfaces of the reacting grains agrees with the reaction is governed by the orientation of the cleavage planes. The chemical analyses on the surfaces of reacting grains agrees with a chemical-controlled reaction rate and the removal of $Si(OH)_4$ tetrahedra from the surface of the grains. During dissolution, the Si and cations initially are not removed in their stoichiometric ratio, with the M2 site favoured over the M1 site. But, because the reaction proceeds along the cleavage planes, the entire silicate structure of that plane needs to be removed before the reaction can continue. Therefore the grain retains its stoichiometric ratio, and the dissolution reaction remains reaction-controlled. This agrees with the activation energies of the pyroxene minerals. The high activation energies for the pyroxenes rule out transport-limited kinetics; and therefore surface reactions (i.e. desorption of the reacting species) are responsible for the higher activation energy (Schott and Berner, 1985).

6.2.4 Comparison of pyroxene reaction mechanism to other Mg-silicates

Olivine and serpentine were not investigated in this study; however, because of their high reactivity and use in mineral carbonation, there is a vast amount of literature and rates available for these minerals. The enstatite sample used in these experiments is close to pure enstatite and therefore the comparison between this sample and olivine and serpentine is beneficial. Bond lengths and bond strengths were not investigated in this study and therefore the data used to compare these pyroxene reactivity may differ slightly because of natural chemical and structural changes within samples.

The major difference in reactivity between the Mg-silicates olivine, serpentine, and enstatite, is their individual silicate structure, and bond type and strength. In olivine, the silicate tetrahedra are not bonded through a bridging oxygen and therefore the silicate structure is less stable. Although the serpentine has a higher Si:O ratio, than pyroxene, it is more reactive because of the reactive OH^- functional group which increases its reactivity (Terry, 1983). The M-O bond for olivine is longer than the M-O bond lengths for serpentine and enstatite (Table 6.3). The addition of the H^+ to the O-M1 and O-M2 bond increases the bond length from 2.08 Å and 2.14 Å to 2.30 Å and 2.51 Å, respectively (Liu *et al.*, 2006). This makes the removal of metal cations from olivine faster than for pyroxenes.

As seen from the bond length, the metal-oxygen bond is closer, and therefore stronger, in the serpentine and enstatite minerals (Table 6.3). Therefore the metal cations are easier to remove from the olivine structure than the serpentine and enstatite structures. In serpentine, the cleavage exposes the metal site and therefore the reaction is much faster than for enstatite. Although the cleavage plane of enstatite exposes the M2 site, the low reactivity of the pyroxenes can be attributed to the removal of the entire silicate structure by the breaking of the strong Si-O bridging bond before further cations

Table 6.3: Bond lengths of the Mg-silicates: forsterite, lizardite, and enstatite in angstroms (Å). Non-bridging oxygen lengths are shorter than the bridging oxygens. Olivine does not have bridging oxygens and serpentine only has one metal site.

Bond	**Forsterite** **Liu *et al.* (2006)**	**Lizardite** **Melline (1982)**	**Enstatite** **Ohashi and Burnham (1972)**
Si-O (non-bridging)	1.62	1.616	1.628
Si-O (bridging)	–	1.646	1.640
M1-O	2.14	2.067	2.077
M2-O	2.23	–	2.144

can be removed. The Si-O-Si bond is strong and therefore not likely to break during dissolution on relatively short time scales.

6.3 Consequence of pyroxene reaction mechanisms and reaction kinetics on the dissolution of pyroxene-rich PGM tailings

The large difference in cation extraction between Al, Ca, Fe, Mg, and Si indicates that a different mineral is responsible for each cation. As indicated in Table 4.3 and Table 4.2, the Ca is leached from the plagioclase and a small amount from clinopyroxene but the Mg is leached from the clinopyroxene. The dissolution of cations from the pyroxene-rich PGM tailings was low for all the cations investigated due to the almost 90 % orthopyroxene, a relatively unreactive mineral. The low reactivity of the Lonmin tailings has a direct impact on the feasibility of Bushveld PGM tailings for mineral carbonation. Vögeli (2012) calculated that the Lonmin PGM tailings could sequester 868 kt of CO_2 per annum, however these calculations do not reflect slow kinetics of cation extraction and extents of subsequent carbonation. The calculation of theoretical carbon storage is computed on the total available tailings, multiplied by the total percent of each oxide in sequesterable minerals (Table 6.4). Sequesterable minerals include: olivine, Fe-oxides, clinopyroxene, hornblende, serpentine, plagioclase, orthopyroxene (abundances in Table 3.2). When the carbonation efficiency calculated from the experiments of Vögeli (2012) is included, the total available CO_2 storage decreases from 868 kt to 600 kt per annum, a $\sim$30 % decrease.

On the basis of the experimentally determined extraction in this study, the total CO_2 storage is only between 53 kt to 61 kt per annum. Plagioclase is a relatively rich Ca-silicate that showed medium Ca extraction in the organic mixture experiments (Table 4.2). By increasing the extraction of Ca from plagioclase with organic acid mixtures and leaving the reaction to continue for a longer period of time at ambient temperature (difference between 2 M HCl and 100-day leach), an extra 4.6 kt CO_2

Table 6.4: Theoretical CO_2 storage based on an experimentally determined carbonation efficiency percentage at 100 % dissolution of cations.

Oxide	Available oxide* (%)	Moles of oxide (n)	Carbonation**	Moles Carbonated
CaO	4.58	1.8×10^9	96	1.8×10^9
FeO	12	3.9×10^9	98	3.8×10^9
MgO	21.7	1.4×10^{10}	58.6	8.1×10^9
TOTAL				1.36×10^{10}
CO_2 stored				600×10^3 t

*Sequesterable mineral phases include: Olivine, Fe-oxides, clinopyroxene, hornblende, serpentine, plagioclase, orthopyroxene (talc excluded)

** The calculation does not take into account the fact that not all the product formed was stable carbonate

per annum can be stored (based on the 2 M HCl extraction for Fe and Mg). Complete extraction of Ca from plagioclase is responsible for 81 kt CO_2 per annum from the theoretical 600 kt. For a more ideal reaction where extraction reaches 90 % for Ca, 15 % for Fe, and 50 % for Mg, the available storage would be 272 kt per annum. Increasing plagioclase dissolution would have a much greater effect than increasing dissolution of Mg from orthopyroxene, as the carbonation efficiency is low for Mg (< 70 %) and high for Ca (< 90 %) investigated for Northam, BRPM, Impala, and Lonmin (Vögeli, 2012). Importantly, other PGM mines in the UG2 and Platreef can contain more or less plagioclase than Merensky.

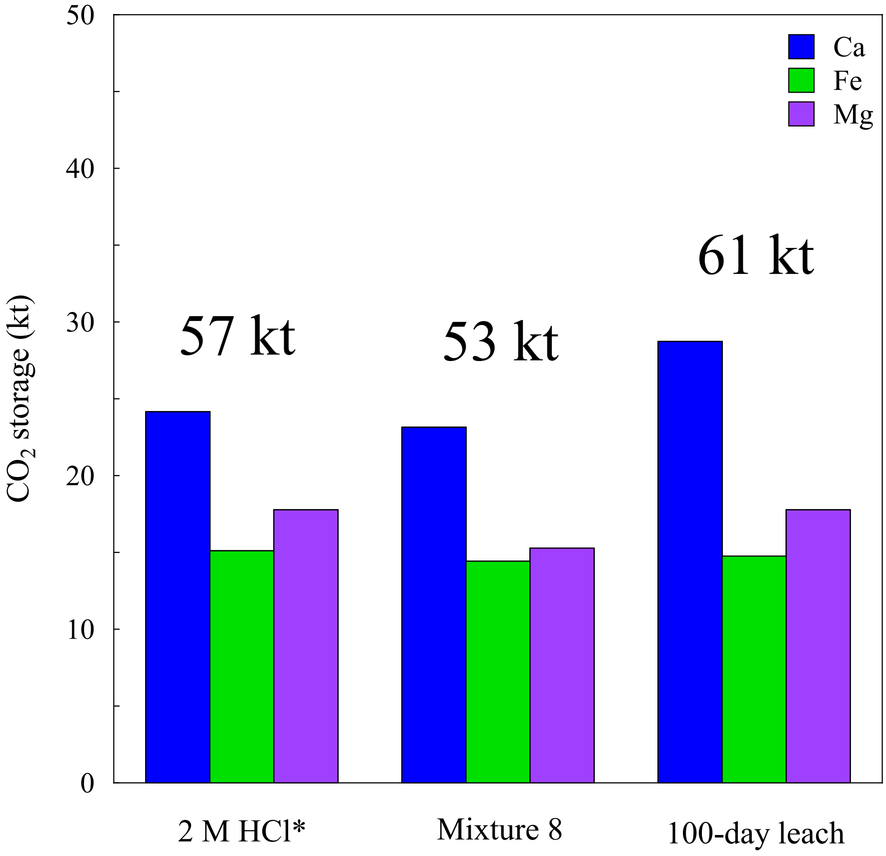

Figure 6.5: The total CO_2 sequestration capacity when the reactivity of the dissolution stage is taken into account. The total sequestration capacity is further divided into the cation responsible for the CO_2 storage.

Chapter 7

Conclusions and recommendations

This study explored the reactivity of pyroxene group minerals and the effect that its reactivity has on the dissolution of pyroxene-rich tailings for mineral carbonation. Merensky PGM tailings offer a relatively inexpensive, fine-grained alternative feedstock for carbon sequestration via mineral carbonation. The Mg-rich tailings could store large tonnages of anthropogenic CO_2; however the low reactivity of orthopyroxene limits the viability of this potential feedstock. Overcoming the rate limitation on pyroxene group minerals would be the foremost challenge for industrial mineral carbonation of these tailings. The objective of this study was to investigate the acid leach behaviour of pyroxene group minerals and pyroxene-rich PGM tailings, as a future potential resource for carbon dioxide sequestration by mineral carbonation. By comparing extraction percentages from dissolution reactions at varying conditions of solution chemistry, mineralogy, temperature, and particle size, an overall mechanism for pyroxene reactivity in pyroxene-rich feedstocks was defined.

Two phases of leach experiments were conducted to answer they key question which are outlined at the end of Chapter 2. The first phase of leach experiments on pyroxene-rich PGM tailings addressed the effect of solution chemistry on the dissolution of silicate minerals by the addition of organic acids. Solid residues from an extended 100-day leach experiment identified the reactive minerals in the tailings and highlighted the unreactive nature of the orthopyroxene. A second phase of leach experiments on pure pyroxene group minerals investigated the effects of particle size and temperature dependence on pyroxene dissolution. Again, analysis of solid residues of the reacted pyroxene minerals highlighted the reaction kinetics during mineral dissolution and the surface features of reacted grains gave insight into the mechanism of pyroxene dissolution.

This chapter begins with a summary of the major findings from the discussion (Chapter 6), followed by concluding remarks on a general approach to improve the viability of CCMC with mine tailings. This is followed by multiple recommendations for future work on pyroxene mineral dissolution.

7.1 Summary of key research findings.

The addition of organic chelators increases the dissolution of silicate minerals by increasing the apparent solubility of Si in solution, and by the addition of the ligand-promoted dissolution mechanism. Organic acids increase the dissolution rates of minerals by increasing the apparent solubility of the cation in solution; and organic ligands complex with the metal cations at the reaction surface to facilitate their removal. The results of this study showed that the addition of oxalic acid resulted in higher Si extraction from the pyroxene-rich tailings, which indicated the formation of Si-complexes. The addition increased the apparent Si solubility in a low-concentration mineral acid up to ten times when compared to a high-concentration of the same mineral acid. Previous studies indicated that the addition of organic acids would be most beneficial at near-neutral pH where the effect of the proton-promoted dissolution is smallest; but the results from this study reflected the positive effects of oxalic acid under acidic conditions (pH$\sim$1). With regard to the pyroxene-rich PGM tailings, plagioclase is the major host of Ca and the addition of oxalic acid results in similar Ca extraction of but at lower mineral acid concentration and pH. Complete extraction of Ca from plagioclase is responsible for 81 kt of the theoretical 600 kt CO_2 storage capacity of the PGM tailings sample investigated. In addition, it also increases the overall extraction of Si from 0.72 % to 6.4 %.

An increase in temperature and a decrease in particle size increases the dissolution of silicate minerals by decreasing the activation energy, and imparting physical defects on grains, respectively. An increase in temperature from ambient temperature to 70 °C and a decrease in particle size fraction from +75/-106 μm to -38 μm reduced the energy required (apparent activation energy) for the dissolution reaction to overcome the minimum energy needed to proceed at a statistically significant rate. Calculations showed that the apparent activation energy of enstatite was less for the -38 μm size fraction (27 kJ.mol^{-1}) when compared to the +75/-106 μm size fraction (66 kJ.mol^{-1}). These calculated activation energies were also much lower than the 80 kJ.mol^{-1} calculated from surface reaction models. Size reduction of the pyroxene samples by grinding imparts structural defects on the grains. The decrease in particle size thus increased the reactivity of pyroxene through both the increase in surface area and through the addition of surface roughness from structural defects as the grains preferentially break along the cleavage planes, creating jagged corners. As the dissolution of pyroxene is reaction-limited, the creation of more sites of high-energy increased the reactivity of the sample. This is important for the pyroxene group minerals, where dissolution is cleavage-controlled. The pyroxene-rich PGM tailings are already finely milled to extract PGEs in the beneficiation process, and the milling not only increases the surface area of the grains but also imparts structural defects on the grains, which increases the pyroxene mineral's reactivity.

The size and chemistry of the cation plays an important role in the reactivity of same-silicate minerals. For the pyroxene group, this results in the greater reactivity of pyroxenoids over pyroxenes and the greater reactivity of clinopyroxenes over orthopyroxenes. The order of reactivity for the pyroxenes investigated was: wollastonite $>$ diopside = augite $>$ enstatite. The reactivity of the pyroxene group is dependent on a combination of size and chemistry of the cations in the M1 and M2 sites. The chemistry of the cation is responsible for the electronegativity difference of the M-O bond, which changes for each cation (e.g. Ca, Fe, Mg); and the size of the cation distorts the length of the M-O bond. In orthopyroxenes, the M1 and M2 cations (Mg and Fe) are small and have 6-fold coordination. However, in clinopyroxenes, the inclusion of a larger cation (usually Ca) distorts the coordination of the M2 cation from 6- to 8-fold coordination. The pyroxenoid wollastonite includes two large cations which twists the silicate chain to accommodate the added strain. This results in a reactive mineral and an increased unit cell length. The effects of the cations in a mineral with respect to their chemistry and size can be described by the Madelung site energy. The Madelung site energy of the M2 site in pyroxenes is less than the M1 site, which results in preferential release of cations from the larger M2 site over the M1 site. The preferential release of the M2 cation results in nonstoichiometric dissolution of the pyroxene and a leachate solution that is rich in cations. Therefore feedstocks with Ca-rich pyroxenes will be more reactive than their orthopyroxene counterparts.

The dissolution of pyroxene group minerals is cleavage-controlled. Acidic dissolution of pyroxene group minerals is cleavage-controlled and follows a protonation reaction. The cleavage of the pyroxene exposes the weaker-bonded M2 cation and is therefore preferentially removed. This results in an initially incongruent dissolution reaction, but the reaction is governed by the presence and orientation of the cleavage. Therefore the complete silicate structure must be removed before the underlying layers can be reacted, which results in an overall congruent reaction. The strongly bonded bridging oxygens of the Si-O tetrahedra chain cause the overall reaction to be slow. The dissolution of pyroxene group minerals is reaction-limited and there is no formation of a leached layer on the surface of the surface of the grain, except for wollastonite, where Si precipitated on the surface of the grain.

The dissolution of pyroxene-rich PGM tailings can be increased by the addition of organic acids, an increase in temperature, and a decrease in particle size. The dissolution of the pyroxene minerals increased with an increase in temperature and a decrease in particle size over the ranges investigated. The dissolution of Ca from plagioclase also increased with the addition of oxalic acid. Orthopyroxene and plagioclase are the major sources of Mg and Ca in the PGM tailings, respectively. As the majority of the Mg extracted from the PGM tailings was from the dissolution of clinopyroxene and to a minor extent from the other Mg minerals. Almost no Mg was leached from the orthopyroxene. The majority of Ca was leached from plagioclase, with $\sim$30 % Ca extracted and between 30 % and 60 % of the plagioclase removed. The plagioclase reacted well in the presence of oxalate because of oxalate's affinity for Ca, and Al, which occupies half the Si sites in the plagioclase mineral structure. Of the calculated 600 kt of CO_2 storage capacity from the pyroxene-rich PGM tailings, the Ca from plagioclase is responsible for 81 kt of CO_2 storage. The addition of organic acids has shown to increase the extraction of Ca, especially from plagioclase, at ambient temperature in a solution of weak acids. Therefore an engineered reaction suited to plagioclase dissolution would greatly increase the overall mineral carbonation rates.

7.2 Concluding remarks: A general approach to increasing the dissolution of pyroxene-rich PGM tailings

From the results, the following hypothesis is true: *For any given silicate mineral, the kinetics of dissolution can be enhanced through manipulation of key influencing parameters. Specifically: by increasing temperature which provides the activation energy, by decreasing particle size which increases the surface area, and by the addition of chelating organic acids which increases the apparent solubility of cations in solution.* The reactions on pyroxene-rich PGM tailings show a distinct increase in Ca and Si extraction when oxalic acid (organic acid) is in the solution as it increases the solubility of Si. Coupled with the use of organic acids, an increase in temperature and a decrease in particle size does increase the extraction of cations from pyroxene group minerals because in addition to an increase in surface area, grinding can produce a number of high energy sites on the surfaces of mineral grains.

The second hypothesis is also true: *In the pyroxene group, clinopyroxenes are more reactive than orthopyroxenes because the addition of a larger cation in the M2 site decreases the activation energy by increasing the metal-oxygen bond length.* The nature of the cation is solely responsible for the reactivity between the pyroxene group minerals. The inclusion of the larger cation distorts the stable octahedral coordination of the pyroxene structure, which makes it more reactive.

Therefore, the reaction rate of pyroxene dissolution can be increased by the increase in temperature and a decrease in particle size. The increase in temperature lowers the activation energy of the mineral, which increases the reaction; and the decrease in particle size increases the amount of high-energy sites. Importantly, the addition of organic acids increases the solubility of Si, and thus aids in silicate mineral dissolution. The organic acids will also increase the dissolution of Ca from plagioclase and target Ca-rich pyroxenes in the tailings. The decrease in particle size and increase in structural irregularities from the upstream milling process, creates high-energy surface sites, and no further size reduction is needed.

7.3 Recommendations

This section details the recommendations for future projects on the dissolution aspect of mineral carbonation studies. These recommendations are put forward and a brief comment for each idea is mentioned.

The use of other organic chelating acids and staged leaching with mineral and organic acids can optimise the dissolution of pyroxene-rich tailings to achieve maximum Ca and Mg extraction. Other authors have studied the effect of other organic acids on silicate mineral dissolution, such as catechol as it too forms a complex with Si. These studies have been limited to olivine and serpentine, and the effect of the complex formation on the mineral surface. However, it is the effect of increased Si solubility that has increased the dissolution of pyroxene-rich tailings. More information is needed on the differences between the organic acids and what effect organic acids have on mineral dissolution when they complex other ions in solution. Organic acids can also be used in these pyroxene-rich tailings to remove Ca before a stronger mineral acid (H_2SO_4) is used to leach the Mg from orthopyroxene. Sulphuric acid has had much success in leaching Mg from serpentine, but it forms gypsum with Ca, which renders the leached Ca useless for mineral carbonation; therefore a multiple-stage leached could be used to optimise the extraction of Ca, Fe, and Mg from each mineral for 100 % dissolution. In addition, acid produced from water contaminated with sulphuric mine wastes (acid rock drainage, ARD) can be neutralised by reaction with pyroxene-rich tailings. Once the Ca is removed from the tailings with organic chelating acids (which can be produced by microbes), ARD can further leach Mg and Fe from the tailings; thereby neutralising ARD, and sequestering anthropogenic CO_2. A further benefit of this ARD-PGM process is that the gold and coal mines that produce ARD and Bushveld PGM tailings are situated $\sim$120 km apart and in a high industrial area with a large production of CO_2.

Calculation of the kinetic reaction parameters (e.g. rate, rate constant, activation energy) for the dissolution of pyroxene would improve the understanding of the pyroxene reaction mechanism for improved pyroxene reactivity. The activation energy of dissolution of pyroxene group minerals varies between studies because of the inaccuracy in the calculated rate of extraction (especially for diopside). A better understanding of the differences between activation energy and reaction rates between the pyroxene group minerals would enhance the understanding of the reaction kinetics and the role organic and mineral acids have on the dissolution of pyroxenes. Reaction rates of diopside and enstatite along each crystallographic axes would confirm the proposed cleavage-controlled dissolution reaction for pyroxene and would also confirm the stoichiometric or nonstoichiometric nature of pyroxene dissolution. The decrease in particle size increased the extraction of cations from pyroxene but the larger size fraction had the greatest dependence on the increase in temperature. Therefore the increase in surface defects imparted by grinding increases the minerals reactivity. An investigation on how the structural defects of pyroxene crystals increases the reaction rate should be conducted. It is also important to know what types of grinding creates the most number of high-energy surface sites. These grinding techniques should be used as they will increase the extraction of cations from pyroxene-rich tailings for mineral carbonation.

An investigation into the mineralogy of other mine tailings The variety of minerals mined over South Africa, has created diverse historic and current tailings deposits around the country. As noted in Chapter 1, these tailings can include serpentine, but are mainly pyroxene-rich; and Ca-rich pyroxenes such as diopside and wollastonite are abundant. The silicate minerals in the tailings have already been brought to the surface and undergone particle size reduction, making them ideal for mineral carbonation. Furthermore, the carbonation process can take place with mineral extraction or a secondary enhanced mineral extraction process. This process would be important for historic tailings, where the beneficiation process may leave valuable product in the tailings. For Bushveld PGM tailings, the extraction of cations for subsequent carbonation could be grouped with enhanced PGM recovery to alleviate the costs of heating and reagents.

References

Alexander, G., Mercedes Maroto-Valer, M., and Gafarova-Aksoy, P. (2007). Evaluation of reaction variables in the dissolution of serpentine for mineral carbonation. *Fuel*, *86*(1-2), 273–281.

Anbeek, C. (1992). Surface roughness of minerals and implications for dissolution studies. *Geochimica et Cosmochimica Acta*, *56*, 1461–1469.

Awad, A., van Groos, A. F., and Guggenheim, S. (2000). Forsteritic olivine: effect of crystallographic direction on dissolution kinetics. *Geochimica et Cosmochimica Acta*, *64*(10), 1765–1772.

Badyga, J., Henczka, M., and Sokolnicka, K. (2010). Utilization of carbon dioxide by chemically accelerated mineral carbonation. *Materials Letters*, *64*(6), 702–704.

Bales, R. and Morgan, J. (1985). Dissolution kinetics of chrysotile at pH 7 to 10. *Geochimica et Cosmochimica Acta*, *49*(11), 2281–2288.

Barker, W. W., Welch, S. A., and Banfield, J. F. (1997). Biogeochemical weathering of silicate minerals. *Reviews in Mineralogy and Geochemistry*, *35*(1), 391–428.

Bennett, P. C. and Casey, W. H. (1994). *Chemistry and Mechanisms of low-temperature dissolution of silicates by organic acids*. Springer-Verlag New York.

Berg, A. and Banwart, S. (2000). Carbon dioxide mediated dissolution of Ca-feldspar: implications for silicate weathering. *Chemical Geology*, *163*(1-4), 25–42.

Berner, R. A. (1978). Rate control of mineral dissolution under earth surface conditions. *American Journal of Science*, *278*(9), 1235–1252.

Berner, R. A., Sjöberg, E. L., Velbel, M. A., and Krom, M. D. (1980). Dissolution of pyroxenes and amphiboles during weathering. *Science*, *207*(4436), 1205–1206.

Boden, T., Marland, G., and Andres, R. (2011). Global, regional, and national fossil-fuel CO_2 emissions. Technical report.

Bonfils, B., Bourgeois, F., Julcour, C., Guyot, F., and Chiquet, P. (2011). Understanding the chemistry of direct aqueous carbonation with additives through geochemical modelling. *Energy Procedia*, *4*, 3809–3816.

Bonfils, B., Julcour-Lebigue, C., Guyot, F., Bodénan, F., Chiquet, P., and Bourgeois, F. (2012). Comprehensive analysis of direct aqueous mineral carbonation using dissolution enhancing organic additives. *International Journal of Greenhouse Gas Control*, *9*, 334–346.

Brady, P. V. and Walther, J. V. (1989). Controls on silicate dissolution rates in neutral and basic pH solutions at 25 °C. *Geochimica et Cosmochimica Acta*, *53*(11), 2823–2830.

Brantley, S. L. (2003). Reaction kinetics of primary rock-forming minerals under ambient conditions. *Treatise on geochemistry*, *5*, 73–117.

Brantley, S. L. (2008). Kinetics of mineral dissolution. In S. L. Brantley, J. D. Kubicki, and A. F. White (Eds.), *Kinetics of water-rock interaction*, Chapter 5, 151–210. Springer.

Cameron, M. and Papike, J. J. (1980). Crystal chemistry of silicate pyroxenes. *Reviews in Mineralogy*, *7*.

Cameron, M. and Papike, J. J. (1981). Structural and chemical variations in pyroxenes. *American Mineralogist*, *66*, 1–50.

CarbFix (2010). CarbFix Annual Status Report. Technical report.

Carroll, D. (1970). *Rock weathering*. New York: Plenum Press.

Casey, W. H. and Ludwig, C. (1995). Silicate mineral dissolution as a ligand-exchange reaction. *Reviews in Mineralogy and Geochemistry*, *31*(1), 87–117.

Casey, W. H. and Sposito, G. (1992). On the temperature dependence of mineral dissolution rates. *Geochimica et Cosmochimica Acta*, *56*(10), 3825–3830.

Casey, W. H., Westrich, H. R., Banfield, J. F., Ferruzzi, G., and Arnold, G. W. (1993). Leaching and reconstruction at the surfaces of dissolving chain-silicate minerals. *Nature*, *366*(6452), 253–256.

Cawthorn, R. G. and Boerst, K. (2006). Origin of the pegmatitic pyroxenite in the Merensky unit, Bushveld Complex, South Africa. *Journal of Petrology*, *47*(8), 1509–1530.

Chen, Y. and Brantley, S. L. (1998). Diopside and anthophyllite dissolution at 25 °C and 90 °C and acid pH. *Chemical Geology*, *147*(3-4), 233–248.

Chen, Y. and Brantley, S. L. (2000). Dissolution of forsteritic olivine at 65 °C and $2 < \text{pH} < 5$. *Chemical Geology*, *165*(3-4), 267–281.

Cloete, M. (2010). Atals on geological storage for carbon dioxide in South Africa. Technical report, Council for Geoscience.

Daval, D., Sissmann, O., Menguy, N., Saldi, G. D., Guyot, F., Martinez, I., Corvisier, J., Garcia, B., Machouk, I., Knauss, K. G., and Hellmann, R. (2011). Influence of amorphous silica layer formation on the dissolution rate of olivine at 90 °C and elevated pCO_2. *Chemical Geology*, *284*(1-2), 193–209.

Deer, W. A., Howie, R. A., and Zussman, J. (1978). *Rock-forming minerals, Volume 2A: Single-chain silicates* (2nd ed.). The Geological Society.

Deer, W. A., Howie, R. A., and Zussman, J. (1992). *An introduction to the rock-forming minerals*. Longman Scientific and Technical.

DeVore, G. W. (1955). Crystal growth and the distribution of elements. *The Journal of Geology*, 471–494.

Dipple, G. M., Southam, G., Wilson, S., Thom, J., and Power, I. M. (2005). Carbon sequestration in mine tailings. Technical report, Diavik Diamond Mine, Inc.

Doucet, F. (2011). Scoping Study on CO_2 Mineralization Technologies. Technical report.

Drever, J. I. and Stillings, L. L. (1997). The role of organic acids in mineral weathering. *Colloids and Surfaces A: Physicochemical and Engineering Aspects*, *120*(1), 167–181.

Fagerlund, J., Nduagu, E., Romão, I., and Zevenhoven, R. (2010). A stepwise process for carbon dioxide sequestration using magnesium silicates. *Frontiers of Chemical Engineering in China*, *4*(2), 133–141.

Fouda, M. F. R., Amin, R. E.-S., and Abd-Elzaher, M. M. (1996). Extraction of magnesia from Egyptian serpentine ore via reaction with different acids: I. reaction with sulfuric acid.

Furrer, G. and Stumm, W. (1986). The coordination chemistry of weathering: I. Dissolution kinetics of δ-Al_2O_3 and BeO. *Geochimica et Cosmochimica Acta*, *50*(9), 1847–1860.

Goldich, S. S. (1938). A study in rock-weathering. *The Journal of Geology*, 17–58.

Golubev, S. V. and Pokrovsky, O. S. (2006). Experimental study of the effect of organic ligands on diopside dissolution kinetics. *Chemical Geology*, *235*(3-4), 377–389.

Grandstaff, D. E. (1978). Changes in surface area and morphology and the mechanism of forsterite dissolution. *Geochimica et Cosmochimica Acta*, *42*(12), 1899–1901.

Gustafsson, J. P. (2011). Visual MINTEQ 3.0 user guide. Technical report.

Hellmann, R., Penisson, J.-M., Hervig, R. L., Thomassin, J.-H., and Abrioux, M.-F. (2003). An EFTEM/HRTEM high-resolution study of the near surface of labradorite feldspar altered at acid pH: evidence for interfacial dissolution-reprecipitation. *Physics and Chemistry of Minerals*, *30*(4), 192–197.

Hietkamp, S., Engelbrecht, A., Scholes, B., and Golding, A. (2004). Carbon capture and storage in South Africa. *CSIR*, 1–7.

Hochella, M. (1995). Mineral surfaces: their characterization and their chemical, physical and reactive nature. *Mineral Surfaces*, 17–60.

Hochella, M. F., Lower, S. K., Maurice, P. A., Penn, R. L., Sahai, N., Sparks, D. L., and Twining, B. S. (2008). Nanominerals, mineral nanoparticles, and Earth systems. *science*, *319*(5870), 1631–1635.

Holdren, G. R. and Berner, R. A. (1979). Mechanism of feldspar weatheringI. Experimental studies. *Geochimica et Cosmochimica Acta*, *43*(8), 1161–1171.

Huang, W. H. and Keller, W. D. (1970). Dissolution of rock-forming silicate minerals in organic acids: simulated first-stage weathering of fresh mineral surfaces. *The American Mineralogist*, *55*, 2076–2094.

Huijgen, W. J. J. and Comans, R. N. J. (2003). Carbon dioxide sequestration by mineral carbonation. *Energy*, *ECN-C–03-*(February), 1–52.

Jonckbloedt, R. C. L. (1998). Olivine dissolution in sulphuric acid at elevated temperatures–implications for the olivine process, an alternative waste acid neutralizing process. *Journal of Geochemical Exploration*, *62*(1-3), 337–346.

Juhász, Z. (1998). Colloidal-chemical aspects of mechanical activation. *Particulate Science and Technology: An International Journal*, *16*(2), 145–161.

Kalinkina, E. V., Kalinkin, A. M., Forsling, W., and Makarov, V. N. (2001). Sorption of atmospheric carbon dioxide and structural changes of Ca and Mg silicate minerals during grinding: I. Diopside. *International journal of mineral processing*, *61*(4), 273–288.

Kehew, A. E. (2001). *Applied chemical hydrogeology*. Prentice Hall.

Kelemen, P. B. and Matter, J. (2008). In situ carbonation of peridotite for CO_2 storage. *Proceedings of the National Academy of Sciences*, *105*(45), 17295–17300.

Klein, C. and Dana, J. D. (2007). *The manual of mineral science*. John Wiley and Sons, Inc.

Knauss, K. G., Nguyen, S., and Weed, H. (1993). Diopside dissolution kinetics as a function of pH, CO_2, temperature, and time. *Geochimica et Cosmochimica Acta*, *57*, 285–294.

Krauskopf, K. B. (1967). *Introduction to Geochemistry* (2nd ed.). New York: McGraw-Hill International.

Krevor, S. and Lackner, K. (2009). Enhancing process kinetics for mineral carbon sequestration. *Energy Procedia*, *1*(1), 4867–4871.

Kump, L. R., Brantley, S. L., and Arthur, M. A. (2000). Chemical weathering, atmospheric CO_2, and climate. *Annual Review of Earth and Planetary Science*, *28*, 611–667.

Lackner, K. (2002). Carbonate Chemistry for Sequestering Fossil Carbon. *Annual Review of Energy and the Environment*, *27*(1), 193–232.

Lackner, K., Joyce, E., Sharp, D., Butt, D., and Wendt, C. (1995). Carbon dioxide disposal in carbonate minerals. *Energy*, *20*(I), 1153–1170.

Lasaga, A. C. (1984). Chemical kinetics of water-rock interactions. *Journal of Geophysical Research*, *89*(B6), 4009–4025.

Lasaga, A. C. (1995). Fundamental approaches in describing mineral dissolution and precipitation rates. *Reviews in Mineralogy and Geochemistry*, *31*(1), 23–86.

Levenspiel, O. (1999). *Chemical reaction engineering* (3rd ed.). New York: John Wiley and Sons.

Liu, Y., Olsen, A. A., and Rimstidt, J. D. (2006). Mechanism for the dissolution of olivine series minerals in acidic solutions. *American Mineralogist*, *91*, 455–458.

Luce, R., Barlett, R., and Parks, G. (1972). Dissolution kinetics of magnesium silicates. *Geochimica et Cosmochimica Acta*, *36*(1), 35–50.

Mast, M. A. and Drever, J. I. (1987). The effect of oxalate on the dissolution rates of oligoclase and tremolite. *Geochimica et Cosmochimica Acta*, *51*(9), 2559–2568.

Mazzotti, M., Abanades, J., and Allam, R. (2005). Mineral carbonation and industrial uses of carbon dioxide. Technical report, IPCC.

Melline, M. (1982). The crystal structure of lizardite 1T: hydrogen bonds and polytypism. *American Mineralogist*, *67*, 587–598.

Meyer, N., Vögeli, J., Becker, M., Broadhurst, J., Reid, D. L., and Franzidis, J.-P. (2014). Mineral carbonation of PGM mine tailings for CO_2 storage in South Africa: A case study. *Minerals Engineering*, *59*, 45–51.

Misra, K. C. (2012). *Introduction to geochemistry: principles and applications* (1st ed.). Chichester, West Sussex: Wiley-Blackwell.

Noack, Y., Colin, F., Nahon, D., Delvigne, J., and Michaux, L. (1993). Secondary-mineral formation during natural weathering of pyroxene: review and thermodynamic approach. *American Journal of Science*, *293*, 111–134.

O'Connor, W. K., Dahlin, D. C., Nilsen, D., Rush, G., Walters, R., and Turner, P. (2001). Carbon dioxide sequestration by direct mineral carbonation: results from recent studies and current status. In *First National Conference on Carbon Sequestration*, Washington. National Energy Technology Laboratory, U.S. Department of Energy.

O'Connor, W. K., Dahlin, D. C., Rush, G., Gerdemann, S. J., Penner, L. R., and Nilsen, D. (2005). Aqueous mineral carbonation: Mineral availability, pretreatment, reaction parametrics and process studies. Technical report, Office of Process Development National Energy Technology Laboratory.

Oelkers, E. H. (2001). An experimental study of forsterite dissolution rates as a function of temperature and aqueous Mg and Si concentrations. *Chemical Geology*, *175*(3-4), 485–494.

Oelkers, E. H. and Schott, J. (2001). An experimental study of enstatite dissolution rates as a function of pH, temperature, and aqueous Mg and Si concentration, and the mechanism of pyroxene/pyroxenoid dissolution. *Geochimica et Cosmochimica Acta*, *65*(8), 1219–1231.

Ohashi, Y. and Burnham, C. W. (1972). Electrostatic and repulsive energies of the M1 and M2 cation sites in pyroxenes. *Journal of Geophysical Research*, *77*(29), 5761–5766.

Olajire, A. A. (2013). A review of mineral carbonation technology in seqestration of CO_2. *Journal of Petroleum Science and Engineering*, *109*, 364–392.

Ollier, C. D. (1969). *Weathering*. Edinburgh: Oliver and Boyd.

Paktunc, A. D. (1999). Characterization of mine wastes for prediction of acid mine drainage. In J. M. Azcue (Ed.), *Environmental impacts of mining activities*, Chapter 3, 19–40. Berlin/Heidelberg: Springer-Verlag.

Park, A.-H. A. and Fan, L.-S. (2004). Mineral sequestration: Physically activated dissolution of serpentine and pH swing process. *Chemical Engineering Science*, *59*(22-23), 5241–5247.

Park, A.-H. A., Jadhav, R., and Fan, L.-S. (2003). CO_2 mineral sequestration: chemically enhanced aqueous carbonation of serpentine. *Canadian Journal of Chemical Engineering*, *81*(August), 885–890.

Pauling, L. (1980). The nature of silicon-oxygen bonds. *American Mineralogist*, *65*, 321–323.

Penner, L. R., O'Connor, W. K., Dahlin, D. C., Gerdemann, S. J., and Rush, G. (2003). Mineral carbonation: energy costs of pretreatment options and insights gained from flow loop reaction studies. Technical report, Albany Research Center.

Poocharoen, B. (1972). *Reaction of aqueous catechol solutions with minerals*. Msc, Portland State University.

Poulson, S. R., Drever, J. I., and Stillings, L. L. (1997). Aqueous Si-oxalate complexing, oxalate adsorption onto quartz, and the effect of oxalate upon quartz dissolution rates. *Chemical Geology*, *140*(1-2), 1–7.

Prigiobbe, V., Hänchen, M., Werner, M., Baciocchi, R., and Mazzotti, M. (2009). Mineral carbonation process for CO_2 sequestration. *Energy Procedia*, *1*(1), 4885–4890.

Prigiobbe, V. and Mazzotti, M. (2011). Dissolution of olivine in the presence of oxalate, citrate, and CO_2 at 90 °C and 120 °C. *Chemical Engineering Science*, *66*(24), 6544–6554.

Putnis, C. V. and Ruiz-Agudo, E. (2013). The mineral-water interface: where minerals react with the environment. *Elements*, 177–182.

Ramberg, H. (1952). Chemical bonds and distribution of cations in silicates. *The Journal of Geology*, *60*(4), 331–355.

Schott, A. and Berner, R. A. (1985). Dissolution mechanisms of pyroxene and olivine during weathering. In J. I. Drever (Ed.), *The chemistry of weathering*, 35–53. Springer.

Seabrook, C. L. (2005). *The Upper Critical and Lower Main Zones of the eastern Bushveld Complex*. Phd, University of the Witwatersrand.

Silberberg, M. S. (2011). *Chemistry: molecular nature of matter and change* (6th ed.). New York: McGraw-Hill Higher Education.

Sipilä, J., Teir, S., and Zevenhoven, R. (2008). Carbon dioxide sequestration by mineral carbonation: Literature review update 2005–2007. *Åbo Akademi Rep. VT*, *1*.

Stat-Ease Inc (2010). Design Expert 8.

Teir, S., Revitzer, H., Eloneva, S., Fogelholm, C.-J., and Zevenhoven, R. (2007). Dissolution of natural serpentinite in mineral and organic acids. *International Journal of Mineral Processing*, *83*(1-2), 36–46.

Terry, B. (1983). The acid decomposition of silicate minerals part I. Reactivities and modes of dissolution of silicates. *Hydrometallurgy*, *10*(2), 135–150.

Torróntegui, M. D. (2010). *Assessing the Mineral Carbonation Science and Technology*. Msc, Swiss Federal Institute of Technology, Zürich, Switzerland.

Velbel, M. A. (1993). Formation of protective surface layers during silicate-mineral weathering under well-leached, oxidizing conditions. *American Mineralogist*, *78*, 405.

Vögeli, J. (2012). *Investigation of the potential for mineral carbonation of PGM tailings in South Africa*. Msc, University of Cape Town, South Africa.

Vögeli, J., Reid, D., Becker, M., Broadhurst, J., and Franzidis, J.-P. (2011). Investigation of the potential for mineral carbonation of PGM tailings in South Africa. *Minerals Engineering*, *24*(12), 1348–1356.

Weissbart, E. J. and Rimstidt, J. D. (2000). Wollastonite: Incongruent dissolution and leached layer formation. *Geochimica et Cosmochimica Acta*, *64*(23), 4007–4016.

Welch, S. A. and Ullman, W. J. (1993). The effect of organic acids on plagioclase dissolution rates and stoichiometry. *Geochimica et Cosmochimica Acta*, *57*(12), 2725–2736.

Wiederhold, J., Kraemer, S., Teutsch, N., Borer, P., Halliday, A., and Kretzschmar, R. (2006). Iron isotope fractionation during proton-promoted, ligand-controlled, and reductive dissolution of goethite. *Environmental science and technology*, *40*, 3787–3793.

Wieland, E., Wehrli, B., and Stumm, W. (1988). The coordination chemistry of weathering: III. A generalization on the dissolution rates of minerals. *Geochimica et Cosmochimica Acta*, *52*(8), 1969–1981.

Willis, J. (1999). Instramental parameters and data quality for routine major and trace element determination by WDXRFS. Technical report, Department of Geological Sciences, University of Cape Town, Cape Town.

Willis, J. P. and Duncan, A. R. (2008). *Understanding XRF Spectrometry: Basic concepts and instrumentation*. Understanding XRF Spectrometry. PANalytical.

Winkler, H., Spalding-Fecher, R., Mwakasonda, S., and Davidson, O. (2002). Sustainable development policies and measures. *Options for Protecting the Climate, World Resource Institute, Washington DC*.

Wogelius, R. and Walther, J. V. (1991). Olivine dissolution at 25 °C: Effects of pH, CO_2, and organic acids. *Geochimica et Cosmochimica Acta*.

Zakaznova-Herzog, V., Nesbitt, H., Bancroft, G., and Tse, J. (2008). Characterization of leached layers on olivine and pyroxenes using high-resolution XPS and density functional calculations. *Geochimica et Cosmochimica Acta*, *72*(1), 69–86.

Zevenhoven, R. (2011). CO_2 mineral sequestration: developments toward large-scale application. *Greenhouse Gasses: Science and Technology*, *57*, 48–57.

Appendix A

Calculations

A.1 Pyroxene composition

Table A.1: Pyroxene composition calculation from Deer *et al.* (1992, p678) for enstatite sample.

	Mass[1]	wt.% oxides	Prop. ox[2]	Atm. prop. ox[3]	No. anions[4]		No. ions[5]	
SiO_2	60.02	55.48	0.9243	1.8487	3.9174	Si	1.959	
Al_2O_3	101.96	1.20	0.0117	0.0352	0.0746	Al	0.050	
TiO_2	79.88	0.12	0.0015	0.0029	0.0062	Ti	0.003	2.01*
FeO	71.85	10.59	0.1474	0.1474	0.3124	Fe	0.312	
MnO	70.94	0.25	0.0035	0.0035	0.0073	Mn	0.007	
MgO	40.30	30.87	0.7661	0.7661	1.6235	Mg	1.623	1.94**
CaO	56.08	1.02	0.0181	0.0181	0.0385	Ca	0.038	
Na_2O	61.98	0.02	0.0003	0.0003	0.0007	Na	0.001	
K_2O	94.20		0.0000	0.0000	0.0000	K	0.000	
Cr_2O_3	151.99	0.46	0.0030	0.0091	0.0194	Cr	0.013	
TOTAL		99.26		2.8314	6		4.008	

[1] Molecular mass

[2] Molecular proportion of oxides

[3] Atomic proportion of oxygen from each molecule

[4] Number of anions on a basis of 6 oxygens

[5] Number of ions in formula

*Number of cations in Si site (includes Si, Al, and Ti)

**Number of cations in M1 and M2 site (includes rest of cations)

A.2 Cation and mineral mass balance

Table A.2: Cation and minerals mass balance calculations for the pyroxene-rich PGM tailings. Cation mass balance calculated on XRF data in Table B.1 and Table D.1; and mineral mass balance calculated on QEMSCAN data in Table B.4 and Table D.2. Start mass = 9.9995 g and residue mass = 9.2113 g.

Oxide	**Prop. in Feed (wt.%)**	**Mass in Feed (g)**	**Prop. in Residue (wt.%)**	**Mass in Residue (g)**	**Mass in Leachate (g)**	**Extent of Reaction (%)**
SiO_2	51.88	5.19	53.21	4.90	0.29	6
TiO_2	0.26	0.03	0.25	0.02	0.00	13
Al_2O_3	9.05	0.91	4.68	0.43	0.47	52
Fe_2O_3	10.96	1.10	11.37	1.05	0.05	4
MnO	0.17	0.02	0.19	0.02	0.00	2
MgO	19.30	1.93	21.65	1.99	−0.06	−3
CaO	5.79	0.58	3.85	0.35	0.22	39
Na_2O	0.85	0.09	0.82	0.08	0.01	12
K_2O	0.17	0.02	0.08	0.01	0.01	57
P_2O_5	0.04	0.00	0.03	0.00	0.00	35
SO_3	0.13	0.01	0.00	0.00	0.01	99
Cr_2O_3	1.02	0.10	1.07	0.10	0.00	3
NiO	0.10	0.01	0.08	0.01	0.00	22
Mineral	**Prop. in Feed (wt.%)**	**Mass in Feed (g)**	**Prop. in Residue (wt.%)**	**Mass in Residue (g)**	**Mass in Leachate (g)**	**Extent of Reaction (%)**
Sulfides	0.5	0.0	0.2	0.0	0.0	70
Olivine	0.3	0.0	1.2	0.1	−0.1	−317
Orthopyroxene	66.8	6.7	67.6	6.2	0.5	7
Clinopyroxene	5.2	0.5	4.4	0.4	0.1	23
Amphibole	2.9	0.3	3.9	0.4	−0.1	−25
Serpentine	0.0	0.0	0.0	0.0	0.0	75
Talc	1.0	0.1	3.9	0.4	−0.3	−255
Chlorite	0.9	0.1	0.3	0.0	0.1	74
Biotite/Phlogopite	0.9	0.1	0.1	0.0	0.1	91
Plagioclase	17.3	1.7	11.2	1.0	0.7	41
Quartz	0.9	0.1	3.1	0.3	−0.2	−237
Carbonates	0.2	0.0	0.0	0.0	0.0	97
Chromite	2.4	0.2	2.3	0.2	0.0	13
Fe oxides/Hydroxides	0.2	0.0	0.1	0.0	0.0	66

Table A.3: Cation and minerals mass balance calculations for enstatite. Cation mass balance calculated on XRF data in Table B.1 and Table D.1; and mineral mass balance calculated on QEMSCAN data in Table B.4 and Table D.2. Start mass = 9.8537 g and residue mass = 8.2613 g.

Oxide	**Prop. in Feed (wt.%)**	**Mass in Feed (g)**	**Prop. in Residue (wt.%)**	**Mass in Residue (g)**	**Mass in Leachate (g)**	**Extent of Reaction (%)**
SiO_2	53.77	5.30	55.25	4.56	0.73	14
TiO_2	0.12	0.01	0.11	0.01	0.00	25
Al_2O_3	1.73	0.17	1.57	0.13	0.04	24
Fe_2O_3	9.78	0.96	9.34	0.77	0.19	20
MnO	0.21	0.02	0.19	0.02	0.00	22
MgO	30.75	3.03	29.50	2.44	0.59	20
CaO	1.84	0.18	1.93	0.16	0.02	12
Na_2O	0.34	0.03	0.13	0.01	0.02	68
K_2O	0.03	0.00	0.01	0.00	0.00	72
P_2O_5	0.03	0.00	0.00	0.00	0.00	100
SO_3	0.00	0.00	0.00	0.00	0.00	100
Cr_2O_3	0.43	0.04	0.40	0.03	0.01	22
NiO	0.06	0.01	0.07	0.01	0.00	2
Mineral	**Prop. in Feed (wt.%)**	**Mass in Feed (g)**	**Prop. in Residue (wt.%)**	**Mass in Residue (g)**	**Mass in Leachate (g)**	**Extent of Reaction (%)**
Orthopyroxene	95.2	9.4	91.5	7.6	1.8	19
Clinopyroxene	1.5	0.2	1.7	0.1	0.0	7
Wollastonite	–	–	–	–	–	–
Fe-Mg alteration min.	0.4	0.0	0.6	0.1	0.0	−24
Other silicates	1.3	0.1	1.8	0.1	0.0	−15
Quartz	0.1	0.0	0.3	0.0	0.0	−269
Fe oxides	1.0	0.1	3.8	0.3	−0.2	−210

Table A.4: Cation and minerals mass balance calculations for augite. Cation mass balance calculated on XRF data in Table B.1 and Table D.1; and mineral mass balance calculated on QEMSCAN data in Table B.4 and Table D.2. Start mass = 10.0786 g and residue mass = 9.4712 g.

Oxide	**Prop. in Feed (wt.%)**	**Mass in Feed (g)**	**Prop. in Residue (wt.%)**	**Mass in Residue (g)**	**Mass in Leachate (g)**	**Extent of Reaction (%)**
SiO_2	46.77	4.71	49.77	4.71	0.00	0
TiO_2	1.35	0.14	1.41	0.13	0.00	2
Al_2O_3	2.55	0.26	2.52	0.24	0.02	7
Fe_2O_3	15.53	1.57	13.06	1.24	0.33	21
MnO	0.66	0.07	0.23	0.02	0.04	67
MgO	12.63	1.27	12.43	1.18	0.10	8
CaO	17.86	1.80	18.12	1.72	0.08	5
Na_2O	0.57	0.06	0.37	0.04	0.02	38
K_2O	0.06	0.01	0.06	0.01	0.00	14
P_2O_5	0.03	0.00	0.01	0.00	0.00	76
SO_3	0.17	0.02	0.04	0.00	0.01	75
Cr_2O_3	0.04	0.00	0.05	0.00	0.00	3
NiO	0.05	0.00	0.04	0.00	0.00	32
Mineral	**Prop. in Feed (wt.%)**	**Mass in Feed (g)**	**Prop. in Residue (wt.%)**	**Mass in Residue (g)**	**Mass in Leachate (g)**	**Extent of Reaction (%)**
Orthopyroxene	3.8	0.4	1.0	0.1	0.3	75
Clinopyroxene	77.0	7.8	49.1	4.7	3.1	40
Wollastonite	–	–	–	–	–	–
Fe-Mg alteration min.	10.3	1.0	14.5	1.4	−0.3	−32
Other silicates	2.6	0.3	17.4	1.6	−1.4	−518
Quartz	0.5	0.1	0.5	0.0	0.0	15
Fe oxides	5.1	0.5	16.9	1.6	−1.1	−210

Table A.5: Cation and minerals mass balance calculations for diopside. Cation mass balance calculated on XRF data in Table B.1 and Table D.1; and mineral mass balance calculated on QEMSCAN data in Table B.4 and Table D.2. Start mass = 10.4742 g and residue mass = 10.4095 g.

Oxide	**Prop. in Feed (wt.%)**	**Mass in Feed (g)**	**Prop. in Residue (wt.%)**	**Mass in Residue (g)**	**Mass in Leachate (g)**	**Extent of Reaction (%)**
SiO_2	52.28	5.48	54.33	5.66	−0.18	−3
TiO_2	0.21	0.02	0.23	0.02	0.00	−7
Al_2O_3	0.08	0.01	0.10	0.01	0.00	−25
Fe_2O_3	2.04	0.21	1.95	0.20	0.01	5
MnO	0.05	0.01	0.05	0.01	0.00	−7
MgO	18.17	1.90	17.56	1.83	0.07	4
CaO	24.05	2.52	24.03	2.50	0.02	1
Na_2O	0.27	0.03	0.18	0.02	0.01	35
K_2O	0.09	0.01	0.05	0.01	0.00	43
P_2O_5	0.04	0.00	0.01	0.00	0.00	84
SO_3	0.01	0.00	0.00	0.00	0.00	83
Cr_2O_3	0.06	0.01	0.07	0.01	0.00	−18
NiO	0.01	0.00	0.01	0.00	0.00	−7
Mineral	**Prop. in Feed (wt.%)**	**Mass in Feed (g)**	**Prop. in Residue (wt.%)**	**Mass in Residue (g)**	**Mass in Leachate (g)**	**Extent of Reaction (%)**
Orthopyroxene	–	–	–	–	–	–
Clinopyroxene	94.4	9.9	91.9	9.6	0.3	3.2
Wollastonite	–	–	–	–	–	–
Fe-Mg alteration min.	2.9	0.3	6.3	0.7	−0.3	−113.4
Other silicates	0.6	0.1	0.6	0.1	0.0	−0.2
Quartz	0.2	0.0	0.4	0.0	0.0	−57.9
Fe oxides	0.2	0.0	0.3	0.0	0.0	−84.3

Table A.6: Cation and minerals mass balance calculations for wollastonite. Cation mass balance calculated on XRF data in Table B.1 and Table D.1; and mineral mass balance calculated on QEMSCAN data in Table B.4 and Table D.2. Start mass = 10.2991 g and residue mass = 9.2238 g.

Oxide	**Prop. in Feed (wt.%)**	**Mass in Feed (g)**	**Prop. in Residue (wt.%)**	**Mass in Residue (g)**	**Mass in Leachate (g)**	**Extent of Reaction (%)**
SiO_2	49.20	5.07	54.67	5.04	0.02	0
TiO_2	0.09	0.01	0.06	0.01	0.00	34
Al_2O_3	1.24	0.13	1.19	0.11	0.02	14
Fe_2O_3	0.49	0.05	0.48	0.04	0.01	11
MnO	0.09	0.01	0.09	0.01	0.00	11
MgO	0.49	0.05	0.44	0.04	0.01	19
CaO	47.81	4.92	35.36	3.26	1.66	34
Na_2O	0.19	0.02	0.18	0.02	0.00	15
K_2O	0.08	0.01	0.10	0.01	0.00	−11
P_2O_5	0.08	0.01	0.06	0.01	0.00	31
SO_3	0.00	0.00	0.00	0.00	0.00	−305
Cr_2O_3	0.00	0.00	0.01	0.00	0.00	−629
NiO	0.00	0.00	0.01	0.00	0.00	−224
Mineral	**Prop. in Feed (wt.%)**	**Mass in Feed (g)**	**Prop. in Residue (wt.%)**	**Mass in Residue (g)**	**Mass in Leachate (g)**	**Extent of Reaction (%)**
Orthopyroxene	–	–	–	–	–	–
Clinopyroxene	1.6	0.2	2.6	0.2	−0.1	−46
Wollastonite	84.7	8.7	77.7	7.2	1.6	18
Fe-Mg alteration min.	0.8	0.1	5.8	0.5	−0.5	−559
Other silicates	6.9	0.7	10.1	0.9	−0.2	−31
Quartz	0.4	0.0	2.1	0.2	−0.2	−362
Fe oxides	–	–	–	–	–	–
Carbonates	4.4	0.5	1.0	0.1	0.4	79

A.3 Activation energy

Example of enstatite for the -38 μm sample:

$$\begin{aligned}
\text{Extraction rate} &= \text{Extent of dissolution } (\%) \div \text{Time (s)} \\
\text{r} &= 1.2\ \%\ \text{Mg} \div (48 \times 60 \times 60) \\
\text{r} &= 6.94 \times 10^{-6} \\
ln\,\text{r}\ &= -11.88 \\
\text{Equation of graph: } ln\,\text{r} &= \frac{E}{R}\cdot\frac{1}{T} + ln\,\text{k} \\
\text{Best-fit line: } ln\,\text{r} &= -3238.9\cdot\frac{1}{T} - 1.0536 \\
\therefore\ \frac{-E}{R} &= -3238.9,\ \text{where R is 8.314 J.mol}^{-1} \\
E &= 26\,928\ \text{J.mol}^{-1} \\
E &= 27\ \text{kJ.mol}^{-1}
\end{aligned}$$

Table A.7: Calculation of the activation energy of enstatite for the -38 μm and +75/-106 μm size fractions using the Arrhenius equation.

Temperature (°C)	Extraction (%)	Time (h)	Time (s)	r	ln r	Temperature (K)	1/T (K^{-1})
-38 μm							
25	1.2	48	172800	6.944×10^{-6}	-11.877	298	0.00336
40	1.8	48	172800	1.042×10^{-5}	-11.472	313	0.00319
70	4.9	48	172800	2.836×10^{-5}	-10.471	343	0.00292
+75/-106 μm							
25	0.25	48	172800	1.447×10^{-6}	-13.446	298	0.00336
40	0.9	48	172800	5.208×10^{-6}	-12.165	313	0.00319

Appendix B

Feed Mineralogy

B.1 XRF

Table B.1: Chemical mineralogy of samples determined by XRF.

Oxide	**Tailings**	**Enstatite**	**Augite**	**Diopside**	**Wollastonite**
SiO_2	51.90	53.77	46.77	52.28	49.20
TiO_2	0.26	0.12	1.35	0.21	0.09
$Al2O_3$	9.05	1.73	2.55	0.08	1.24
FeO*	9.86	9.78	15.53	2.04	0.49
MnO	0.18	0.21	0.66	0.05	0.09
MgO	19.30	30.75	12.63	18.17	0.49
CaO	5.79	1.84	17.86	21.75	47.67
Na_2O	0.85	0.34	0.57	0.27	0.19
K_2O	0.17	0.03	0.06	0.09	0.08
P_2O_5	0.04	0.03	0.03	0.04	0.08
SO_3	0.13	0.00	0.17	0.01	0.00
Cr_2O_3	1.02	0.43	0.04	0.06	0.00
NiO	0.10	0.06	0.05	0.01	0.00
H_2O-	0.10	0.10	0.11	0.12	0.05
LOI	0.17	−0.28	−0.13	2.30	0.14
Total	100	100	100	100	100

*Ferrous iron recalculated to ferric iron

B.2 Microprobe analysis

Table B.2: Microprobe analysis of selected pyroxene grains by EMP.

					Enstatite					
	SiO_2	MgO	TiO_2	Al_2O_3	Na_2O	Cr_2O_3	CaO	MnO	FeO	K_2O
	55.45	30.74	0.11	1.40	0.03	0.50	0.45	0.24	11.08	–
	55.71	30.77	0.12	1.15	–	0.40	0.92	0.23	10.69	–
	55.39	30.96	0.16	1.17	–	0.47	0.61	0.24	11.02	–
	55.43	30.23	0.11	1.23	0.02	0.50	1.86	0.21	10.42	–
	55.42	31.02	0.11	1.21	0.01	0.46	0.58	0.28	10.91	–
	55.85	31.52	0.10	1.31	–	0.51	0.72	0.26	9.73	–
	55.24	30.92	0.15	1.16	0.00	0.50	0.64	0.29	11.10	–
	55.93	31.14	0.08	1.04	0.03	0.34	0.48	0.23	10.74	–
	55.22	31.26	0.10	1.18	0.01	0.44	0.64	0.25	10.91	–
	55.26	30.76	0.20	1.06	0.02	0.45	1.28	0.24	10.73	–
	55.47	30.64	0.18	1.12	0.01	0.50	0.81	0.27	11.00	–
	55.66	30.10	0.10	1.29	0.04	0.56	2.95	0.24	9.06	–
	55.60	31.57	0.09	1.14	0.01	0.44	1.29	0.19	9.65	–
	55.55	30.73	0.12	1.17	0.04	0.48	0.62	0.25	11.04	–
	55.50	29.47	0.12	1.41	0.03	0.48	2.30	0.29	10.40	–
	55.39	30.67	0.11	1.15	0.01	0.49	1.49	0.27	10.41	–
	55.49	31.73	0.10	1.21	0.03	0.49	0.89	0.24	9.82	–
	55.12	30.96	0.12	1.27	–	0.43	0.66	0.26	11.17	–
	55.63	30.98	0.08	1.16	–	0.43	0.78	0.25	10.70	–
	55.45	31.25	0.09	1.14	–	0.46	0.65	0.19	10.77	–
	55.30	30.94	0.11	1.15	0.03	0.40	0.74	0.25	11.08	–
Average	55.48	30.87	0.12	1.20	0.02	0.46	1.02	0.25	10.59	–
Std. dev.	0.20	0.51	0.03	0.09	0.01	0.05	0.65	0.03	0.57	–
RDS (%)	0.36	1.65	25.92	7.86	54.85	10.09	63.86	11.05	5.42	–
					Augite					
	SiO_2	MgO	TiO_2	Al_2O_3	Na_2O	Cr_2O_3	CaO	MnO	FeO	K_2O
	52.73	12.16	0.01	0.27	0.03	0.04	23.21	0.28	11.27	–
	52.01	12.35	0.27	1.34	0.16	0.02	21.62	0.28	11.95	–
	51.01	12.69	0.48	1.69	0.18	0.02	14.89	0.35	18.67	0.01
	51.13	12.62	0.43	1.71	0.15	0.05	20.10	0.28	13.53	–
	51.96	12.22	0.24	1.08	0.11	0.02	21.69	0.33	12.35	–
	52.15	11.69	0.31	1.68	0.19	0.04	21.31	0.35	12.28	0.00
	52.69	12.02	0.03	0.17	0.02	–	22.31	0.33	12.43	0.00
	52.19	12.01	0.11	0.89	0.17	0.01	21.70	0.34	12.59	–
	52.02	13.28	0.37	2.17	0.19	0.06	20.10	0.25	11.54	0.00
	52.12	13.14	0.35	2.15	0.26	0.08	19.80	0.24	11.85	0.01
	51.28	12.13	0.48	2.18	0.28	0.02	18.81	0.35	14.47	0.01
	50.99	12.90	0.46	2.15	0.19	0.07	20.71	0.30	12.24	–
	51.46	12.54	0.27	1.59	0.21	0.03	20.88	0.31	12.70	–
	52.35	12.74	0.09	0.61	0.06	0.01	22.25	0.28	11.62	–
	51.21	13.66	0.46	2.54	0.21	0.05	19.81	0.19	11.87	0.00
	50.53	12.42	0.42	2.41	0.25	0.07	21.15	0.29	12.46	0.01
	51.43	11.64	0.32	1.51	0.23	–	20.18	0.31	14.38	0.00
	51.92	13.38	0.41	4.11	0.64	0.03	11.75	0.20	17.55	0.00
	51.15	12.07	0.39	2.01	0.22	0.05	20.79	0.28	13.03	0.01
Average	51.70	12.51	0.31	1.70	0.20	0.04	20.16	0.29	13.09	0.00
Std. dev.	0.62	0.57	0.15	0.91	0.13	0.02	2.68	0.05	1.97	0.00
RDS (%)	1.20	4.56	49.02	53.36	65.50	53.31	13.29	16.04	15.07	66.17

Continued on next page

Table B.2 – continued from previous page

					Diopside					
	SiO_2	MgO	TiO_2	Al_2O_3	Na_2O	Cr_2O_3	CaO	MnO	FeO	K_2O
	54.86	17.92	0.24	0.08	0.06	0.03	24.63	0.13	2.05	0.00
	54.99	17.50	0.21	0.04	0.14	0.05	24.88	0.07	2.13	0.00
	54.84	17.85	0.17	0.10	0.10	0.05	24.75	0.04	2.08	0.02
	54.76	17.90	0.24	0.10	0.08	0.07	24.83	0.09	1.91	0.02
	54.89	17.74	0.19	0.04	0.13	0.08	24.82	0.03	2.07	0.01
	54.89	17.76	0.22	0.07	0.13	0.06	24.81	0.05	2.01	0.00
	54.74	18.01	0.24	0.08	0.07	0.03	24.77	0.06	1.98	0.01
	54.93	17.87	0.20	0.08	0.06	0.08	24.71	0.12	1.94	0.01
	55.00	17.99	0.22	0.08	0.06	0.04	24.64	0.05	1.92	0.00
	54.83	17.71	0.21	0.08	0.05	0.09	24.87	0.11	2.03	0.01
	54.62	18.19	0.23	0.57	0.06	0.09	23.39	0.05	2.18	0.61
	54.80	17.93	0.24	0.07	0.05	0.07	24.65	0.11	2.08	–
	54.89	17.93	0.18	0.06	0.03	0.04	24.68	0.12	2.06	–
	54.62	17.77	0.21	0.02	0.17	0.05	24.77	0.07	2.28	0.05
	54.98	17.91	0.22	0.08	0.07	0.06	24.62	0.05	2.00	0.01
	54.42	17.97	0.29	0.10	0.10	0.16	24.98	0.06	1.92	0.01
	54.70	17.99	0.20	0.04	0.04	0.06	24.79	0.04	2.11	0.02
	54.67	18.03	0.25	0.06	0.08	0.07	24.75	0.05	2.04	0.00
	54.57	17.70	0.31	0.10	0.11	0.04	25.09	0.01	2.05	0.01
	54.63	17.68	0.16	0.06	0.06	0.11	24.97	0.05	2.25	0.02
Average	54.78	17.87	0.22	0.10	0.08	0.07	24.72	0.07	2.05	0.04
Std. dev.	0.16	0.16	0.04	0.11	0.04	0.03	0.34	0.03	0.10	0.13
RDS (%)	0.29	0.88	15.89	119.02	43.68	44.95	1.36	50.35	4.95	336.15
					Wollastonite					
	SiO_2	MgO	TiO_2	Al_2O_3	Na_2O	Cr_2O_3	CaO	MnO	FeO	K_2O
	51.73	0.07	0.01	0.01	–	0.02	47.89	0.12	0.14	0.01
	51.85	0.09	–	0.01	–	0.01	47.74	0.14	0.17	–
	51.81	0.02	–	0.01	–	0.02	47.86	0.08	0.20	0.01
	51.71	0.08	0.02	0.02	–	0.04	47.82	0.12	0.19	–
	51.46	0.10	–	0.01	0.02	0.03	48.08	0.13	0.18	–
	51.68	0.04	0.02	0.02	0.00	–	47.91	0.15	0.18	–
	51.51	0.15	0.05	0.02	0.00	0.02	47.92	0.11	0.21	–
	51.54	0.06	0.00	0.02	0.01	–	48.01	0.15	0.21	–
	51.67	0.09	–	0.01	0.02	–	47.95	0.09	0.17	–
	51.95	0.05	–	0.03	0.03	–	47.65	0.16	0.12	0.01
	52.01	0.01	–	0.03	–	–	47.72	0.12	0.12	0.00
	51.99	0.03	0.02	0.03	0.01	0.03	47.71	0.12	0.06	–
	51.99	0.12	–	0.03	–	0.01	47.57	0.10	0.18	–
	52.07	0.06	–	0.03	–	–	47.49	0.14	0.19	0.02
	51.94	0.03	0.02	–	–	0.03	47.69	0.15	0.14	–
	52.24	0.09	–	0.01	–	0.00	47.43	0.05	0.18	0.00
	52.03	0.09	–	0.00	–	0.01	47.49	0.15	0.23	–
	51.90	0.06	0.04	0.00	–	0.00	47.76	0.09	0.14	0.01
	52.03	0.07	0.01	–	–	–	47.52	0.15	0.22	0.00
	52.01	0.07	–	–	0.01	0.02	47.70	0.10	0.10	–
	51.97	0.05	0.02	–	–	0.03	47.60	0.15	0.18	–
	51.87	0.10	0.03	0.01	0.00	–	47.59	0.15	0.24	–
Average	51.86	0.07	0.02	0.02	0.01	0.02	47.73	0.12	0.17	0.01
Std. dev.	0.20	0.03	0.01	0.01	0.01	0.01	0.18	0.03	0.04	0.01
RDS (%)	0.39	49.63	65.61	56.13	80.63	59.64	0.38	22.92	26.29	83.66

B.3 XRD and QXRD

Table B.3: QXRD mineralogy data for feed samples

Mineral	**wt.%**
Tailings	
Biotite	1.6
Chalcopyrite	0.8
Pentlandite	0
Pyrrhotite	0
Chromite	0
Diopside	7.5
Hornblende	5.9
Serpentine (Lizardite)	0.4
Plagioclase (An85)	27.2
Talc	1.8
Quartz	0
Pyrite	0.3
Enstatite	40.7
Epidote	6.8
Calcite	1.9
Chlorite	5.1
TOTAL	100
Enstatite	
Enstatite	52
Bytownite An85	7
Bronzite	41
TOTAL	100
Augite	
Augite Px	96
Magnetite	1
Ilmenite	3
TOTAL	100
Diopside	
Diopside	100
TOTAL	100
Wollastonite	
Wollastonite 1T	41
Wollastonite 2M	59
TOTAL	100

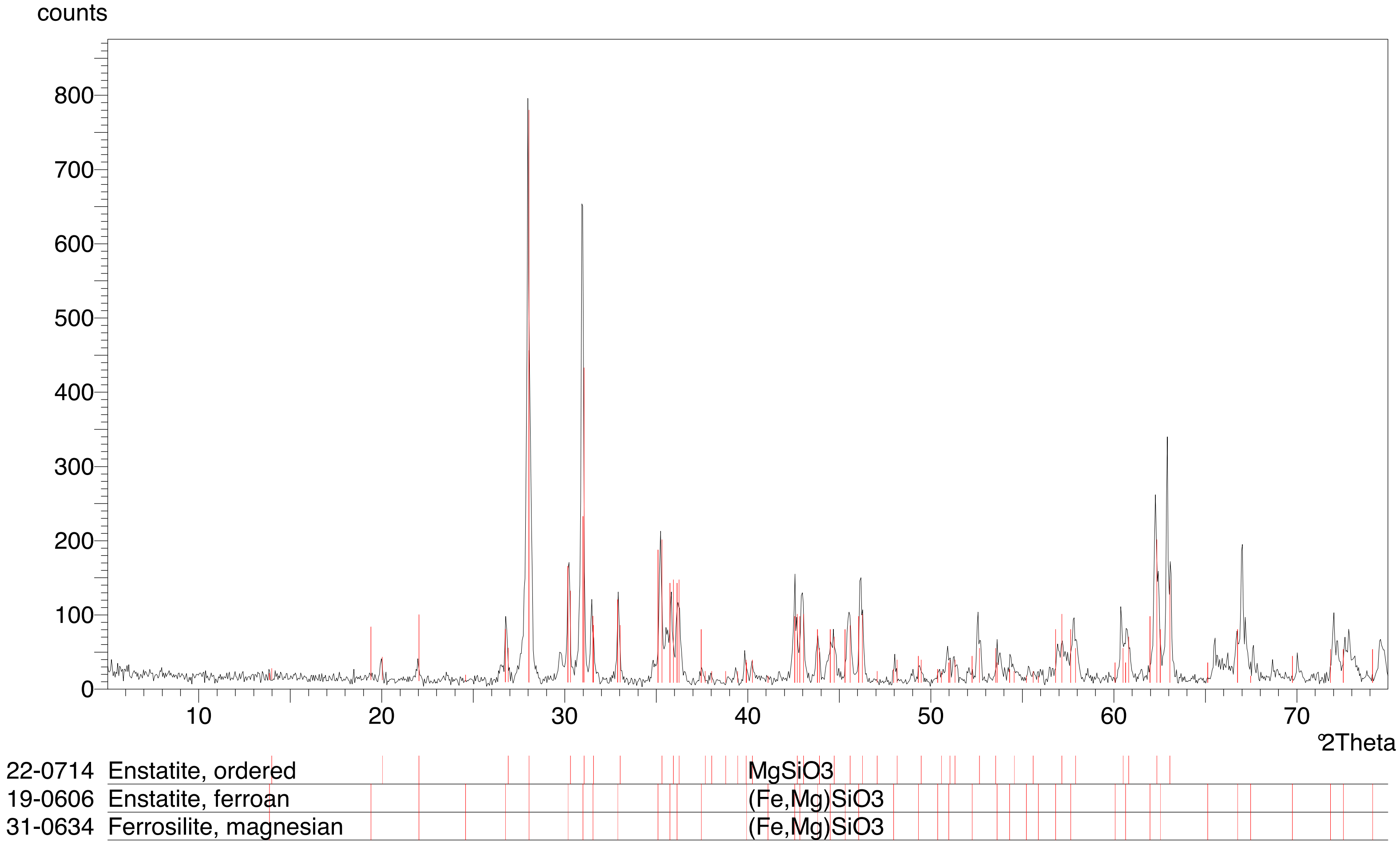

Figure B.1: Enstatite sample diffraction pattern with peak match for enstatite compositions.

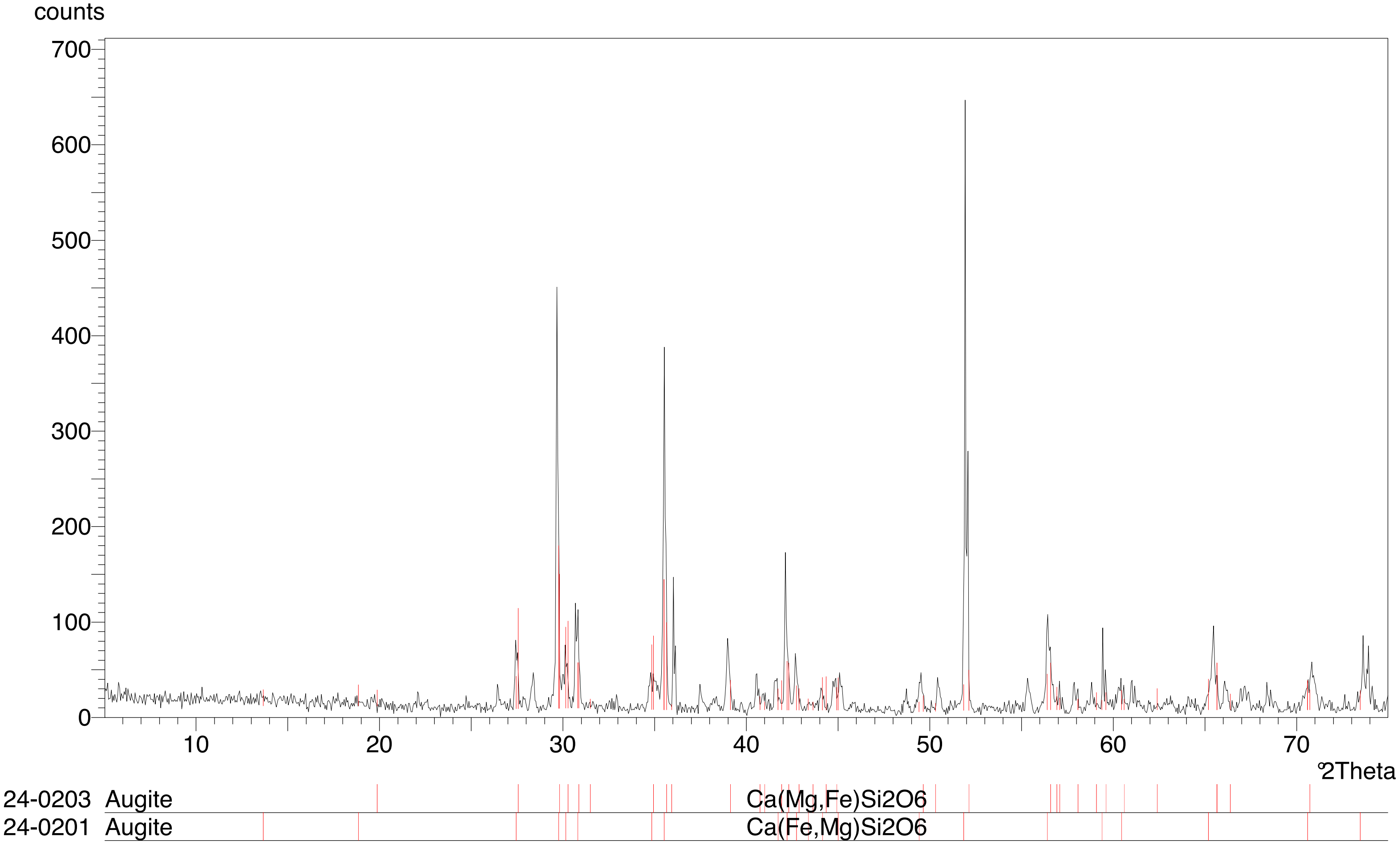

Figure B.2: Augite sample diffraction pattern with peak match for augite compositions.

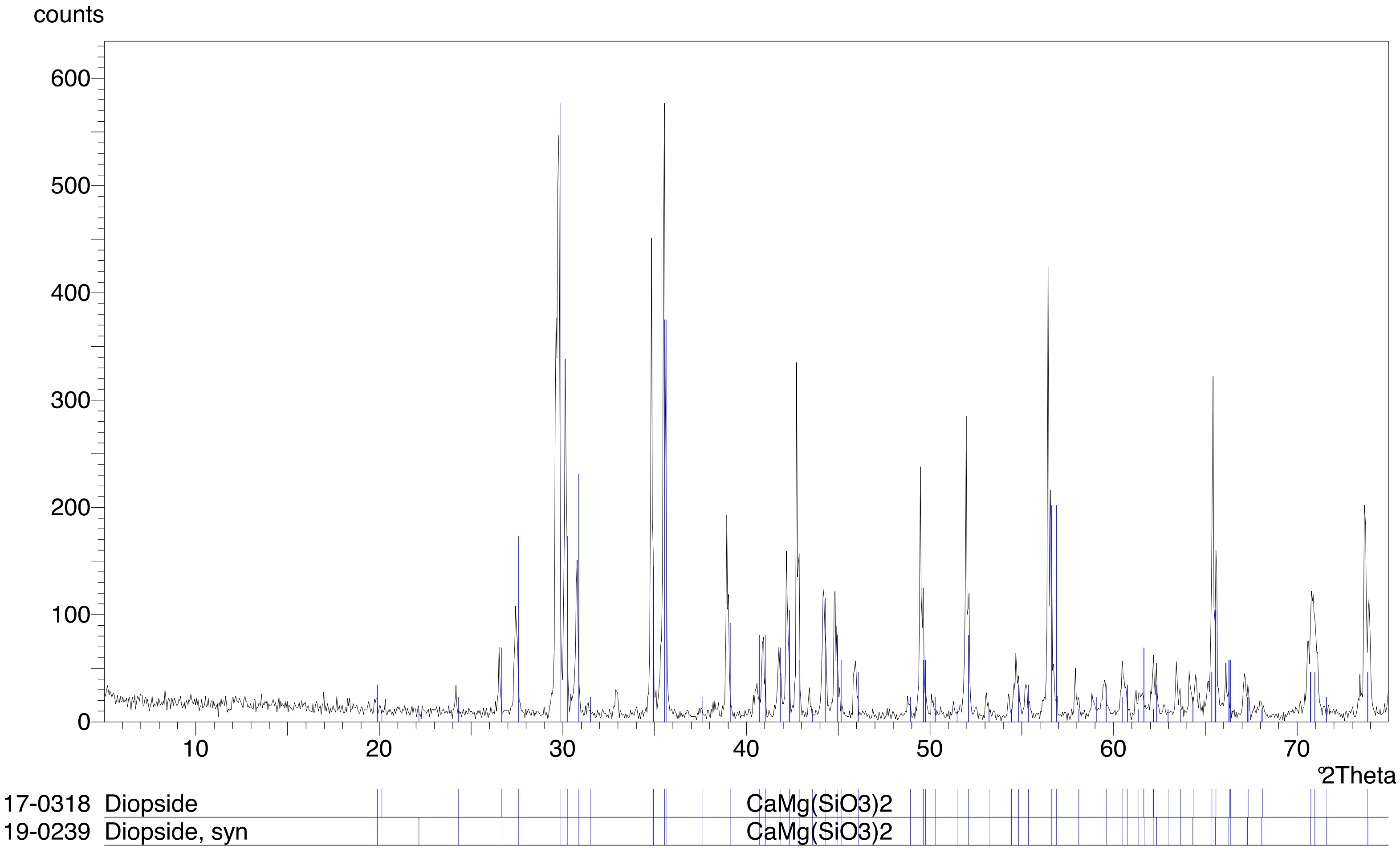

Figure B.3: Diopside sample diffraction pattern with peak match for diopside compositions.

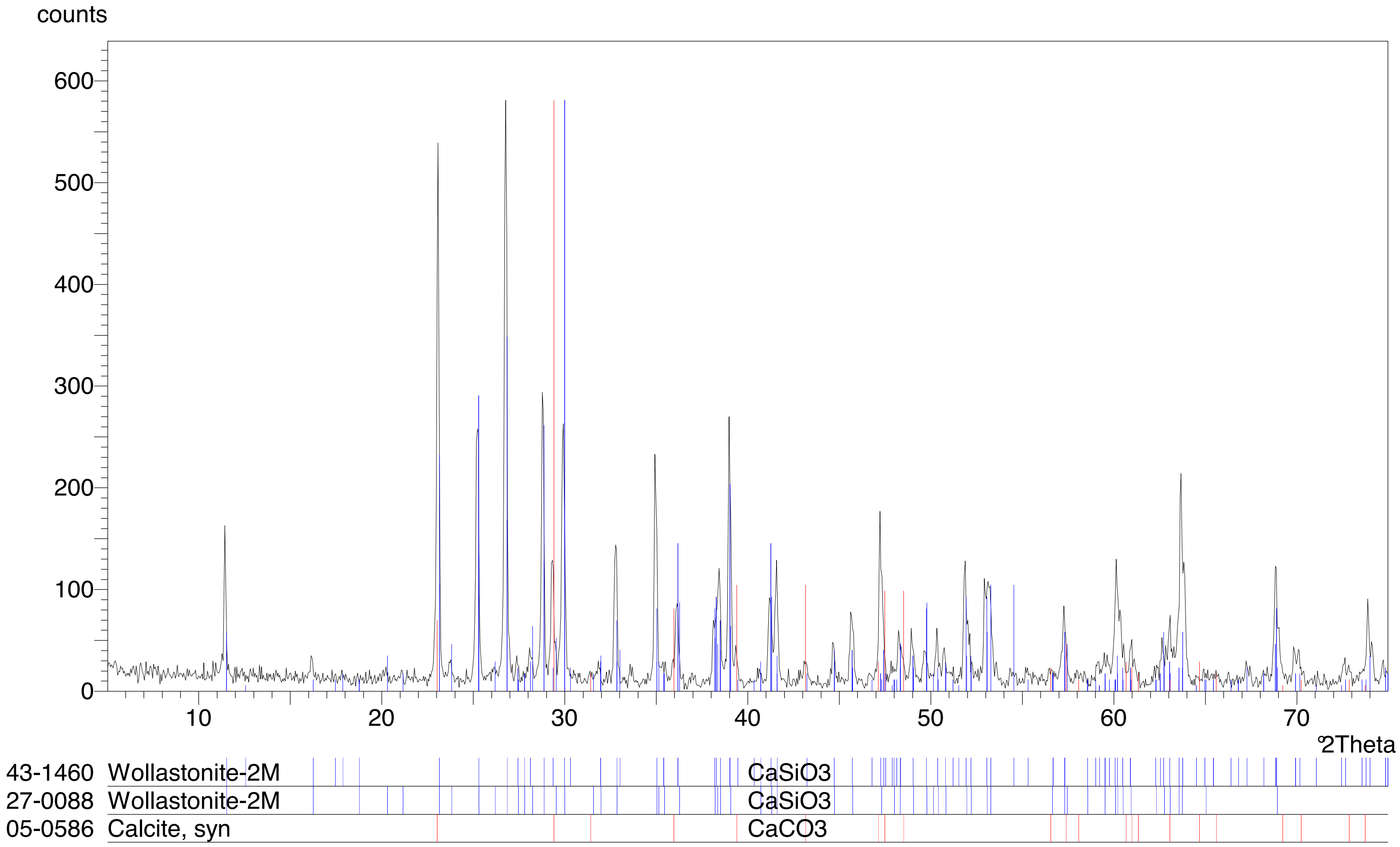

Figure B.4: Wollastonite sample diffraction pattern with peak match for wollastonite composition.

B.4 QEMSCAN

Table B.4: QEMSCAN mineralogy data for feed samples

Cation	**Tailings**	**Enstatite**	**Augite**	**Diopside**	**Wollastonite**
Al	3.1	0.2	3.0	0.5	0.7
Ca	2.8	0.4	13.1	17.8	29.7
Fe	16.6	20.8	4.1	0.0	1.9
K	0.0	0.0	0.0	0.0	–
Mg	8.3	9.7	9.5	11.0	0.3
Mn	0.0	0.0	0.0	0.0	–
Na	0.6	0.0	0.8	0.0	–
Si	23.7	25.5	22.8	25.6	22.8
Ti	0.1	0.0	1.1	0.0	–
Mineral	**Tailings**	**Enstatite**	**Augite**	**Diopside**	**Wollastonite**
Sulphides	0.5	–	–	–	–
Olivine	0.3	2.4	2.3	0.0	0.0
Orthopyroxene	67.4	84.8	1.5	0.1	0.1
Clinopyroxene	6.7	1.5	77.0	94.5	86.3
Amphibole	1.6	0.3	8.9	2.9	0.8
Serpentine	0.0	0.0	0.0	0.0	0.0
Talc	0.8	0.0	0.9	0.0	0.0
Chlorite	0.8	0.1	0.2	0.0	0.0
Biotite	0.9	–	–	–	–
Plagioclase	17.8	1.3	1.1	0.3	0.4
Alkali Feldspar	0.3	0.0	0.0	0.1	0.1
Quartz	1.0	8.1	2.1	0.5	1.4
Carbonate	0.0	0.0	0.0	0.0	4.4
Chromite	2.4	–	–	–	–
Fe oxides	3.0	1.0	5.1	0.2	0.1
Other	0.2	0.0	0.9	0.8	5.7
TOTAL	100.0	99.6	99.9	99.3	99.3

B.5 Mineral deportment

Table B.5: Al, Ca, Fe, Mg, and Si deportment of pyroxene-rich PGM tailings of each mineralogical phase present.

	Element				
	Al	**Ca**	**Fe**	**Mg**	**Si**
Sulphides	0.0	–	2.3	–	0.0
Olivine	–	–	0.5	0.5	0.2
Orthopyroxene	–	–	74.4	88.8	70.9
Clinopyroxene	4.7	26.5	1.7	4.0	5.1
Amphibole	–	7.0	1.1	2.7	3.0
Serpentine	–	–	0.1	0.1	0.1
Talc	–	–	–	1.4	1.2
Chlorite	2.5	0.2	1.5	0.8	0.5
Biotite	2.3	–	0.5	0.8	0.7
Plagioclase	83.8	63.1	6.6	0.1	16.1
Alkali Feldspar	0.4		–	–	0.1
Quartz	0.0	0.0	–	–	1.6
Carbonate	–	2.0	–	0.0	0.3
Chromite	5.2	–	7.4	0.7	–
Fe oxides	0.1	–	3.0	–	–
Other	1.0	1.1	1.0	0.0	0.1
TOTAL	100.0	100.0	100.0	100.0	100.0

Table B.6: Ca, Fe, Mg, and Si deportment of pyroxene and pyroxenite feed samples of each mineralogical phase present.

Ca deportment				
	Enstatite	**Augite**	**Diopside**	**Wollastonite**
Orthopyroxene	0.6	24.9	35.0	–
Clinopyroxene	0.0	0.0	0.0	0.6
Wollastonite	–	–	–	58.5
Other Fe-Mg minerals	0.1	1.2	0.6	0.1
Al-silicates	0.1	0.1	0.0	0.0
Quartz	–	–	–	–
Fe deportment				
	Enstatite	**Augite**	**Diopside**	**Wollastonite**
Orthopyroxene	41.5	1.4	0.0	0.1
Clinopyroxene	0.0	5.3	0.0	0.0
Wollastonite	–	–	–	–
Other Fe-Mg minerals	0.0	1.6	0.0	0.0
Al-silicates	–	–	–	3.7
Quartz	–	–	–	–
Mg deportment				
	Enstatite	**Augite**	**Diopside**	**Wollastonite**
Orthopyroxene	19.0	1.5	0.0	0.0
Clinopyroxene	0.3	15.1	21.2	0.4
Wollastonite	–	–	–	–
Other Fe-Mg minerals	0.1	2.4	0.9	0.2
Al-silicates	–	–	–	–
Quartz	–	–	–	–
Si deportment				
	Enstatite	**Augite**	**Diopside**	**Wollastonite**
Orthopyroxene	49.4	1.6	0.0	0.1
Clinopyroxene	0.8	36.2	49.0	0.8
Wollastonite	0.0	0.0	0.0	41.0
Other Fe-Mg minerals	0.2	5.4	1.6	0.4
Al-silicates	0.5	1.9	0.4	2.9
Quartz	0.1	0.5	0.2	0.4

Appendix C

Leach reactions

C.1 Mixture experiments

Table C.1: Leachate results from the mixture experiments from the first phase of experiments.

	Al			**Ca**			**Fe**			**Mg**			**Si**		
Time (h)	**ppm**	**%RSD**	**Xal%**	**ppm**	**%RSD**	**Xca%**	**ppm**	**%RSD**	**Xfe %**	**ppm**	**%RSD**	**Xmg %**	**ppm**	**%RSD**	**Xsi%**
Mixture 1, Run 1															
0.5	65.76	1.3	6.86	56.09	0.4	6.78	60.60	0.2	3.95	48.16	2.0	2.07	39.26	0.6	0.81
1	98.12	0.6	10.13	69.20	0.5	8.27	72.95	0.5	4.70	60.25	1.2	2.56	55.62	0.4	1.13
1.5	121.24	1.3	12.53	80.54	0.6	9.63	79.22	1.4	5.11	67.14	0.1	2.85	67.59	0.5	1.38
2	142.42	0.7	14.74	90.61	0.6	10.85	85.95	0.8	5.55	72.96	0.4	3.10	77.48	0.5	1.58
2.5	154.19	0.5	15.98	98.19	0.4	11.77	87.94	0.6	5.68	75.61	0.4	3.21	83.97	0.7	1.71
3	165.03	0.7	17.14	104.12	0.5	12.50	91.11	0.9	5.89	79.41	1.0	3.38	89.46	0.8	1.82
3.5	179.47	0.6	18.68	111.56	0.4	13.41	94.19	0.2	6.09	81.26	0.2	3.46	95.63	0.3	1.95
4	190.29	0.5	19.85	117.59	0.2	14.16	97.33	0.3	6.30	84.49	0.7	3.59	101.08	0.3	2.06
4.5	199.16	0.7	20.83	122.59	0.2	14.79	98.16	0.6	6.36	85.55	0.3	3.64	104.70	0.3	2.14
5	210.19	0.9	22.03	129.16	0.5	15.61	100.88	0.6	6.54	88.57	0.8	3.77	109.90	0.2	2.24
Mixture 2, Run 2															
0.5	85.65	1.3	8.94	61.61	1.9	7.44	71.41	2.0	4.66	57.87	1.7	2.49	66.16	0.5	1.36
1	137.97	0.3	14.35	95.24	0.2	11.47	81.51	0.2	5.29	68.88	0.1	2.95	97.87	0.0	2.01
1.5	147.97	1.3	15.40	105.44	1.4	12.70	95.45	1.3	6.20	81.00	0.8	3.47	118.37	0.5	2.43
2	163.32	0.7	17.00	120.09	1.0	14.47	98.37	2.0	6.39	84.34	0.7	3.61	132.82	0.8	2.73
2.5	176.25	0.5	18.36	132.11	1.2	15.93	101.40	1.9	6.59	87.87	1.2	3.76	145.44	0.2	2.99
3	189.88	0.2	19.80	145.95	0.3	17.61	104.94	0.4	6.82	90.29	0.8	3.87	158.47	4.0	3.26
3.5	200.49	0.9	20.92	158.47	0.2	19.13	105.95	0.4	6.89	93.22	0.4	3.99	167.56	0.2	3.44
4	211.09	0.1	22.04	169.88	0.5	20.53	108.88	0.3	7.08	93.73	1.2	4.01	176.95	0.5	3.64
4.5	219.37	0.5	22.93	181.09	0.2	21.90	111.50	0.4	7.26	97.06	0.4	4.16	184.93	1.0	3.80
5	226.04	0.3	23.65	189.58	0.2	22.95	111.61	0.9	7.26	98.58	0.4	4.22	189.88	0.5	3.90
Mixture 2, Run 12															
0.5	48.78	3.1	5.09	38.18	0.8	4.61	47.67	0.9	3.11	35.35	0.6	1.52	20.50	2.3	0.42
1	95.65	0.0	9.91	59.39	0.2	7.12	70.50	0.9	4.56	56.46	0.4	2.41	43.13	0.6	0.88
1.5	120.49	0.7	12.49	68.48	0.9	8.22	70.30	3.6	4.55	59.29	2.6	2.53	52.02	0.5	1.06
2	160.29	1.7	16.63	85.75	0.7	10.30	85.75	0.3	5.55	72.92	0.9	3.11	69.59	0.8	1.42
2.5	183.21	0.7	19.04	98.37	0.2	11.82	91.81	0.6	5.95	79.39	0.4	3.38	78.88	0.8	1.61
3	207.35	0.5	21.58	108.88	0.6	13.10	95.85	0.8	6.21	83.33	0.4	3.55	87.47	1.0	1.79
3.5	219.98	0.8	22.93	113.52	0.1	13.67	97.26	0.5	6.31	84.23	0.9	3.59	92.52	0.3	1.89
4	230.28	0.3	24.05	120.19	0.1	14.49	98.88	0.7	6.41	85.95	0.1	3.67	96.86	0.7	1.98
4.5	249.57	0.4	26.11	128.98	0.2	15.56	102.31	0.1	6.64	89.49	0.6	3.82	103.93	0.5	2.13
5	258.76	0.7	27.13	134.84	0.2	16.29	103.93	0.3	6.75	89.89	0.3	3.84	107.26	0.4	2.20

Continued on next page

Table C.1 – continued from previous page

	Al			Ca			Fe			Mg			Si		
Time (h)	**ppm**	**%RSD**	**Xal%**	**ppm**	**%RSD**	**Xca%**	**ppm**	**%RSD**	**Xfe %**	**ppm**	**%RSD**	**Xmg %**	**ppm**	**%RSD**	**Xsi%**
Mixture 3, Run 3															
0.5	87.87	0.8	9.17	69.59	0.3	8.41	66.16	0.4	4.31	51.91	0.8	2.23	62.92	1.5	1.30
1	134.03	0.7	13.86	90.90	0.4	10.88	79.08	0.1	5.11	65.15	0.4	2.77	95.95	0.6	1.96
1.5	174.53	0.4	18.07	116.86	0.1	14.01	89.08	0.3	5.76	75.35	0.5	3.21	122.72	0.8	2.51
2	201.80	0.3	20.94	128.67	0.1	15.44	93.53	0.2	6.05	79.59	0.6	3.39	136.75	0.6	2.79
2.5	222.91	0.7	23.18	138.88	0.2	16.70	96.35	0.8	6.23	82.42	0.3	3.51	146.45	0.4	2.99
3	243.61	0.7	25.39	150.29	0.4	18.10	99.69	0.7	6.45	85.95	0.3	3.66	157.66	0.1	3.22
3.5	259.07	0.3	27.07	159.08	0.3	19.19	101.61	0.2	6.58	85.75	0.1	3.65	166.45	0.2	3.40
4	276.13	0.7	28.93	167.66	0.6	20.27	105.44	0.6	6.83	89.69	0.6	3.82	175.94	0.2	3.60
4.5	287.75	0.2	30.24	173.82	0.2	21.05	106.76	0.8	6.92	90.09	0.8	3.84	180.49	0.2	3.69
5	297.55	0.7	31.36	178.16	0.1	21.63	106.05	0.5	6.88	89.69	0.3	3.83	183.52	0.3	3.76
Mixture 4, Run 4															
0.5	74.44	2.0	7.77	58.78	0.5	7.10	64.03	0.2	4.18	45.45	0.8	1.95	44.54	0.4	0.92
1	119.99	0.6	12.43	80.09	0.4	9.61	80.50	0.4	5.21	62.52	0.4	2.66	70.30	0.3	1.44
1.5	154.53	0.1	16.02	93.02	0.6	11.17	89.18	1.0	5.77	71.21	1.4	3.03	87.97	0.6	1.80
2	180.99	1.1	18.79	104.13	0.4	12.51	96.25	0.7	6.23	78.48	0.4	3.35	102.82	0.3	2.10
2.5	202.30	0.6	21.04	113.52	0.3	13.65	99.38	1.0	6.44	81.91	0.5	3.49	112.72	0.4	2.31
3	219.57	0.0	22.87	121.60	0.4	14.64	103.32	0.4	6.70	86.66	0.9	3.70	119.69	0.9	2.45
3.5	233.51	0.5	24.37	130.39	0.2	15.72	104.54	0.5	6.78	88.88	0.3	3.79	125.85	0.6	2.58
4	244.22	0.8	25.54	131.40	0.5	15.86	106.35	1.0	6.90	89.99	0.5	3.84	130.90	0.1	2.68
4.5	257.75	0.3	27.01	139.68	0.2	16.88	110.29	0.7	7.16	92.31	0.6	3.94	137.46	0.7	2.81
5	267.95	0.4	28.14	143.72	0.3	17.39	111.10	0.3	7.22	95.24	0.9	4.07	142.81	0.8	2.93
Mixture 5, Run 5															
0.5	33.53	2.4	3.50	19.80	3.8	2.39	38.68	2.2	2.52	28.28	0.9	1.21	32.42	1.2	0.67
1	88.17	0.9	9.13	56.86	1.2	6.82	69.99	0.9	4.53	58.68	0.9	2.50	50.80	0.4	1.04
1.5	126.35	0.2	13.09	82.42	0.6	9.89	80.60	0.1	5.22	71.31	1.0	3.04	61.51	0.1	1.26
2	151.20	1.4	15.69	90.50	1.1	10.86	83.63	0.3	5.41	75.25	0.7	3.21	68.88	0.5	1.41
2.5	173.92	0.5	18.07	107.77	0.3	12.95	91.20	0.4	5.91	82.32	0.6	3.51	75.75	0.2	1.55
3	204.12	4.2	21.23	125.75	5.1	15.12	99.89	1.9	6.47	89.99	3.3	3.84	83.83	3.3	1.72
3.5	214.42	0.8	22.34	127.97	0.3	15.41	99.49	0.5	6.45	90.09	0.1	3.84	85.75	0.2	1.75
4	233.61	0.9	24.39	138.37	0.7	16.68	105.44	0.4	6.84	92.31	0.5	3.94	91.20	0.7	1.87
4.5	238.36	1.2	24.93	140.19	0.3	16.93	102.41	0.7	6.65	91.91	1.1	3.92	92.72	0.2	1.90
5	256.04	0.4	26.84	151.60	0.1	18.33	106.45	0.5	6.91	94.54	0.5	4.04	97.26	0.1	1.99

Continued on next page

Table C.1 – continued from previous page

	Al			Ca			Fe			Mg			Si		
Time (h)	**ppm**	**%RSD**	**Xal%**	**ppm**	**%RSD**	**Xca%**	**ppm**	**%RSD**	**Xfe %**	**ppm**	**%RSD**	**Xmg %**	**ppm**	**%RSD**	**Xsi%**
Mixture 6, Run 6															
0.5	83.33	0.4	8.70	38.38	1.1	4.64	66.36	1.0	4.33	51.51	0.6	2.21	42.62	0.7	0.88
1	123.62	1.9	12.81	68.68	0.9	8.24	78.98	0.6	5.11	63.13	1.1	2.69	55.15	0.2	1.13
1.5	164.43	0.7	17.05	90.90	0.8	10.91	91.91	0.3	5.95	74.84	1.4	3.19	69.79	0.3	1.43
2	182.20	0.3	18.92	99.99	0.6	12.01	95.75	0.5	6.20	78.38	0.7	3.34	76.05	0.2	1.56
2.5	193.01	0.9	20.08	102.72	0.7	12.35	93.93	0.8	6.09	78.07	1.2	3.33	78.17	1.2	1.60
3	215.53	0.3	22.45	116.05	0.7	13.96	100.50	0.6	6.51	83.22	1.7	3.55	86.05	0.2	1.76
3.5	234.12	1.7	24.43	124.94	2.0	15.05	105.44	1.9	6.84	87.97	2.3	3.75	92.01	2.1	1.88
4	255.63	0.2	26.73	135.24	0.2	16.31	112.62	0.9	7.31	92.52	0.5	3.95	99.89	0.5	2.04
4.5	254.62	0.5	26.68	137.16	0.2	16.57	109.38	0.3	7.10	90.90	0.5	3.88	98.68	0.2	2.02
5	273.91	0.8	28.77	144.73	0.2	17.50	114.43	0.3	7.43	96.15	1.0	4.11	104.43	0.4	2.14
Mixture 7, Run 7															
0.5	122.82	1.7	12.82	66.96	0.4	8.09	84.74	1.0	5.53	66.46	1.4	2.85	56.56	0.4	1.17
1	178.77	0.2	18.53	98.58	0.3	11.82	102.41	0.0	6.63	81.20	0.5	3.46	75.65	1.0	1.55
1.5	203.21	0.7	21.09	110.80	0.3	13.30	103.53	0.3	6.70	83.83	1.1	3.57	83.63	0.5	1.71
2	228.77	1.0	23.78	122.92	0.4	14.77	108.17	0.5	7.01	88.07	1.2	3.76	92.31	0.5	1.89
2.5	259.17	1.0	27.00	137.26	0.5	16.52	116.45	0.3	7.55	95.45	0.6	4.07	102.62	0.5	2.10
3	277.55	0.1	28.98	147.86	0.6	17.82	121.50	1.3	7.88	99.79	0.7	4.26	109.59	0.8	2.24
3.5	291.69	0.4	30.52	155.64	0.2	18.78	124.23	0.7	8.06	101.51	0.5	4.33	113.52	0.2	2.32
4	296.33	0.4	31.09	154.23	0.4	18.64	121.00	0.6	7.86	98.48	0.8	4.20	112.82	0.1	2.31
4.5	299.77	0.6	31.52	154.83	0.5	18.74	119.18	0.3	7.74	97.47	0.8	4.16	113.42	0.5	2.32
5	315.63	0.7	33.28	162.81	0.5	19.74	123.93	0.8	8.06	102.01	1.1	4.36	118.47	0.4	2.43
Mixture 7, Run 8															
0.5	59.19	0.7	6.18	26.16	3.2	3.16	62.12	1.1	4.05	43.03	2.3	1.85	33.94	0.8	0.70
1	110.09	0.7	11.40	59.79	0.4	7.17	86.15	0.5	5.57	61.41	1.3	2.62	51.91	0.6	1.06
1.5	139.99	0.5	14.51	76.05	0.6	9.12	94.64	0.2	6.13	68.48	1.4	2.92	61.11	0.6	1.25
2	178.97	0.6	18.58	99.79	0.5	11.98	112.51	0.3	7.29	79.99	1.1	3.41	74.94	0.3	1.53
2.5	197.46	0.8	20.53	108.98	0.4	13.10	117.26	0.4	7.60	84.34	0.3	3.60	80.90	0.8	1.66
3	214.22	1.0	22.31	116.66	0.5	14.03	123.73	0.6	8.02	87.47	0.3	3.73	86.96	0.3	1.78
3.5	230.28	0.3	24.02	124.53	0.3	15.00	128.27	0.7	8.32	90.19	1.0	3.85	92.11	0.4	1.88
4	249.87	0.5	26.12	133.42	0.5	16.09	134.33	0.8	8.72	93.63	0.6	4.00	98.07	0.2	2.01
4.5	256.44	0.7	26.86	136.55	0.6	16.49	135.64	1.2	8.81	93.63	0.3	4.00	100.19	0.9	2.05
5	266.54	0.3	27.98	141.20	0.4	17.07	138.57	0.4	9.01	96.25	1.0	4.11	103.22	5.0	2.11

Continued on next page

Table C.1 – continued from previous page

	Al			Ca			Fe			Mg			Si		
Time (h)	**ppm**	**%RSD**	**Xal%**	**ppm**	**%RSD**	**Xca%**	**ppm**	**%RSD**	**Xfe %**	**ppm**	**%RSD**	**Xmg %**	**ppm**	**%RSD**	**Xsi%**
Mixture 8, Run 9															
0.5	126.65	0.2	13.22	96.25	0.5	11.63	78.07	0.3	5.09	64.24	0.5	2.76	122.51	0.7	2.53
1	181.19	1.9	18.78	127.66	0.8	15.32	93.83	0.7	6.07	75.75	1.7	3.23	172.71	0.8	3.53
1.5	217.15	1.7	22.54	150.09	0.3	18.03	99.18	0.4	6.42	83.02	0.7	3.54	202.00	0.8	4.13
2	246.84	1.1	25.67	170.89	0.4	20.56	103.22	0.3	6.69	87.57	1.5	3.73	225.13	2.9	4.61
2.5	281.49	0.4	29.33	194.93	0.4	23.49	108.98	0.6	7.06	91.30	0.2	3.89	251.39	0.4	5.15
3	305.73	0.0	31.93	208.97	0.5	25.23	110.49	1.3	7.16	92.42	0.5	3.94	265.83	0.9	5.45
3.5	323.20	0.4	33.84	215.84	0.5	26.11	113.22	0.8	7.35	94.13	0.5	4.02	279.97	1.0	5.74
4	340.98	1.2	35.80	234.93	0.6	28.48	116.55	1.0	7.57	96.76	0.5	4.13	292.60	4.0	6.00
4.5	358.25	1.1	37.73	243.21	0.9	29.55	116.96	0.7	7.60	98.07	0.6	4.19	298.66	0.5	6.13
5	372.69	1.4	39.37	244.62	1.4	29.79	119.69	0.4	7.78	99.69	0.9	4.26	312.09	0.9	6.40
Mixture 9, Run 10															
0.5	49.19	0.3	5.13	59.49	0.7	7.19	49.19	0.3	3.21	36.87	1.1	1.58	27.37	1.2	0.56
1	108.47	0.2	11.23	66.76	0.6	8.01	71.21	1.0	4.61	56.16	0.9	2.39	53.33	0.4	1.09
1.5	146.65	1.6	15.20	86.76	0.2	10.41	79.08	0.7	5.12	65.85	0.5	2.81	72.32	0.8	1.48
2	195.23	0.2	20.26	107.46	0.4	12.91	95.75	0.6	6.20	78.78	0.4	3.36	93.12	0.4	1.90
2.5	217.86	0.6	22.65	118.47	0.4	14.24	97.77	0.6	6.33	82.11	0.2	3.50	104.43	0.6	2.14
3	245.33	0.7	25.55	131.30	0.0	15.80	103.63	0.2	6.72	86.96	0.9	3.71	115.04	0.5	2.35
3.5	264.72	0.7	27.63	140.49	0.1	16.93	106.35	0.4	6.90	89.08	0.3	3.80	122.51	0.2	2.51
4	270.68	0.3	28.31	147.97	0.1	17.86	105.65	0.4	6.85	89.18	0.6	3.81	124.53	0.2	2.55
4.5	293.61	0.1	30.78	157.36	0.3	19.02	111.30	0.1	7.23	92.82	0.6	3.96	133.22	0.6	2.73
5	306.94	0.9	32.26	164.02	0.7	19.86	112.72	0.5	7.32	95.45	1.3	4.08	138.77	0.9	2.84
Mixture 10, Run 11															
0.5	60.30	1.4	6.29	52.12	0.0	6.30	58.08	0.6	3.79	44.74	1.1	1.92	34.24	1.5	0.71
1	101.20	1.8	10.48	68.38	0.4	8.20	74.24	0.7	4.80	61.21	0.8	2.61	54.74	0.6	1.12
1.5	137.87	0.6	14.29	80.50	0.6	9.66	84.13	0.9	5.45	70.80	0.2	3.02	70.70	0.8	1.45
2	161.30	0.7	16.74	93.43	0.8	11.22	88.48	0.8	5.73	76.26	0.9	3.25	80.80	0.3	1.65
2.5	190.59	1.6	19.81	108.98	0.6	13.10	95.75	0.7	6.20	82.21	1.2	3.51	92.11	0.1	1.88
3	214.22	0.4	22.30	118.98	0.4	14.32	100.70	0.4	6.53	87.67	1.1	3.74	100.09	0.5	2.05
3.5	225.13	0.9	23.48	122.51	0.3	14.76	100.80	0.6	6.54	88.17	1.0	3.76	107.77	0.6	2.21
4	234.32	0.1	24.48	136.25	0.2	16.43	100.39	0.2	6.51	89.49	0.5	3.82	110.39	0.5	2.26
4.5	251.79	1.0	26.36	136.65	0.5	16.50	103.63	0.5	6.73	92.01	0.5	3.93	117.97	0.2	2.42
5	267.85	1.0	28.10	144.33	0.5	17.46	105.85	0.8	6.88	93.73	0.5	4.00	123.42	0.7	2.53

Continued on next page

Table C.1 – continued from previous page

	Al			Ca			Fe			Mg			Si		
Time (h)	**ppm**	**%RSD**	**Xal%**	**ppm**	**%RSD**	**Xca%**	**ppm**	**%RSD**	**Xfe %**	**ppm**	**%RSD**	**Xmg %**	**ppm**	**%RSD**	**Xsi%**
Mixture 11, Run 12															
0.5	48.78	3.1	5.09	38.18	0.8	4.61	47.67	0.9	3.11	35.35	0.6	1.52	20.50	2.3	0.42
1	95.65	0.0	9.91	59.39	0.2	7.12	70.50	0.9	4.56	56.46	0.4	2.41	43.13	0.6	0.88
1.5	120.49	0.7	12.49	68.48	0.9	8.22	70.30	3.6	4.55	59.29	2.6	2.53	52.02	0.5	1.06
2	160.29	1.7	16.63	85.75	0.7	10.30	85.75	0.3	5.55	72.92	0.9	3.11	69.59	0.8	1.42
2.5	183.21	0.7	19.04	98.37	0.2	11.82	91.81	0.6	5.95	79.39	0.4	3.38	78.88	0.8	1.61
3	207.35	0.5	21.58	108.88	0.6	13.10	95.85	0.8	6.21	83.33	0.4	3.55	87.47	1.0	1.79
3.5	219.98	0.8	22.93	113.52	0.1	13.67	97.26	0.5	6.31	84.23	0.9	3.59	92.52	0.3	1.89
4	230.28	0.3	24.05	120.19	0.1	14.49	98.88	0.7	6.41	85.95	0.1	3.67	96.86	0.7	1.98
4.5	249.57	0.4	26.11	128.98	0.2	15.56	102.31	0.1	6.64	89.49	0.6	3.82	103.93	0.5	2.13
5	258.76	0.7	27.13	134.84	0.2	16.29	103.93	0.3	6.75	89.89	0.3	3.84	107.26	0.4	2.20
Mixture 12, Run 13															
0.5	26.16	1.5	2.73	31.71	0.7	3.83	28.79	0.9	1.88	18.48	1.3	0.79	6.77	1.0	0.14
1	49.39	0.7	5.11	38.38	0.7	4.60	42.12	0.9	2.72	31.71	1.7	1.35	19.09	1.3	0.39
1.5	82.82	1.6	8.58	56.06	0.8	6.72	58.38	1.2	3.78	47.17	0.7	2.01	34.14	0.7	0.70
2	96.56	0.2	10.01	58.88	0.4	7.07	60.20	0.6	3.90	50.20	0.9	2.14	40.40	1.4	0.83
2.5	126.86	6.0	13.16	72.42	6.8	8.69	70.20	5.4	4.54	61.71	5.6	2.63	53.13	6.3	1.09
3	150.39	0.5	15.62	83.63	0.1	10.05	78.68	0.1	5.10	68.38	0.6	2.91	63.53	0.3	1.30
3.5	165.74	0.4	17.23	91.10	0.4	10.95	80.90	0.8	5.24	71.00	0.2	3.03	69.89	0.4	1.43
4	177.96	2.3	18.53	94.94	2.0	11.43	83.33	0.6	5.40	71.91	3.1	3.07	75.45	2.3	1.54
4.5	193.11	0.4	20.14	102.21	0.2	12.31	86.25	0.3	5.59	76.76	0.6	3.27	80.50	0.4	1.65
5	203.52	0.4	21.26	106.86	0.1	12.89	88.58	0.3	5.75	78.28	0.1	3.34	85.04	0.4	1.74

C.2 Extended 100-day leach

Table C.2: Leachate results from the extended 100-day leach experiment from the first phase of experiments.

	Al		**Ca**		**Fe**		**Mg**		**Si**	
Day	**ppm**	**Xal%**	**ppm**	**Xca%**	**ppm**	**Xfe %**	**ppm**	**Xmg %**	**ppm**	**Xsi%**
1	41.11	4.30	17.88	2.17	58.28	3.81	34.24	1.47	26.26	0.54
2	73.93	7.74	41.71	5.05	73.23	4.79	48.78	2.10	36.46	0.75
3	89.59	9.38	50.40	6.11	77.87	5.09	53.63	2.31	41.01	0.85
4	87.97	9.22	46.76	5.67	71.31	4.67	51.01	2.20	39.79	0.82
5	96.66	10.14	51.71	6.27	74.34	4.87	54.04	2.33	41.92	0.87
6	120.19	12.62	66.56	8.08	86.96	5.69	62.01	2.67	48.48	1.00
7	128.37	13.49	71.31	8.66	88.38	5.79	64.34	2.77	50.10	1.04
8	135.95	14.30	76.15	9.26	89.08	5.84	66.46	2.87	51.91	1.07
9	199.98	21.06	164.33	19.99	116.76	7.66	90.80	3.92	164.13	3.39
10	178.97	18.88	128.37	15.64	100.60	6.60	75.95	3.28	145.74	3.01
11	182.81	19.31	126.65	15.45	99.49	6.53	76.96	3.32	147.06	3.04
13	223.21	23.62	152.71	18.65	115.44	7.58	88.27	3.81	169.48	3.51
14	237.96	25.23	161.30	19.73	119.69	7.87	90.60	3.91	180.39	3.73
15	213.51	22.68	158.37	19.40	113.52	7.47	84.84	3.66	152.51	3.16
18	252.60	26.88	138.88	17.04	117.56	7.74	95.34	4.12	87.37	1.81
22	214.02	22.82	111.71	13.72	90.60	5.97	75.04	3.24	60.80	1.26
25	253.81	27.12	127.16	15.64	104.43	6.88	85.95	3.72	74.13	1.54
31	297.34	31.84	147.97	18.22	117.36	7.74	97.36	4.21	81.31	1.68
37	319.26	34.27	122.31	15.09	119.08	7.85	96.35	4.17	115.95	2.40
44	358.05	38.54	219.17	27.06	123.93	8.18	98.58	4.26	190.59	3.95
51	387.44	41.83	215.13	26.62	130.49	8.62	106.56	4.61	118.47	2.46
65	386.22	41.84	193.92	24.05	129.28	8.54	111.50	4.83	84.23	1.75
80	410.77	44.65	–	–	134.53	8.90	115.75	5.01	185.84	3.85
94	421.93	46.03	299.82	37.25	127.61	8.45	109.59	4.75	109.38	2.27
100	421.62	46.17	276.29	34.43	124.03	8.21	102.11	4.43	178.01	3.69

C.3 Pyroxene and pyroxenoid dissolution

Table C.3: Leachate results from the pyroxene and pyroxenoid dissolution experiments from the second phase of experiments.

	Ca		**Fe**		**Mg**		**Si**	
Time (h)	**ppm**	**Xca%**	**ppm**	**Xfe %**	**ppm**	**Xmg %**	**ppm**	**Xsi%**
Experiment 1								
1	–	–	56	8.29	29	0.79	19	0.39
3	–	–	59	8.68	34	0.92	32	0.63
7	–	–	63	9.26	39	1.05	46	0.92
12	–	–	65	9.65	43	1.16	56	1.13
24	–	–	70	10.28	50	1.35	75	1.50
48	–	–	77	11.38	60	1.62	92	1.85
Experiment 2								
1	1961	27.94	–	–	–	–	102	2.16
3	2066	29.27	–	–	–	–	61	1.28
7	1870	26.55	–	–	–	–	93	1.95
12	1987	28.27	–	–	–	–	108	2.26
24	2227	31.76	–	–	–	–	47	0.99
48	1777	25.41	–	–	–	–	81	1.69
Experiment 3								
1	139	4.18	–	–	16	0.39	22	0.42
3	144	4.32	–	–	26	0.66	28	0.53
7	153	4.56	–	–	54	1.34	53	1.01
12	176	5.28	–	–	72	1.82	75	1.42
24	188	5.62	–	–	84	2.11	88	1.68
48	235	7.05	–	–	109	2.73	111	2.10
Experiment 4								
1	72	2.81	117	10.65	50	3.23	55	1.24
3	78	3.02	162	14.70	60	3.88	73	1.64
7	86	3.30	185	16.83	65	4.19	90	2.03
12	94	3.62	208	18.93	70	4.55	86	1.94
24	100	3.84	224	20.35	73	4.74	85	1.91
48	120	4.64	253	23.06	81	5.21	93	2.09
Experiment 5 – Samples lost before analysis								
Experiment 6								
1	118	43.44	8	1.19	7	0.18	2	0.04
3	100	36.60	9	1.22	7	0.19	3	0.07
7	88	32.44	12	1.75	10	0.26	6	0.11
12	88	32.62	19	2.66	14	0.38	10	0.19
24	212	78.41	22	3.13	19	0.49	14	0.26
48	328	122.08	41	5.81	35	0.90	29	0.56
Experiment 7								
1	903	29.15	36	25.41	38	1.02	33	0.67
3	475	15.24	54	38.09	61	1.64	52	1.06
7	521	16.74	89	62.35	134	3.60	103	2.11
12	795	25.59	113	79.95	174	4.68	143	2.91
24	869	28.03	162	114.91	237	6.37	222	4.53
48	1048	33.89	229	164.15	322	8.65	352	7.18
Experiment 8								
1	648	25.41	672	62.00	220	14.50	256	5.87
3	821	32.00	1482	136.22	468	30.58	559	12.71
7	868	33.93	2639	245.26	818	53.53	987	22.47
12	736	28.87	3523	334.10	1098	72.23	1314	29.96
24	855	33.61	4059	395.49	1294	85.56	1492	34.10
48	514	20.24	4649	467.94	1458	97.11	1612	36.96

Continued on next page

Table C.3 – continued from previous page

	Ca		Fe		Mg		Si	
Time (h)	**ppm**	**Xca%**	**ppm**	**Xfe %**	**ppm**	**Xmg %**	**ppm**	**Xsi%**
Experiment 9								
1	288051	4125.00	366	1050.45	495	825.21	19210	407.51
3	300793	6377.61	301	935.78	508	900.13	17427	379.09
7	289269	12628.34	330	1110.54	632	1207.10	17352	389.36
12	307019	-727874.16	215	793.00	547	1157.59	16904	391.59
24	289337	-11490.13	244	964.04	532	1241.91	15873	379.70
48	322295	-6643.19	154	658.93	824	2138.33	16184	399.37
Experiment 10								
1	55	20.78	69	10.11	46	1.24	57	1.12
3	67	25.00	75	10.82	56	1.50	81	1.60
7	79	29.65	85	12.23	73	1.94	109	2.13
12	95	36.02	97	14.02	91	2.42	132	2.59
24	94	35.40	121	17.52	129	3.44	169	3.33
48	112	42.44	163	23.61	182	4.84	204	4.01
Experiment 11								
1	91	38.39	15	2.48	8	0.23	5	0.11
3	99	41.31	17	2.71	12	0.36	8	0.17
7	104	43.56	19	2.98	19	0.57	14	0.31
12	123	51.58	23	3.63	31	0.91	23	0.51
24	147	61.89	34	5.45	66	1.95	49	1.08
48	176	74.55	39	6.20	99	2.93	84	1.83
Experiment 12								
1	50	1.59	66	45.25	45	1.19	51	1.02
3	64	2.02	70	48.35	54	1.43	74	1.49
7	81	2.53	78	53.90	69	1.83	100	2.00
12	90	2.85	84	58.37	83	2.19	119	2.38
24	102	3.22	107	74.63	135	3.56	167	3.34
48	120	3.78	133	93.45	187	4.93	198	3.95
Experiment 13 – Samples lost before analysis Experiment 14 – Samples lost before analysis								
Experiment 15								
1	306474	4438.02	1457	4230.25	1492	2516.39	48931	1049.62
3	341900	7615.08	1195	5199.01	1748	3662.82	22935	532.77
7	354168	20442.41	258	1930.74	1305	3879.79	15779	383.01
12	286705	-25514.85	900	7987.53	862	3728.45	15788	395.43
24	282870	-8232.99	220	5494.81	550	3405.15	15715	406.57
48	282768	-4946.07	382	17124.80	506	4316.85	14995	401.10
Experiment 16								
1	274220	3976.41	810	2354.75	465	785.77	37723	810.31
3	266911	5630.63	274	974.30	429	767.52	17749	404.41
7	276587	10687.97	168	647.80	475	905.69	15200	358.01
12	333462	93329.95	237	963.93	1379	2836.02	14892	361.19
24	266907	-11445.82	865	3815.38	596	1589.82	14584	364.33
48	297223	-6627.95	151	961.20	988	3019.71	14247	366.68
Experiment 17								
1	231798	3243.94	991	2780.52	470	766.40	51235	1062.14
3	227982	4274.24	566	2027.04	770	1325.68	35553	799.03
7	277642	7943.29	539	2304.72	610	1176.10	38038	913.76
12	240551	19148.33	480	2522.29	495	1054.65	30259	784.72
24	270115	-39509.12	129	852.87	420	978.32	9736	269.54
48	267012	-9329.48	103	728.85	367	927.22	8002	226.47
72	290861	-5799.41	168	1265.76	843	7888.91	7747	223.32
96	274654	-3731.20	139	1167.42	582	1954.50	7580	222.52

Continued on next page

Table C.3 – continued from previous page

	Ca		Fe		Mg		Si	
Time (h)	**ppm**	**Xca%**	**ppm**	**Xfe %**	**ppm**	**Xmg %**	**ppm**	**Xsi%**
Experiment 18								
1	64	2.53	89	8.24	32	2.10	27	0.61
3	59	2.31	186	17.02	59	3.86	60	1.36
7	60	2.35	283	25.99	85	5.54	91	2.07
12	62	2.42	301	27.70	90	5.85	97	2.20
24	68	2.64	393	36.15	112	7.35	119	2.71
48	80	3.13	465	42.99	127	8.33	133	3.03
72	130	5.07	446	41.34	122	11.17	129	2.93
96	80	3.13	490	45.60	131	8.55	136	3.09
Experiment 19								
1	27	10.64	48	7.26	19	0.53	8	0.16
3	31	11.84	55	8.28	25	0.68	12	0.23
7	29	11.44	58	8.71	29	0.80	17	0.35
12	58	22.54	59	8.89	33	0.90	22	0.44
24	52	20.10	63	9.38	38	1.05	32	0.65
48	54	21.06	65	9.70	43	1.18	42	0.85
72	50	19.59	66	9.87	44	6.63	47	0.96
96	59	23.08	67	10.07	48	1.33	56	1.13
Experiment 20								
1	1554	63.34	3486	333.94	1100	75.13	1040	24.76
3	1649	67.01	4482	437.62	1317	89.78	1180	27.93
7	1930	78.84	4795	485.29	1356	93.13	1214	28.80
12	1774	72.95	5336	562.02	1548	107.12	1325	31.49
24	1541	63.73	6058	668.41	1784	124.52	1506	35.89
48	1499	62.33	6882	802.55	1734	122.23	1720	41.10
Experiment 21								
1	1405	56.81	3473	329.96	1120	75.88	1072	25.30
3	1338	53.91	4415	427.37	1365	92.30	1258	29.53
7	1458	59.00	4669	468.07	1440	98.09	1303	30.65
12	1710	69.51	5434	566.07	1718	117.95	1533	36.16
24	1999	81.71	5977	652.50	1937	134.31	1715	40.55
48	2693	110.82	6526	751.95	2245	157.34	1934	45.89
Experiment 22								
1	128	46.44	13	1.77	7	0.17	2	0.04
3	118	42.87	16	2.21	10	0.27	5	0.09
7	121	44.00	19	2.62	15	0.37	9	0.17
12	126	45.91	20	2.75	21	0.53	14	0.27
24	130	47.47	26	3.62	41	1.05	29	0.56
48	171	62.84	36	4.95	76	1.95	52	0.98
72	170	62.86	37	5.12	82	11.36	63	1.20
96	189	70.09	37	5.13	89	2.28	75	1.41
Experiment 23								
1	2572	38.03	10	30.20	4	6.24	656	14.36
3	3183	46.84	11	32.39	7	12.07	653	14.21
7	3032	44.78	6	16.71	6	10.53	298	6.49
12	2695	39.95	4	13.12	6	10.63	105	2.28
24	3424	50.92	6	17.14	9	15.39	124	2.70
48	3230	48.23	2	6.30	12	19.77	109	2.38
Experiment 24								
1	40	15.32	12	1.78	13	0.36	10	0.21
3	84	31.78	14	2.08	20	0.55	17	0.34
7	86	32.71	18	2.55	28	0.75	28	0.55
12	105	39.89	18	2.68	36	0.96	39	0.77
24	131	49.85	22	3.13	52	1.40	63	1.25
48	179	68.36	29	4.20	79	2.11	102	2.02

Continued on next page

Table C.3 – continued from previous page

	Ca		**Fe**		**Mg**		**Si**	
Time (h)	**ppm**	**Xca%**	**ppm**	**Xfe %**	**ppm**	**Xmg %**	**ppm**	**Xsi%**
Experiment 25								
1	15	6.76	3	0.45	2	0.06	1	0.01
3	10	4.66	4	0.60	2	0.08	1	0.02
7	12	5.22	4	0.74	3	0.11	2	0.04
12	13	5.58	6	0.95	4	0.14	2	0.05
24	9	4.00	6	0.95	6	0.19	4	0.08
48	9	4.23	7	1.12	8	0.25	5	0.13
72	10	4.35	12	1.97	10	1.76	7	0.17
96	9	4.10	36	–	13	0.40	10	0.23
168	11	5.05	37	–	19	0.59	18	0.42
264	12	5.59	38	–	22	0.70	23	0.54
Experiment 26								
1	21	1.06	11	1.24	4	0.34	3	0.09
3	23	1.11	27	3.06	9	0.74	9	0.25
7	24	1.18	62	7.19	17	1.43	22	0.62
12	22	1.06	101	11.61	27	2.23	36	1.03
24	22	1.10	179	20.71	48	3.98	65	1.87
48	22	1.09	281	32.57	74	6.12	104	2.97
72	25	1.22	322	37.50	85	9.79	117	3.36
96	28	1.37	336	39.34	89	7.30	123	3.53
168	30	1.48	344	40.47	92	7.62	125	3.60
264	46	2.24	368	43.53	101	8.35	136	3.91
Experiment 27								
1	24	11.42	1	0.24	2	0.05	1	0.02
3	24	10.99	2	0.29	2	0.06	1	0.02
7	28	12.86	2	0.36	2	0.08	1	0.03
12	24	11.25	2	0.44	4	0.12	2	0.06
24	22	9.98	4	0.77	9	0.29	7	0.17
48	29	13.36	6	1.00	14	0.44	12	0.28
72	32	15.01	6	1.02	14	2.55	15	0.36
96	32	14.87	6	1.04	15	0.49	17	0.42
168	43	20.32	7	1.20	21	0.67	27	0.64
264	52	24.41	8	1.40	27	0.90	38	0.92
Experiment 28								
1	125	45.50	18	2.48	13	0.34	7	0.12
3	130	47.02	22	3.03	25	0.64	14	0.27
7	149	54.06	31	4.29	55	1.40	34	0.64
12	145	52.94	34	4.68	68	1.73	47	0.89
24	204	74.64	40	5.57	94	2.39	73	1.37
48	229	84.41	47	6.57	129	3.30	109	2.05
Experiment 29								
1	882	64.25	4	62.08	2	19.09	274	29.51
3	988	71.69	5	69.64	3	26.53	284	30.38
7	1133	82.81	5	77.83	3	25.00	295	31.66
12	1136	83.73	5	76.32	2	20.78	296	31.88
24	1179	87.59	6	82.19	2	20.98	288	31.18
48	1273	95.46	6	91.21	3	26.94	284	30.78

Continued on next page

Table C.3 – continued from previous page

	Ca		**Fe**		**Mg**		**Si**	
Time (h)	**ppm**	**Xca%**	**ppm**	**Xfe %**	**ppm**	**Xmg %**	**ppm**	**Xsi%**
Experiment 30								
1	30	10.18	69	9.11	33	0.81	19	0.34
3	39	13.15	74	9.70	44	1.06	34	0.61
7	50	16.88	78	10.18	53	1.28	50	0.89
12	56	19.07	81	10.61	59	1.41	62	1.10
24	70	23.82	90	11.74	69	1.66	82	1.45
48	85	29.13	104	13.57	83	1.99	103	1.82
Experiment 31								
1	61	2.43	221	20.60	82	5.48	69	1.61
3	69	2.70	325	30.05	116	7.66	102	2.34
7	75	2.95	390	36.21	135	8.90	117	2.69
12	81	3.19	420	39.12	142	9.38	120	2.75
24	96	3.77	489	45.73	161	10.63	126	2.90
48	108	4.23	558	52.50	182	12.03	134	3.07
Experiment 32								
1	31	11.96	67	10.14	24	0.67	23	0.48
3	16	6.07	8	1.19	5	0.15	3	0.06
7	15	5.94	11	1.61	7	0.20	5	0.10
12	16	6.39	13	1.94	9	0.25	7	0.14
24	17	6.47	16	2.34	11	0.31	9	0.19
48	19	7.53	19	2.82	15	0.41	14	0.28
Experiment 33								
1	15	0.87	6	0.74	4	0.37	2	0.05
3	33	1.87	155	20.41	54	5.10	57	1.87
7	36	2.03	273	35.98	95	8.88	102	3.32
12	39	2.18	350	46.20	121	11.37	128	4.20
24	40	2.26	395	52.48	136	12.78	142	4.65
48	46	2.56	419	55.94	144	13.57	145	4.76

Appendix D

Residue

D.1 XRF

Table D.1: Chemical mineralogy of samples determined by XRF on residue.

Oxide	**Tailings**	**Enstatite**	**Augite**	**Diopside**	**Wollastonite**
SiO_2	53.21	55.25	49.77	54.33	54.67
TiO_2	0.25	0.11	1.41	0.23	0.06
Al_2O_3	4.68	1.57	2.52	0.10	1.19
Fe_2O_3	11.37	9.34	13.06	1.95	0.48
MnO	0.19	0.19	0.23	0.05	0.09
MgO	21.65	29.50	12.43	17.56	0.44
CaO	3.85	1.93	18.12	22.96	29.36
Na_2O	0.82	0.13	0.37	0.18	0.18
K_2O	0.08	0.01	0.06	0.05	0.10
P_2O_5	0.03	0.00	0.01	0.01	0.06
SO_3	0.00	0.00	0.04	0.00	0.00
Cr_2O_3	1.07	0.40	0.05	0.07	0.01
NiO	0.08	0.07	0.04	0.01	0.01
H_2O^-	1.04	0.11	0.19	0.13	1.30
LOI	1.68	0.31	0.25	1.08	6.00
Total	100	100	100	100	100

D.2 QEMSCAN

Table D.2: QEMSCAN mineralogy data for residue samples.

Cation	**Tailings**	**Enstatite**	**Augite**	**Diopside**	**Wollastonite**
Al	3.1	0.2	3.0	0.5	0.7
Ca	2.8	0.4	13.1	17.8	29.7
Fe	16.6	20.0	4.1	0.0	1.9
K	0.0	0.0	0.0	0.0	–
Mg	8.3	10.2	9.5	11.0	0.3
Mn	0.0	0.0	0.0	0.0	–
Na	0.6	0.0	0.8	0.0	–
Si	23.7	24.1	22.8	25.6	22.8
Ti	0.1	0.0	1.1	0.0	–
Mineral	**Tailings**	**Enstatite**	**Augite**	**Diopside**	**Wollastonite**
Orthopyroxene	6.2	91.5	1.0	0.4	0.1
Clinopyroxene	0.4	1.7	49.1	91.9	2.6
Wollastonite	–	0.0	0.0	0.0	77.7
Amphibole*	0.4	–	–	–	–
Other Mg-Fe mineral	0.5	0.6	14.5	6.3	5.8
Al-silicate	1.0	1.8	17.4	0.6	10.1
Quartz	0.3	0.3	0.5	0.4	2.1
Fe oxides	0.2	3.8	16.9	0.31	0.32
Carbonates	–	–	–	–	1.05
Other	1.9	0.2	0.6	0.11	0.25

D.3 EDS

Table D.3: Elemental distribution data from the surfaces of residue pyroxene and pyroxenite samples.

Element	**O**	**Mg**	**Al**	**Si**	**Ca**	**Fe**	**Total**
Enstatite 1.1	51.5	53.2	17.0	23.1	0.3	6.3	100
Enstatite 1.2	43.5	45.8	17.6	26.1	1.2	9.2	100
Enstatite 1.3	32.9	53.9	17.3	22.8	0.0	6.0	100
Enstatite 2.1	49.6	17.4	–	25.0	0.6	7.4	100
Enstatite 2.2	49.4	17.7	0.6	25.2	0.4	6.8	100
Enstatite 2.3	53.0	16.5	–	22.9	0.5	7.2	100
Enstatite 3.1	43.3	17.9	–	28.3	–	10.6	100
Enstatite 3.2	46.1	18.0	–	27.4	–	8.5	100
Enstatite 3.3	49.3	16.1	–	23.7	–	10.9	100
Enstatite 3.4	36.0	18.5	–	32.0	–	13.6	100
Enstaite 4.1	51.5	15.4	0.8	24.0	0.6	7.7	100
Enstaite 4.2	43.5	18.9	–	28.2	–	9.5	100
Enstaite 4.3	32.9	18.3	–	30.0	–	18.8	100
Enstaite 4.4	42.6	18.3	–	29.0	–	10.2	100
Augite 1.1	54.2	6.7	1.1	21.2	9.9	7.0	100
Augite 1.2	55.2	7.2	0.9	20.3	9.6	6.8	100
Augite 1.3	51.9	6.6	1.4	21.6	9.4	8.7	100
Augite 1.4	48.7	6.8	0.7	23.4	11.4	9.0	100
Augite 1.5	52.5	7.1	0.9	21.8	11.2	6.6	100
Augite 2.1	56.2	8.3	1.2	20.7	6.8	6.9	100
Augite 2.2	51.3	7.9	1.1	22.8	10.4	6.6	100
Augite 2.3	52.1	7.4	1.0	21.7	10.3	7.6	100
Augite 2.4	47.7	7.7	1.1	23.8	11.2	8.4	100
Augite 2.5	44.6	7.4	1.0	24.2	15.1	7.6	100
Diopside 1.1	50.6	10.1	–	24.0	14.3	1.0	100
Diopside 1.2	57.8	9.7	–	20.6	10.7	1.3	100
Diopside 1.3	53.8	9.3	–	22.1	13.0	1.7	100
Diopside 1.4	47.0	10.4	–	25.0	16.3	1.3	100
Diopside 2.1	52.3	10.3	–	23.0	13.2	1.2	100
Diopside 2.2	57.3	10.0	–	20.9	10.9	1.0	100
Diopside 2.3	51.8	10.5	–	22.7	14.3	0.8	100
Diopside 2.4	45.8	10.4	–	25.8	16.9	1.1	100
Wollastonite 1.1	12.5	–	–	17.5	70.0	–	100
Wollastonite 1.2	47.2	–	–	20.1	32.7	–	100
Wollastonite 1.3	40.7	–	–	25.2	34.2	–	100
Wollastonite 1.4	62.5	–	–	26.3	11.2	–	100
Wollastonite 2.1	56.4	–	–	22.7	20.9	–	100
Wollastonite 2.2	56.2	–	–	22.7	21.1	–	100
Wollastonite 2.3	51.4	–	–	24.8	23.9	–	100
Wollastonite 2.4	53.7	–	–	23.4	22.9	–	100
Wollastonite 2.5	61.7	–	–	22.1	16.2	–	100